Lehrstuhl für Elektrische Energiespeichertechnik
Fakultät für Elektrotechnik und Informationstechnik
Technische Universität München

Influence of Initial Cell-to-Cell Variations, Different Self-Discharge and Aging Rates on the Utilization of Large Lithium-Ion Battery Packs

Ilya Zilberman M.Sc.

Vollständiger Abdruck der von der Fakultät fü Elektrotechnik und Informationstechnik der Technischen Universität München zur Erlangung des akademischen Grades eines

Doktor-Ingenieur (Dr.-Ing.)

genehmigten Dissertation.

Vorsitzender: Prof. Dr.-Ing. Hans-Georg Herzog
Prüfer der Dissertation: 1. Prof. Dr.-Ing. Andreas Jossen
2. Prof. Dr.-Ing. Julia Kowal

Die Dissertation wurde am 22.04.2020 bei der Technischen Universität Müchen eingereicht und durch die Fakultät für Elektrotechnik und Informationstechnik am 29.07.2020 angenommen.

Kurzfassung

Der Antriebsstrang und insbesondere das Lithium-Ionen-Batteriepack stellen die entscheidenden Kostentreiber für Elektroautos dar. Für die Wettbewerbsfähigkeit gegenüber Autos mit Verbrennungsmotoren ist die vollständige Ausnutzung der Batteriepacks daher maßgeblich. Große Batteriepacks umfassen bis zu Tausende von Lithium-Ionen Zellen und sind in der Leistungsfähigkeit durch die schwächste Zelle begrenzt. Aufgrund von Fertigungstoleranzen weisen Lithium-Ionen Zellen eine Streuung in der Kapazität, Impedanz und den Selbstentladungsraten auf. Trotz gleicher Betriebsbedingungen zeichnen sich Unterschiede im Alterungsverhalten der Zellen ab, was die Streuung der Zellparameter über die gesamte Lebensdauer erhöht. Dieses Verhalten führt zu einer verminderten Ausnutzung des Batteriepacks, was mit unausgeglichenen Spannungen innerhalb der Serienschaltung zusammenhängt und somit die Nutzung von Zellausgleichsystemen erfordert. Der Fokus dieser Arbeit liegt auf der Untersuchung wesentlicher Einflussfaktoren auf das Spannungsungleichgewicht in großen Lithium-Ionen-Batteriepacks. Diese sind verschiedene Selbstentladeraten, unterschiedliche Entropien und Enthalpien aufgrund von unterschiedlichen Alterungsraten, sowie das Lithium-Plating.

Für die experimentelle Evaluierung wurde eine flexible Plattform für Batteriemanagementsysteme (EES-BMS) entwickelt und aufgebaut. Zur Quantifizierung der reversiblen Selbstentladung wurde zudem eine neue spannungsbasierte Messmethode entwickelt. Diese Methode wurde bei 24 Zellen angewandt, um den Einfluss der Streuung der Selbstentladung auf das Spannungsungleichgewicht zu untersuchen. Darüber hinaus wurde eine präzise spannungsbasierte Messmethode der Entropie erarbeitet, mit der der Einfluss der unterschiedlichen Alterungsraten auf die Zellentropie analysiert werden konnte. Des Weiteren wurde ein ganzheitliches Simulationsframework für Batteriesysteme entwickelt und implementiert, welches die Streuung der Zellparameter, unterschiedliche Alterungs- und Selbstentladeraten, Temperaturverteilungen innerhalb des Batteriepacks und verschiedene Ausgleichsalgorithmen abbildet. Unter Verwendung des Frameworks wurde eine Monte Carlo Simulation durchgeführt, um die Auswirkungen der Einflussfaktoren auf das Spannungsungleichgewicht ganzheitlich zu analysieren. Abschließend wurde der Einfluss unterschiedlicher Betriebsbedingungen innerhalb eines 6s1p Moduls auf das Spannungsungleichgewicht evaluiert.

Die Ergebnisse der Arbeit zeigen, dass das Spannungsungleichgewicht sowohl durch unterschiedliche Selbstentladungsraten, als auch durch veränderte Entropien und Enthalpien aufgrund von ungleichen Verlusten des zyklisierbaren Lithiums in einer Serienschaltung verursacht werden können. Diese Effekte tragen im Vergleich zum Lithium-Plating jedoch wesentlich weniger zu einem möglichen Spannungsungleichgewicht bei. Es liegt daher nahe, auf die Ausgleichsysteme zu verzichten, falls ein Batteriesystem weit unter den maximalen Grenzen betrieben wird und die Lithium-Ionen Zellen eine geringe Streuung der intrinsischen Alterungsraten aufweisen. Batteriepacks mit bereits integrierten Ausgleichssystemen können von einem zusätzlichen Signal profitieren, da die kumulierte Ausgleichsladung als Indikator für Lithium-Plating im untersuchten 6s1p Modul verwendet werden konnte.

Abstract

In current electric vehicles (EVs), the powertrain and the battery pack in particular, represent the main contributors to overall cost. With this in mind, full utilization of available battery pack capacity is indispensable if EVs are to compete on price with internal combustion engine (ICE) vehicles. Large battery packs, which can potentially be composed of thousands of cells are usually limited by the performance of the weakest cell. Due to manufacturing tolerances, lithium-ion cells vary slightly in capacity, impedance and self-discharge rates. Furthermore, even under the same operational conditions, such cells exhibit slightly different aging behaviors, aggravating the parameter variations even more. Such behavior results in diminished pack utilization, which is closely linked to voltage imbalance between cells connected in series and provides the motivation for cell balancing. Therefore, the goals of this thesis were to investigate the influence of different self-discharge rates, varying reaction entropies and enthalpies induced through non-identical aging and lithium plating on the voltage imbalance within large lithium-ion battery packs.

For the purpose of the experimental evaluation, a new flexible prototyping platform for battery management systems (EES-BMS) was designed and constructed. In order to quantify the reversible self-discharge, a new voltage-based measurement method was developed. This method was applied to 24 cells, which allowed the investigation of how self-discharge variations influence the voltage imbalance. A novel, precise voltage-based entropy determination method was developed in order to analyze the influence of different aging rates on full-cell entropy profiles. Furthermore, a holistic battery pack lifetime simulation framework was designed and implemented. The framework included cell-to-cell parameter variations, differing aging and self-discharge rates, temperature gradients among the cells and various balancing strategies. A Monte Carlo simulation using this framework was performed in order to investigate the possible interaction between the influencing factors and the voltage imbalance. The outcomes of four studies were verified in the final work presented here, which experimentally evaluated the influence of differing operational conditions within a 6s1p module.

The results presented in this thesis show that voltage imbalance can be caused by both differing self-discharge rates and varying reaction entropies and enthalpies due to non-identical loss of lithium inventory (LLI) in series- connected cells. However, both of these phenomena contribute far less to voltage drift than lithium plating. Therefore, it stands to reason that if the battery system is operated far below the absolute maximum ratings set by the cell manufacturer and the lithium-ion cells exhibit low intrinsic aging variations, balancing circuits can be omitted. Furthermore, battery systems, which are already equipped with balancing hardware or with to retain cell balancing, might profit from utilizing an extra signal, as cumulated balancing charge was successfully used as an indicator of lithium plating in the investigated 6s1p module.

Acknowledgment

This thesis originates from my time as a research associate at the Institute for Electrical Energy Storage Technology (EES) at Technical University of Munich (TUM). First of all, I would like to express my gratitude to Prof. Dr.-Ing. Andreas Jossen for giving me the opportunity to carry out the research work and for supporting me throughout my time at the institute. Furthermore, I would like to thank Prof. Dr.-Ing. Julia Kowal for the co-evaluation of my thesis and Prof. Dr.-Ing. Hans-Georg Herzog for the chairmanship of the defence committee.

During my time at the EES, I was very fortunate to work with many talented and inspiring people. I thank all my colleagues at EES for a consistently pleasant working environment and motivating discussions. I would particularly like to thank Simon Erhard and Andreas Noel for always advising me to identify the right and not the obvious questions and Alexander Rheinfeld for supporting me on finding the path to the corresponding answers. I would also like to thank the whole team BMS for highly valuable exchange and in particular Sebastian Ludwig for steady support during the experimental work. Furthermore, without the technical assistance especially from Korbinian Schmidt, presented experimental results would not have been possible.

Finally, I would like to express my special thanks to Camilla, my family and friends. I was very fortunate to receive unceasing support and love throughout all ups and downs. Without you, this journey would not be possible.

List of Publications

Conference Contributions

(1) **I. Zilberman**, A. Jossen. Influences of the cell and system quality on balancing. IQPC 2016 - Automotive Battery Management Systems, 2016. Berlin.

(2) **I. Zilberman**, A. Jossen. Efficiency of dissipative balancing systems. Batterieforum Deutschland 2017. Berlin.

(3) **I. Zilberman**, A. Jossen. Influence of Long-term Equalization Processes on the Voltage Based Self-discharge Measurements in Li-Ion Cells. IMLB 2018. The 19th International Meeting on Lithium Batteries 2018. Kyoto, Japan.

(4) **I. Zilberman**, F.B. Spingler, A. Rheinfeld A. Jossen. Temperature Path Dependent Voltage and Thermal Expansion Hysteresis in Li-Ion Cells. ECS Meeting 233 2018. Seattle, USA.

(5) **I. Zilberman**, S. Ludwig, A. Jossen. Online Aging Determination with Dissipative Balancing Circuits. Kraftwerk Batterie 2019

Peer-Reviewed Journal Contributions (Co-Author)

(1) C. Campestrini, M.F. Horsche, **I. Zilberman**, T. Heil, T. Zimmermann, A. Jossen. Validation and benchmark methods for battery management system functionalities: State of charge estimation algorithms. In: Journal of Energy Storage (7). P. 38-51. DOI: 10.1016/j.est.2016.05.007.

(2) J. Sturm, A. Rheinfeld, **I. Zilberman**, F.B. Spingler, S. Kosch, F. Frie, A. Jossen. Modeling and simulation of inhomogeneities in a 18650 nickel-rich, silicon-graphite lithium-ion cell during fast charging. In: Journal of Power Sources (412). P. 204-223 DOI: 10.1016/j.jpowsour.2018.11.043

Peer-Reviewed Journal Contributions (Lead Author) *

(1) **I. Zilberman**, A. Rheinfeld, A. Jossen. Uncertainties in Entropy due to Temperature Path Dependent Voltage Hysteresis in Li-Ion Cells. In: Journal of Power Sources (395). P. 179-184. DOI: 10.1016/j.jpowsour.2018.05.052.

(2) **I. Zilberman**, J. Sturm, A. Jossen. Reversible self-discharge and calendar aging of 18650 nickel-rich, silicon-graphite lithium-ion cells. In: Journal of Power Sources (425). P. 217-226. DOI: 10.1016/j.jpowsour.2019.03.109.

(3) **I. Zilberman**, S. Ludwig, A. Jossen. Cell-to-cell variation of calendar aging and reversible self-discharge in 18650 nickel-rich, silicon–graphite lithium-ion cells. In: Journal of Energy Storage (26).

100900. DOI: 10.1016/j.est.2019.100900.

(4) **I. Zilberman**, S. Ludwig, M. Schiller, A. Jossen. Online aging determination in lithium-ion battery module with forced temperature gradient. In: Journal of Energy Storage (28). 101170. DOI: 10.1016/j.est.2019.101170.

(5) **I. Zilberman**, J. Schmitt, S. Ludwig, M. Naumann, A. Jossen. Simulation of Voltage Imbalance in Large Lithium-Ion Battery Packs Influenced by Cell-to-Cell Variations and Balancing Systems. In: Journal of Energy Storage (32). 101828. DOI: 10.1016/j.est.2020.101828.

* Self-produced sections of peer-reviewed lead author journal contributions are partially contained in this thesis without further reference in the running text.

List of Contents

List of Abbreviations

ADC	analog to digital converter
BEV	battery electric vehicle
BMS	battery management system
CC	constant current
CCCV	constant current constant voltage
CV	constant voltage
DC	direct current
DOD	depth of discharge
DVA	differential voltage analysis
EOL	end of line
EV	electric vehicle
IC	integrated circuit
ICE	internal combustion engine
LAM	loss of active material
LFP	lithium iron phosphate
LLI	loss of lithium inventory
LTO	lithium titanate oxide
MJ1	18650 lithium-ion cell from LGChem
NMC	nickel manganese cobalt oxide
OCV	open circuit voltage
PHEV	plug-in hybrid electric vehicle
SEI	solid electrolyte interface
SEM	scanning electron microscope

SiC	silicon-carbon
SNR	signal to noise ratio
SOC	state of charge

1 Introduction to the utilization of lithium-ion battery packs

The rising trend towards decentralized green energy infrastructure, as well as the increasing demand for environmental friendly mobility, have created a need for reliable, economically reasonable and emission-free energy storage solutions. Lithium-ion technology has shown high potential for use in many applications by overcoming the problems of high costs, safety hazards and short system life during the last decades [1][2]. Especially in case of EVs, despite the recent success of fuel cells [3], lithium-ion batteries have become the most widely used energy storage solution.

The vast majority of the world's largest economies represent highly attractive markets for EVs [4]. However, despite the fact that the number of EVs sold has been increasing, especially in China, Europe and the USA [5], the absolute automotive market share is estimated to not exceed 1 % worldwide by the end of 2020 [6]. Despite many efforts, battery electric vehicles (BEVs) still struggle to compete with conventional internal combustion engine (ICE) vehicles. The BEV user experience still differs from the ICE vehicle user experience due to a more limited driving range [7], comparably long charging time [8][9] and sparsely established charging infrastructure [10]. However, the main reason for the disparity is linked to the cost disadvantages of BEVs [11]. The major discrepancy in price between BEVs and ICE vehicles is due to differing cost of their powertrains, although battery pack prices have been falling lately [12][13]. While in the ICE vehicle the powertrain represents only 18 % of the total vehicle cost, the powertrain of a BEV makes up approx. 50 % of the total price. A detailed cost breakdown is shown in Fig. 1.1. The battery pack, at around 35 % of the total vehicle cost, is the most expensive component of a BEV. Of total, 25 % are attributable to battery cell costs and the remaining 10 % to the battery housing, thermal and battery management system (BMS).

In the case that the capacity of the battery pack is not completely utilized, extra capacity must be added to the pack during the design process to achieve the desired energy/power storage capability. Subsequently, due to the high price of lithium-ion cells, a less than total utilization of a battery pack may lead to a significant increase in overall vehicle costs. For instance, a utilization of 10 % less than expected will lead to a 2.5 % increase in the total price of a BEV according to the above mentioned cost structure. Therefore, it stands to reason that the full utilization of the energy content of the pack is essential. In general, the negative effects of a less than total utilization could be reduced by improving the current lithium-ion cell technology or by the deployment of the next generation lithium-ion cells with higher energy densities. However, the energy density of the current lithium-ion storage technology is gradually approaching its limit [14]. Improvements can be expected from the application of high-voltage cathodes [15] and nano-structured anodes [16], but nonetheless, even such improvements do not alter the fact that a complete utilization of the stored energy is desired. A commercial application of the next generation technologies such as lithium-oxygen, lithium-sulfur and sodium-ion systems, which promise higher energy density or highly accessible materials, is still not feasible in the near future [17][18][19]. Finally, despite recent positive technological developments, the promised energy densities typically refer to active materials rather than complete cells, whose ultimate

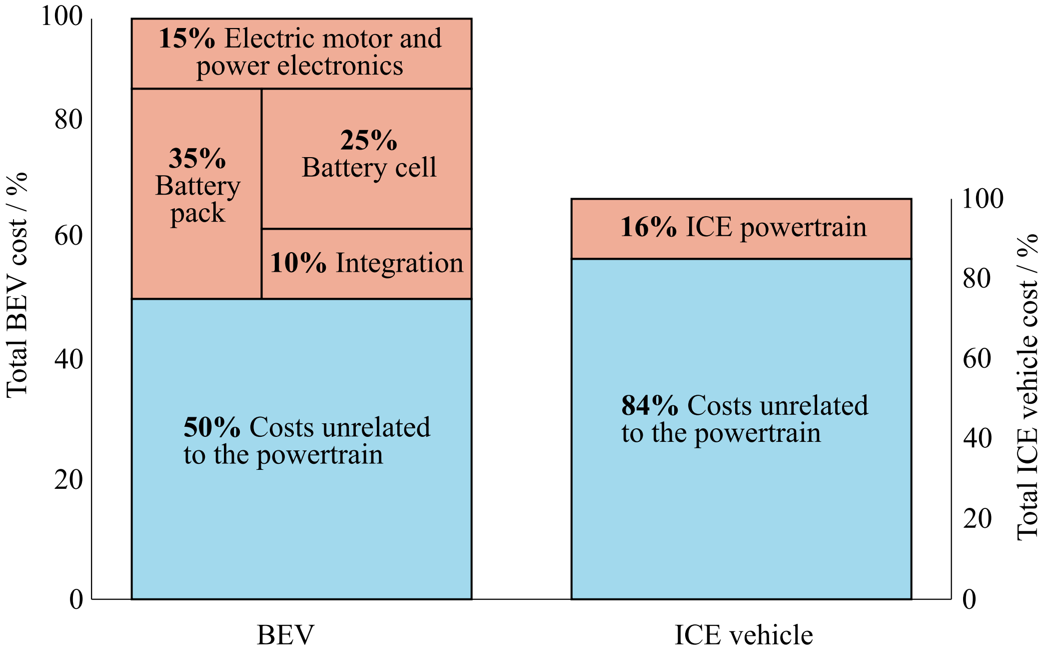

Figure 1.1: Cost breakdown of BEV and an ICE vehicle components. The overall powertrain costs exhibit 16 % for an ICE vehicle, while the powertrain costs for a BEV amount to 50 % of the overall vehicle costs. This figure is based on the data from [13] (2018).

volumetric energy densities are less easy to predict [20] and which may be therefore unsuitable for mobile applications.

In sum, it can be expected that the energy density of the state of art energy storage technology will improve slowly in the next few years. Further cost reduction of battery packs might be achieved by optimizing the cell manufacturing processes [21][22][23]. However, production costs are highly dominated by the costs of raw materials [24], which might even increase due to possible high demand for lithium-ion based energy storage in the near future [25]. Therefore, in order to achieve any significant reduction of cell manufacturing costs, completely new approaches to production are required. In this context, full utilization of each battery pack represents one of the most effective levers to reduce BEV costs and thereby improve their competitiveness with conventional ICE vehicles.

1.1 The cause of the diminished pack utilization

1.1.1 The roots of cell imbalance

Electric mobility in particular requires both high power and high energy storage capabilities, which are usually provided by large battery packs, consisting of up to thousands of single lithium-ion cells. In order to reduce load currents and consequent ohmic losses within both the battery packs and the charging infrastructure, system voltage is usually increased by connecting cells in series. State of the art battery packs exhibit system voltages of up to 800 V with almost 200 cell blocks in serial configuration [26], whereby the number of cells in parallel is determined by the capacity of the selected cell and the power/energy demand of the application. In order to ease the assembly and maintainability of the battery pack, blocks of cells in parallel are usually connected in series within battery modules. Overall, the battery pack configuration influences the energy content, power capability and the reliability of the entire battery system.

In order to guarantee a safe operation throughout a specified life time, each lithium-ion cell in the battery pack is restricted to certain voltage, current and temperature limits, which are defined by the cell manufacturer [27]. The goal of such restrictions is to minimize the chance of a possible damage of the cell including accompanied side effects such as thermal runaway. Thermal runaway is an uncontrolled reaction resulting in exposure of high temperature fluids and gases, flames during venting and even explosion of a lithium-ion cell [28]. Furthermore, a single thermal failure might lead to the propagation of thermal runaway, resulting in uncontrolled explosion of the whole battery pack [29][30]. Some of the cell parameter limits are fixed, while others depend on the operational conditions. The cell temperature is usually limited, in order to mitigate decomposition processes of the internal cell components and subsequently prevent the cell from thermal abuse [31]. In a similar way, the end of charge and the end of discharge voltage limits are fixed in order to prevent the cell from overcharging, which would lead to irreversible structural changes within the active materials often accompanied by a thermal fault [32][33] and over-discharge, which would be accompanied by copper dissolution and consequently would result in an internal short-circuit during a subsequent charging operation, also causing a thermal fault[34]. On the other hand, maximum charge current might depend on the temperature and the state of charge (SOC) of the cell, in order to reduce the possibility of lithium plating [35][36], which also might lead to a thermal fault. Overall, exceeding the operational limits usually leads to premature cell degradation and deterioration of the battery performance and might even result in safety related issues. Therefore, independently of the application requirements, it has to be ensured that all cells in the battery pack are operated within the defined limits at all times.

Making sure that the battery pack does not exceed the voltage, current and temperature limits during operation is the task of the BMS. Besides protecting the battery from being damaged, a BMS is also responsible for battery state determination in order to prolong the lifetime while fulfilling the requirements of the application [37][38]. In order to achieve these tasks, each cell block voltage is usually monitored in addition to the battery pack's current. To keep the wiring complexity as low as possible, only a few temperature sensors are integrated into the module at the known hot spots. There are different types of BMS architectures, which differ in their control effort, wiring complexity and reliability. One of the most used concepts is the master/slave architecture [39]. Each battery module is equipped with a measurement slave unit, which allows local sensor wiring and analog to digital conversion of measured signals. A master unit is usually connected to each slave unit over a standardized communication bus and is responsible for interpretation of the measured signals and calculation of battery states. Based on the results, the master unit is able to take action and adjust the operational limits. For instance, in the case of a low SOC, the maximum power that can be provided by the battery must be reduced or the discharge must be stopped to avoid violation of the operating limits.

A standard voltage protection method during cycling is shown in Fig. 1.2, which depicts the voltage progression of each cell within a 6s1p module during a constant current discharge and charge sequence. Despite the fact that each cell block is exposed to the same load current, slightly different cell behaviors can be observed. Not all cells reach the end of charge and the end of discharge voltage simultaneously resulting in different depth of discharges (DODs). Cell one (blue) reaches the end of discharge and the end of charge voltage first and therefore limits further charge and discharge of the entire serial

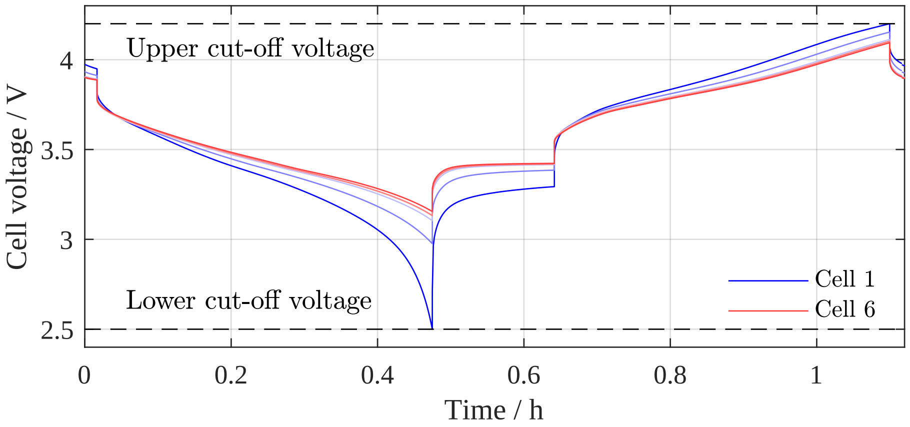

Figure 1.2: Progression of six cell voltages of a 6s1p module during a 1C discharge, 10 min pause and subsequent 1C charge. Due to a voltage imbalance, cell 1 (blue) reaches the lower and upper cut-off voltages first, while the capacity of the remaining cells is not completely utilized.

connection, leaving the remaining capacity of cells two to six unused. As the BMS ensures that both charge and discharge cut-off voltage limits of the used lithium-ion cell are not exceeded during the operation, the discharge and charge operation is terminated as soon as the voltage limit is reached. The presented 6s1p module exhibits a voltage imbalance, which is caused by different voltage responses of cells connected in series, despite the same load current.

Generally, different voltage responses and therefore voltage imbalances are caused by intrinsic as well as extrinsic factors. Intrinsic factors are linked to the finite accuracy of cell manufacturing processes, which cause slightly different properties and behaviors of the produced lithium-ion cells. Cell parameter variations are usually linked to minimal differences in the electrode thickness, material composition, overall component connectivity, etc. among the same type of produced lithium-ion cells [40]. Such differences result in slightly varying capacities and impedances [41], as shown in Fig. 1.3a and Fig. 1.3b respectively. In addition, intrinsic aging behavior, which results in capacity loss and impedance increase, varies under the same operational conditions, as has been shown in [42]. Such intrinsic aging variations deteriorate the capacity and impedance spread across the battery pack even more and increase the variance of cell parameters over the lifetime of the battery. Differing self-discharge rates deteriorate the available pack capacity even further [43]. As cell parameters of mass-produced lithium-ion cells are usually normally distributed, which is symptomatic of random - and not systematic - deviations during cell manufacturing [44], there will always be negative outliers in a battery pack, assuming no cell matching took place before the pack assembly. By connecting cells in parallel, certain parameter variations can be compensated [45], but not completely erased. However, within the cell block, variations of cell parameters comes with an uneven load current distribution among the cells connected in parallel. In literature, there are contradictory statements regarding whether such load deviations enable a convergence of the cell parameters [46][47] and therefore homogeneous aging within the cell block or whether the deviations facilitate parameter drift [48]. Nevertheless, even if each battery module within the battery pack experiences the same operational conditions, it can be assumed that there will always be a cell block, which limits the discharge or charge of the whole battery pack. Furthermore, it can be also expected that inhomogeneities will increase during the lifetime [49].

Due to geometric restrictions of cells and battery packs including the thermal management it is almost

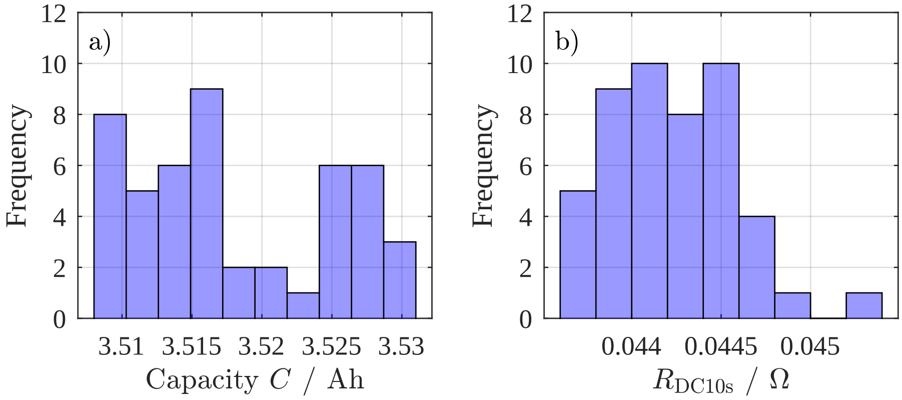

Figure 1.3: (a) Measured distribution of constant current constant voltage (CCCV) capacities of pristine 48 MJ1 cells (parameters are summarized in Table 1.3) at 25 °C, (b) measured distribution of R_{DC10s} values, which is a direct current (DC) resistance, calculated after 10 s discharge pulse at 50 % SOC of of pristine 48 LG MJ1 cells at 25 °C.

impossible to provide the same thermal condition to each cell [50][51], which leads to temperature gradients during operation [52][53]. Several studies have reported that the major cell degradation mechanisms are influenced by the temperature [54][55]. Furthermore, it has been shown that temperature gradients deteriorate the capacity spread among the cells in battery packs [48][49][56], causing further cell imbalance. One of the goals of a thermal management is to keep those temperature gradients low, however, a complete absence of such inhomogeneities is rather unlikely, especially during high current loads such as experienced during fast charging [57]. In addition to temperature gradients, the malfunction of the BMS hardware due to measurement slave unit failure or poor electronic design, may cause single cells or modules to be discharged at a higher rate than other cells. Such variation in discharge current would also result in cell imbalance.

Added together, inevitable manufacturing tolerances lead to initially different cell capacities, impedances and self-discharge rates. An exposure to temperature gradients might enhance these differences in self-discharge and promote different aging rates, which result in an even greater variation of capacities and impedances. Finally, due to constraints imposed by safe operation limits, not every cell in the battery pack can be completely charged and discharged, diminishing the overall pack utilization during operation even more.

1.1.2 The goal of pack utilization

Depending on the application, potential benefits of optimal pack utilization may include the maximization of the available discharge energy, minimization of energy losses, maximization of the available charge and discharge power, extending the lifetime of the battery pack or a combination of any of these results. For instance, the minimization of overall energy losses in energy storage systems is more important in the area of stationary energy storage than in mobile applications [58]. Many business cases for stationary energy storage applications, in which the energy is stored at one point and is sold or used at a later point in time, rely on high energy efficiencies. If energy is the commodity, efficiency of the storage system is directly linked to profits. Electrical power, within the primary net control, can also be a commodity, for example, allowing the regulation of electric grids [59]. In such applications, stationary energy storage systems compensate load peaks and stabilizes the frequency of the energy grid. Maximum energy and power utilization of the battery pack is often required from plug-in hybrid electric vehicle (PHEV), which employ a combination of a combustion engine and electric powertrain [60]. In that way, the main engine of a PHEV can be downsized and be turned off during standstill reducing overall fuel consumption. The recuperating energy can be reused and the brakes can be minimized. Furthermore, the main engine can be operated in optimal operating points [61].

Fully electric vehicles are usually subjected to multiple utilization goals. For instance, a specified torque relies on constant power regardless of the SOC and operating temperature of the battery pack. On the other hand, the charge energy efficiency is less important, since it is much cheaper to fully charge an EV than to fill up an ICE vehicle with gasoline. However, the distance, which can be traveled with a fully-charged battery pack is, in addition to the price, often claimed to be one of the most important criteria for new EV buyers [62], making it a reasonable utilization criteria. The driving range depends on two factors: the available discharge energy and the energy consumption per travel distance, whereby the latter factor depends to a lesser extent on the battery pack. Therefore, it stands to reason that the optimal utilization of a battery pack is identified as the maximization of the discharge energy.

In order to maximize the discharge energy, each cell in the battery pack has to be fully charged and subsequently completely discharged. However, previously mentioned cell parameter variations are able to influence the charging and discharging process of cells connected in series, as shown in Fig. 1.4. The resulting imbalance between two cells with the same capacities but different initial SOCs is depicted in Fig. 1.4a. During the charge, the SOCs of both cells increase at an equal rate. However, since cell number one exhibits a higher starting SOC, it reaches the end of charge first, limiting the charge of cell number two. In the second case, shown in Fig. 1.4b, both cells exhibit same starting SOCs, but different capacities. In this case, the limiting cell is the cell with the smaller capacity, which could potentially be either cell number one or cell number two. If both cells exhibit the same capacity, they both reach the end of charge at the same time. Fig. 1.4c depicts a scenario, in which the starting SOC as well as the capacities of both cells differ from each other. Although there is a possibility that both cells are fully charged at the end of the charging process, it is more likely that the utilization of both cells is not optimal. The influence of capacity and SOC variations on the discharge behavior is similar to the charging process. Assuming that all cells are fully charged, the smallest capacity of two cells connected in series determines the overall discharge capacity, as shown in Fig. 1.4d.

Until now, the utilization of the battery pack was linked to the SOC of each cell at the end of charge and at the end of discharge. Although the use of the SOC seems to be the most obvious measure, it does not completely reflect the reality. This is owed to the fact that there is no possible way to measure SOC directly. In the past, many efforts were undertaken in order to establish reliable SOC estimation methods, such as Kalman filtering [63][64], Fuzzy logic approaches [65] and observer methods [66][67]. However, most of the estimation algorithms relied on the perfect knowledge of the open circuit voltage (OCV). Since the cell's OCV slightly changes during its lifetime [68], most SOC estimation algorithms provide good estimation results at the beginning, however, show rapid decay in performance after a short deployment time, making them unsuitable for a deployment over the whole lifetime of a battery [69]. The most common method for SOC determination is Coulomb counting [70], which is based on the integration of the load current. The accuracy of this determination method relies on the accuracy of the current sensor and inevitably, frequent re-calibration, without which the SOC error would increase with time. Furthermore, as the Coulomb counter usually utilizes the main current sensor, no information about the SOCs of single cells or cell blocks in series can be obtained.

Therefore, it stands to reason that the cell voltage is the most reliable measure for determination of

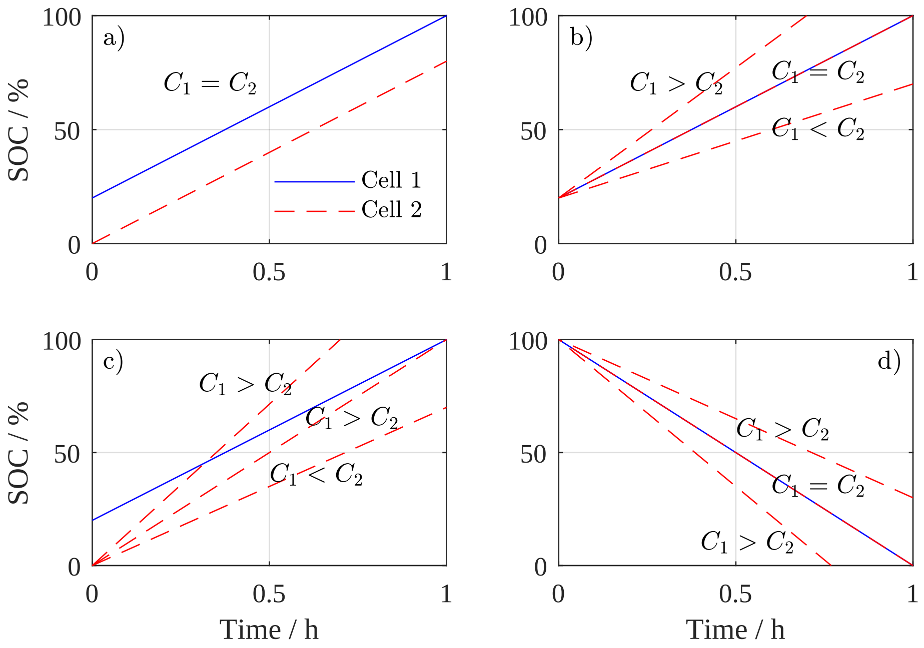

Figure 1.4: Influence of different capacities and SOCs on the utilization of two cells connected in series. (a) Different initial SOCs but same capacities result in cells with lower starting SOCs not being completely charged, (b) same initial SOCs but different capacities limit the charging process, (c) different initial SOCs and different capacities might limit the charging process or allow the charging of both cells completely, (d) in case of fully charged cells, the discharge energy is limited by the smallest capacity.

cell imbalance during the operation. Following this approach, the utilization goal of a battery pack can be formulated as follows: each cell in a battery pack exhibits the maximum voltage at the end of charge and the minimum voltage at the end of discharge.

1.1.3 Trends in commercial balancing ICs

The problem of the voltage imbalance is well-known and in order to counteract the diminished pack utilization, cell balancing systems are usually deployed [71]. Balancing circuits are electronic devices, which are connected to each cell block in a battery pack, allowing individual charge adjustments. The ability to manipulate charge may serve several utilization goals at the same time. For instance, simulative undertakings were made in order to maximize the discharge energy while at the same time decreasing temperature gradients in the battery modules [72].

Overall, a distinction is made between dissipative and non-dissipative balancing systems. Dissipative balancing systems are able to adjust the charge within the cell blocks by discharging them [73]. In order to do so, each cell block is connected to an electric switch and a dissipating resistor. Such realization has many advantages regarding costs and reliability, since only one control signal per cell block is required. In order to limit the dissipated power in the form of heat, the discharging or balancing current is usually limited to approx. 200 mA. Therefore, due to low balancing currents and high capacity of the cell blocks, the balancing procedure might take a long time in case of a significant voltage imbalance prevails. Non-dissipative balancing systems are able to transfer the charge from one cell block to another. Such charge transfer is usually realized by a short term energy storage device, such as a choke or capacitor. There are various implementations of non-dissipative balancing circuits based on flyback converters, switched capacitors and reconfiguration networks [74], resulting in different topologies, such as cell-to-cell, cell-to-stack or stack-to-cell configurations [75]. In theory, non-dissipative balancing systems allow each cell block to be fully utilized, which implies that each cell or cell block in a battery pack can be fully charged and fully discharged. However, in a scenario in which charge is transferred multiple times from one cell block to another, the overall transmission efficiency might become quite low. In contrast to a simple resistor and a switch, non-dissipative circuits require much more hardware and control effort. This results in higher costs but also additional volume and weight, lowering the energy density of the battery pack. In other words, due to limited space, the hardware required to improve utilization would displace battery capacity in the EV and the resulting loss of energy content may not be compensated for by the improvement in utilization. Therefore, the use of non-dissipative balancing is not very common. Self-contained and highly isolated applications, such as space missions, in which the reliability of battery modules is much lower than of electronic circuits due to harsh environment is one of the possible deployments of non-dissipative balancing.

Despite the established use of dissipative balancing circuits in battery management systems, the real benefit is still not completely understood. However, it stands to reason that the need for cell balancing is closely linked to the voltage imbalance during the operation, which is the cause of the diminished battery pack utilization. Since technological problems usually lead to customer requirements and subsequently improved products, technological trends of commercially available balancing integrated circuits (ICs) for multicell energy storage applications over the past 10 years were analyzed. Table 1.1 lists the balancing devices, which were proposed for automotive and energy storage applications. In general, those devices represent complete measurement slave solutions for battery management systems, including such functionality as the cell voltage and module current measurements, temperature measurements, cell balancing and hardware safety features such as overcharge protection.

Table 1.1: A list of commercial BMS and voltage monitoring devices, which were introduced to the market over the past 10 years, including the IC manufacturer, name of the device and the introduction year.

Number	Manufacturer	Name	Year
1	Analog Devices	LTC6802-1	01/10
2	Texas Instruments	BQ76PL536A-Q1	05/11
3	Analog Devices	LTC6803-2	08/12
4	Analog Devices	BQ76940	10/13
5	Maxim Integrated	MAX14920	03/15
6	Texas Instruments	BQ76PL455A-Q1	04/15
7	Analog Devices	LTC6804-1	10/16
8	Analog Devices	LTC6811-1	08/17
9	Analog Devices	LTC6813-1	02/18
10	Maxim Integrated	MAX17843	03/18

From Table 1.1 it can be seen that there is not much variety in regard to the vendors for mass produced BMS and balancing ICs on the market. Furthermore, all listed devices offered integrated dissipative balancing solutions. Non-dissipative balancing was only offered among ICs from Analog Devices, however extra hardware such as fly-back converters had to be integrated in order to be able to use it. The listed devices were characterized regarding the number of measurement channels, measurement resolution, measurement accuracy and finally the maximum allowed balancing current for the integrated dissipative balancing. The results are shown in Fig. 1.5. The number of channels per device, which is shown in Fig. 1.5a, increased over the years from approx. 10 to 14 channels. Due to regulations

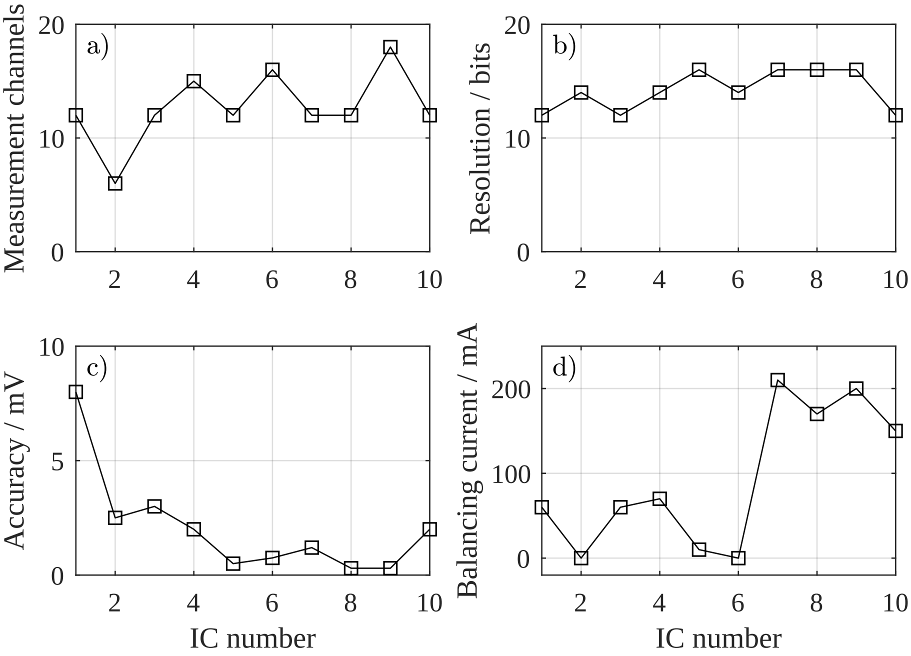

Figure 1.5: Evaluation of commercial BMS and voltage monitoring devices introduced to the market according to Table 1.1 over the past 10 years. (a) Maximum number of channels, which can be measured by one measurement slave, (b) resolution of the built-in analog to digital converter (ADC) given in bit, (c) accuracy of the voltage measurement for the given operational range, (d) maximum allowed integrated balancing current.

regarding the pack assembly safety and logistic standards, the maximum voltage of a battery module is often limited. Since the design usually aims to use one battery management slave per module, the increase in measurement channels is most likely linked to the optimal utilization of the regulations regarding the pack assembly and price reduction efforts. The measurement resolution increased from 12 to 16 bit on average, allowing the measurement accuracy to improve from 8 mV to <1 mV, as shown in Fig. 1.5b and 1.5c respectively. As accurate voltage measurement is important for precise battery state determination and safety monitoring and therefore pack utilization, it can be expected that the increase in accuracy was driven by the overall system optimization, instead of deployment of new cell materials. The development of the maximum allowed integrated balancing current is depicted in Fig. 1.5d. It reveals a significant increase from <100 mA to approx. 200 mA, which might be linked to initially underestimated influence of cell-to-cell variations or voltage imbalance in general. Further possible explanation could be linked to increased cell capacities. On the other hand, integrated electric switches for dissipative balancing might be associated with the fact that balancing currents above 200 mA are basically not needed.

1.2 Fundamentals of lithium-ion cells

Since 1991, when Sony commercialized the lithium-ion technology developed during the 1970s-1980s, lithium-ion cells have been utilized for various applications. Despite the efforts of the scientific community and the accompanying improvements to the technology, the basic working principles have remained the same. In order to understand the mechanisms leading to voltage imbalance, the working principle of lithium-ion cells is described in the following focusing on processes affecting the overall cell voltage during operation and resting phases.

1.2.1 Working principle and active materials

In general, lithium-ion cells consist of two porous electrodes, a microporous separator and an electrolyte, as shown in Fig. 1.6. In combination with the porous structure of the electrodes, which provides a maximized surface area between the solid active material particles and the liquid electrolyte, facilitating reaction kinetics, the electrolyte enables the movement of lithium-ions between the two electrodes.

Typically, non-aqueous electrolytes consisting of organic solvents, conducting salts and various additives are used [76]. There are different types of electrolytes, which are optimized for a certain application of the cell in terms of power capability, cycle and calendar life, etc. [77][78]. The porous separator prevents an electronic short circuit between both electrodes, by allowing only lithium-ions to move from one electrode to another. In addition to the required ionic conductivity, the separator must ensure mechanical stability owing to the mechanical expansion of both electrodes during the operation [79].

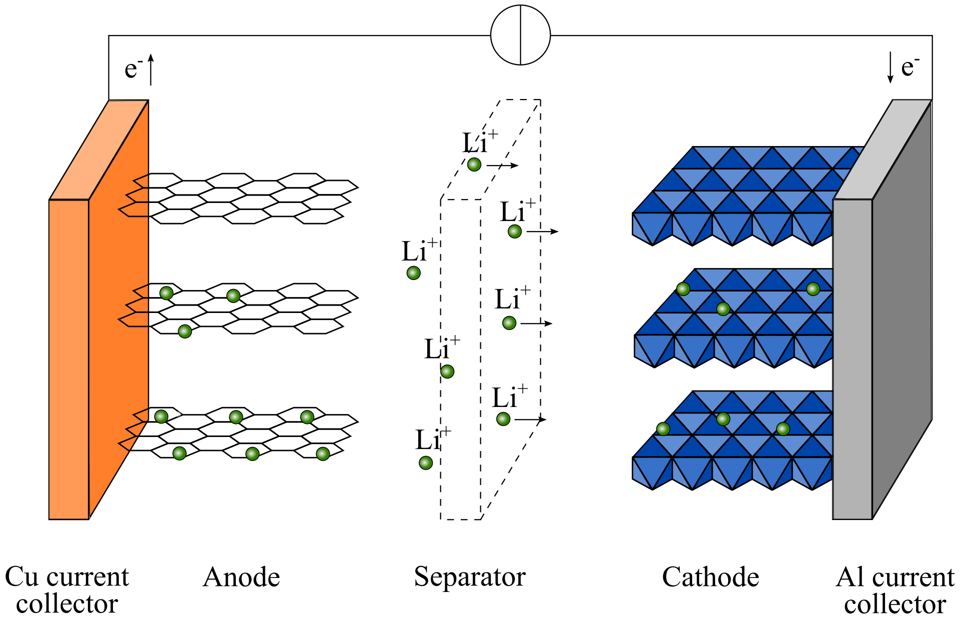

Figure 1.6: Schematic representation of a lithium-ion cell, including both current collectors, host lattices of the anode and the cathode, the separator and lithium ions moving through the electrolyte.

Each electrode consists of a current collector and a coated composite material. In order to ensure long-term and safe operation, current collectors must display high electrical conductivity while remaining electrochemically stable in the presence of the remaining cell components. This also presupposes that the cell is operated within its specified limits in regard to temperature, current and voltage. Usually, the current collector at the cathode is made of aluminum and the current collector at the anode out of copper. Low anode potential, at which the negative electrode is usually operated, prevents the copper current collector from oxidation and being dissolved, which otherwise might severely shorten the lifespan of the cell and introduce safety hazards [80][81]. In a similar fashion, aluminum, which is usually used as current collector at the cathode is highly stable at standard cathode potentials. The aluminum current collector is protected from corrosion by a surface film formed by reaction of the metal with the electrolytic salts [82][83]. The composite electrode materials consist of active materials, storing lithium-ions, carbon black and a polymer binder. The binder enables mechanical integrity despite small volume changes during operation and thereby sustains electrical conductivity [84], whereas carbon black is usually used in order to increase the electrical conductivity of the active materials [85].

During discharge, the anode is oxidized and an electron is released to the external current path. Subsequently, the lithium ion arrives via the electrolyte solution at the cathode. With the electron at the positive tab of the cell, the cathode is reduced. On the way to the positive tab the electron releases work. If work is done in order to move the electron in the reverse direction, the cathode is oxidized and subsequently the anode is reduced. The main principle behind this process is that of intercalation, which allows lithium ions to enter the host lattice of the electrode via the reaction with the active materials in the cell. The main reaction can be separated into two reactions, each at the positive and at the negative electrode. For a lithium-metal oxide ($\mathrm{LiMO_2}$) at the cathode, with M representing Ni, Co and/or Mn, the reaction at the positive electrode is given by

$$\mathrm{LiMO_2} \longleftrightarrow \mathrm{Li_{1-x}MO_2} + x\mathrm{Li^+} + x\mathrm{e^-} \tag{1.1}$$

and the reaction at the negative electrode with graphite ($\mathrm{C_6}$) as the active material becomes

$$\mathrm{C_6} + x\mathrm{Li^+} + x\mathrm{e^-} \longleftrightarrow \mathrm{Li_xC_6} \tag{1.2}$$

where x depicts the grade of lithiation ($0 \leq x \leq 1$).

In order to increase the energy density of commercial lithium-ion cells, electrode sheets are usually coated with composite materials on both sides of the current collector foil [86]. Subsequently, the sheets are rolled or stacked, depending on the format of the lithium-ion cell. Generally, commercial formats fall into three main categories: cylindrical, prismatic formats with a stiff metallic housing and pouch cells, which are encapsulated in aluminum laminated film. Due to widespread use of cylindrical cells in consumer electronics the formats 18650 and 21700 were the first to be able to profit form economies of scale [87]. However, prismatic cells, which can be larger, offer more opportunity for cost reduction [88]. The established manufacturing processes of cylindrical formats allow the production of high quality lithium-ion cells with low parameter variations. Furthermore, due to their relatively small capacities, cylindrical cells are highly manageable in the laboratory environment. Therefore, the focus of this work was the investigation of 18650 cylindrical cells.

In general, active materials differ in their structure, specific capacity, potential and intercalation processes. In addition to theoretical parameters, they also vary in cycle stability and especially cost. An overview of frequently used materials is presented in Table 1.2. Due to high energy density and

Table 1.2: Popular intercalation materials with their potential and specific capacity.

Material	Potential vs. $\mathrm{Li/Li^+}$ / V	Specific capacity / $\mathrm{mAhg^{-1}}$
NMC	4.0 [89]	148 [90]
NCA	3.7 [89]	160 [91]
LFP	3.6 [92]	120 [89]
Graphite (C)	0.1 [93]	372 [94]
Silicon (Si)	0.37 [95]	4212 [95]

good safety properties, nickel manganese cobalt oxide (NMC) became the cathode material of choice, especially in mobile applications [92][96]. However, first generations of NMC cathodes are now gradually being replaced by nickel-rich materials, which provide even higher achievable specific capacity [97] with explicit price advantages due to the scarcity of cobalt [98][93]. Lithium iron phosphate (LFP) has shown several advantages with regards to safety, costs and long-term cycle life compared to NMC, but due to lower energy density is more suited for stationary energy storage applications.

The anode is usually made from synthetic or natural graphite, soft or hard carbon or lithium titanate oxide (LTO). Due graphite's comparably high energy density of $372\,\mathrm{mAhg}^{-1}$, low electrical potential and low cost, graphite is currently the most common material for negative electrodes. However, silicon, having a much higher specific energy density than graphite, has been recently used as an additional compound for graphitic host lattices, in order to increase the gravimetric energy density of the negative electrode [99][100][101]. High volumetric expansion of silicon, however, constitutes a limiting factor in the silicon to graphite ratio, since it leads to possible instability of the mechanical structure during the lithiation and delithiation of the anode [95].

Due to higher energy density and price advantages, lithium-ion cells containing nickel-rich cathodes and silicon-carbon (SiC) anodes are predicted to be deployed in the next generation EVs [102][103]. Therefore, the scope of this work includes the investigation of lithium-ion cells with nickel-rich cathodes (NMC811) and silicon graphite blend anodes. The object of all studies conducted in this work was a commercial NMC(nickel-rich)/SiC 18650 high energy lithium-ion cell INR18650-MJ1 from LGChem with a nominal capacity of 3.5 A h and specific energy density of $259.6\,\mathrm{Whkg}^{-1}$. Further datasheet parameters are summarized in Table 1.3.

Table 1.3: Nominal specification of the INR18650 MJ1 cell. Further parameters can be found in [104]

Item	Condition	Specification
Capacity	Std. charge / discharge	Nominal 3500 mAh
Nominal voltage	Average	3.635 V
Standard charge	CCCV	0.5 C (1675 mAh), 4.2 V (50 mA)
Max. charge voltage		4.2 V
Max. charge current		1 C (3350 mAh)
Standard discharge	constant current (CC)	0.2 C (670 mAh), 2.5 V
Max. discharge current		10 A
Operating temperature	Charge	0 °C~45 °C
Operating temperature	Discharge	−20 °C~60 °C

1.2.2 Dynamic overpotentials

Due to the main reaction, the finite conductivity of the cell components and mass transport limitations of the electrolyte and active materials, lithium-ion cells are exposed to overpotentials during operation [105]. Electronic conductivity of the electrode active materials, binders and current collectors cause an instant voltage drop due to Ohms law. A hampered motion of lithium-ions in the liquid phase can be also interpreted as ionic resistivity [105]. Despite the fact that ionic resistivity is linked to both migration and diffusion processes and therefore is dependent on temperature [106], both overpotentials are often treated as a single ohmic potential drop ΔU_{ohm} [107].

The process of intercalation and deintercalation at each individual electrode is fundamentally based on reaction kinetics which forms the link between the movement of ions and electrons between the two electrodes. Depending on the sign of reaction overpotential, either an anodic or cathodic reaction is triggered at the respective electrode. The relation between the current density and the polarization can be described by the Butler-Volmer equation, which follows an exponential characteristic. The Butler-Volmer relation states that the rate of an electrochemical reactions (de-/intercalation) depends exponentially on the driving potential η. The relation for one electrode is given by

$$I = i_0 \cdot \left[\exp\left(\frac{\alpha \cdot n \cdot F}{R \cdot T} \cdot \eta\right) - \exp\left(\frac{(1-\alpha) \cdot n \cdot F}{R \cdot T} \cdot \eta\right)\right] \tag{1.3}$$

where α is the charge transfer coefficient, n is the number of electrons involved in the electrode reaction, F is the Faraday constant, R is the universal gas constant and i_0 is the exchange current density. The Butler-Volmer characteristic implies that increase in the overpotential leads to a non-linear, exponential increase in the load current, which is not the case for a simple resistor obeying Ohm's law, which describes a linear relation between the current and the voltage. Overpotentials, based on reaction kinetics at both electrodes are summarized in ΔU_{ct}.

During the process of charge transfer, at the interface between the electrode/particle and the electrolyte, naturally, there are charge carriers with different polarizations [108]. A separation of charge carriers with different polarization generates an electric field, which is, by definition, a capacitor. Due to the large, cumulated surface area of particles in the active mass, such capacitance cannot be neglected. Thus, so called double layer capacitance acts like a first order delay element for the charge transfer reaction. In other words, the double layer capacitance has to be first charged or discharged before the process of intercalation or deintercalation can occur, which causes further dynamic overpotentials. In addition to reaction kinetics, the double layer effects at both electrodes are summarized in $\Delta U'_{\mathrm{ct}}$.

Intercalated lithium ions diffuse from the interface inside the particle due to concentration gradients. Such gradients are caused by the mass transfer inhibition described by Fick's law. The resulting overpotentials depend on temperature and diffusion coefficients of the active materials [105]. The maximum current density is known as the diffusion-limited current density and caused voltage drop ΔU_{diff} is known as the the diffusion overpotential.

Overall, the terminal voltage between the positive and negative tabs U_{t} during the current flow is composed of

$$U_{\mathrm{t}} = \Delta U_{\mathrm{ohm}} + \Delta U'_{\mathrm{ct}} + \Delta U_{\mathrm{diff}} + U_0 \tag{1.4}$$

where U_0 is the open circuit voltage in thermodynamic equilibrium state. As already described, the overpotentials depend on the applied current, the actual concentration of lithium ions in electrodes and the temperature of the cell [109][38]. Additionally, the process of electrolyte decomposition and formation of passivation films continues during the lifetime of a lithium-ion cell [110]. As a consequence, the dynamic behavior of the cell also changes, usually resulting in a higher overall impedance and a slower cell voltage relaxation [49][54].

Despite this fact, it is assumed that overpotentials play a rather minor role in the voltage imbalance. This assumption is based in particular on the fact that the major part of the overpotentials correlates with the load current [111], which is usually reduced towards the end of charge [112]. Even if there are cells, which exhibit different dynamic behavior, in other words different overpotentials at the same current load, the differences in overpotentials are negligible in case of low currents. For instance, assuming a given constant voltage (CV) phase cut-off current of 50 mA for the MJ1 cell, the differences in polarization are below 5 mV even for a doubling of the impedance from 50 mΩ to 100 mΩ. Therefore it is assumed that the main influence on the voltage imbalance is likely to be the differences in equilibrium potentials between cells connected in series, rather than differing impedances, which will be further discussed in this thesis.

1.2.3 Open circuit voltage in thermodynamic equilibrium

Thermodynamic equilibrium exists, when a system, displays no processes of equalization of the temperature, pressure or electrochemical potential. For a lithium-ion cell this implies that the concentration of ions in all phases is constant and is the same at each location. Further, no temperature gradients exist within the cell and the pressure is constant everywhere. In this case, the equilibrium or OCV of a lithium-ion cell is given by the difference between the potential of the positive and the negative electrode in their thermodynamic equilibrium states [113]. Those equilibrium potentials especially depend in particular on the concentration of lithium-ions within the electrodes and to a lesser extent on the temperature [113] and are derived in the following.

According to thermodynamics of an electrochemical system, the Gibbs free energy ΔG, which is the maximum available electrical energy, can be expressed as

$$\Delta G = \Delta H - T\Delta S \tag{1.5}$$

where ΔH is the reaction enthalpy and ΔS is the reaction entropy. At constant pressure and physical composition ΔG can be also expressed by

$$\Delta G = -nFU_0(x) \tag{1.6}$$

whereas n is the number of electrons participating in the reaction, F is the Faraday constant, $U_0(x)$ is the equilibrium voltage and x is the concentration. Combination of the equations 1.5 and 1.6 yields the theoretically determinable equilibrium voltage

$$U_0(x) = \frac{T\Delta S(x)}{nF} - \frac{\Delta H(x)}{nF} \tag{1.7}$$

Assuming that the number of electrons, which participate in the reaction is constant, the equilibrium voltage, which can be theoretically measured at the terminals once all dynamic overpotentials have decayed, depends on the reaction enthalpy, reaction entropy and the temperature. The temperature dependency of the equilibrium potential is linked to the reaction entropy ΔS and has been reported several times in the literature [69][68]. Entropy expresses the part of a system's energy, which cannot be converted into mechanical work and is therefore commonly considered to be a measure of disorder within a macroscopic thermodynamic system, and in turn to be linked to structural properties of the active material on the molecular level. In the context of lithium-ion cells it also describes the reversible heat effect and is then given by

$$\Delta S(x) = nF\frac{\mathrm{d}U_0(x)}{\mathrm{d}T} \tag{1.8}$$

The entropic coefficient for a constant pressure and a constant concentration of lithium-ions is proportional to a change of the equilibrium voltage for a change in temperature. Therefore, according to equation 1.4, the entropic coefficient is measurable at the terminals of the cell, assuming all dynamic overpotentials have decayed. Fig. 1.7a and 1.7c show measured entropic coefficients of the negative and positive electrode $U_{\mathrm{th,neg}}$ and $U_{\mathrm{th,pos}}$. Both curves exhibit positive as well as negative values, which implies that both electrodes absorb and release reversible heat during the lithiation or delithiation depending on the concentration of lithium in the active mass. The full-cell entropy is composed of half-cell entropies, as shown in Fig. 1.7e with a good resemblance between the measured full-cell entropy and combined half-cell entropies. The full-cell entropy is dominated by the entropy of the anode.

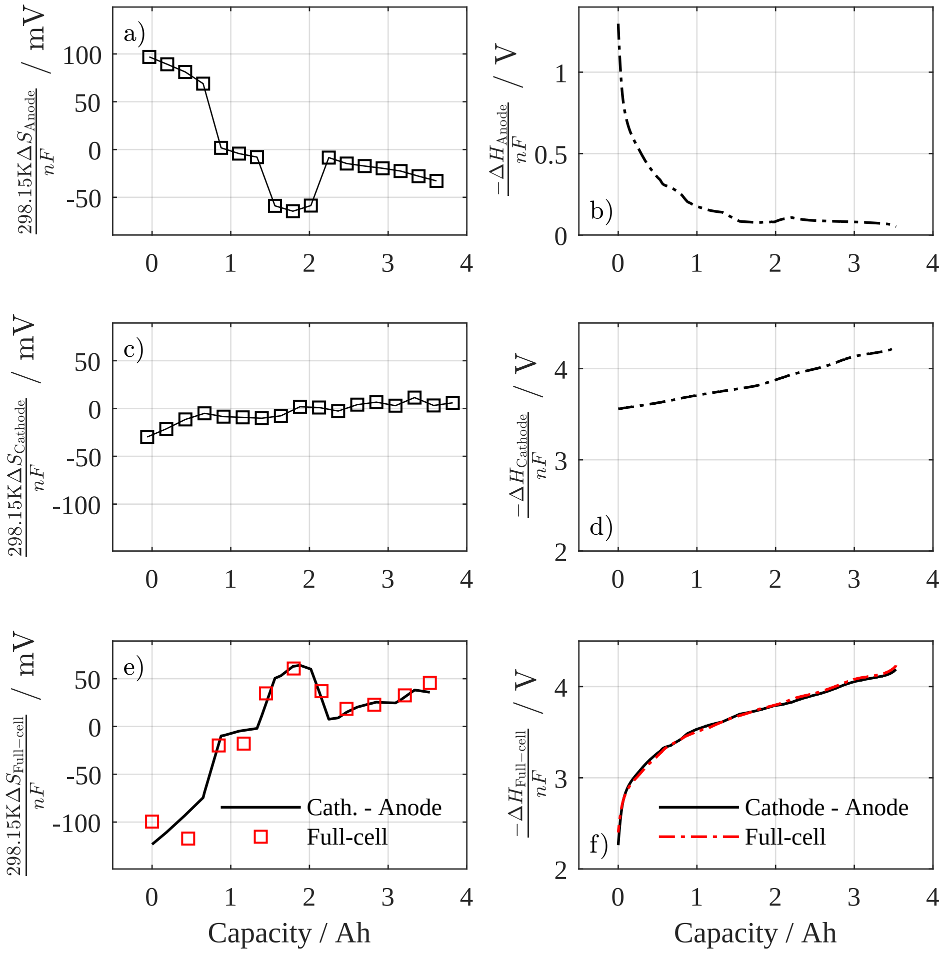

Figure 1.7: Half-cell and full-cell entropy profiles and quasi reaction enthalpy profiles of the LG MJ1 cell. (a) Entropy profile of the MJ1 anode, measured within a half-cell configuration (SiC vs. Li coin cell), (c) entropy profile of the MJ1 cathode, measured on the coin-cell within a half-cell configuration (NMC vs. Li coin cell), (e) entropy profile measured on the MJ1 full-cell and calculated full-cell entropy profile formed out of the half-cell measurements. (b) Calculated reaction enthalpy of the MJ1 anode, measured on the coin-cell (SiC vs. Li), (d) calculated reaction enthalpy of the MJ1 cathode, measured on the coin-cell (SiC vs. Li), calculated full-cell and combined half-cell reaction enthalpies of the MJ1 cell.

Due to cell manufacturing tolerances, cells might exhibit different entropic coefficients, while being at the same SOC. Fig. 1.8 depicts the voltage response of 24 pristine LG MJ1 cells at 90 % SOC to a temperature change from 55 °C to 40 °C. In order to compare the voltage response, the voltage progressions are corrected by the initial voltage offset. According to Fig. 1.7e the entropic coefficient of the cell at 90 % SOC (3.15 A h) amounts to approx. 32 mV / 298.15 K ≈ 0.1 mVK^{-}1, which implies that a change of temperature by -15 K results in a voltage decrease of approx. 1.5 mV, which is the case in Fig. 1.8. However, since the voltage differences among the cells after the temperature step are under 100 µV, the production related variation of the entropy can be neglected.

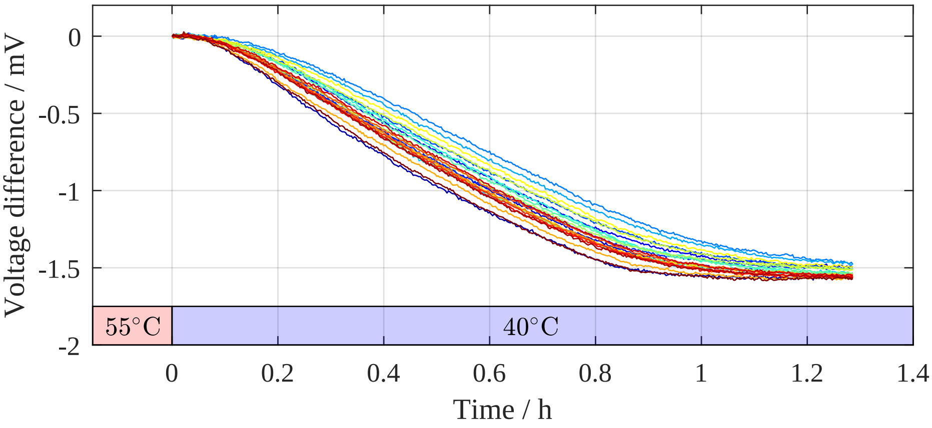

Figure 1.8: Voltage response of 24 pristine LG MJ1 cells at 90 % SOC to a temperature change from 55 °C to 40 °C, while being in a climate chamber and measured with a high-impedance voltage board.

According to equation 1.7, the reaction enthalpy can be defined as the difference between the equilibrium potential measured at the terminals and the entropy. Fig. 1.7b shows the calculated reaction enthalpy of the negative electrode, which still displays the typical phase transitions of graphite [114]. The calculated reaction enthalpy of the cathode is shown in 1.7d. The combination of half-cell reaction enthalpies of both electrodes reassemble the calculated full-cell reaction enthalpy closely, as shown in Fig. 1.7f. The full-cell enthalpy is calculated using the full-cell OCV and the full-cell entropy profile.

In comparison to the entropy profiles, the full-cell reaction enthalpies and thereby the OCVs exhibit slightly greater variations, as shown in Fig. 1.9. Although the differences are below 3 mV, this illustrates that two cells with identical capacities and levels of stored charge may exhibit slightly different equilibrium potentials. Full cell OCV depends on the stoichiometric properties of both electrodes, such as loading ratio and electrode balancing [115]. As stoichiometric properties might vary slightly during the cell manufacturing process, slightly different OCVs are evident for the identically produced lithium-ion cell, as shown in Fig. 1.9.

Added together, the full-cell equilibrium voltage becomes the combination of half-cell entropy profiles and reaction enthalpies of both electrodes, which depend on the stoichiometric properties of both electrodes and is described by the following equation:

$$U_0 = \left(\frac{T\Delta S_{\text{Cathode}}(x_c)}{nF} - \frac{\Delta H_{\text{Cathode}}(x_c)}{nF} \right) - \left(\frac{T\Delta S_{\text{Anode}}(x_a)}{nF} - \frac{\Delta H_{\text{Anode}}(x_a)}{nF} \right) \tag{1.9}$$

where x_c is the concentration in the cathode and x_a is the concentration in the anode.

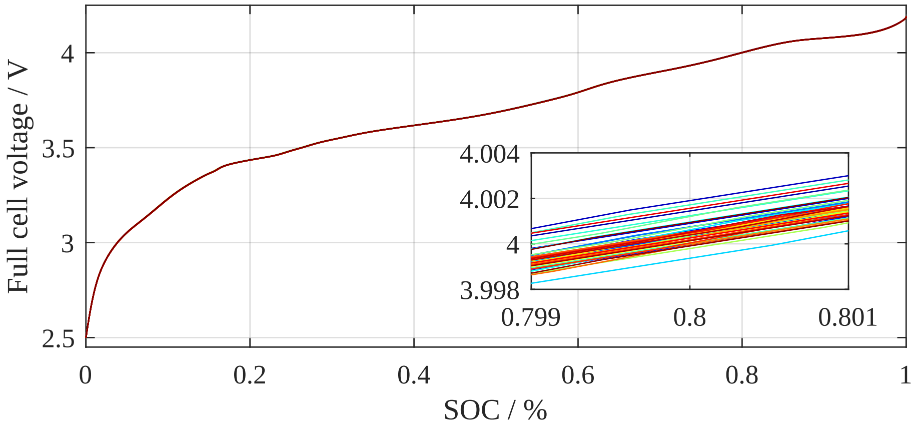

Figure 1.9: A quasi OCV, which is a discharge curve with C/30 discharge current of 48 pristine MJ1 cells. The difference in cell voltage at 80 % SOC amounts to 3 mV.

1.3 Factors influencing voltage imbalance in battery packs

Based on the previous statements, different terminal voltages in serial connection of cells are most likely linked to different equilibrium voltages, whereby differences in the dynamic behavior cannot be completely ruled out as a cause of the voltage imbalance. Varying terminal cell voltages can generally be treated as differences between loading ratios, electrode balancing and degree of lithiation of each electrode and are described by

$$U_{\mathrm{t}} = \left(\frac{T\Delta S_{\mathrm{Cathode}}(x_c)}{nF} - \frac{\Delta H_{\mathrm{Cathode}}(x_c)}{nF}\right) - \left(\frac{T\Delta S_{\mathrm{Anode}}(x_a)}{nF} - \frac{\Delta H_{\mathrm{Anode}}(x_a)}{nF}\right) + U_{\mathrm{rest}} \quad (1.10)$$

where U_{rest} quantifies remaining effects such as differences in the dynamic behavior. If variation of one of these aspects occurs, it can be expected to cause differences in the terminal cell voltages. The cause of different concentrations within the cells and the roots of different stoichiometric properties are discussed in the following.

As with every energy storage system, lithium-ion batteries suffer from reversible self-discharge, which is defined as the charge which the battery looses during the operation without any capacity loss. Since there is a monotonically increasing relationship between the charge stored in the cell and its terminal voltage, any loss of charge results in a voltage decay of the cell, as emphasized in Fig. 1.10. The exhibition of differing self-discharge rates between cells or cell blocks in series would cause the battery pack to display a voltage drift. For instance, assuming that all cells connected in series have equal capacities and exhibit high but equal self-discharge rates, no voltage drift will be observed. On the other side, even if the absolute value of the self-discharge in the cell is low, high variance of self-discharge rates might still result the voltage drift, taking into account that EV battery packs are usually expected to operate over a long period of time. **The first goal of this thesis is to identify the impact of the variance of reversible self-discharge rates on the voltage imbalance within battery packs.** Therefore, in addition to the absolute value of the self-discharge current as well as its dependency on the SOC and the temperature, the distribution and variance parameters must also be determined.

Over the lifetime of a battery pack, lithium-ion cells usually exhibit power fade and deteriorating energy storage ability [54][55], which are often linked to side reactions and a loss of active materials (LAMs)

$$U_\mathrm{t} = \left(\frac{T\Delta S_\mathrm{Cathode}(x_c)}{nF} - \frac{\Delta H_\mathrm{Cathode}(x_c)}{nF}\right) - \left(\frac{T\Delta S_\mathrm{Anode}(x_a)}{nF} - \frac{\Delta H_\mathrm{Anode}(x_a)}{nF}\right) + U_\mathrm{rest}$$

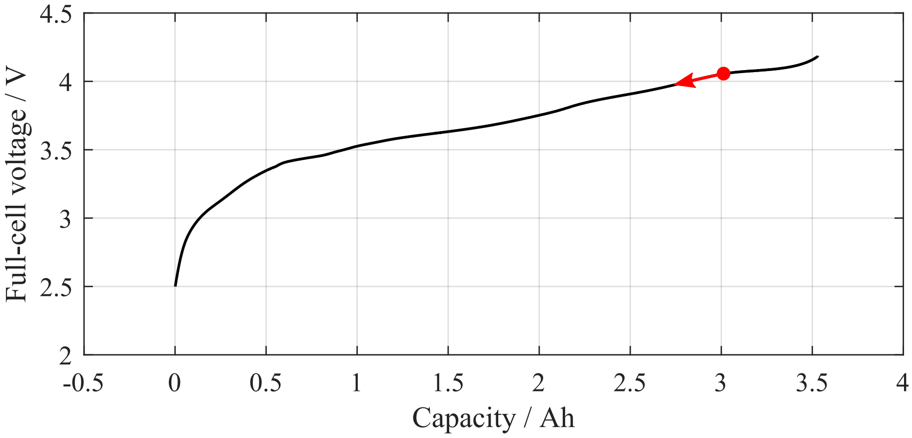

Figure 1.10: Emphasized self-discharge of a lithium-ion cell, which results in a voltage decay.

on both electrodes [116][110], which implies a change in loading ratios. Those degradation mechanisms in lithium-ion cells have an influence on half-cell potentials and consequently on the stoichiometric properties of both electrode and therefore full-cell OCV [116]. LAM is usually attributed to particle cracking and loss of electrical contact [116]. This means that, a part of the electrode's active mass is no longer available for the intercalation and deintercalation of lithium, which can be observed in the compression of the half-cell potential [117]. Anodic side reactions, such as the growth and repair of the solid electrolyte interface (SEI), result in the LLI, which leads to a delithiation of the negative electrode and an associated shift of the anode half-cell potential, resulting in a capacity decrease [118]. Cathodic side reactions, such as electrolyte oxidation and transition-metal dissolution, provoke a reinsertion of lithium into the positive electrode that can be observed in form of potential decrease and might even lead to an increase in cell capacity [119].

Several studies have shown that both degradation mechanisms might occur simultaneously in cells with a pure graphite anode [120] as well as those with a silicon-graphite blend anode [121][122]. Furthermore, LAM at low SOCs was considered to be responsible for the degradation of the negative electrode due to high mechanical stress during lithiation [123][124]. However, the exact implication for the voltage imbalance is not yet clear, since there is no information about the relative effect of each degradation mechanism on the overall aging. Nevertheless, LLI at the negative electrode is often claimed to be the dominant degradation mechanism [125][126][127][128]. It can be additionally assumed that temperature has a stronger influence on LLI [129], since it is an electrochemical process, than on LAM, which depends more on the mechanical properties. Therefore, due to the presence of temperature gradients in the battery pack it is most likely to observe different aging rates due to different rates of LLI. Since entropy coefficients rely on the balancing and loading ratios of both electrodes, **the second goal of this thesis is to identify how different aging rates influence the entropy and impact the voltage imbalance**, as emphasized in Fig. 1.11. A change of entropic coefficient at the same SOC would lead to a change in equilibrium voltage and consequently to a voltage drift within serial connection.

Subsequently, **the third goal of this thesis is to identify how different aging rates influence the reaction enthalpy, which dominates the full-cell OCVs, and impact the voltage im-**

$$U_{\mathrm{t}} = \left(\frac{T\Delta S_{\mathrm{Cathode}}(x_c)}{nF} - \frac{\Delta H_{\mathrm{Cathode}}(x_c)}{nF}\right) - \left(\frac{T\Delta S_{\mathrm{Anode}}(x_a)}{nF} - \frac{\Delta H_{\mathrm{Anode}}(x_a)}{nF}\right) + U_{\mathrm{rest}}$$

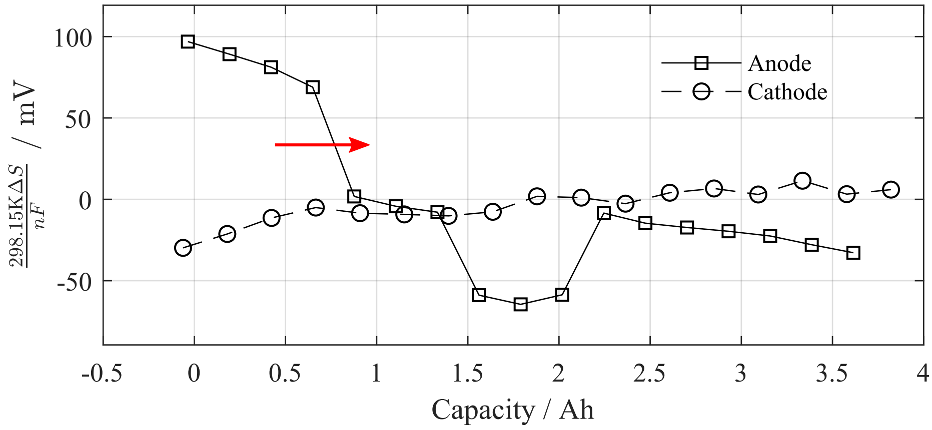

Figure 1.11: Emphasized shift of the anode entropy profile due to LLI.

balance, as emphasized in Fig. 1.12. A shift of half-cell OCVs would result in a change of the full-cell OCV, leading to a voltage drift within in series connection of cells.

$$U_{\mathrm{t}} = \left(\frac{T\Delta S_{\mathrm{Cathode}}(x_c)}{nF} - \frac{\Delta H_{\mathrm{Cathode}}(x_c)}{nF}\right) - \left(\frac{T\Delta S_{\mathrm{Anode}}(x_a)}{nF} - \frac{\Delta H_{\mathrm{Anode}}(x_a)}{nF}\right) + U_{\mathrm{rest}}$$

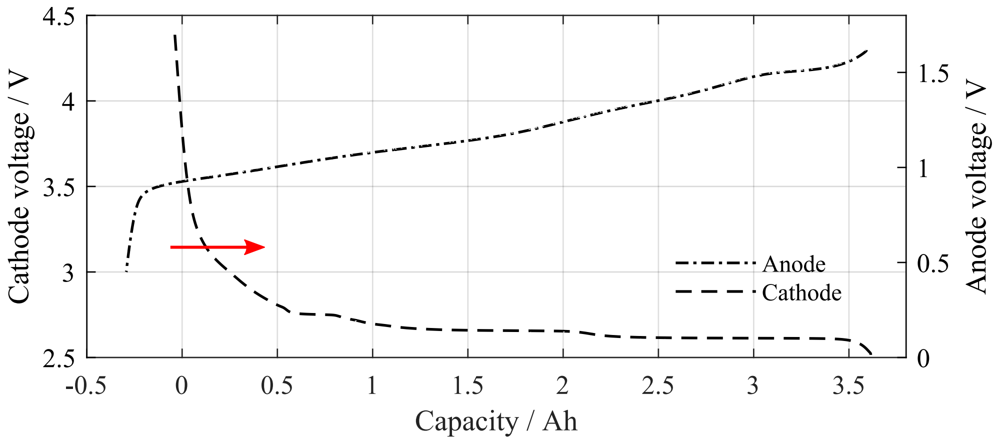

Figure 1.12: Emphasized shift of the anode OCV due to LLI.

As previously noted, LAM and LLI effects are assumed to appear during normal battery operation. However, deteriorated aging behavior is often linked to the deposition of metallic lithium, also referred to as lithium plating, which occurs on the negative electrode during charging [130]. Triggered by cell operation at high charge rates and/or low temperatures, lithium plating leads to severe capacity loss due to the formation of passivating surface films and due to consumption of lithium [131][36]. Lithium plating occurs if the potential at the graphite electrode-electrolyte interface falls below 0 V vs. Li/Li$^+$. Under certain circumstances a reverse reaction - lithium stripping - can be observed, however this process is not completely reversible [132][133]. It has been reported that temperature differences, which might occur within in series connection of cells, lead to different relaxation voltages after the striping reaction [134][135]. **Therefore, the last goal of this thesis is to identify the influence of lithium plating on the voltage imbalance between cells connected in series.**

In order to comply with energy/power demand of the application and in order to increase the reliability of the overall battery system, lithium-ion cells are usually connected in parallel. Due to slightly different OCV characteristics, cell capacities and impedances, short-term and long-term load deviations along the parallel connection might occur, as reported in [136][137]. Even cell connectors and their placing in regard to the load point play an important role in current distribution among the cells connected in parallel [138]. In the literature, there are contradictory statements regarding whether such load deviations enable a convergence of the cell parameters [46][47] and therefore homogeneous aging within the cell block or whether the deviations facilitate parameter drift [48]. However, assuming that the load current is not highly dynamic and that there is no temperature gradient along the parallel connection and no manufacturing outliers, homogeneous aging among cells in parallel is further considered.

1.4 Methods and resources

The identification of parameters influencing the voltage imbalance requires reliable measurement methods and simulation approaches. In addition to the description of state of the art measurement methods of the reversible self-discharge and entropic coefficients, this section pays particular attention to their limitations. Furthermore, the idea of a new holistic simulation approach of the whole energy system is presented, which is essential for the identification of the influence of cell-to-cell variations induced by intrinsic and extrinsic factors on the utilization of battery packs. Finally, new experimental validation techniques of the influence of differing operational conditions on the voltage imbalance are presented.

1.4.1 Determination of reversible self-discharge

Generally, there are three different self-discharge determination methods. The first method is based on the measurement of the discharge capacity before energy storage, and residual and discharge capacity after the energy storage [139]. The capacity based method does not require any specific resources, besides a cell cycler and a climate chamber. However, due to small self-discharge currents, an ascertainable reversible capacity loss implicates long storage time. In order to shorten the self-discharge determination, the second method measures the floating current, while the cell voltage is held constant [140] [141]. This current combines all side reactions, which influence the half-cell potentials. However, such storage conditions are not equivalent to the real storage, since a potentiostat provides an external path for electrons. The third method, voltage based measurement, similar to the current based method, also utilizes the influence of side reactions on half-cell potentials, which leads to voltage decay $\mathrm{d}U/\mathrm{d}t$. Combined with the derivative of the OCV $\mathrm{d}Q/\mathrm{d}U$ the self-discharge current is calculated as follows:

$$\frac{\mathrm{d}Q}{\mathrm{d}U} \cdot \frac{\mathrm{d}U}{\mathrm{d}t} = \frac{\mathrm{d}Q}{\mathrm{d}t} = \sum I_{\mathrm{sd}} \tag{1.11}$$

where $\sum I_{\mathrm{sd}}$ is the sum of all side reaction currents which have an influence on half-cell potentials of both electrodes, and $\mathrm{d}U/\mathrm{d}t$ is the stabilized slope of the observed voltage decay. In order to differentiate between voltage relaxation, including overpotentials from the charge transfer and diffusion, Schmidt *et al.* applied a discharge pulse before evaluating the voltage of cells with a blended NCA/$LiCoO_2$

cathode and graphite anode [142]. After the cell voltage exhibited a constant negative slope, the self-discharge processes were considered to be more pronounced than the voltage relaxation processes. However, during the period of the experiment, no voltage between 70 % and 10 % SOC exhibited a negative slope and therefore there is no data regarding the self-discharge in this SOC window. In a further voltage based self-discharge study with NMC/graphite cells, only values over 70 % SOC were presented [143].

In short, the reported voltage based measurement methods are not sufficient for reliable characterization of reversible self-discharge over the whole SOC range and at different temperatures. On the other hand, potentiostatic measurement methods are not representative of real operating conditions and capacity based methods rely on large laboratory infrastructure, as multiple climate chambers. Therefore, within the scope of this thesis, a novel self-discharge measurement method will be developed, which will be used for characterization of self-discharge and its variations in commercial lithium-ion cells.

1.4.2 Measurement of non-linear entropic coefficients

There are two major techniques for the determination of entropic coefficients. The calorimetric method utilizes reversible heat effects, by separating the reversible and irreversible heat losses for a subsequent charge and discharge of the cell, which is only applicable if other effects contributing to the energy balance are negligible [144]. The potentiometric method, however, utilizes the relationship given by equation 1.8. A temperature pulse is applied under open circuit conditions and the terminal voltage is measured. Schmidt *et al.* have shown that both methods deliver results in good accordance to each other [145]. Due to its simplicity, the potentiometric method has been used repeatedly in the battery research. The entropy profiles of different cathode and anode materials were analyzed in order to investigate theoretically feasible entropy profiles of full-cells [146]. Hudak *et al.* and Osswald *et al.* have shown that there are trackable entropy changes during cyclic aging [147][148]. Forgez *et al.* have used the potentiometric method to implement a detailed thermal model of a lithium-ion cell [149].

In most cases, a temperature dependent change of the OCV is assumed to be linear, regardless of the positive or negative temperature change and regardless of the initial temperature [150]. However, non-linear behavior of the entropy has been previously observed. Schmidt *et al.* have shown an entropy hysteresis depending on the direction of the current [145]. Bazinksi *et al.* observed different entropy coefficients for the same temperature change at the same SOC at different initial temperatures [151].

In order to precisely determine entropic coefficients of half and full-cells, the voltage based method has to be investigated for its validity. Therefore, within the scope of this thesis, a new enhanced entropy measurement method will be derived.

1.4.3 Optimized battery pack simulations applying a Monte Carlo approach

The majority of the experimental and simulation based studies regarding the influence of cell-to-cell parameter variance, aging and extrinsic system factors on battery performance usually consider only a selective set of cell/system parameters or upper/lower limits of a cell parameter distribution [152][153]. Either way, the results represent only a snapshot of the battery performance given for one set of cell and system parameters. In order to provide a statistically relevant statement about battery pack performance, a simulation or an experiment has to be repeated many times, due to the complex non-linear relationship between the cell and pack parameters. This method, called Monte

Carlo simulation, is usually used when the analytical calculation of the statistical result is not possible or at least is very demanding [154]. For instance, a battery pack's lifetime is simulated many times using a given temperature gradient, but in each simulation, cell parameters are randomly distributed. As a result, there is a statistical statement regarding the battery pack's behavior with fixed system properties and cell variation data can be made. By changing a system property, a statistically relevant change can be observed.

However, a holistic simulation of a battery pack's lifetime, which accounts for cell variations, balancing strategies and temperature distributions demands vast amount of time and computational resources. In order to perform thousands of lifetime simulations in a reasonable time, several model simplifications have to be made. Therefore, within the scope of this thesis, an optimized battery pack simulation approach will be developed, which allows representation of stoichiometric changes on the cell level and at the same time, temperature gradients and balancing strategies on the system level.

1.4.4 Prototyping platform for battery management systems

Experimental investigation of self-discharge and entropy via voltage based methods relies on accurate and stable voltage measurement hardware. Therefore, the voltage will be measured with a custom-built measurement unit on the basis of the ADS1278 from Texas Instruments, a 24 Bit ADC with 8 differential input channels. All channels underwent gain and offset calibration with a high precision voltage source LTC6655 from Linear Technology. The noise level for each channel was below 15 µV for a 10 Hz sampling rate. Due to the high input impedance of 20 GΩ it was ensured that leakage current of the circuit was negligible and that there was no interference with the voltage measurement by slowly discharging the cell. This voltage measurement board was designed as a part of a flexible prototyping platform for battery management systems (EES-BMS), which was developed within the scope of this thesis.

Experimental validation of different aging rates within a battery module or pack relies on controllable operational conditions for each cell. A forced temperature gradient was applied by Klein *et al.* in order to investigate the influence of non-uniform temperature conditions on current distributions among cells in parallel [155]. In that investigation, all cells were placed in an enclosing aluminum casing, while Peltier elements on each side of the aluminum block controlled the non-uniform temperature distribution. Using two lithium-ion cells in series, one of which was placed in a climate chamber at 55 °C and another at 25 °C, Chiu *et al.* showed that temperature gradients have a negative impact on pack performance and can induce safety issues, if cell voltage supervision is neglected [152]. However, no detailed information on the voltage imbalance was presented. Cordoba *et al.* demonstrated via simulation that the lifetime of a battery pack depends on the topology, thermal properties, cell balancing and intrinsic cell parameter variations, although the latter were not significant for the aging progression of the pack [156]. Unfortunately, voltage-drift progression was not also presented. Wang *et al.* compared the aging behaviors of four different battery pack typologies, including those connected in series with uniform temperature distribution among all cells [153]. The presented empirical study revealed a higher degradation rate of battery packs compared to single cell aging. More details on possible roots of such behavior were provided by Zheng et al. [157]. Reduced capacity of a battery pack consisting of two cells at 30 °C and 45 °C connected in series was linked to voltage imbalance, which was induced by different rates of loss of lithium inventory. However, no cell balancing during the cycling was applied. A comprehensive aging study of two 8s14p modules with dissipative balancing and naturally emerged temperature gradients was carried out by Campestrini *et al.* [46]. Results revealed no considerable deviations between single cell and battery pack aging. Owing to the fact that dissipative balancing was active during the entire time and not only during the idle phases, no statement regarding balancing charges and voltage imbalance could be made, since the influence of impedances was more dominant than the influence of different capacities.

To date, no study has been presented, which investigated module aging with forced temperature gradients, while evaluating the root of the voltage imbalance and balancing effort. Therefore, this will be covered within this thesis.

1.5 Thesis outline

As mentioned above, the root causes of diminished pack utilization of cells connected in series most likely lay with the voltage imbalance and the voltage drift during the lifetime of the battery packs. As this problem is well known in the engineering community, most battery packs are equipped with balancing circuits, which are able to adjust the cell voltages. Despite the common use of balancing systems, true benefits and interpretation of balancing efforts are not yet completely understood. A true understanding of the roots of voltage imbalance might not only allow an optimal BMS design, but may possibly enable the use of balancing charges as a further description of the state of a battery system.

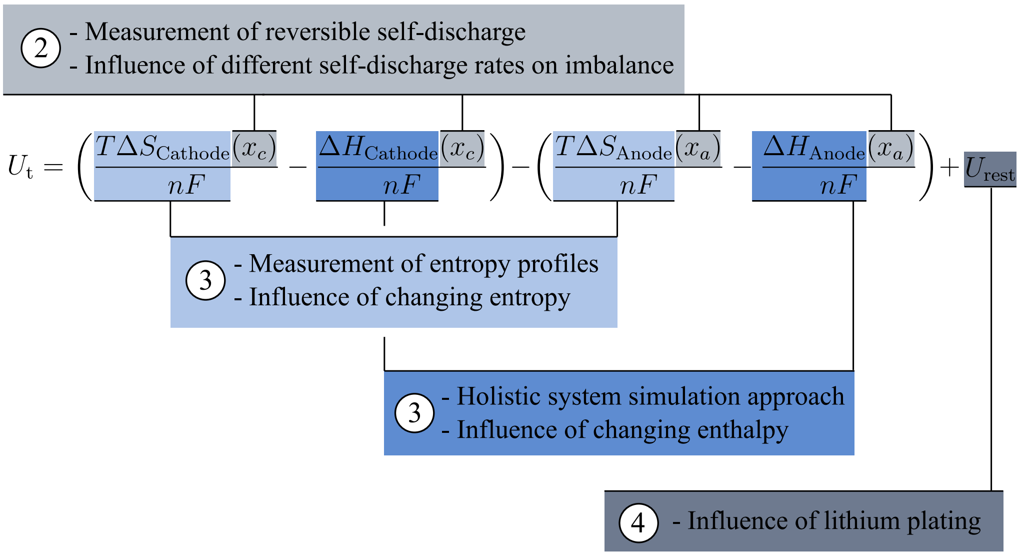

Figure 1.13: Thesis outline according to the equation 1.10.

This thesis is structured according to the goals, which were previously defined and is outlined in Fig. 1.13 using the influencing factors suggested by the equation 1.10 describing the terminal voltage of a lithium-ion cell. After the introduction, the influence of self-discharge rates on voltage imbalance is discussed in Chapter 2. For that purpose, a new reliable measurement method of reversible self-discharge is developed and validated. Subsequently, this measurement method is applied to determine the self-discharge variations among a batch lithium-ion cells of the same type. In Chapter 3, the influence of different aging rates on voltage imbalance is described, whereby a distinction is made between changes in half-cell OCVs, dominated by the enthalpy and entropic coefficients. Chapter 3 begins by presenting a new accurate measurement method for entropic coefficients, which is used for the discussion of the influence of half-cell reaction entropies on the voltage imbalance. Subsequently, an optimized holistic simulation approach for the battery system lifetime simulation according to system parameters, such as balancing strategy and temperature gradients, is presented. This simulation approach is then integrated into a Monte Carlo simulation, which investigates the influence, of a change in stoichiometric parameters on half-cell profiles and therefore full-cell voltages in large battery packs. In Chapter 4, an experimental investigation of the influence of different aging rates on the module with a forced temperature gradient, focusing on lithium plating, is presented. Finally, in Chapter 5, the results of this work are summarized and concluded.

2 Influence of self-discharge on the voltage imbalance

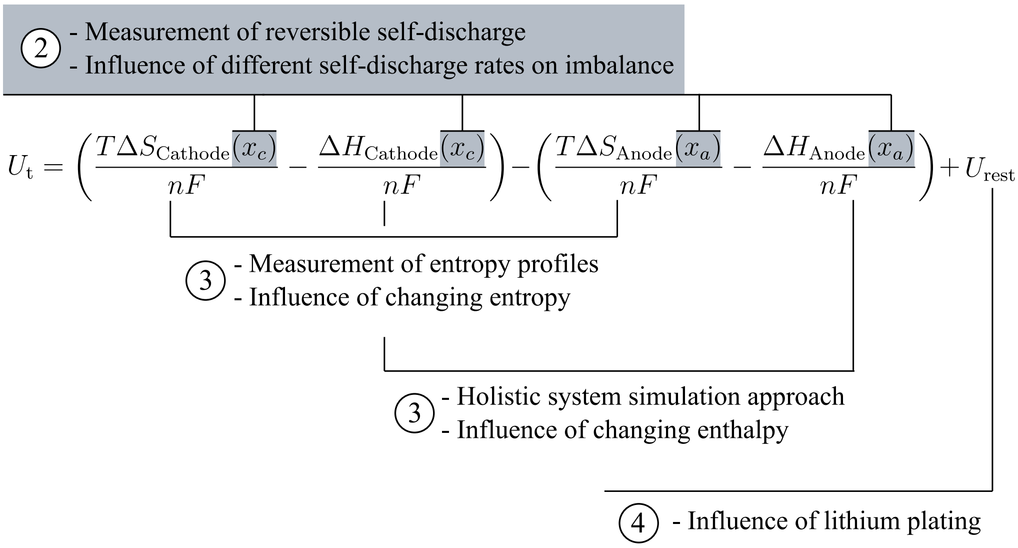

Figure 2.1: Outline of chapter 2.

In the literature to date, the reversible self-discharge of lithium-ion cells has not been granted much attention, due to its low absolute values. The often stated 1 %-2 % loss in SOC per month [158] appeared very low, compared with other energy storage systems such as, flywheel or pneumatic storage techniques [159]. As it did not appear to be a significant problem at the cell level, little effort was made to understand the underlying mechanisms in detail. However, the determination of the self-discharge still plays an important role, especially in the quality control of cell manufacturing. As part of so called end of line (EOL) test, each cell is checked for manufacturing defects. Since the outcome of a self-discharge measurement within the production line usually only decides whether a cell should be further considered for shipping or be recycled, the exact variations in the self-discharge rates of the cells are not evaluated. However, by taking the long operating time of an energy storage system into account, even small differences in self-discharge rates might lead to diminished battery pack utilization.

This chapter includes two articles, which present results regarding the voltage based measurement of the self-discharge, the origins of the self-discharge and finally, the influence of different self-discharge rates on the voltage imbalance in large battery packs.

2.1 Reliable measurement of the reversible self-discharge current

The goal of this article was to optimize the voltage based measurement method and to apply it to commercial lithium-ion cells for precise characterization of the self-discharge current at different SOCs and temperatures. The voltage based measurement was applied, since this technique forms a good trade-off between its need for resources and its relevance to real-life application scenarios. Determination of the self-discharge is based on the following equation:

$$\frac{\mathrm{d}Q}{\mathrm{d}U} \cdot \frac{\mathrm{d}U}{\mathrm{d}t} = \frac{\mathrm{d}Q}{\mathrm{d}t} = \sum I_{\mathrm{sd}} \tag{2.1}$$

which implies that the slope of the voltage decay, multiplied with the change of charge related to a change in voltage, can be interpreted as a current. However, several problems regarding the implementation of this method arise. First, as described in the introduction, lithium-ion cells exhibit dynamic overpotentials, even long after a load current was applied. Such long term equalization processes are dominated by the inter-particle diffusion, which is highly non-linear and depends on the SOC and temperature [160]. In other words, the time which has to pass after a discharge pulse until the self-discharge processes dominate the progression of the terminal voltage, is uncertain. Furthermore, despite the presence of a negative voltage gradient, the influence of equalization processes is still unknown at that moment, which might lead to a changing negative slope over time, delaying further the determination of the self-discharge.

Typically, OCV measurements can be utilized to determine the quotient between the charge and the voltage. However, this method has disadvantages regarding the accuracy of the calculated self-discharge. There are two ways to determine the OCV of a lithium-ion cell: via incremental or constant current measurement methods. The latter method is based on the charge and discharge of the cell with a low current. Usually, the applied current lies between 0.05 C [161] and 0.025 C [162]. Afterwards, the charge and discharge curves are averaged in order to reduce the influence of the overpotentials and hysteresis effects. As a result, a continuous OCV curve is produced at the cost of the cell terminal voltage being superimposed with the overpotentials, even at the smallest load current. The incremental measurement method addresses this problem by evaluating the terminal voltage in the no-load condition after several hours of relaxation at defined SOCs [163]. Due to inevitable hysteresis effects, the incremental method is also usually applied in both the charge and discharge direction, after which both curves are averaged. In that way, the OCV, which is determined via the incremental method, is more precise, as it has been shown in [164][165]. However, the accuracy comes at the cost of either the resolution or the duration of the measurement, since a finite number of SOC points are used for the OCV determination. The charge and discharge curves obtained at 25 °C using both OCV measurement methods of the full cell are shown in Fig. 2.2. Owing to the 10 h relaxation time at each SOC, incremental charge and discharge curves exhibit a smaller gap between each other than the curves obtained with the constant current method, especially at the low SOCs. However, a simple averaging of the charge and discharge curves would lead to a blurring of the OCV curves, worsening the accuracy of the self-discharge measurement.

In order to investigate the duration of equalization processes, the voltage of 13 selected cells between 10 % and 90 % SOC was monitored over the 11 months of storage, which made it possible to decide after which point in time, the voltage decay could be interpreted as self-discharge. The charge over voltage quotient was determined via small discharge pulse, after all equalization processes had finished.

The results presented in the following article show that the voltage based measurement method is generally suitable for determination of the self-discharge current. However, several limitations have to be taken into account. Even after the point at which the gradient of the voltage progression as a function of time became negative, it took about 62 days until the voltage gradient of each cell was constant. The causes of such long-term voltage relaxation were linked to the equalization between

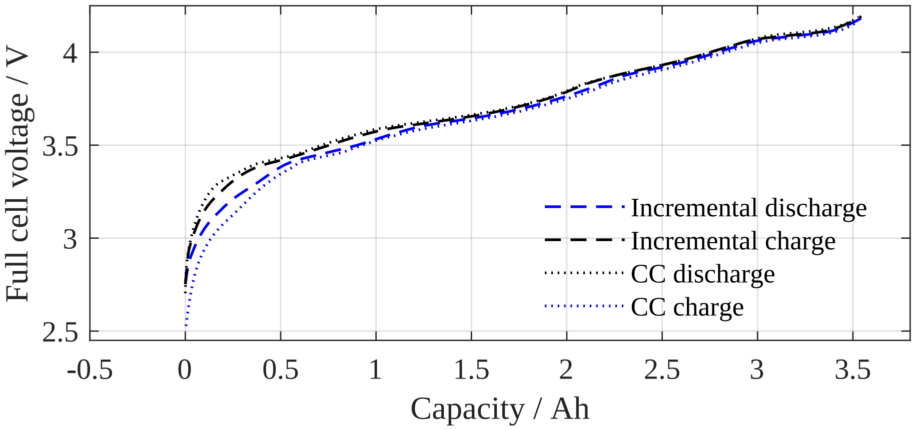

Figure 2.2: Charge and discharge curves of the MJ1 cell, derived using both incremental and constant current measurement methods.

the active and inactive areas of the anode. After these equalization processes were completed, the self-discharge recorded was in very good accordance with results from capacity based measurements. Furthermore, the self-discharge rate showed an exponential dependency on the SOC and Arrhenius characteristic with regard to temperature. The absolute values at 25 °C were below 7 µA, which amounts to approximately 0.1 % reversible self-discharge per month. The results further revealed that the self-discharge was most likely caused by coupled side reaction between the positive and the negative electrode, triggered by the loss of lithium inventory at the anode.

Authors contribution Design, execution of the experiment and development of the custom-build voltage measurement hardware were performed by Ilya Zilberman. Data processing and simulations were also performed by Ilya Zilberman. Johannes Sturm provided the half-cell profile data. Andreas Jossen supervised this work, the manuscript was written by Ilya Zilberman and was edited by all authors.

Reversible self-discharge and calendar aging of 18650 nickel-rich, silicon-graphite lithium-ion cells

Ilya Zilberman, Johannes Sturm, Andreas Jossen

Journal of Power Sources 425, pp. 217–226, 2019

Permanent weblink:
`https://doi.org/10.1016/j.jpowsour.2019.03.109`

Journal of Power Sources 425 (2019) 217–226

Contents lists available at ScienceDirect

Journal of Power Sources

journal homepage: www.elsevier.com/locate/jpowsour

Reversible self-discharge and calendar aging of 18650 nickel-rich, silicon-graphite lithium-ion cells

I. Zilberman*, J. Sturm, A. Jossen

Institute for Electrical Energy Storage Technology, Technical University of Munich (TUM), Arcisstr. 21, 80333, Munich, Germany

HIGHLIGHTS

- Capacity fade during the storage is driven by the LAM at the anode.
- Self-discharge current is below 4.5uA at 25°C and is caused by side reactions.
- Anode overhang severely disturbs the self-discharge measurement.

ARTICLE INFO

Keywords:
lithium-ion
Self-discharge
Aging
Silicon
Anode overhang

ABSTRACT

Lithium-ion cells with nickel-rich cathodes and silicon-graphite (SiC) anodes are expected to be deployed in the next generation electric vehicles (EV) due to their high specific energy density and price advantages. While the majority of current research focuses on cycle performance of nickel-rich/SiC cells, there is no general understanding of reversible self-discharge processes and degradation mechanisms during calendar aging. In this study, capacity fade of commercial 18650 nickel-rich/SiC cells after 11 months of storage was analyzed using differential voltage analysis (DVA). Reversible self-discharge losses were determined via capacity measurements before and after the storage and via decay of cell voltages, which were monitored throughout the experiment. The results obtained in this work reveal that capacity fade was mainly caused by the loss of active material (LAM) of the anode, which was linked to the presence of silicon. In the range between 33% and 58% state of charge (SOC), in which anode overhang and active area of the anode exhibited similar potential, both self-discharge measurement methods showed consistent results. Calculated reversible self-discharge current ranged between 2 μA and 4.5 μA at 25°C and was linked to coupled side reactions between the negative and positive electrode.

1. Introduction

Increasing demand for environmental friendly mobility, as well as the rising trend for decentralized energy infrastructure, require reliable and economical solutions for electrical energy storage. Lithium-ion technology has shown a high potential to fulfill these needs due to its high energy density. Additionally, it has overcome disadvantages, such as high price and short life time [1]. In the meanwhile, lithium-ion batteries can be found in applications ranging from mobile phones to electric vehicles. First generations of cathodes are now gradually replaced by nickel-rich materials, which provide similar achievable specific capacity with explicit price advantages due to reduced amount of cobalt [2,3]. Silicon, having a much higher specific energy density than graphite, has been recently used as an additional compound for graphitic host lattices, in order to increase the gravimetric energy density of the negative electrode [4–6]. High volumetric expansion of silicon, however, implicates a limitation of silicon to graphite ratio, since it leads to possible instability of the mechanical structure during the lithiation and delithiation of the anode [7]. Due to higher energy density and price advantages, lithium-ion cells containing nickel-rich cathodes and SiC anodes are assumed to be deployed in the next generation EV [8,9]. However, successful use of this technology requires a comprehensive understanding of cell degradation mechanisms during cycle and calendar life, including reversible self-discharge behavior.

Cycle performance is usually affiliated to the containment of mechanical stress in cells with SiC anodes. For instance, electrolyte composition has been identified to play the crucial role of attenuating the expansion of a particle's surface in the development of a thicker solid

---

* Corresponding author.
E-mail address: ilya.zilberman@tum.de (I. Zilberman).

https://doi.org/10.1016/j.jpowsour.2019.03.109
Received 21 February 2019; Received in revised form 25 March 2019; Accepted 26 March 2019
0378-7753/

electrolyte interface (SEI) layer [10,11]. Although, Dupré et al. pointed out that extended cycling experiments of cells with SiC anodes in full cell configurations show major differences from cells in half cell configurations due to lack of cyclable lithium [12], only a few aging studies of nickel-rich full cells with SiC anodes have been published. Wetjen et al. distinguished between silicon particle degradation and electrode degradation in full cells with $LiFePO_4$ cathodes, both being caused by mechanical stress [13]. Additionally, a linear correlation between irreversible capacity loss and decomposition of fluoroethylene carbonate (FEC) on silicon particles was observed. Recent cycle aging study on commercial 18650 nickel-rich/SiC cells revealed a loss of active materials on both electrodes [14]. High volume expansion of silicone particles supported SEI cracking and concurrent SEI growth, which additionally led to loss of lithium inventory (LLI) [14].

While the majority of current research in degradation mechanisms of nickel-rich/SiC cells focuses on cycle performance, only few studies on calendar aging have been published. Owing to the fact, that during the storage no mentionable mechanical stress occurs, the calendar aging behavior of cells with SiC anodes is expected to be similar to the aging behavior of cells with graphite anodes. Keil et al. showed that the main reason for capacity loss in cells consisting of a graphite anode during the storage is a shift in electrode balancing depending on the anode potential, indicating LLI and not a degradation of electrode materials [15]. Kalaga et al. performed storage tests with potentiostatic hold on nickel-rich/SiC cells [16]. It was concluded in similar fashion that, the capacity fade was mainly brought from the passivation of the SEI and associated LLI. However, despite almost non-existing volume expansion during potentiostatic hold, infrequent current bursts were measured, indicating sudden accelerated SEI passivation. In contrast, potentiostatic hold of standard $LiFePO_4$/graphite cells revealed declining floating current, indicating the self-limiting feature of the SEI passivation [17], which was not observed in cells with SiC anodes.

Additionally, there is no information about the ratio between irreversible capacity loss and reversible self-discharge of nickel-rich/SiC cells. Reversible self-discharge is noticeable due to voltage decay without measurable capacity loss of the full cell. Such behavior was usually attributed to transition metal dissolution and electrolyte oxidation, which would lead to shuttle effects [18,19]. Soft short circuits between both electrodes are also able to cause a slow discharge of the cell.

Generally, there are three different self-discharge determination methods. The first method is based on measurement of the discharge capacity before the storage, and residual and discharge capacity after the storage [20]. The capacity based method does not require any specific resources, besides the cell cycler and a climate chamber. However, due to small self-discharge currents, an ascertainable reversible capacity loss implicates long storage time. In order to shorten the self-discharge determination, floating current was measured, while the cell voltage was held constant [17–21], which is the second method. This current combines all side reactions, which influence half-cell potentials. However, such storage conditions are not equivalent to the real storage, since a potentiostat provides an external path for electrons, which might result in differently proceeding side reactions. The third method, voltage based measurement, similar to the current based method, also utilizes the influence of side reactions on half-cell potentials, which leads to voltage decay $\mathrm{d}U/\mathrm{d}t$. Combined with the derivative of the open circuit voltage (OCV) $\mathrm{d}Q/\mathrm{d}U$ the self-discharge current is calculated as follows:

$$\frac{\mathrm{d}Q}{\mathrm{d}U}\cdot\frac{\mathrm{d}U}{\mathrm{d}t}=\frac{\mathrm{d}Q}{\mathrm{d}t}=\sum I_{\mathrm{sd}} \tag{1}$$

where $\sum I_{\mathrm{sd}}$ is the sum of all side reaction currents which have an influence on half-cell potentials of both electrodes, and $\mathrm{d}U/\mathrm{d}t$ is the stabilized slope of the observed voltage decay. In order to differentiate between voltage relaxation, including overpotentials from charge transfer and diffusion, Schmidt et al. applied a discharge pulse before evaluating the voltage of cells with a blended NCA/$LiCoO_2$ cathode and graphite anode [22]. After the cell voltage exhibited a constant negative slope, the self-discharge processes were considered to be more pronounced than the voltage relaxation processes. However, during the period of the experiment, no voltage between 70% and 10% SOC exhibited a negative slope. In a further voltage based self-discharge study with NMC/graphite cells, only values over 70% SOC were presented [23].

This work reveals new insights, regarding the mechanisms of capacity fade of nickel-rich/SiC cells during storage. Additionally, reversible self-discharge is determined over the whole SOC range using capacity and voltage based measurements. Both methods are evaluated and compared. This paper is organized as the following. First, cell characteristics are described using differential voltage analysis (DVA). Afterwards, experimental setup, including measurement equipment, temperature control and detailed test sequences are presented. Finally, experimental results on capacity fade during storage and reversible self-discharge of nickel-rich/SiC cells are presented and discussed.

2. Experimental

2.1. Cell characteristics

The object of this study was a commercial NMC(nickel-rich)/SiC 18650 high energy lithium-ion cell INR18650-MJ1 from LGChem with nominal capacity of 3.5 Ah and specific energy of 259.6 $\mathrm{Whkg^{-1}}$. According to the cell manufacturer the recommended operation window is between 4.2 V and 2.5 V. For this experiment 13 pristine cells were selected with minimum and maximum constant charge - constant phase (CCCV) capacity of 3.5086 Ah and 3.5307 Ah respectively. The R_{DC10s} value, which is a DC resistance, calculated after 10 s discharge pulse at 50% SOC, ranged from 43.67 mΩ to 45.26 mΩ. Each cell was assigned to different SOC throughout the whole SOC range, and relevant extreme values in the differential voltage were also covered, as listed in Table 1.

Sturm et al. performed analysis of active materials and measured half-cell open circuit voltage (OCV) curves for both electrodes of MJ1, shown in Fig. 1a for a 0.033C discharge scenario [24]. Electrode balancing revealed an oversized cathode (~ 9.4%) and an almost complete use of the anode (> 99%) [24]. Such extreme utilization of the anode facilitated the high energy density of the cell. Fig. 1b shows that reconstructed and full cell differential voltages are in good accordance with each other. The amount of silicon in graphite was measured via inductively coupled plasma-optical emission spectroscopy (ICP-OES) and amounted to ~ 3.5 wt % [24]. The ratio of nickel, manganese and cobalt in the active material of the cathode, determined via ICP-OES,

Table 1
Overview of parameters of 13 cells used in the experiment, including the capacity of the cell, the internal resistance and storage SOC.

Parameter	1	2	3	4	5	6	7	8	9	10	11	12	13	μ	σ
C/Ah	3.51	3.52	3.51	3.53	3.53	3.52	3.53	3.52	3.51	3.51	3.52	3.53	3.51	3.5188	0.0078
R_{DC10s} /mΩ	44.7	44.6	44.9	43.9	43.8	44.2	43.9	44	45.3	44.4	44.1	43.7	44.5	44.31	0.4769
SOC/%	10	21	24	27	32	40	50	58	61	64	70	80	90		

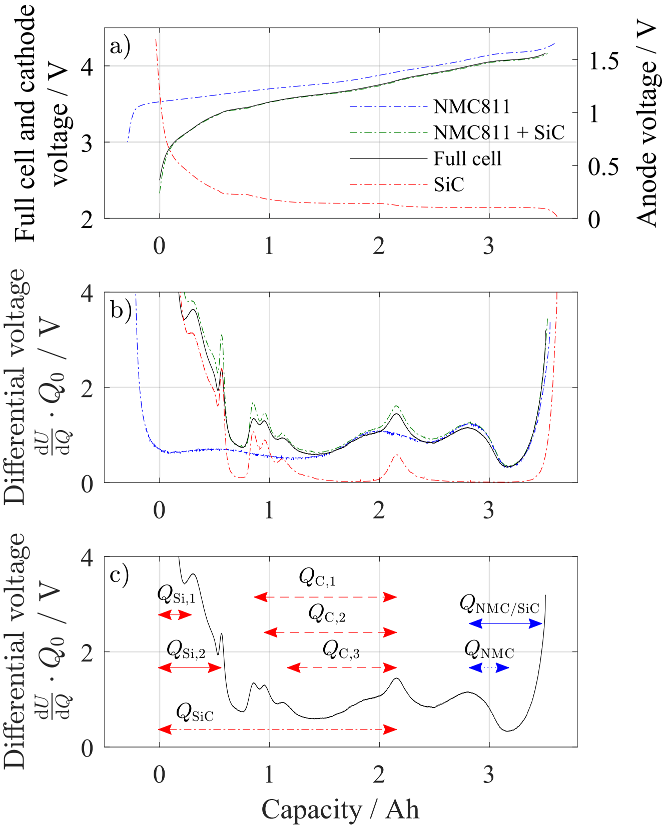

Fig. 1. (a) Measured half-cell cathode, anode and full cell voltages, and reconstructed full cell voltage for a 0.033C discharge [24], (b) DVA of cathode, anode and full cell voltages, and reconstructed full cell voltage, (c) Assignment of characteristic capacities to material distinctive DVA markers.

amounted to 82%-6.3%-11.7% respectively, indicating the dominance of nickel in the cathode.

The presence of silicon can be also observed by means of the anode potential. Graphite electrodes usually exhibit a steep ascent of the potential after reaching ca. 0.3V vs. Li + /Li. Silicon-graphite composite electrodes on the other hand, exhibit more smooth increase towards delithiation [4], as shown in Fig. 1a. Such smooth increase results in two distinctive peaks in the differential voltage of the negative electrode between 0% and 15% SOC, which were attributed to silicon. Fig. 1c shows affiliations of relevant extreme values within the full cell differential voltage with distinction between anode and cathode characteristics. Q_{SiC} represents the distance between 0% SOC and the main graphite peak at 2.17Ah. This peak indicates the phase transition between LiC$_{12}$ and LiC$_6$ [25]. In general, change in absolute value of capacity Q_{SiC} is linked to change in storage capabilities of the anode [26]. Capacities $Q_{Si,1}$ and $Q_{Si,2}$ represent the distance between 0% SOC and both silicon peaks, and describe the storage capability of silicon. On the other hand, capacities $Q_{C,1-3}$ between the main graphite peak and local maxima between 0.8 Ah and 1.2 Ah describe the storage capability of graphite. Such differentiation can be achieved, since there is no overlap between distinctive material markers in differential voltage. Similarly to the anode markers, $Q_{NMC/SiC}$ usually provides information about storage capabilities of the cathode [26]. However, due to almost entire utilization of the negative electrode, $Q_{NMC/SiC}$, specifically for MJ1, contains also a characteristic of the anode or rather electrode balancing. Near full capacity, differential voltages of cathode and anode are both higher than zero, as shown in Fig. 1b. Q_{NMC}, on the other hand, is solely based on cathode characteristics and is therefore used to describe the storage capability of the cathode.

2.2. Setup and test sequence

Checkup routines and OCV measurements before and after the 330 days of storage were performed with the Cell Testing System (CTS) from Basytec. During the storage the voltage was measured with a custom-built measurement unit on the basis of ADS1278 from Texas Instruments, a 24 Bit analog digital converter (ADC) with 8 differential input channels. All channels underwent gain and offset calibration with a high precision voltage source LTC6655 from Linear Technology. The noise level for each channel was below 15 µV for a 10Hz sampling rate. Due to the high input impedance of 20 GΩ it was insured that leakage current of the circuit was negligible and that there was no interference with the voltage measurement by slowly discharging the cell. During the experiment, all cells were placed in a Binder KT115 climate chamber, which provided constant ambient temperature with an accuracy of 15 mK. The temperature was measured on the surface of each cell with mounted PT100 sensors.

The overall testing procedure is summarized in Table 2. A checkup routine contained determination of the residual capacity, followed by two CCCV charge and discharge cycles. Subsequently, R_{DC10s} value at 50% SOC was determined using a 1C discharge pulse. Exact parameters and termination values are summarized in Table 3.

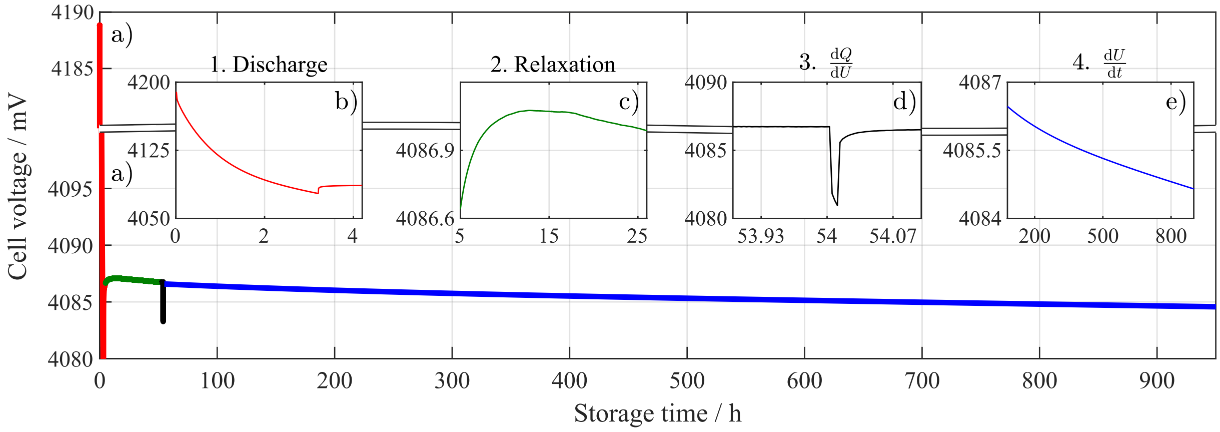

Fig. 2. Cell voltage progression during the first 40 days of the experiment. (a) Overall overview, (b) discharge to storage capacity, (c) voltage relaxation, till self-discharge processes predominate relaxation processes, (d) discharge pulse for isolated $\frac{dQ}{dU}$ determination, (e) voltage decay throughout the experiment.

Table 2
Overall test procedure.

Sequence	Description
1. Checkup 1	Checkup according to Table 3
2. 5 Cycles	Activation cycles. Charge CC (I= 0.5C), Discharge CC (I= 0.2C)
3. Checkup 2	Checkup according to Table 3
4. Initial OCV	OCV measurement according to Table 4
5. Storage	Storage and I_{sd} measurement according to Fig. 2
6. Checkup 3	Checkup according to Table 3
7. Checkup 4	Checkup according to Table 3
8. Checkup 5	Checkup according to Table 3
9. Final OCV	OCV measurement according to Table 4

Table 3
Checkup sequence consists of determination of residual charge $Q_{\mathrm{CUx,res}}$ (steps 1–2), two redundant, consecutive cycles for cell capacity determination $Q_{\mathrm{CUx,1}}$ and $Q_{\mathrm{CUx,2}}$ (steps 3–6), and determination of internal resistance R_{DC10s} (steps 7–9).

	Step	Parameters	Termination
$Q_{\mathrm{CUx,res}}$	1. Discharge CCCV	I= -0.2C, U= 2.5V	I> -50 mA
	2. Pause		t> 30 min
$Q_{\mathrm{CUx,1}}$	3. Charge CCCV	I= 0.5C, U= 4.2V	I< 50 mA
	4. Pause		t> 30 min
$Q_{\mathrm{CUx,2}}$	5. Discharge CCCV	I= -0.2C, U= 2.5V	I> -50 mA
	6. Pause & Repeat 3-5		t> 30 min
R_{DC10s}	7. Charge CC	I= 0.5C	SOC > 50%
	8. Pause		t> 10 min
	9. Discharge CC	I= -1C	t> 10 s

After the first checkup, all 13 cells underwent five activation cycles, after which a second checkup was performed. For possible detection of changes in storage capabilities and balancing of both electrodes via DVA, OCV curve measurements were conducted before and after the actual storage. The OCV curve was determined using constant current (CC) with 0.033C and constant voltage (CV) with current termination at 0.001C for charge and discharge direction. Such a long CV phase enabled a reliable reference point for the purpose of DVA of pristine and aged cells. All steps of OCV measurement sequence are summarized in Table 4.

Table 4
OCV measurement sequence.

Step	Parameters	Termination
1. Charge CCCV	I= 0.2C, U= 4.2V	I< 0.001C
2. Pause		t> 6 h
3. Discharge CCCV	-I= 0.033C, U= 2.5V	I> -0.001C
4. Pause		t> 6 h
5. Charge CCCV	I= 0.033C, U= 4.2V	I< 0.001C

After initial OCV measurement, each cell was fully charged (CCCV) with current termination at 0.001C and discharged after a pause (6 h) to the corresponding storage SOC according to its capacity and differential voltage. The reduction of the overpotential after the discharge pulse resulted in asymptotic incline of the cells terminal voltage, as shown in Fig. 2b. Ideally, such behavior enables a separation between voltage relaxation and self-discharge processes, since the latter usually results in a voltage decline. Therefore, while not taking into account the cycling history of the cell, the voltage progression should be evaluated according to Equation (1) after reaching a constant negative slope, as shown in Fig. 2c. The storage and self-discharge measurement procedure used in this paper supplemented the standard practice by two further steps. After a discharge step to according storage SOC (Fig. 2b) and relaxation step (Fig. 2c), a small discharge pulse (Fig. 2d) was applied. In that way an isolated $\mathrm{d}Q/\mathrm{d}U$ quotient could be determined after the voltage attained a negative slope, since use of the OCV curve for the self-discharge determination might be too inaccurate. A 0.033C discharge pulse was applied for 30 s, which resulted in $2.7 \times 10^{-14}\%$ change of SOC. For the sake of comparability, this pulse was additionally applied after 50 and 67 days of storage.

Finally, the progression of the voltage was measured during the whole storage time of 330 days, of which only the first 40 days are shown in Fig. 2a. Derivative of the voltage was calculated using linearization of 24 h. During the most storage time, checkup and OCV measurements, the temperature of the climate chamber was set to 25°C. In order to investigate the temperature dependency of self-discharge, two identical temperature profiles were applied. The temperature was varied from 25°C to 40°C–55°C and back to 25°C, remaining at each temperature for 96 h. The first temperature profile was applied after 50 days and the second profile after 67 days.

After the storage, three subsequent checkups were conducted, resulting in six cycles, which were used to asses the stability of the available capacity. The residual capacity in the first checkup after the storage $Q_{\mathrm{CU3,res}}$ enabled the separation between reversible self-discharge and irreversible capacity loss according to following equations

$$Q_{\mathrm{irr}} = Q_{\mathrm{CU2,2}} - Q_{\mathrm{CU3,1}} \tag{2}$$

and

$$Q_{\mathrm{rev}} = Q_{\mathrm{CU3,1}} - (Q_{\mathrm{DCH,SOC}} + Q_{\mathrm{CU3,res}}) \tag{3}$$

where $Q_{\mathrm{DCH,SOC}}$ is the charge, which was extracted during the discharge to storage SOC, $Q_{\mathrm{CU2,2}}$ is the capacity determined by the last cycle before the storage and $Q_{\mathrm{CU3,1}}$ is the capacity determined by the first cycle after the storage.

3. Results and discussion

3.1. Irreversible capacity loss

In the following, the evaluation of calendar aging of INR18650-MJ1 cells is presented. Fig. 3a shows the relative capacity decrease for each checkup cycle after 11 months of storage depending on the storage SOC. The results reveal familiar SOC dependency, which resembles the anode potential, shown in Fig. 3c, including a lower and higher plateau separated by the graphite phase transition at 61% SOC. The absolute values for the relative capacity loss reach from 2% at 10% SOC to 4.5% at 90% SOC. Keil et al. presented similar results for three different cell types with NCA, NMC and LFP cathode and graphite anode and demonstrated, that the anode potential was the driving force for capacity fade during calendar aging [15]. Relative resistance gain is shown in Fig. 3b. The data reveals a reverse dependency on SOC in comparison to capacity loss. In the range below 58% SOC, the R_{DC10s} gain amounts to 4%, while values above 58% SOC reach up to 6%. Fig. 3d shows the capacity differences referring to the first cycle after storage for all SOCs. The assessment of the capacity stability, reveals a capacity recovery effect, which can be clustered in three groups. Cells, which were stored at SOCs above 58% (group ①, low voltage plateau) gain capacity within two first cycles and retain this gain during the further cycling. Cells, which were stored at SOCs below 33% (group ③), on the other hand, showed immediate capacity loss after the first cycle. Cells between 58% and 33% (group ②, middle voltage plateau) revealed a small gain of the capacity during first two cycles, however, showed a moderate capacity loss during further cycling. Capacity recovery effect has been already reported for LFP/graphite, as well as NMC/graphite self-made and commercial cells [27,28]. Wilhelm et al. showed that after storage at high SOCs coulombic efficiency was higher than 1 for 1200h, resulting in rising capacity during 50 days [29]. XRD and color analysis showed that large overhang regions of the anode, which had no cathode

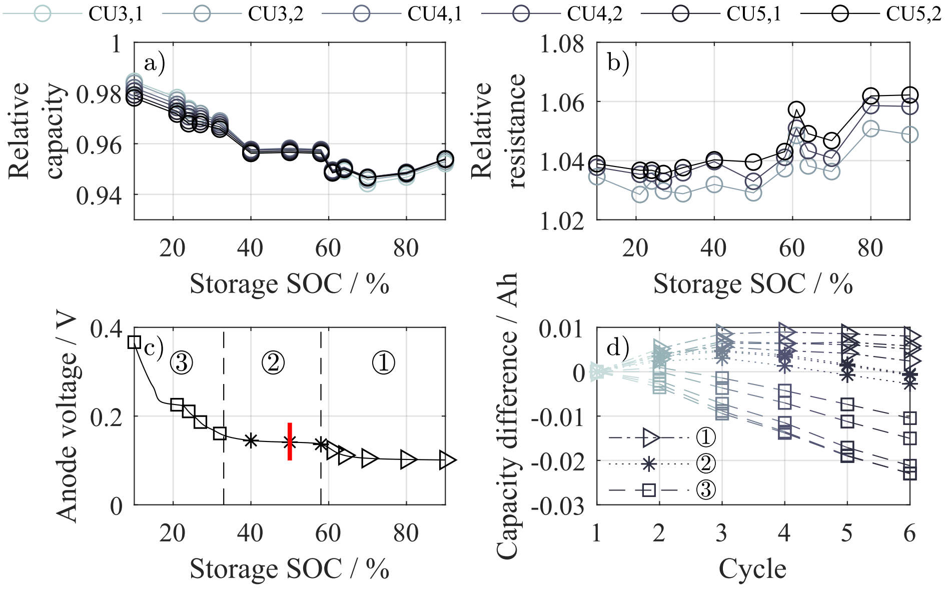

Fig. 3. (a) Relative capacity of all 6 cycles after the storage, (b) relative resistance after second, fourth and sixth checkup cycle, (c) measured anode OCV with segmentation in three areas and indicated storage SOCs, red line marks the average SOC of the active anode area, (d) capacity differences referred to the first cycle after storage for all SOCs.

counterpart, revealed different lithiation levels in comparison to active areas and were denoted responsible for capacity recovery effect. An oversized negative electrode is a common manufacturing practice for lithium-ion cells, which ensures that even due to possible small misalignment during stacking or cell winding, there is an anode counterpart across the whole cathode surface. Additionally, 1 mm overhang along the electrode is sufficient to prevent lithium plating on the edge of the anode [30].

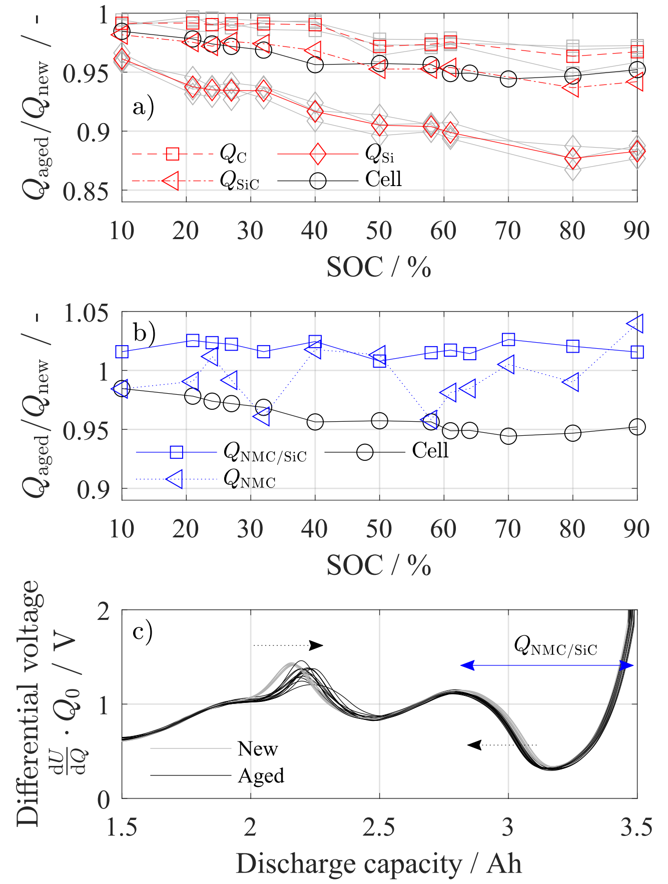

Fig. 4. (a) Relative change of distinctive anode markers, relative changes of capacities $Q_{\mathrm{Si},1-2}$ (gray) and $Q_{\mathrm{C},1-3}$ (gray) were averaged to relative changes of Q_{Si} (red) and Q_{C} (red), (b) relative change of distinctive cathode markers, (c) measured differential voltages before and after the storage for all SOCs. All curves are aligned on the right side of the plot. (For interpretation of the references to color in this figure legend, the reader is referred to the Web version of this article.)

Despite the absence of the cathode counterpart, inactive anode area is able to participate in equalization processes and store lithium, since it is soaked with electrolyte. However, such processes are very slow, since they are dominated by interparticle transport and are driven by potential differences of the flat OCV of graphite [31]. Therefore, the amount of lithium, which is moved during the equalization process, depends on the average potential of the active and inactive anode area, but also on its size ratio. The ratio between the overall and active area of the anode in the INR18650-MJ1 cell amounts to 1.084. The aggregated overhang includes both 1 mm stripes along the electrode as well as inactive areas at the beginning and the end of the jelly roll. In comparison, the ratio between overall and active anode area of commercial NMC/graphite cells, which showed a similar capacity recovery effect, amounted to 1.09 [32]. In case of a long storage at high SOC, equalization of active and inactive areas would result in high lithium concentration of the anode overhang. During cycling with depth of discharge (DOD) 100%, the average SOC of active area would amount to ca. 50%, as highlighted in Fig. 3c with the red line. Due to anode potential difference between 50% SOC and SOCs above 58% (group ①), the active area could slowly draw the extra lithium, stored in the inactive area, resulting in observed capacity recovery effect. In case of storage at low SOCs the effect would be reversed and it would cause a slow draining of lithium out of the active area and result in apparently accelerated aging. Fig. 3c emphasizes this effect by the evident potential difference between 50% SOC and SOCs below 33% (group ③).

In order to distinguish between different aging mechanisms, OCV curves of full cells before and after the storage were compared via DVA. Anode peaks between 24% and 32% SOC in differential voltage of both cells stored at 64% and 70% SOC were blurred and therefore were not taken into account. Fig. 4a shows the relative changes in anode related markers. For the sake of simplicity, relative changes of capacities $Q_{\mathrm{Si},1-2}$ and $Q_{\mathrm{C},1-3}$ were averaged to relative changes of Q_{Si} and Q_{C}. The first thing to be noticed in Fig. 4a is the decrease of Q_{SiC}, representing the storage capability of the anode. It indicates that the silicon-graphite blend anode of MJ1 cell experienced a loss of active material (LAM) during calendar aging. LAM is usually attributed to particle cracking and loss of electrical contact or blocking of active sites by resistive surface layers [33]. In that way, a part of the electrode's active mass is no longer available for intercalation and deintercalation of lithium.

Uniform LAM on the negative electrode would theoretically imply uniform compression of gaps between all relevant DVA markers. However, by differentiating between change in graphite Q_C and silicon Q_{Si} markers, it becomes evident, that compression of silicon markers is much stronger. While relative compression of Q_C ranges only from 99.12% to 96.73% with increasing SOC, Q_{Si} decreases in the range from 96.14% to 88.29%, as shown in Fig. 4a. Since there are no reports of LAM in pure graphite electrodes during calendar aging, it is assumed, that the non-uniform LAM is triggered by the presence of silicon.

DVA results of the positive electrode are depicted in Fig. 4b. They show, that relative change in Q_{NMC} exhibits high fluctuation over the whole SOC range without any regularity. On the one hand, it might be linked to the fact that the detection of exact maximum and minimum points of cathode relevant characteristics in full cell differential voltage was aggravated by flat dU/dQ curve. On the other hand, there was almost no absolute change in Q_{NMC} capacities and values fluctuated around 1. Therefore, LAM at the cathode of MJ1 was assumed to be highly unlikely.

Furthermore, in all cells a change of the combined cathode and anode marker was observed. $Q_{NMC/SiC}$ marker increased without any distinct SOC dependency. Charge wise this increase was rather small, as shown in Fig. 4c, where a small shift of the $Q_{NMC/SiC}$ peak can be observed for all measured differential voltages of pristine and aged cells. Additionally, a shift of the main graphite peak to the right was noticeable. Usually this shift indicates a change of electrode balancing as a result of LLI at the anode, if there is no LAM at the negative electrode. However, since the anode experienced LAM during the storage, no direct interpretation is possible.

In order to investigate the origin of increased $Q_{NMC/SiC}$ capacity, measured half-cell OCVs of anode and cathode were shifted and compressed. In that way different aging phenomena could be imitated and observed in differential voltage. Afterwards, differential voltages of initial and artificially aged cell were compared, whereby both curves were aligned on the right side. Similar techniques were already successfully applied in cell degradation diagnostics [33,34]. In the following a differentiation is made between LAM at the anode and side reactions (SR), which discharge the negative electrode and charge the positive electrode, causing a shift in electrode balancing. As LAM at the cathode is assumed to be very unlikely, it is not considered in further analysis. The results are presented in Fig. 5.

Anodic side reactions, such as growth and repair of the SEI, result in LLI [35,36]. It leads to a delithiation of the negative electrode and associated shift of the anode half-cell potential to the right, as shown in Fig. 5a. Since the anode is limiting in discharge direction, the overall

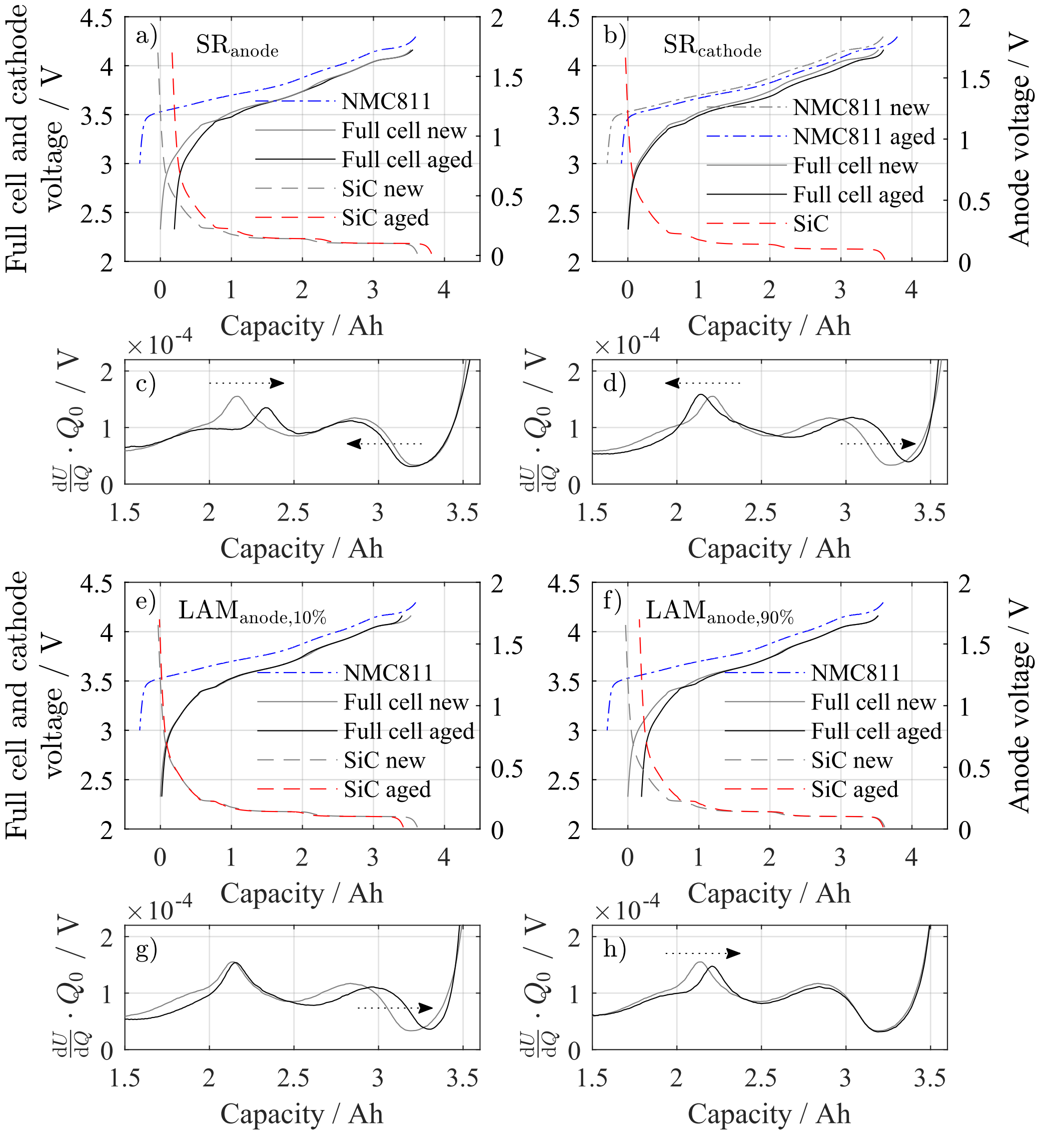

Fig. 5. Reconstructed impact of different degradation modes on the differential voltage. (a) and (c) Loss of lithium inventory at the anode, (b) and (d) loss of lithium inventory at the cathode, (e) and (g) loss of active material at the anode at 10% SOC, (f) and (h) loss of active material at the anode at 90% SOC.

cell capacity decreases. The differential voltage comparison in Fig. 5c depicts that the main anode peak moves to the right and the cathode peak moves to the left. Shift of electrode balancing might be also caused by cathodic side reactions, such as electrolyte oxidation and transit metal dissolution [37,38]. In that way the cathode half-cell potential would move to the right, as shown in Fig. 5b. At certain circumstances this effect can lead to an increase of the cell's capacity. In the differential voltage the main graphite peak moves to the left and the cathode peak moves to the right, as shown in 5d. Due to particle cracking and loss of electrical contact, small parts of the electrode might be unavailable for lithium intercalation [33]. Since, theoretically, the concentration of ions in particles does not change during LAM, no change in voltage is expected. However, the SOC at which the LAM occurs is crucial for the reconstruction of the full cell OCV. Fig. 5e and f shows a 10% loss of anode active material at 10% and 90% SOC respectively, and Fig. 5g and h shows associated differential voltages. In both cases, LAM leads to decrease of cell capacity. In case of LAM at 10% SOC only the cathode marker moves to the right, whereas in case of LAM at 90% SOC only the main graphite peak moves to the right. By comparing the results of calculated and measured differential voltages from Figs. 4c and 5, it can be concluded that increase of $Q_{\mathrm{NMC/SiC}}$ is most likely linked to side reactions at the anode, as only in that case the qualitative change of main anode and cathode peak is in accordance between experiment and simulation.

Evaluation of irreversible capacity loss via checkup measurements and DVA showed, that investigated cells exhibited a capacity recovery effect, which might be linked equalization processes between active and inactive area of the anode. Additionally, LAM in the anode, most likely caused by the presence of silicon, could be identified as the main reason for capacity fade during the calendar aging. Further, no clear evidence of loss of active material at the cathode could be found and increase of $Q_{\mathrm{NMC/SiC}}$ was linked to anodic SR, such as LLI.

3.2. *Reversible self-discharge*

In the following, results on reversible self-discharge, including the comparison of voltage and capacity based measurement methods, are presented. The derivative of cell voltages were evaluated after 4, 8, 16, 32, 64, 80 and 300 days of storage and are shown in Fig. 6a. Results reveal that after 16 days, all cells exhibited a negative voltage slope. However, even after the point in time, when self-discharge processes dominated relaxation processes of prior discharge, in some cases the voltage slope did not remain constant for the further 50 days. Observed long term voltage relaxation revealed also SOC dependency. Cells with storage SOCs above 58% (group ①) overestimated, and cells below 33% (group ③) underestimated the final slope of the voltage decay. Whereas cells with SOCs between 33% and 58% (group ②) reached the final voltage slope most rapidly. All cells were delivered with terminal voltage of 3.589V, which corresponded to ca. 33% SOC, highlighted with a red line in Fig. 6a. Based on the production date code, printed on the plastic cover of the cell, 11 months passed between the start of experiment and the end of production. Therefore, it is assumed that inactive and active area of the anode shared the same lithiation level at the beginning of experiment, which was near 33% SOC, referring to the full cell. Therefore, overestimated values of the voltage slope at high SOCs (group ①) were likely due to slow draining of lithium out of active area. Until the equalization of lithium concentrations in the active and inactive areas of the anode was finished, this effect possibly continued to aggravate the voltage decline.

Since an OCV curve does not exhibit a constant slope, there is a possibility that measured voltage decay (Fig. 6a) was yielded by an actual self-discharge and associated shift to a different OCV area. However, this reason was ruled out by determining the isolated $\mathrm{d}U/\mathrm{d}Q$ spectrum throughout the experiment. The first discharge pulse was applied after voltages of each cell exhibited a negative slope. Fig. 6b shows the calculated isolated $\mathrm{d}U/\mathrm{d}Q$ quotient after 4, 80 and 300 days.

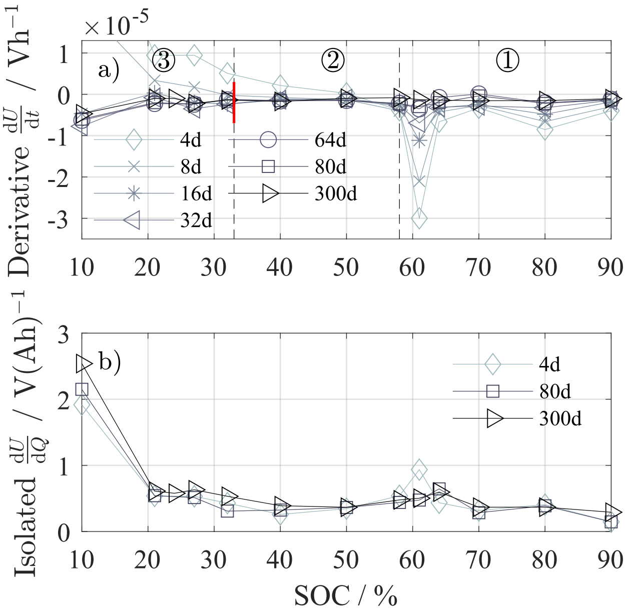

Fig. 6. (a) Calculated slope of the cell voltage during the experiment, red line marks the SOC of the anode overhang area, (b) measured isolated $\frac{\mathrm{d}U}{\mathrm{d}Q}$ during the experiment. (For interpretation of the references to color in this figure legend, the reader is referred to the Web version of this article.)

Except for graphite phase transition at 61% SOC, the derivative of the OCV does not show considerable changes. Therefore, long term voltage relaxation was rather linked to equalization phenomena between active and inactive areas in the anode, than a change in the OCV slope due to actual self-discharge.

After the impact of long term equalization processes onto the voltage were diminished, the self-discharge current was calculated after 64 days according to Equation (1) for 25°C, 40°C and 55°C. Results are shown in Fig. 7a. The first thing to notice is that self-discharge increased with increasing temperature and amounted 135 μA at 90% SOC at 55°C. However, at 25°C, the calculated self-discharge current ranged from 2 μA to 4.5 μA, which is equivalent to 0.04%–0.1% reversible capacity loss in one month. As shown in Fig. 7b, the temperature dependency revealed an Arrhenius-like behavior. Such relationship supports rather an electrochemical origin of reversible self-discharge, than a soft short circuit within the cell. Overall, self-discharge current depicts an exponential characteristic over the SOC range, however there is an deviation for all temperatures between 20% and 50% SOC. That might be brought by cell intrinsic parameter variation, or by the fact that the calculated self-discharge contains all side reaction currents with an influence on the half-cell potentials.

Further, reversible self-discharge during 11 months of storage was measured using the capacity based method and was compared with the voltage based technique. Results, which are shown in Fig. 7c, reveal that measured reversible loss via the capacity based method and calculated reversible loss via the voltage based method are not consistently in accordance with each other. The difference between both methods is depicted in Fig. 7d. The deviation increases at SOCs above 58% (group ①) and the capacity based method overestimates the voltage based results. Values at SOCs below 33% (group ③) show a reversed behavior, the capacity based data underestimates the results of the voltage based measurement. Self-discharge results from both measurement methods are in good accordance with each other only at SOCs between 33% and 58% (group ②).

Such discrepancy might be caused by overhang areas of the anode, which were lithiated to 33% SOC at the beginning of the experiment due to cell manufacturing process. The voltage slope was evaluated after most equalization processes were finished or at least were not

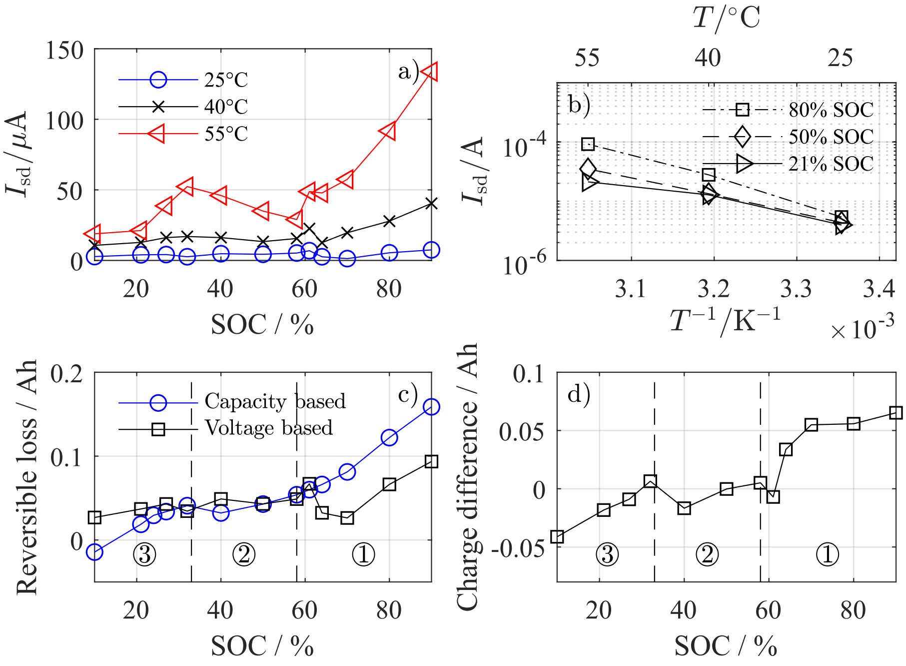

Fig. 7. (a) Calculated self-discharge current for different temperatures, (b) Arrhenius-like behavior of self-discharge, (c) overall reversible losses during 330 days of storage (including both temperature profiles), determined by capacity based and voltage based measurement, (d) difference between capacity based and voltage based measurement results.

longer observable in the terminal voltage, and therefore it can be assumed that the voltage based method determined only self-discharge current. On the other hand, the capacity method included all effects between the last cycle before and first cycle after the storage, including equalization processes between active and inactive area and actual self-discharge. The potential differences between anode active and inactive areas of cells from group ② were rather small, and therefore there was no driving force for equalization. Assuming that the initial SOC of the inactive area was around 33%, potential wise, all active and inactive areas of cells from group ② were in the middle voltage plateau of the anode OCV curve. Potential differences of group ① and ③ most likely caused draining current into and out of the active area of the anode. This draining current was able to disturb the storage based measurement or voltage based measurement before finalizing the equalization between active and inactive anode part. Therefore, in case of storage based measurement of reversible self-discharge, anode overhang areas must be taken into account in order to avoid measurement inaccuracies.

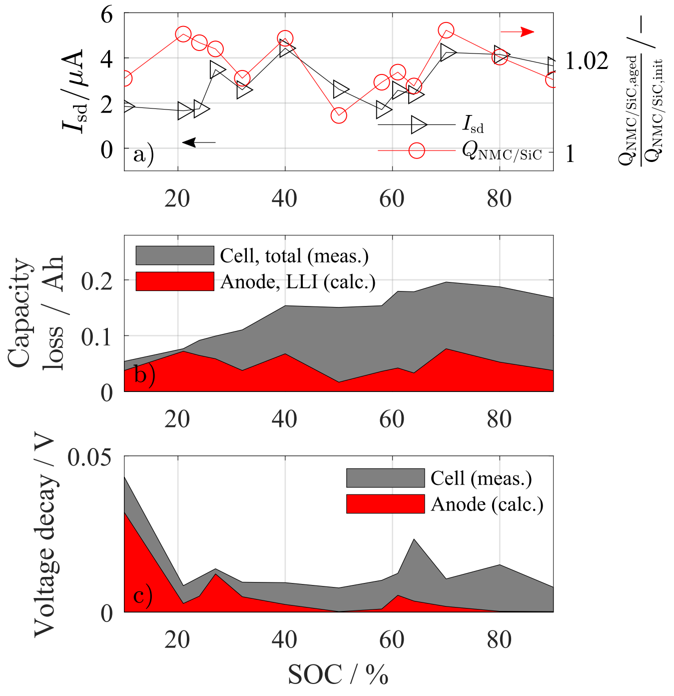

Fig. 8. Analysis of self-discharge. (a) Self-discharge current at 25°C and relative change in $Q_{NMC/SiC}$, (b) measured total capacity loss after the storage and simulated capacity loss due to LLI, (c) simulated and measured voltage decay during the experiment.

The calculated self-discharge current at 25°C via the voltage based method is depicted in Fig. 8a in black. The values were determined using dU/dQ and dQ/dt quotients, which were measured after 300 days of storage at 25°C. The self-discharge current does not show a distinctive dependency on the SOC, however a slightly increasing trend is noticeable. It is likely that the results at 25°C are more influenced by intrinsic variance of self-discharge between the cells than SOC dependency. The right ordinate in Fig. 8a depicts the relative change in $Q_{NMC/SiC}$ over the evaluated SOC range. The comparison reveals, that there is an evident correlation between calculated self-discharge currents and measured increase of $Q_{NMC/SiC}$, except for low SOC range. As already derived in previous section, an increase of $Q_{NMC/SiC}$ was most likely caused by LLI at the negative electrode. Therefore, it can be assumed that there is a link between reversible self-discharge and LLI at the anode, which is discussed in the following.

Using both half-cell OCVs, the capacity loss evoked by the LLI at the anode was calculated. The half-cell OCV was shifted to the right, until the calculated $Q_{NMC/SiC}$ in the artificial full cell differential voltage matched the measured $Q_{NMC/SiC}$. The capacity, which was required for the shift to the right, represented the capacity loss, solely caused by the LLI at the anode. Fig. 8b shows the LLI loss and additionally the total capacity loss, where the LLI share is non-dominant. Associated discharge of the negative electrode due to LLI would lead to a voltage decay of the full cell. By taking into account solely anodic SR and by shifting half-cell OCV of the anode by the LLI capacity from Fig. 8b, voltage decay of the full cell was calculated and is shown in Fig. 8c in red. Additionally, measured voltage decay during the experiment is depicted in gray. For that, voltage decay of the last 200 days of the experiment was linearly scaled up to the whole duration. First 130 days of the experiment were not taken into account in order to avoid any interference of equalization processes with anode overhang areas. From Fig. 8c it can be seen, that measured and simulated voltage decay share similar characteristics over the whole SOC range. However, solely anodic SRs are incapable of reproducing the measured voltage decay of the full cell. For instance measured voltage decay in upper SOC range amounted from 8 to 15 mV, whereas the calculated voltage decay caused by LLI amounted only to 0.1–0.2 mV. Therefore, it stands to reason that observed voltage decay was also caused by SR on the positive electrode. Due to the high voltage slope of the half-cell OCV curve, even small changes in lithium concentration at the cathode would lead to observable changes in terminal voltage of the full cell.

Results on reversible self-discharge of the MJ1 cell have shown that the origin of the self-discharge lies in coupled SR between negative and positive electrode, possibly initiated by SR at the anode. Absolute values of the self-discharge were smaller by 20 times than the usually stated 1%–3% reversible capacity loss per month. The voltage based method has been evaluated and shown trusted results after equalization processes were finished. The storage based measurement of reversible self-discharge, however, was disturbed by the presence of anode overhang areas.

4. Summary and conclusion

In this work irreversible capacity loss during storage and reversible self-discharge of commercial 18650 lithium-ion cells with nickel-rich cathodes and silicon-graphite anodes were investigated. 13 pristine cells were discharged to SOCs between 10% and 90% and were stored for 11 months in a climate chamber. At the same time the terminal voltage of each cell was logged with a high input impedance measurement unit. Degradation mechanisms were analyzed using differential voltages before and after the storage. Additionally, capacity and voltage based self-discharge measurement methods were evaluated and compared with each other. Main findings are summarized in the following:

1. Loss of active material at the anode was found to be the main reason for capacity fade during the storage. Exact mechanisms behind this phenomena are not clear yet and have to be investigated further. Although, loss of lithium inventory at the anode was observed, it played only a minor role in capacity fade during calendar aging.
2. Reversible self-discharge current ranged between 2 μA and 4.5 μA at 25 °C and was most likely caused by coupled side reactions between negative and positive electrode, triggered by LLI at the anode.
3. Anode overhang disturbed the capacity based self-discharge measurement, caused long-term voltage relaxation and evoked capacity recovery effect during cycling after the storage. The overall influence was not negligible and has to be taken into account, when performing similar experiments in the future.

Overall, the results of this study suggest, that nickel-rich/SiC cells should be stored at low SOCs, in order to avoid premature degradation. Due to small self-discharge currents, the storage SOC can be even set below 15%. Storing the MJ1 cell (3.5 Ah) at 10% SOC and 25 °C would theoretically result in 20 years, until the cell would be exhaustively discharged. Future work will address the intrinsic variance of self-discharge rates and its implications for in series connection of cells.

Acknowledgements

This work has received funding from the European Unions Horizon 2020 research and innovation program under the grant “Electric Vehicle Enhanced Range, Lifetime And Safety Through INGenious battery management” (EVERLASTING 713771). The presented data of this work is available under [http://doi.org/10.4121/uuid:74e3e15c-1575-4d0d-bd38-f63148259158].

References

[1] B. Scrosati, J. Garche, Lithium batteries: status, prospects and future, J. Power Sources 195 (9) (2010) 2419–2430, https://doi.org/10.1016/j.jpowsour.2009.11.048.

[2] S.-T. Myung, F. Maglia, K.-J. Park, C.S. Yoon, P. Lamp, S.-J. Kim, Y.-K. Sun, Nickel-rich layered cathode materials for automotive lithium-ion batteries: achievements and perspectives, ACS Energy Letters 2 (1) (2017) 196–223, https://doi.org/10.1021/acsenergylett.6b00594.

[3] N. Nitta, F. Wu, J.T. Lee, G. Yushin, Li-ion battery materials: present and future, Mater. Today 18 (5) (2015) 252–264, https://doi.org/10.1016/j.mattod.2014.10.040.

[4] V.G. Khomenko, V.Z. Barsukov, J.E. Doninger, I.V. Barsukov, Lithium-ion batteries based on carbon–silicon–graphite composite anodes, J. Power Sources 165 (2) (2007) 598–608, https://doi.org/10.1016/j.jpowsour.2006.10.059.

[5] B. Fuchsbichler, C. Stangl, H. Kren, F. Uhlig, S. Koller, High capacity graphite–silicon composite anode material for lithium-ion batteries, J. Power Sources 196 (5) (2011) 2889–2892, https://doi.org/10.1016/j.jpowsour.2010.10.081.

[6] R. Dash, S. Pannala, Theoretical limits of energy density in silicon-carbon composite anode based lithium ion batteries, Sci. Rep. 6 (2016) 27449, https://doi.org/10.1038/srep27449.

[7] J.R. Szczech, S. Jin, Nanostructured silicon for high capacity lithium battery anodes, Energy Environ. Sci. 4 (1) (2011) 56–72, https://doi.org/10.1039/C0EE00281J.

[8] D. Andre, S.-J. Kim, P. Lamp, S.F. Lux, F. Maglia, O. Paschos, B. Stiaszny, Future generations of cathode materials: an automotive industry perspective, J. Mater. Chem. 3 (13) (2015) 6709–6732, https://doi.org/10.1039/C5TA00361J.

[9] National Platform for Electric Mobility, Roadmap for an Integrated Cell and Battery Production in germany, (2016) http://nationale-plattform-elektromobilitaet.de/fileadmin/user_upload/Redaktion/Publikationen/AG2_Roadmap_Zellfertigung_eng_bf.pdf , Accessed date: 1 February 2019.

[10] L.J. Krause, T. Brandt, V.L. Chevrier, L.D. Jensen, Surface area increase of silicon alloys in li-ion full cells measured by isothermal heat flow calorimetry, J. Electrochem. Soc. 164 (9) (2017) A2277–A2282, https://doi.org/10.1149/2.0501712jes.

[11] A. Rezqita, M. Sauer, A. Foelske, H. Kronberger, A. Trifonova, The effect of electrolyte additives on electrochemical performance of silicon/mesoporous carbon (si/mc) for anode materials for lithium-ion batteries, Electrochim. Acta 247 (2017) 600–609, https://doi.org/10.1016/j.electacta.2017.06.128.

[12] N. Dupré, P. Moreau, E. de Vito, L. Quazuguel, M. Boniface, A. Bordes, C. Rudisch, P. Bayle-Guillemaud, D. Guyomard, Multiprobe study of the solid electrolyte interphase on silicon-based electrodes in full-cell configuration, Chem. Mater. : a publication of the American Chemical Society 28 (8) (2016) 2557–2572, https://doi.org/10.1021/acs.chemmater.5b04461.

[13] M. Wetjen, D. Pritzl, R. Jung, S. Solchenbach, R. Ghadimi, H.A. Gasteiger, Differentiating the degradation phenomena in silicon-graphite electrodes for lithium-ion batteries, J. Electrochem. Soc. 164 (12) (2017) A2840–A2852, https://doi.org/10.1149/2.1921712jes.

[14] X. Li, A. Colclasure, D. Finegan, D. Ren, Y. Shi, X. Feng, L. Cao, Y. Yang, K. Smith, Degradation mechanisms of high capacity 18650 cells containing si-graphite anode and nickel-rich nmc cathode, Electrochim. Acta:10.1016/j.electacta.2018.11.194.

[15] P. Keil, S.F. Schuster, J. Wilhelm, J. Travi, A. Hauser, R.C. Karl, A. Jossen, Calendar aging of lithium-ion batteries, J. Electrochem. Soc. 163 (9) (2016) A1872–A1880, https://doi.org/10.1149/2.0411609jes.

[16] K. Kalaga, M.-T.F. Rodrigues, S.E. Trask, I.A. Shkrob, D.P. Abraham, Calendar-life versus cycle-life aging of lithium-ion cells with silicon-graphite composite electrodes, Electrochim. Acta 280 (2018) 221–228, https://doi.org/10.1016/j.electacta.2018.05.101.

[17] M. Lewerenz, S. Käbitz, M. Knips, J. Münnix, J. Schmalstieg, A. Warnecke, D.U. Sauer, New method evaluating currents keeping the voltage constant for fast and highly resolved measurement of arrhenius relation and capacity fade, J. Power Sources 353 (2017) 144–151, https://doi.org/10.1016/j.jpowsour.2017.03.136.

[18] A.J. Smith, J.C. Burns, D. Xiong, J.R. Dahn, Interpreting high precision coulometry results on li-ion cells, J. Electrochem. Soc. 158 (10) (2011) A1136–A1142, https://doi.org/10.1149/1.3625232.

[19] T. Joshi, K. Eom, G. Yushin, T.F. Fuller, Effects of dissolved transition metals on the electrochemical performance and sei growth in lithium-ion batteries, J. Electrochem. Soc. 161 (12) (2014) A1915–A1921, https://doi.org/10.1149/2.0861412jes.

[20] Y. Ozawa, R. Yazami, B. Fultz, Self-discharge study of licoo2 cathode materials, J. Power Sources 119–121 (2003) 918–923, https://doi.org/10.1016/S0378-7753(03)00227-1.

[21] X. Zeng, G.-L. Xu, Y. Li, X. Luo, F. Maglia, C. Bauer, S.F. Lux, O. Paschos, S.-J. Kim, P. Lamp, J. Lu, K. Amine, Z. Chen, Kinetic study of parasitic reactions in lithium-ion batteries: a case study on lini(0.6)mn(0.2)co(0.2)o2, ACS Appl. Mater. Interfaces 8 (5) (2016) 3446–3451, https://doi.org/10.1021/acsami.5b11800.

[22] J.P. Schmidt, A. Weber, E. Ivers-Tiffée, A novel and fast method of characterizing the self-discharge behavior of lithium-ion cells using a pulse-measurement technique, J. Power Sources 274 (2015) 1231–1238, https://doi.org/10.1016/j.jpowsour.2014.10.163.

[23] T. Deutschen, S. Gasser, M. Schaller, J. Siehr, Modeling the self-discharge by voltage decay of a nmc/graphite lithium-ion cell, Journal of Energy Storage 19 (2018) 113–119, https://doi.org/10.1016/j.est.2018.07.003.

[24] J. Sturm, A. Rheinfeld, I. Zilberman, F.B. Spingler, S. Kosch, F. Frie, A. Jossen, Modeling and simulation of inhomogeneities in a 18650 nickel-rich, silicon-graphite lithium-ion cell during fast charging, J. Power Sources 412 (2019) 204–223, https://doi.org/10.1016/j.jpowsour.2018.11.043.

[25] T. Ohzuku, I. Yasunobi, S. Keijiro, Formation of lithium-graphite intercalation compunds in nonaqueous electrolytes and their application as a negative electrode for a lithium ion (shuttlecock) cell, J. Electrochem. Soc. 140 (9) (1993) 2490–2498, https://doi.org/10.1149/1.2220849jes.

[26] P. Keil, A. Jossen, Calendar aging of nca lithium-ion batteries investigated by differential voltage analysis and coulomb tracking, J. Electrochem. Soc. 164 (1) (2017) A6066–A6074, https://doi.org/10.1149/2.0091701jes.

[27] B. Gyenes, D.A. Stevens, V.L. Chevrier, J.R. Dahn, Understanding anomalous behavior in coulombic efficiency measurements on li-ion batteries, J. Electrochem. Soc. 162 (3) (2014) A278–A283, https://doi.org/10.1149/2.0191503jes.

[28] M. Lewerenz, J. Münnix, J. Schmalstieg, S. Käbitz, M. Knips, D.U. Sauer, Systematic aging of commercial lifepo 4 —graphite cylindrical cells including a theory explaining rise of capacity during aging, J. Power Sources 345 (2017) 254–263, https://doi.org/10.1016/j.jpowsour.2017.01.133.

[29] J. Wilhelm, S. Seidlmayer, P. Keil, J. Schuster, A. Kriele, R. Gilles, A. Jossen, Cycling capacity recovery effect: a coulombic efficiency and post-mortem study, J. Power Sources 365 (2017) 327–338, https://doi.org/10.1016/j.jpowsour.2017.08.090.

[30] T. Ohzuku, I. Yasunobi, S. Keijiro, Two-dimensional modeling of lithium deposition during cell charging, J. Electrochem. Soc. 156 (5) (2009) A390–A399, https://doi.org/10.1149/1.3095513jes.

[31] F.M. Kindermann, A. Noel, S.V. Erhard, A. Jossen, Long-term equalization effects in li-ion batteries due to local state of charge inhomogeneities and their impact on impedance measurements, Electrochim. Acta 185 (2015) 107–116, https://doi.org/10.1016/j.electacta.2015.10.108.

[32] M. Lewerenz, G. Fuchs, L. Becker, D.U. Sauer, Irreversible calendar aging and quantification of the reversible capacity loss caused by anode overhang, Journal of Energy Storage 18 (2018) 149–159, https://doi.org/10.1016/j.est.2018.04.029.

[33] C.R. Birkl, M.R. Roberts, E. McTurk, P.G. Bruce, D.A. Howey, Degradation diagnostics for lithium ion cells, J. Power Sources 341 (2017) 373–386, https://doi.org/10.1016/j.jpowsour.2016.12.011.

[34] K. Kleiner, P. Jakes, S. Scharner, V. Liebau, H. Ehrenberg, Changes of the balancing between anode and cathode due to fatigue in commercial lithium-ion cells, J. Power Sources 317 (2016) 25–34, https://doi.org/10.1016/j.jpowsour.2016.03.049.

[35] T. Utsunomiya, O. Hatozaki, N. Yoshimoto, M. Egashira, M. Morita, Influence of particle size on the self-discharge behavior of graphite electrodes in lithium-ion batteries, J. Power Sources 196 (20) (2011) 8675–8682, https://doi.org/10.1016/j.jpowsour.2011.06.070.

[36] T. Utsunomiya, O. Hatozaki, N. Yoshimoto, M. Egashira, M. Morita, Self-discharge behavior and its temperature dependence of carbon electrodes in lithium-ion batteries, J. Power Sources 196 (20) (2011) 8598–8603, https://doi.org/10.1016/j.jpowsour.2011.05.066.

[37] X. Liao, Q. Huang, S. Mai, X. Wang, M. Xu, L. Xing, Y. Liao, W. Li, Understanding self-discharge mechanism of layered nickel cobalt manganese oxide at high potential, J. Power Sources 286 (2015) 551–556, https://doi.org/10.1016/j.jpowsour.2015.04.032.

[38] N.N. Sinha, A.J. Smith, J.C. Burns, G. Jain, K.W. Eberman, E. Scott, J.P. Gardner, J.R. Dahn, The use of elevated temperature storage experiments to learn about parasitic reactions in wound licoo2graphite cells, J. Electrochem. Soc. 158 (11) (2011) A1194, https://doi.org/10.1149/2.007111jes.

2.2 Influence of cell-to-cell variations in self-discharge on the pack utilization

The measurement method presented in the previous section was applied to 24 selected lithium-ion cells in order to determine the variation in reversible self-discharge between them. First, all cells underwent initial characterization, which revealed rather low capacity and impedance variance. This result was interpreted as a sign of a well-controlled manufacturing or at least matching process. In order to identify possible further manufacturing tolerances, which were not observable by the standard capacity and impedance measurements, a differential voltage analysis (DVA) was performed for each cell. The deviations of distinctive material markers in the DVA results were statistically analyzed with the aim of identifying possible correlations between stoichiometric properties of the anode and cathode and measured capacity. However, no significant correlations were observed, which implied that the cell quality of the investigated batch was most likely influenced by random deviations within the manufacturing process, rather than systematic causes.

Evaluation of self-discharge rates revealed high variance, whereby the absolute value was in accordance with the previous publication. No correlations between the self-discharge current and other cell parameters such as capacity and impedance were found. The reason for such high variation of self-discharge was most likely linked to the fact, that in contrast to capacity and impedance, a precise measurement of self-discharge is too demanding within the context of a cell manufacturing line and cells are categorized simply by their ability to pass the EOL test.

Based on the SOC and temperature dependent self-discharge values from the previous publication a self-discharge model was proposed, which included a controlled current sink. The variation data provided plausible maximum and minimum values for the self-discharge current. Using the model, a simple simulation was performed. Since in a large battery pack there are almost up to 200 cell blocks connected in series, it is likely that both maximum and minimum self-discharge values would appear among the cells. It was assumed that there were no cells connected in parallel, which would drastically reduce the influence of self-discharge variation. The simulation evaluated the voltage drift during one year of storage starting at 90 % SOC, in which the simulated battery packs were exposed to different temperature profiles. The simulation results revealed that even without any parallel connection, the voltage drift caused by the different self-discharge rates was under 3 mV. With a parallel connection, a large reduction of the voltage drift could be expected and therefore it was implied that differing self-discharge rates were unlikely to be the major reason for the voltage imbalance in battery packs.

Authors contribution Design, execution of the experiment and development of the custom-build voltage measurement hardware were performed by Ilya Zilberman. Data processing and simulations were also performed by Ilya Zilberman. Sebastian Ludwig supported the initial characterization of cells. Andreas Jossen supervised this work, the manuscript was written by Ilya Zilberman and was edited by all authors.

Cell-to-cell variation of calendar aging and reversible self-discharge in 18650 nickel-rich, silicon–graphite lithium-ion cells

Ilya Zilberman, Sebastian Ludwig, Andreas Jossen

Journal of Energy Storage 26, 100900, 2019

Permanent weblink:
`https://doi.org/10.1016/j.est.2019.100900`

Journal of Energy Storage 26 (2019) 100900

Contents lists available at ScienceDirect

Journal of Energy Storage

journal homepage: www.elsevier.com/locate/est

Cell-to-cell variation of calendar aging and reversible self-discharge in 18650 nickel-rich, silicon–graphite lithium-ion cells

I. Zilberman*, S. Ludwig, A. Jossen

Institute for Electrical Energy Storage Technology, Technical University of Munich (TUM), Arcisstr. 21, Munich 80333, Germany

ARTICLE INFO

Keywords:
Lithium-ion
Self-discharge
Variation
Battery pack
Balancing

ABSTRACT

The origin of the voltage imbalance in lithium-ion battery packs is often linked to different self-discharge rates. However, there is no information regarding the variance of self-discharge currents nor possible implications for cells connected in series. In this study, initial cell parameter distributions were analyzed via differential voltage analysis (DVA) and variations of calendar aging and reversible self-discharge rates of 24 commercial 18650 nickel-rich/SiC cells were statistically evaluated. After initial characterization, all cells were stored for 10 month at 70% state of charge (SOC) at 25 °C, whereby last two weeks of storage were used for reversible self-discharge determination via voltage decay. The results obtained in this work reveal that initial capacity and impedance variations do not depend on electrode balancing, nor storage capabilities of NMC, silicon or graphite. Furthermore, the evaluation of calendar aging showed, that all cells exhibited constant but different aging rates. However, whereas the relative variance of the impedance remained almost the same, the relative variance of the capacity almost doubled during the storage. The average self-discharge current amounted to 4.2 µA (3.5 Ah cell) with the relative variance of 10%. Model based assessment of different self-discharge currents revealed almost no influence on the voltage imbalance in battery packs.

1. Introduction

Lately, lithium-ion technology has found a place in various applications, ranging from mobile phones to electric vehicles. Especially electric mobility requires high power and high energy storage capabilities, which are usually provided by large battery packs, consisting of up to thousands of single lithium-ion cells. In order to reduce load currents and consequently ohmic losses within battery packs and charging infrastructure, system voltage is usually increased by connecting cells in series. State-of-the-art battery packs exhibit system voltages of up to 800 V with almost 200 cell blocks in serial connection [1], whereby the number of cells in parallel is determined by the capacity of the selected cell and power/energy demand of the battery pack. As a consequence, large number of cells increases the chance of having a negative production outlier in the battery pack, which might deteriorate the operation of the whole energy storage system.

Automated cell manufacturing combines a variety of different production processes from chemical, machine and electrical engineering domains. All processes, including electrode production, cell assembly and cell finishing exhibit tolerances, which result in inevitable cell parameter variations [2]. Studies on initial variance of capacity and impedance in commercial cells were already published [3,4]. Over the last decade, a positive trend regarding the parameter variance in commercially available lithium-ion cells could be observed. For instance, the relative capacity variance decreased from around 1% [5,6] to 0.8% [3] and finally to 0.16% [7]. However, similar improvement could also be yielded by targeted selection of cells and not necessarily by improved cell production techniques. Although there is no experimentally verified information about possible origins of cell parameter variations, several simulative studies addressing this issue were carried out. Using a single particle model, Kenney et al. showed, that electrode thickness and porosity have the most influence on the capacity variation [8]. Santhanagopalan et al. proposed a model based method for identification of tolerances in cell production steps using electrochemical impedance spectroscopy (EIS) [9]. However, further important production steps as formation were not taken into account.

Reversible self-discharge current is defined as the current, which evokes a decay of the terminal voltage without any capacity loss [10] and is most likely linked to coupled side reactions between the anode and the cathode [11,12]. In contrast to impedance and capacity values,

---

[*] Corresponding author.
E-mail address: ilya.zilberman@tum.de (I. Zilberman).

https://doi.org/10.1016/j.est.2019.100900
Received 3 June 2019; Received in revised form 12 August 2019; Accepted 12 August 2019
2352-152X/

there is no information about variation of reversible self-discharge rates and irreversible capacity loss during calendar aging. Especially the former is often made responsible for the voltage drift within in series connection of cells, which might limit the available capacity of the battery pack [13]. Although, Hausmann et al. presented leakage resistances of 123 automotive cells at 50% SOC using voltage decay, evaluation of voltage slopes took place during first 100 h after cycling [14], which turned out being too short [12]. Similar approach was used for determination of reversible self-discharge of single cells at different SOCs and temperatures [15,16]. Therefore, the main goal of this work is to experimentally determine the variation of true self-discharge currents and to derive possible implications for battery packs. For that purpose, self-discharge currents of pristine 24 cells in 18650 format with NMC (nickel-rich) cathodes and silicon–graphite anodes were determined via voltage based measurement, presented in [12]. It was shown that too early evaluation of voltage decay led to divergent results due to equalization processes between the active area of the anode and the anode overhang. However, after the equalization processes were finished, voltage slope $\mathrm{d}U/\mathrm{d}t$ remained constant and represented the reversible losses, as shown by the comparison between the capacity and voltage based measurement methods in our previous work [12]. Combined with the derivative of the open circuit voltage (OCV) $\mathrm{d}Q/\mathrm{d}U$, which was determined by a small discharge pulse (0.033C), the self-discharge current was calculated as follows:

$$\frac{\mathrm{d}Q}{\mathrm{d}U}\cdot\frac{\mathrm{d}U}{\mathrm{d}t} = \frac{\mathrm{d}Q}{\mathrm{d}t} = \sum I_{\mathrm{sd}} \tag{1}$$

where $\sum I_{\mathrm{sd}}$ is the sum of all side reaction currents which have an influence on half-cell potentials of both electrodes. By taking the capacity based measurement as the reference, voltage based measurement method achieved an accuracy of ± 15%.

Above mentioned anode overhang is the result of an oversized negative electrode, which is a common manufacturing practice for lithium-ion cells. It ensures that even due to possible small misalignment during stacking or cell winding, there is an anode counterpart across the whole cathode surface. Additionally, 1mm overhang along the electrode is sufficient to prevent lithium plating on the edge of the anode [17]. Since the overhang area is soaked with electrolyte, it is able to participate in equalization processes and store lithium, despite the absence of the cathode counterpart. However, such processes are very slow, since they are dominated by interparticle transport and are driven by potential differences of the flat OCV of graphite [18]. In general, equalization processes between active anode area and anode overhang can cause a change in coulombic efficiency [19,20] and disturb calendar aging experiments [21].

Origins of initial cell parameter variations were analyzed via DVA, which is often used to describe changes in storage capabilities and in balancing of positive and negative electrode [11]. In order to determine variation of calendar aging the same 24 cells were stored for 10 month at 25 °C, after which cell capacities and impedances before and after the storage were compared.

It was assumed that all cell parameters in this work were normally distributed and therefore could be described by the mean value μ and standard deviation σ. The mean value is given by

$$\mu = \frac{1}{n}\sum_{i=1}^{n} x_{\mathrm{i}} \tag{2}$$

where x_{i} is a data point and n is the amount of data points in one data set. The standard deviation is calculated by

$$\sigma = \sqrt{\frac{1}{n-1}\sum\nolimits_{i=1}^{n}(x_{\mathrm{i}}-\mu)^2} \tag{3}$$

The standard deviation describes how far away are single data points from the mean value. The range between ± 3σ around the mean value contains 99.6% of a normal distribution. The linear dependency between two data sets was analyzed using Pearson product-moment correlation coefficient (PPMCC). PPMCC is a measure of the strength of a linear association of a sampled paired data and is given by [22]

$$\mathrm{Pearson}_{\mathrm{xy}} = \frac{\sum\nolimits_{i=1}^{n}(x_{\mathrm{i}}-\mu_{\mathrm{x}})(y_{\mathrm{i}}-\mu_{\mathrm{y}})}{\sqrt{\sum\nolimits_{i=1}^{n}(x_{\mathrm{i}}-\mu_{\mathrm{x}})^2\sum\nolimits_{i=1}^{n}(y_{\mathrm{i}}-\mu_{\mathrm{y}})^2}} \tag{4}$$

Depending on whether there is a positive or negative correlation between two data sets, Pearson value can become 1 or −1 respectively. For the purpose of better evaluation, a finer graduation is proposed:

$|\mathrm{Pearson}_{\mathrm{xy}}| < 0.3$: Missing correlation
$0.3 \le |\mathrm{Pearson}_{\mathrm{xy}}| < 0.5$: Weak correlation
$0.5 \le |\mathrm{Pearson}_{\mathrm{xy}}| < 0.8$: Moderate correlation
$0.8 \le |\mathrm{Pearson}_{\mathrm{xy}}| < 1$: Strong correlation
$1 = |\mathrm{Pearson}_{\mathrm{xy}}|$: Perfect correlation

This paper is organized as follows. First, investigated cells, experimental setup and all test sequences are described. After that, possible origins of initial variation of capacity and impedance are discussed using DVA. Subsequently, statistical evaluation of calendar aging is presented. Finally, variation of self-discharge rates is derived and its implication on the voltage drift within battery packs is demonstrated.

2. Experimental

The object of this study was a commercial 18650 high energy lithium-ion cell INR18650-MJ1 from LGChem with nominal capacity of 3.5 Ah and specific energy of 259.6 $\mathrm{Whkg^{-1}}$. Sturm et al. performed analysis of active materials [23]. The amount of silicon in graphite was measured via inductively coupled plasma-optical emission spectroscopy (ICP-OES) and amounted to ~ 3.5 wt % [23]. The ratio of nickel, manganese and cobalt in the active material of the cathode, determined via ICP-OES, amounted to 82%–6.3%–11.7% respectively, indicating the dominance of nickel in the cathode. For this experiment 48 pristine cells were purchased from the same production batch. All test routines in this work were performed with the Cell Testing System (CTS) from Basytec. During the storage and also during initial test routines all cells were placed in a Binder KT170 climate chamber.

The overall testing procedure is summarized in Table 1. First, all cells were weighed with the precision weighing scale Sartorius TE313S. After that cells underwent a checkup routine, which contained determination of the residual capacity, followed by two constant-current constant–voltage (CCCV) charge and discharge cycles. Subsequently, R_{DC10s}, which is a DC resistance, calculated after 10 s of 1C discharge at 50% state of charge (SOC) was determined. Exact test parameters and termination values of the checkup routine are summarized in Table 2.

Table 1
Overall test procedure.

Sequence	Description
1. Weight	Measurement of cell weights
2. Checkup 1	Checkup according to Table 2
3. 5 Cycles	Activation cycles. Charge CC (I= 0.5C), discharge CC (I= 0.2C)
4. Checkup 2	Checkup according to Table 2
5. OCV	OCV measurement
6. Storage	Storage at 70% SOC at 25 °C for 10 month
7. Checkup 3	Checkup according to Table 2
8. Checkup 5	Checkup according to Table 2
9. Checkup 4	Checkup according to Table 2

Table 2
Checkup sequence consists of determination of residual charge (steps 1–2), two redundant, consecutive cycles for cell capacity determination (steps 3–6), and determination of internal impedance R_{DC10s} (steps 7–9).

Step	Parameters	Termination
1. Discharge CCCV	$I = -0.2C$, $U = 2.5$ V	$I > -50$ mA
2. Pause		$t > 30$ min
3. Charge CCCV	$I = 0.5C$, $U = 4.2$ V	$I < 50$ mA
4. Pause		$t > 30$ min
5. Discharge CCCV	$I = -0.2C$, $U = 2.5$ V	$I > -50$ mA
6. Pause & Repeat 3–5		$t > 30$ min
7. Charge CC	$I = 0.5C$	SOC $>$ 50%
8. Pause		$t > 10$ min
9. Discharge CC	$I = -1C$	$t > 10$ s

After the first checkup, all 48 cells underwent five activation cycles, after which a second checkup was performed. Subsequently, OCV curves for the DVA were obtained. Activation cycles were applied in order to ensure, that the process of the solid electrolyte interface (SEI) formation was completely finished. In the course of activation cycles all cells lost ca. 0.7% of the initial capacity. The OCV curve was determined using constant current (CC) with 0.033C and constant voltage (CV) with current termination at 0.001C for charge and discharge direction. After initial OCV measurement, each cell was fully charged (CCCV) to 4.2 V with current termination at 0.001C and discharged after a pause (6 h) to 70% SOC according to the actual capacity of each cell. Due to limited resources 24 cells were selected out of the initial batch of 48 cell without interfering with parameter distribution and were subsequently stored for 10 month at 25 °C. Last two weeks of the storage were used to measure the voltage decay and to apply a discharge pulse for isolated dQ/dU determination. A 0.033C discharge pulse was applied for 30 s, which resulted in 2.7E − 4% change of SOC. The voltage decay was measured with a custom-built measurement unit on the basis of ADS1278 from Texas Instruments, a 24 Bit analog digital converter (ADC) with 8 differential input channels. All channels underwent gain and offset calibration with a high precision voltage source LTC6655 from Linear Technology. The noise level for each channel was below 15 μV for a 10 Hz sampling rate. Due to the high input impedance of 20 GΩ it was insured that leakage current of the circuit was negligible and that there was no interference with the voltage measurement by slowly discharging the cell. After the storage, checkup 3 was carried out in order to assess the capacity fade and impedance gain. Two further subsequent checkups 4 and 5 were used in order to quantify the influence of possibly varying anode overhang areas on the calendar aging results. Capacity based self-discharge determination method led to inaccurate results at 70% SOC due to equalization processes between active and inactive area of the anode, as it was already shown in [12]. Therefore, in this work, only results from the voltage based measurements were taken into account.

3. Results and discussion

3.1. Initial cell parameter variation

In the following, the evaluation of the initial checkup routine of 48 pristine LG MJ1 cells is presented. Histograms of capacities and R_{DC10s} values, which were determined after the five initial cycles, are shown in Fig. 1a and b respectively. Cell weight distribution, which was ascertained after the delivery is shown in Fig. 1c. Although capacity and impedance values do not show apparent characteristics of a normal distribution, fitting parameters μ and σ are still calculated for the sake of comparability. It is justified by a small amount of samples and already observed normal cell parameter distribution in the past [4,6]. Relative variance of capacity amounts to 0.2%, whereas R_{DC10s} values exhibit 0.68%. Such low relative variances are not uncommon and are in accordance with literature [7].

Fig. 1d shows a scatter plot with a least-square line for 48 measured capacity and R_{DC10s} values. The Pearson coefficient amounts to −0.67 and describes that with increasing cell capacity, the impedance decreases. Such behavior might be explained by the fact, that R_{DC10s} value is determined by 1C discharge pulse at 50% SOC, whereby C is referred to the nominal capacity according to the data sheet (3.5 Ah) and not to the actual capacity of each cell. Assuming that cell capacity variation is linked to the accessibility of the active material, same discharge pulse creates higher current density in a cell with less active material and thus a cell with smaller capacity seems to exhibit a higher impedance. Fig. 1a and b additionally show distributions of 24 cells, which were chosen for the storage experiment.

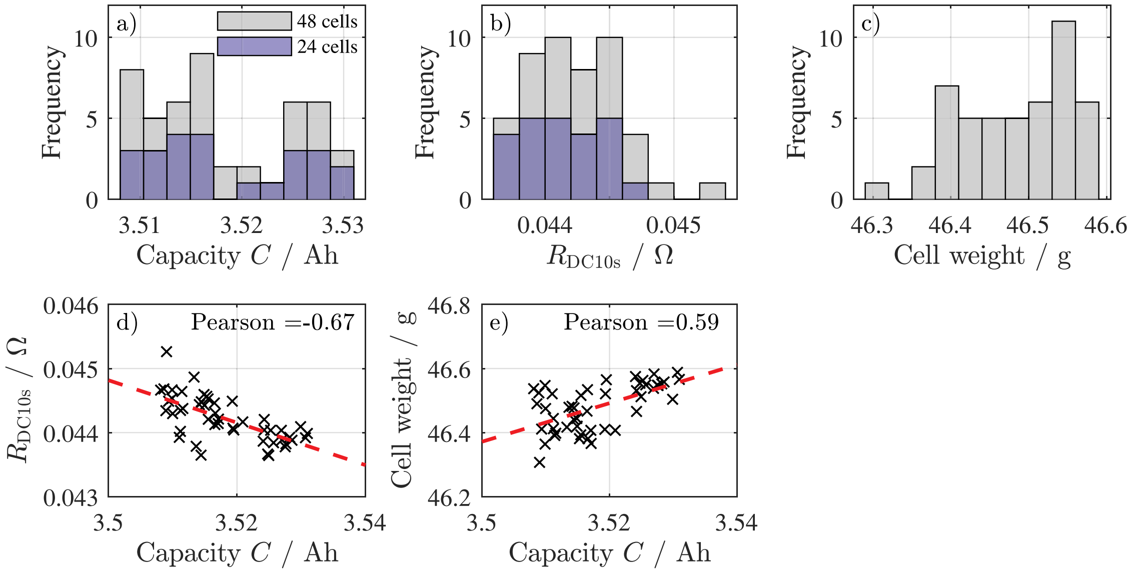

Fig. 1. Evaluation of initial check-up routines. (a) Histogram of capacity, (b) histogram of cell impedance R_{DC10s}, (c) histogram of cell weights, (d) scatter plot between R_{DC10s} and cell capacity, (e) scatter plot cell weights and capacities.

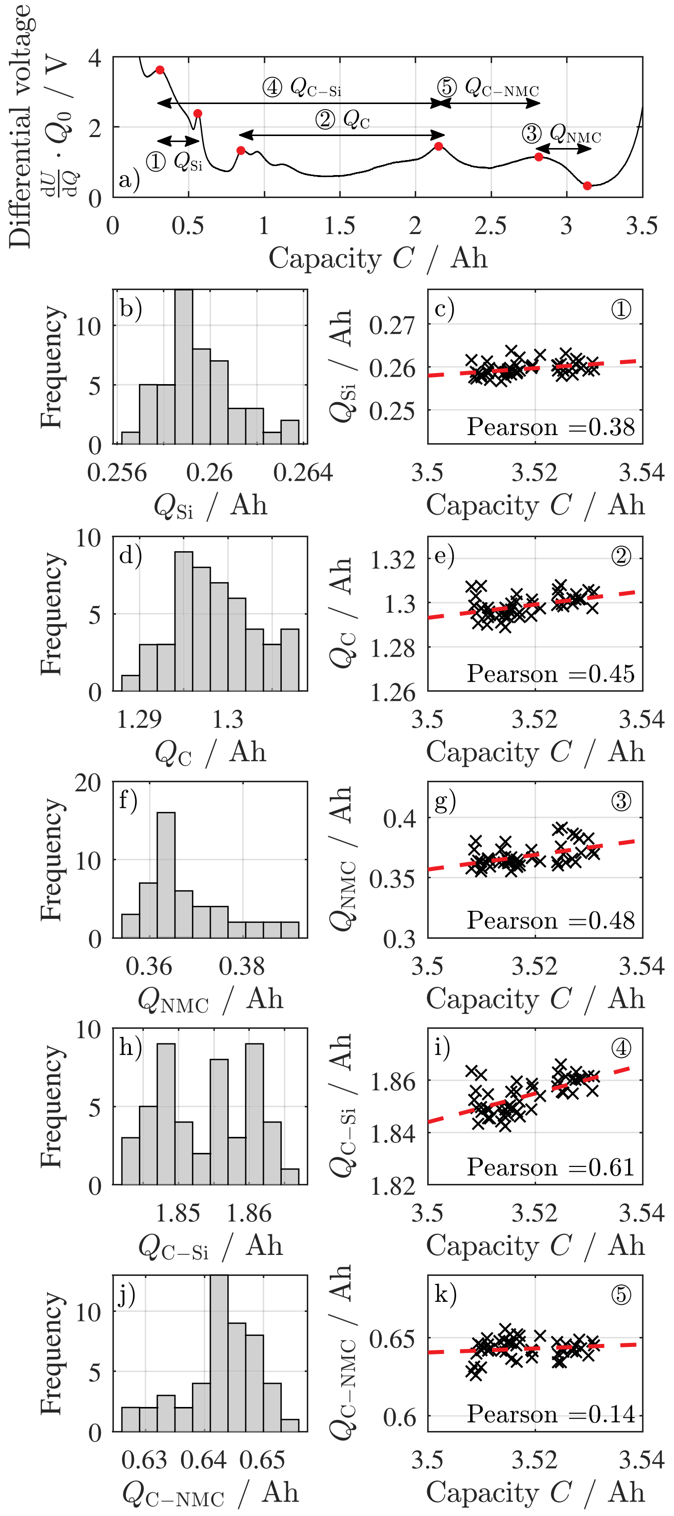

Fig. 2. DVA and correlation analysis of capacity variation of 48 MJ1 cells. (a) Assignment of characteristic capacities to material distinctive DVA markers, (b)–(c) histogram and scatter plot of Q_{Si}, (d)–(e) histogram and scatter plot of Q_C, (f)–(g) histogram and scatter plot of Q_{NMC}, (h)–(i) histogram and scatter plot of $Q_{C\text{-}Si}$, (j)–(k) histogram and scatter plot of $Q_{C\text{-}NMC}$.

A moderate correlation between cell weights and capacities was observed and is shown in Fig. 1e. Usually, the cell weight can be linked to geometrical properties of the jelly roll, which is influenced by actual electrode dimensions, including electrode thickness. However, variation in the quantity of electrolyte filling can not be completely ruled out. Either way, increased amount of active materials or simply electrode length would positively influence the cell capacity.

Additionally, the origin of cell parameter variation was investigated via DVA. DVA is a technique for electrical characterization of lithium-ion cells, which is based on the differential voltage of a slow charge or discharge [24]. For the purpose of DVA, 0.033C discharge curves were used in this work. Each differential voltage exhibits certain local minima and maxima, which can be attributed to distinctive material markers. For instance, the peak at 2.17 Ah, which is shown in differential voltage of the LG MJ1 cell in Fig. 2a, indicates the phase transition between LiC_{12} and LiC_6 and is therefore attributed to the anode [25]. Further phase changes of graphite are visible in the form of DVA peaks at ca. 0.8 Ah. Changes in distances between those peaks are usually attributed to changes in storage capabilities of the anode [26]. Therefore the distance between the first graphite peak at ca. 0.8 Ah and the main peak at 2.17 Ah Q_C is used to describe the storage capability of the graphite. Furthermore, it has been shown, that both peaks at ca. 0.3 Ah and 0.6 Ah are due to the smooth increase of the silicon–graphite electrode's potential towards delithiation and are attributed to the presence of silicon [12]. Therefore, the distance between those peaks Q_{Si} is used to describe the storage capability of silicon. The distance between the local maxima and minima at 2.8 Ah and 3.2 Ah Q_{NMC} is attributed to the storage capability of the cathode material NMC [12], however due to flat differential voltage, the determination of exact extreme points was aggravated. The distance between the main graphite peak and the cathode peak $Q_{C\text{-}NMC}$ describes the balancing of negative and positive electrode. Finally, the distance between the main graphite peak and silicon peak $Q_{C\text{-}Si}$ defines a relation between the amount of silicon and graphite in the anode. Scatter plots on the right side of the Fig. 2 outline the correlation between distinctive DVA markers and capacity variation. The left side of Fig. 2 depicts histograms of DVA markers. Storage capability of silicon, as well as the storage capability of graphite show weak correlation and therefore are most likely not responsible for capacity variation, which is shown in Fig. 2c and e respectively. Storage capability of NMC also does not reveal a distinctive dependency either, as shown in Fig. 2g. The balancing between both electrode showed also weak correlation and therefore can be excluded from possible causes of cell capacity variance. Only DVA marker $Q_{C\text{-}Si}$ showed a moderate correlation with the capacity with the Pearson coefficient amounting to 0.61. However, due to non-dominant Pearson coefficient, it is more likely that the capacity variation does not depend on any material parameter or on any certain manufacturing process during electrode production, cell assembly or cell finishing. Similar analysis was also carried out for variation of R_{DC10s} values, however, no correlation was found.

Regardless of low initial capacity and impedance relative variances, both parameters showed moderate correlation. The analysis of material relevant DVA markers and capacity variation of 48 cells did not reveal any strong correlation. Therefore, it is likely that all production processes exhibit good quality management and very low manufacturing tolerances.

3.2. Variation of calendar aging

Capacity fades and impedance gains of 24 cells after 10 month of storage at 70% SOC at 25 °C were analyzed and are presented in the following. Capacity and impedance progressions, which were determined via checkup measurements before and after the storage are shown in Fig. 3a and b respectively. All cells exhibited a slight capacity recovery effect between cycle 5 and 10. Capacity recovery effect has been already reported for LFP/graphite, as well as NMC/graphite self-made and commercial cells [19,27] and was linked to the presence of anode overhang areas. In case of a long storage at high SOC, equalization of active and inactive areas would result in high lithium concentration of the anode overhang. During cycling with depth of discharge (DOD) 100%, the average SOC of active area would amount to ca. 50%. Due to anode potential difference between 50% and 70% SOC, the active area could slowly draw the extra lithium, stored in the inactive area, resulting in observed capacity recovery effect.

All capacity and impedance values were fitted by a normal distribution. On average, each cell lost 5.7% of its initial capacity and gained 4.6% in impedance. The relative capacity variance σ_C/μ_C almost doubled from 0.2% to 0.38%, whereas the relative impedance variance $\sigma_{R_{\mathrm{DC10s}}}/\mu_{R_{\mathrm{DC10s}}}$ remained almost the same exhibiting 0.68% before and 0.75% after the experiment. Exact numbers are summarized in Table 3. Strong correlation was observed between initial and aged capacities, as well initial and aged impedances, as it can be seen by the unchanged color order shown in Fig. 3a and b. Any influence of different anode overhang areas was ruled out, since the color order in Fig. 3a and 3b remained constant even after the cycling, which is an indicator that all cells exhibited the same capacity recovery. The results reveal that cells with initially higher capacity exhibited also higher capacity after the storage, which also applied for the impedance gain. Results presented by Baumhoefer et al., where 48 cells were cycled with the same load profile at the same temperature, showed on the other hand no correlation before and after the experiment [28]. Such behavior might be caused by different but almost constant calendar aging rates. In case that after the manufacturing process, all cells from one production batch exhibit almost the same capacity, the cell with the lowest aging rate will always exhibit the highest capacity. On the other hand a cell with the highest aging rate will always exhibit the lowest capacity within this batch. Consequently, relative variance of capacity and impedance would constantly increase. Reversible capacity loss due to calendar aging usually exhibits a decelerating behavior [29,30], however, for further considerations it is assumed that calendar aging rates remain constant, since it depicts the worst case.

Fig. 4 shows such theoretical worst case progression of the increase of capacity and impedance variance. Based on the printed code on the cells, the production date could be identified, which depicts the starting point on the x-coordinate. At the time of delivery ② cells were 8 month old and were stored after initial checkup for three month ②–③ at 50% SOC at approximately 7 °C. Since Keil et al. have shown that storage at SOC below main graphite peak and at lower temperature does not evoke severe aging [31], it was assumed that during three month no change in relative variance of cell parameters occurred. Subsequently, all cells were stored at 25 °C for 10 month ③–④ and were finally analyzed via checkup measurements. By linearly interpolating the increase rate of the relative variance, the initial relative variance of capacity and impedance amounted to 0.056% and 0.624% respectively. It stands to reason that cell matching process for this batch prioritized cells with the same capacity, rather than with the same impedance. By extrapolating the increase of the relative cell parameter variance for further 7 years ⑤, cells would exhibit an estimated relative capacity variance of 1.73% and relative impedance variance of 1.275%. However, such extrapolation is only valid for storage at 25 °C and not decelerating aging.

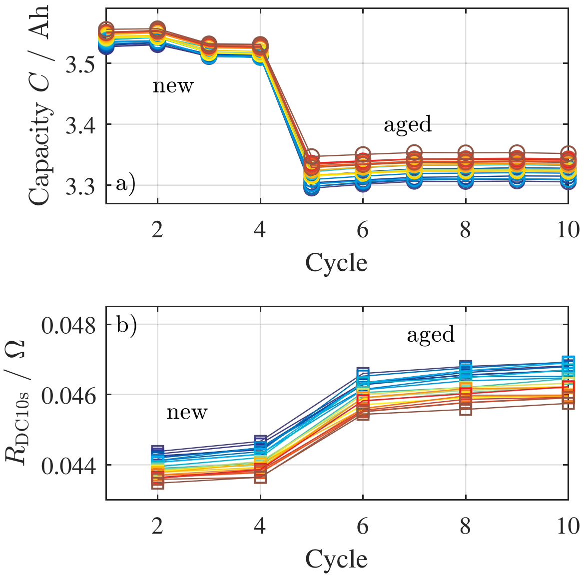

Fig. 3. (a) and (b) Capacity and R_{DC10s} before and after the storage.

Table 3
Mean and variance values of pristine and aged cell parameter distributions.

Parameter	μ_{new}	$\sigma_{\mathrm{new}}/\mu_{\mathrm{new}}$	μ_{aged}	$\sigma_{\mathrm{aged}}/\mu_{\mathrm{aged}}$	$\mu_{\mathrm{aged}}/\mu_{\mathrm{new}}$	$\frac{\sigma_{\mathrm{aged}}/\mu_{\mathrm{aged}}}{\sigma_{\mathrm{new}}/\mu_{\mathrm{new}}}$
C / Ah	3.52	0.2%	3.32	0.38%	0.943	1.9
R_{DC10s} / Ω	0.044	0.68%	0.046	0.75%	1.046	1.1

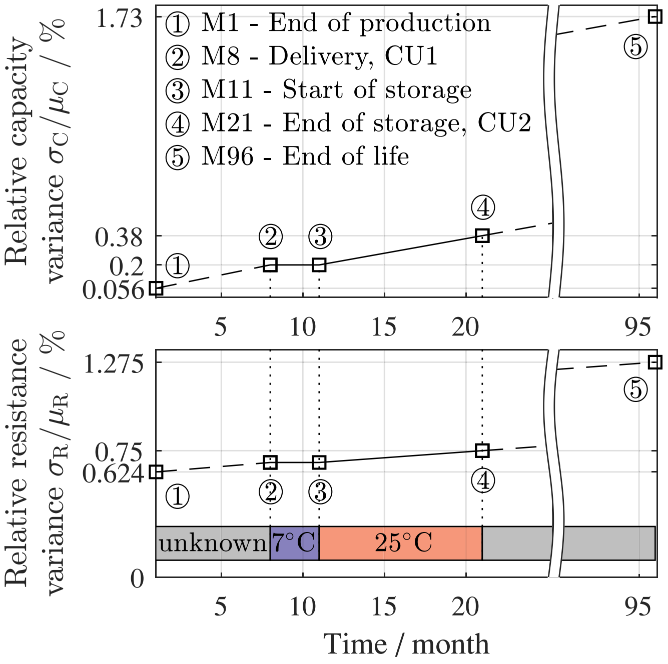

Fig. 4. Theoretical reconstruction of the increase of relative capacity variance (a) and relative resistance variance (b) over 8 years.

After cycling under the same conditions till the end of life in [28], relative capacity variance amounted to 1.7%, starting at 0.25%, without any correlation between the initial and final state. Since the relative variance of cycle and calendar aging of the INR18650-MJ1 cell are in the same order of magnitude, it can be concluded, that overall capacity fade and impedance increase during the operation of battery pack would exhibit a weak to no correlation at all between initial and final cell parameters, given that there would be no extrinsic cell variation sources.

3.3. Variation of reversible self-discharge

In the following section results on variation of self-discharge currents and its implication for the battery pack operation are presented. Derivatives of voltages were evaluated after 9.5 month in order to ensure that all voltage equalization processes were decayed. After that, discharge pulses were applied in order to determine isolated $\mathrm{d}Q/\mathrm{d}U$ coefficients. The distribution of calculated self-discharge currents and associated Gaussian normal fit are shown in Fig. 5a. Compared to capacity distributions, the relative variance of self-discharge currents exceeds it by the factor of 50 and amounts to 10.51%. Usually, after the manufacturing process, the voltage decay of a lithium-ion cell is measured during several weeks, as a part of the End-of-Line (EOL) test [32]. During that process cells with soft short circuits are detected, which is a crucial step in order to insure safe future operation of the lithium-ion cells. It is most likely that the applied EOL test was based on a threshold value for the voltage decay, which has led to a pass or fail without any further categorization of self-discharge behavior. However, high self-discharge variance could be also linked to the missing resolution and accuracy of the voltage based self-discharge determination, owing to the fact, that absolute values of self-discharge currents were below 7 µA. Nevertheless, evaluated self-discharge losses with capacity based measurement showed similar variance, but divergent absolute values due to influence of the anode overhang.

Fig. 5 b and c show a scatter plot with according Pearson correlation coefficients between self-discharge current, capacity and impedance. Absolute values of Pearson coefficients are lower than 0.3, which implies no dependency between self-discharge currents and other cell parameters. Capacity and impedance are probably more linked to variation in geometrical properties of the cell, since the capacity, usually has a correlation with the weight of the cell, as shown in Fig. 1e. Whereas self-discharge current, as already shown in our previous work, is more linked to electrochemical processes within the cell [12].

Previously, self-discharge currents for 13 SOCs between 10% and 90% at 25 °C, 40 °C and 55 °C were determined via voltage based measurement method for the MJ1 cell [12]. Hereby, a simple mathematical model for self-discharge current is proposed. The model is based on the exponential function with an offset and depends on the SOC and temperature T:

$$I_{\mathrm{sd}}(\mathrm{SOC},\,T) = a(T)\cdot e^{b(T)\cdot \mathrm{SOC}} + c(T) \tag{5}$$

Table 4

Overview of fitting parameters.

Parameter	Function
$a(T)$	$2.\,753^{-141}\cdot T^{53.6}$
$b(T)$	$-\,4.\,275^{-19}\cdot e^{0.1301T} + 6.015$
$c(T)$	$1.\,033^{-39}\cdot T^{13.59}$

Model parameters are summarized in Table 4. As shown in Fig. 6a the fitted model is in good accordance with measurements results except for the SOC range between 20% and 50%. Such mismatch might be brought by the fact that the calculated self-discharge contains all side reaction currents with an influence on the half-cell potentials. The filled transparent area determines the maximum and minimum possible self-discharge currents based on the relative variance from Fig. 5a.

3.4. Implications of different self-discharge rates on the voltage drift

In order to investigate possible implications of different self-discharge rates on the voltage drift within the battery pack, above proposed mathematical description can be integrated in a cell model using a controllable current source, which depends on the SOC and temperature. Such simple equivalent circuit based cell model is shown in Fig. 6b. It consists of already described controllable current source $I_{\mathrm{sd}}(\mathrm{SOC},\,T)$ and a controllable voltage source $U_{\mathrm{OCV}}(\mathrm{SOC})$ for the cell's OCV, which depends on the SOC. In general, the terminal voltage of a lithium-ion cell also depends on the temperature [33]. The exact relation between the OCV and the temperature is defined by the entropy. Although it has been shown, that entropy exhibits a non-linear, hysteresis-like behavior [34], it can be neglected, since differences in terminal voltage before and after the same absolute temperature change amount only to several 100 µV. Implemented Ah counter adjusts the SOC, based on the nominal capacity of the cell. Dynamic behavior of the cell can be reproduced using polarization RC networks, represented by Z_{p}, which have shown good and robust results in the past [35]. However, since self-discharge processes are rather slow, polarization networks are not further considered.

In order to increase power capability of the pack, cells are usually connected in parallel. Resulting self-discharge currents of entire cell blocks depend on the amount of cells in parallel and the distribution of cell self-discharge currents. According to the proposed model, parallel connection of cells leads to a parallel connection of different current sources, since the voltage in a parallel connection is always the same and therefore can be represented by a single voltage source. Applying the first law of Kirchhoff the entire self-discharge current of a cell-block is the sum of self-discharge currents of cells in parallel. Assuming that self-discharge rates are normally distributed and are independent random variables, self-discharge rates of cell-blocks consisting of p cells in parallel amount to [22]:

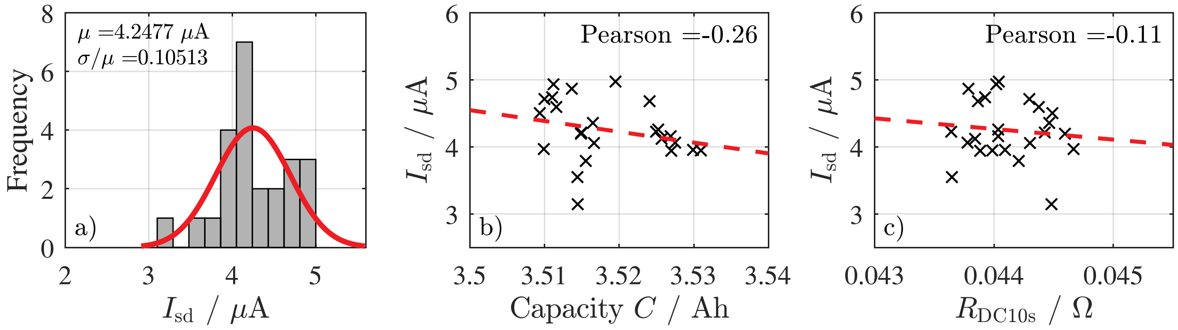

Fig. 5. (a) Histogram of calculated self-discharge currents with corresponding Gaussian fit, scatter plot between self-discharge currents and cell capacities (b) and R_{DC10s} (c).

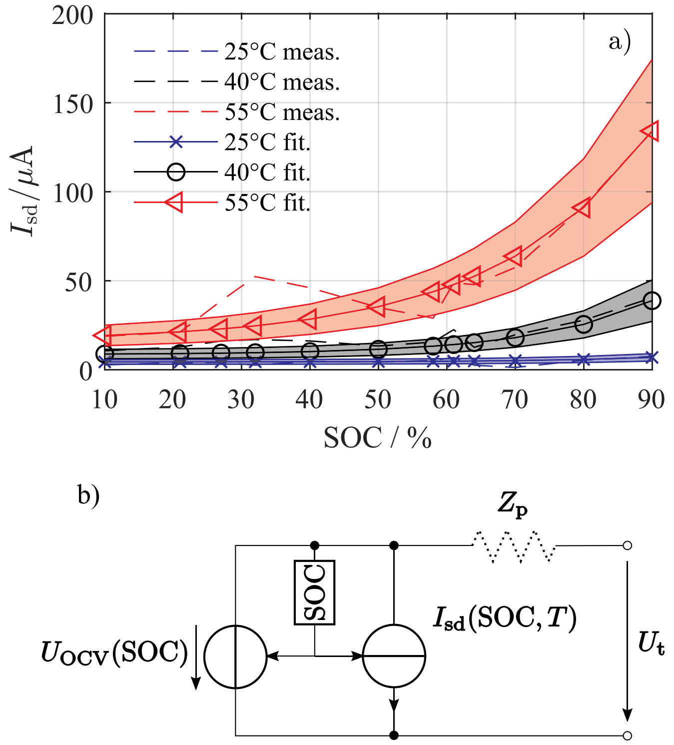

Fig. 6. (a) Fitting results of the self-discharge model, including possible maximum and minimum self-discharge current, (b) equivalent circuit cell model.

$$I_{\mathrm{sd,block}} = \sum_{i=1}^{p} I_{\mathrm{sd,cell}} \sim \mathcal{N}\Big(\underbrace{p \cdot \mu_{I_{\mathrm{sd,cell}}}}_{\mu_{I_{\mathrm{sd,block}}}}, \underbrace{\sqrt{p} \cdot \sigma_{I_{\mathrm{sd,cell}}}}_{\sigma_{I_{\mathrm{sd,block}}}}\Big), \tag{6}$$

Even a small amount of parallel cells can reduce the relative variance of self-discharge currents within a battery pack. Already four cells in parallel reduce the relative variance by a half. However, for further analysis, the worst case was assumed and therefore no cells in parallel were considered. In order to investigate a possible maximum voltage drift in an automotive battery pack within one year, two cells with the highest and the lowest self-discharge rate were taken into account. For the sake of simplicity it was assumed, that during one year both cells were exposed to the ambient temperature. Furthermore, effects of direct sunlight and temperature increase during operation were neglected. Such simplification seems to be valid, since the average travel distance in Germany amounts to 38 km per day and usually takes only about one hour [36].

Fig. 7a–c show three different temperature profiles recorded throughout the year 2018 in Munich (GER), Los Angeles (USA) and in Singapore. All temperature profiles were extracted from CDO database of National Oceanic and Atmospheric Administration. The geographic locations were chosen in order to mimic three different climate zones. At the beginning of each simulation, cells exhibited the same capacity and were at 90% SOC. Fig. 7e–g show associated voltage decays of two cells with the lowest and the highest self-discharge rate. In case of Munich based temperature profile, the voltage difference after one year amounted to 1.2 mV. In Los Angeles, the voltage difference amounted to 1.8 mV and in Singapore to 2.9 mV. 2.9 mV in voltage difference at 90% SOC for LG MJ1 cell results in a charge difference of 5.25 mA h, which is 0.15% of the nominal capacity. Therefore such small voltage imbalance would not cause any severe capacity limitations within the battery pack. Furthermore, balancing circuits are usually activated after the maximum voltage difference exceeding a threshold of 5 mV [7].

Despite the high relative variance of self-discharge rates compared to the relative variance of capacity and impedance it is highly unlikely, that self-discharge is the main origin for the voltage imbalance in MJ1 battery packs. Therefore, it stands to reason, that inhomogeneous aging, for example due to temperature gradients within the pack, could evoke such voltage imbalance. Variation in loss of lithium inventory or in loss of active materials at both electrodes would cause a change in terminal voltage and OCV curve, leading to different voltage drifts within in series connection.

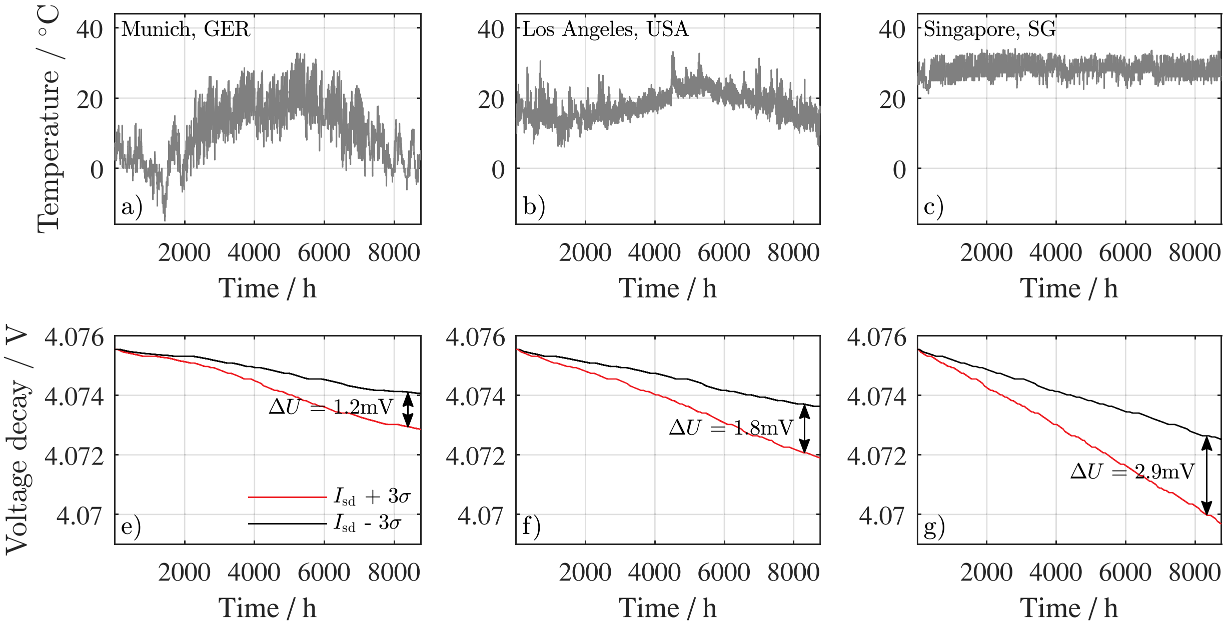

Fig. 7. Ambient temperature during the year 2018 in Munich (GER) (a), Los Angeles (USA) (b) and in Singapore (SG) (c). Voltage decay of a cell with the highest and the lowest self-discharge exposed to the ambient temperature in Munich (GER) (e), Los Angeles (USA) (f) and in Singapore (SG) (g).

4. Summary and conclusion

In this work, variation of reversible self-discharge and calendar aging of 24 commercial 18650 lithium-ion cells with nickel-rich cathodes and silicon–graphite anodes were investigated. Before the storage all cells underwent an initial checkup routine and origins of initial cell parameter variations were analyzed via differential voltage. After that, all cells were stored for 10 month at 70% SOC at 25 °C. During the last two weeks of storage, the self-discharge currents were determined via decay of terminal voltage. Main findings are summarized in the following.

1 Relative variance of initial capacity and impedance distributions amounted to 0.2% and 0.68% respectively. Besides a moderate correlation between the capacity and silicon to graphite ratio in the anode, no further dependencies on material markers in differential voltage were found.
2 Statistical evaluation of calendar aging revealed, that examined cells exhibited constant aging rates. Relative capacity variance doubled during the storage, whereas the relative variance of the impedance remained almost the same. Further analysis revealed that after the manufacturing process all cells were most likely matched by capacity.
3 Relative variance of self-discharge currents amounted to 10%. Furthermore, no correlations between self-discharge and remaining cell parameters were observed. Using a proposed self-discharge model, it was shown, that the maximum voltage difference within the battery pack remained under the typical cell balancing activation threshold.

Due to very low voltage difference, it is most likely that different self-discharge rates are not the main reason for the voltage drift within battery packs and consequently the need for cell balancing. Already a low number of cells in parallel would decrease the possible voltage drift even further, which would also apply for battery packs with large format cells. However, the exact behavior of large format cells has to be evaluated with additional experimental data. Future work will address the remaining reasons for voltage imbalance, such as different aging rates and will discuss the purpose of cell balancing.

Acknowledgments

This work has received funding from the European Unions Horizon 2020 research and innovation program under the grant “Electric Vehicle Enhanced Range, Lifetime And Safety Through INGenious battery management” (EVERLASTING 713771). The presented data of this work is available under [http://doi.org/10.4121/uuid:659c29a2-bff9-4901-9551-ecae3b63011a].

References

[1] Volker Reber, 2016 (Accessed 15 March 2019), https://www.porscheengineering.com/filestore/download/peg/de/pemagazin-01-2016-artikel-e-power/default/047e5361-3dfb-11e6-8697-0019999cd470/e-power-%E2%80%93-Neue-M%C3%B6glichkeiten-durch-Laden-mit-800-Volt-Porsche-Engineering-Magazin-01-2016.pdf.

[2] J. Schnell, C. Nentwich, F. Endres, A. Kollenda, F. Distel, T. Knoche, G. Reinhart, Data mining in lithium-ion battery cell production, J. Power Sources 413 (2019) 360–366, https://doi.org/10.1016/j.jpowsour.2018.12.062.

[3] S.F. Schuster, M.J. Brand, P. Berg, M. Gleissenberger, A. Jossen, Lithium-ion cell-to-cell variation during battery electric vehicle operation, J. Power Sources 297 (2015) 242–251, https://doi.org/10.1016/j.jpowsour.2015.08.001.

[4] K. Rumpf, M. Naumann, A. Jossen, Experimental investigation of parametric cell-to-cell variation and correlation based on 1100 commercial lithium-ion cells, J. Energy Storage 14 (2017) 224–243, https://doi.org/10.1016/j.est.2017.09.010.

[5] M. Dubarry, N. Vuillaume, B.Y. Liaw, From single cell model to battery pack simulation for li-ion batteries, J. Power Sources 186 (2) (2009) 500–507, https://doi.org/10.1016/j.jpowsour.2008.10.051.

[6] S. Paul, C. Diegelmann, H. Kabza, W. Tillmetz, Analysis of ageing inhomogeneities in lithium-ion battery systems, J. Power Sources 239 (2013) 642–650, https://doi.org/10.1016/j.jpowsour.2013.01.068.

[7] C. Campestrini, P. Keil, S.F. Schuster, A. Jossen, Ageing of lithium-ion battery modules with dissipative balancing compared with single-cell ageing, J. Energy Storage 6 (2016) 142–152, https://doi.org/10.1016/j.est.2016.03.004.

[8] B. Kenney, K. Darcovich, D.D. MacNeil, I.J. Davidson, Modelling the impact of variations in electrode manufacturing on lithium-ion battery modules, J. Power Sources 213 (2012) 391–401, https://doi.org/10.1016/j.jpowsour.2012.03.065.

[9] S. Santhanagopalan, R.E. White, Quantifying cell-to-cell variations in lithium ion batteries, Int. J. Electrochem. 2012 (12) (2012) 1–10, https://doi.org/10.1155/2012/395838.

[10] P. Arora, Capacity fade mechanisms and side reactions in lithium-ion batteries, J. Electrochem. Soc. 145 (10) (1998) 3647, https://doi.org/10.1149/1.1838857.

[11] P. Keil, A. Jossen, Calendar aging of NCA lithium-ion batteries investigated by differential voltage analysis and coulomb tracking, J. Electrochem. Soc. 164 (1) (2017) A6066–A6074, https://doi.org/10.1149/2.0091701jes.

[12] I. Zilberman, J. Sturm, A. Jossen, Reversible self-discharge and calendar aging of 18650 nickel-rich, silicon–graphite lithium-ion cells, J. Power Sources 425 (2019) 217–226, https://doi.org/10.1016/j.jpowsour.2019.03.109.

[13] L. Lu, X. Han, J. Li, J. Hua, M. Ouyang, A review on the key issues for lithium-ion battery management in electric vehicles, J. Power Sources 226 (2013) 272–288, https://doi.org/10.1016/j.jpowsour.2012.10.060.

[14] P. Haussmann, J. Melbert, Self-discharge observation for onboard safety monitoring of automotive li-ion cells: accelerated procedures and application concept, SAE International400 Commonwealth Drive, Warrendale, PA, United States, SAE Technical Paper Series, (2018), https://doi.org/10.4271/2018-01-0449.

[15] J.P. Schmidt, A. Weber, E. Ivers-Tiffée, A novel and fast method of characterizing the self-discharge behavior of lithium-ion cells using a pulse-measurement technique, J. Power Sources 274 (2015) 1231–1238, https://doi.org/10.1016/j.jpowsour.2014.10.163.

[16] T. Deutschen, S. Gasser, M. Schaller, J. Siehr, Modeling the self-discharge by voltage decay of a nmc/graphite lithium-ion cell, J. Energy Storage 19 (2018) 113–119, https://doi.org/10.1016/j.est.2018.07.003.

[17] M. Tang, P. Albertus, J. Newman, Two-dimensional modeling of lithium deposition during cell charging, J. Electrochem. Soc. 156 (5) (2009) A390, https://doi.org/10.1149/1.3095513.

[18] F.M. Kindermann, A. Noel, S.V. Erhard, A. Jossen, Long-term equalization effects in li-ion batteries due to local state of charge inhomogeneities and their impact on impedance measurements, Electrochim. Acta 185 (2015) 107–116, https://doi.org/10.1016/j.electacta.2015.10.108.

[19] B. Gyenes, D.A. Stevens, V.L. Chevrier, J.R. Dahn, Understanding anomalous behavior in Coulombic efficiency measurements on li-ion batteries, J. Electrochem. Soc. 162 (3) (2015) A278–A283, https://doi.org/10.1149/2.0191503jes.

[20] J. Wilhelm, S. Seidlmayer, P. Keil, J. Schuster, A. Kriele, R. Gilles, A. Jossen, Cycling capacity recovery effect: a Coulombic efficiency and post-mortem study, J. Power Sources 365 (2017) 327–338, https://doi.org/10.1016/j.jpowsour.2017.08.090.

[21] M. Lewerenz, G. Fuchs, L. Becker, D.U. Sauer, Irreversible calendar aging and quantification of the reversible capacity loss caused by anode overhang, J. Energy Storage 18 (2018) 149–159, https://doi.org/10.1016/j.est.2018.04.029.

[22] M. Sachs, Wahrscheinlichkeitsrechnung und Statistik: Für Ingenieurstudierende an Hochhochschulen, fifth auflage, Mathematik - Studienhilfen, Carl Hanser Verlag, München, 2018, https://doi.org/10.3139/9783446456204.

[23] J. Sturm, A. Rheinfeld, I. Zilberman, F.B. Spingler, S. Kosch, F. Frie, A. Jossen, Modeling and simulation of inhomogeneities in a 18650 nickel-rich, silicon–-graphite lithium-ion cell during fast charging, J. Power Sources 412 (2019) 204–223, https://doi.org/10.1016/j.jpowsour.2018.11.043.

[24] I. Bloom, A.N. Jansen, D.P. Abraham, J. Knuth, S.A. Jones, V.S. Battaglia, G.L. Henriksen, Differential voltage analyses of high-power, lithium-ion cells, J. Power Sources 139 (1–2) (2005) 295–303, https://doi.org/10.1016/j.jpowsour.2004.07.021.

[25] T. Ohzuku, I. Yasunobi, S. Keijiro, Formation of lithium-graphite intercalation compounds in nonaqueous electrolytes and their application as a negative electrode for a lithium ion (shuttlecock) cell, J. Electrochem. Soc. 140 (9) (1993) 2490–2498, https://doi.org/10.1149/1.2220849jes.

[26] M. Lewerenz, D.U. Sauer, Evaluation of cyclic aging tests of prismatic automotive $LiNiMnCoO_2$–graphite cells considering influence of homogeneity and anode overhang, J. Energy Storage 18 (2018) 421–434, https://doi.org/10.1016/j.est.2018.06.003.

[27] M. Lewerenz, J. Münnix, J. Schmalstieg, S. Käbitz, M. Knips, D.U. Sauer, Systematic aging of commercial $LiFePO_4$ |graphite cylindrical cells including a theory explaining rise of capacity during aging, J. Power Sources 345 (2017) 254–263, https://doi.org/10.1016/j.jpowsour.2017.01.133.

[28] T. Baumhöfer, M. Brühl, S. Rothgang, D.U. Sauer, Production caused variation in capacity aging trend and correlation to initial cell performance, J. Power Sources 247 (2014) 332–338, https://doi.org/10.1016/j.jpowsour.2013.08.108.

[29] M. Naumann, M. Schimpe, P. Keil, H.C. Hesse, A. Jossen, Analysis and modeling of calendar aging of a commercial $LiFePO_4$/graphite cell, J. Energy Storage 17 (2018) 153–169, https://doi.org/10.1016/j.est.2018.01.019.

[30] M. Ecker, J.B. Gerschler, J. Vogel, S. Käbitz, F. Hust, P. Dechent, D.U. Sauer, Development of a lifetime prediction model for lithium-ion batteries based on extended accelerated aging test data, J. Power Sources 215 (2012) 248–257, https://doi.org/10.1016/j.jpowsour.2012.05.012.

[31] P. Keil, S.F. Schuster, J. Wilhelm, J. Travi, A. Hauser, R.C. Karl, A. Jossen, Calendar aging of lithium-ion batteries, J. Electrochem. Soc. 163 (9) (2016) A1872–A1880, https://doi.org/10.1149/2.0411609jes.

[32] R. Korthauer, Handbuch Lithium-Ionen-Batterien, Springer Berlin Heidelberg, Berlin, Heidelberg, 2013, https://doi.org/10.1007/978-3-642-30653-2.

[33] V.V. Viswanathan, D. Choi, D. Wang, W. Xu, S. Towne, R.E. Williford, J.-G. Zhang, J. Liu, Z. Yang, Effect of entropy change of lithium intercalation in cathodes and anodes on li-ion battery thermal management, J. Power Sources 195 (11) (2010) 3720–3729, https://doi.org/10.1016/j.jpowsour.2009.11.103.

[34] I. Zilberman, A. Rheinfeld, A. Jossen, Uncertainties in entropy due to temperature path dependent voltage hysteresis in li-ion cells, J. Power Sources 395 (2018) 179–184, https://doi.org/10.1016/j.jpowsour.2018.05.052.

[35] A. Jossen, Fundamentals of battery dynamics, J. Power Sources 154 (2) (2006) 530–538, https://doi.org/10.1016/j.jpowsour.2005.10.041.

[36] Plötz, Gnann, Ullrich, Haendel, Globisch, Dütschke, Wietschel, Held, Elektromobilität in Gewerblichen Flotten (2014).

3 Influence of different aging rates on the voltage imbalance

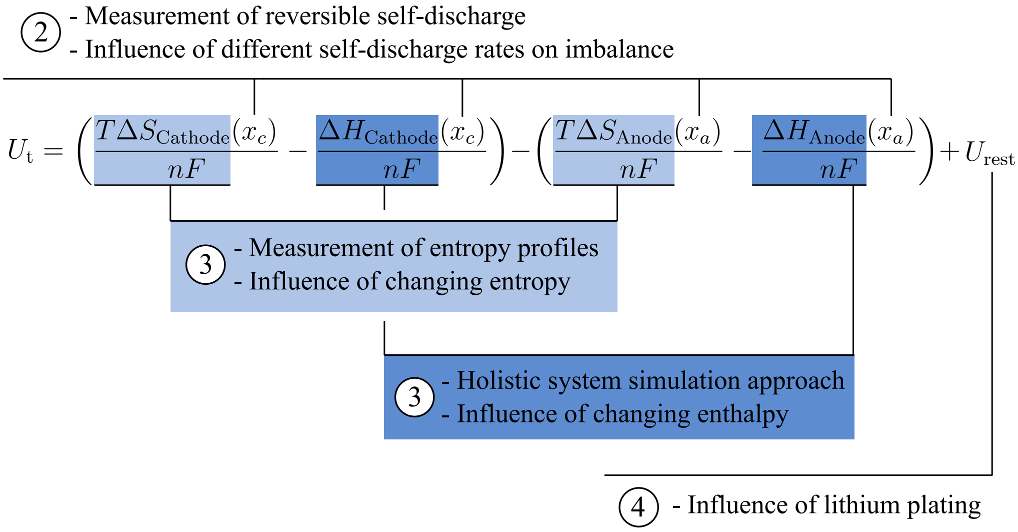

Figure 3.1: Outline of chapter 3.

The previous results outlined in this work revealed that different self-discharge rates are unlikely to be responsible for the voltage imbalance in battery packs. Further influencing factors, as shown in Fig. 3.1, are stoichiometric changes due to different aging rates. This chapter presents two articles, which discuss accurate methods for determining entropic coefficients and some possible implications of different aging rates on pack utilization.

The presented measurement method is then applied to determine the entropy profiles of the cathode and the anode. Furthermore, the entropy half-cell profiles are validated in the full-cell configuration via calorimetric measurements and the implications of changing entropy profiles on voltage imbalance are assessed.

Non-uniformity of aging is a well-known phenomenon and is influenced by both intrinsic and extrinsic factors. Intrinsic factors are closely linked to manufacturing tolerances and to the difficulty of determining the future aging behavior of all cells within the manufacturing process. It implies that even under the same operational conditions, cells age slightly differently. In addition, it is almost impossible to provide the same operational conditions for an entire battery pack due to design limitations, such as maximum cooling power, geometric requirements and electrical contacts. Taken together, these factors suggest that within large battery packs, the aging rates of single cells are expected to vary. Up to this point, the influence of different aging rates on the utilization of battery packs has not yet been completely explained. Therefore, the second article presents a holistic battery pack simulation approach which includes intrinsic cell-to-cell variations and battery system operation parameters, such as temperature gradients and balancing systems. This approach is used for statistical evaluation of how degradation mechanisms, as well as cell and system quality might influence the pack utilization.

3.1 Measurement of the entropic coefficients

In order to investigate the influence of changing entropy profiles on voltage drift, a measurement method was designed to provide a robust and simple entropy determination. As described in the introduction, there are generally two different methods for determination of the entropic coefficients. First, the measurement of the terminal voltage in response to a temperature change and second, the calorimetric measurement of the heat exchanged during a charge and discharge cycle. For the determination of the entropic coefficients of both anode and cathode, coin cells were used from [104]. Since the heat generation of a coin cell is rather small, a calorimetric determination of the entropic coefficients required high precision laboratory equipment. Therefore, the voltage-based method was the preferred choice. Previous experiments have shown that a standard temperature step did not evoke a linear behavior in the voltage response, as depicted in Fig. 3.2. In particular, the change from 50 °C to 25 °C did not result in the same absolute voltage response as the change from 25 °C to 50 °C.

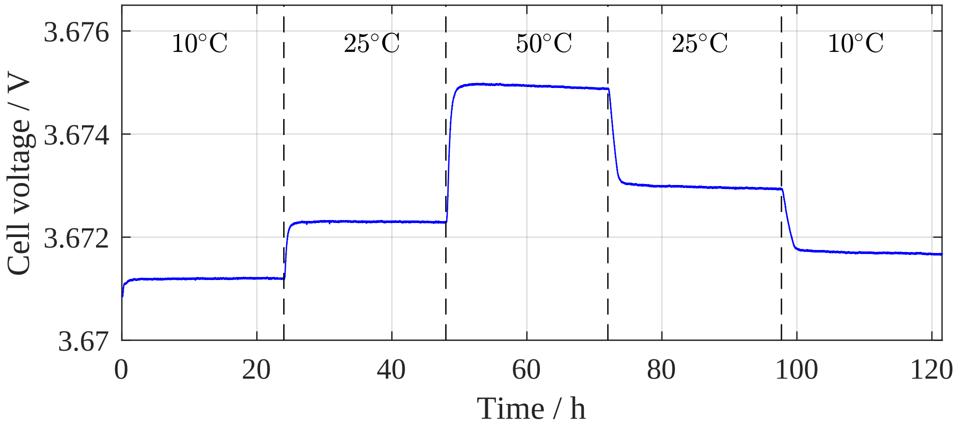

Figure 3.2: Voltage progression of a Moli IHR18650A (NMC111/Graphite, 1.95 Ah) cell at 50 % SOC exposed to a temperature profile, which is controlled by the climate chamber Binder KT115.

The investigation of this behavior, which is reported in the following article, revealed a non-linear, hysteresis like behavior of the entropy for different SOCs, cell formats and chemistries. The duration of the resting time after the temperature change, as well as the amplitude of the temperature excitation both influenced measurement uncertainties. Possible explanation of such behavior was linked to the hysteresis in the mechanical expansion of the cells. In order to minimize measurement uncertainties, a new optimized temperature profile was proposed and validated. The resting time was limited to the thermal relaxation of the lithium-ion cells in order to assure a homogeneous temperature distribution within the cell and the temperature excitation was limited as much as possible, whilst allowing for an acceptable signal to noise ratio (SNR).

Authors contribution Design and execution of the experiment was performed by Ilya Zilberman. Alexander Rheinfeld supported the creation of the manuscript. Andreas Jossen supervised this work, the manuscript was written by Ilya Zilberman and was edited by all authors.

Uncertainties in entropy due to temperature path dependent voltage hysteresis in Li-ion cells

Ilya Zilberman, Alexander Rheinfeld, Andreas Jossen

Journal of Power Sources 395, P. 179-184, 2018

Permanent weblink:
`https://doi.org/10.1016/j.jpowsour.2018.05.052`

Journal of Power Sources 395 (2018) 179–184

Contents lists available at ScienceDirect

Journal of Power Sources

journal homepage: www.elsevier.com/locate/jpowsour

Short communication

Uncertainties in entropy due to temperature path dependent voltage hysteresis in Li-ion cells

I. Zilberman*, A. Rheinfeld, A. Jossen

Institute for Electrical Energy Storage Technology, Technical University of Munich (TUM), Arcisstr. 21, 80333 Munich, Germany

HIGHLIGHTS

- The existence of the temperature path dependent voltage hysteresis is shown.
- Minimal temperature pulse duration and amplitude reduce measurement uncertainty.
- Optimized temperature profile for potentiometric entropy measurement is presented.

GRAPHICAL ABSTRACT

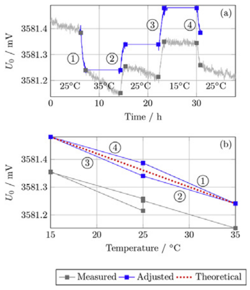

ARTICLE INFO

Keywords:
Lithium-ion
Entropy
Reversible heat
Open circuit voltage
Hysteresis

ABSTRACT

The determination of reversible heat is often carried out by means of a potentiometric measurement of entropy related effects. In this work, the potentiometric method is more closely investigated regarding the often assumed linear relationship between the open circuit potential (OCP) and temperature and possible associated measurement inaccuracies. Four different, completely equalized lithium-ion cells comprising different chemistries and cell formats are object of this study. Two different temperature profiles with varying frequency and amplitude components were applied and according entropic coefficients were calculated based on the preceding data. The results obtained in this work clearly reveal a non-linear behavior of the voltage to temperature relationship regardless of the cell format, state of charge (SOC), cell chemistry or sign of the derived entropic coefficient. This non-linearity manifests in a certain hysteresis of the OCP depending on the temperature history of the cells. The results suggest to minimize the temperature pulse duration whilst still allowing for a thermal equalization of the cell. Additionally, the authors suggest to minimize the amplitude of the temperature pulse as much as possible, whilst still allowing for an acceptable signal to noise ratio (SNR) for the measured voltage response.

1. Introduction

The rising trend of decentralized energy production as well as growing market for electric vehicles (EV) has created a demand for economically reasonable, persistent and reliable energy storage systems. Lithium-ion technology has recently become a key player in the energy storage domain by improving its cycle life and safety properties. Whilst currently used materials are reaching their maximum theoretical potential in terms of energy density, further improvements can be achieved on the system level. Thermal management can guarantee both, a high efficiency and a long lifetime of a battery pack. However, proper dimensioning and design of such thermal management systems requires precise thermal characterization of the battery cells.

The major heat losses in a lithium-ion cell can be divided into

---

* Corresponding author.
E-mail address: ilya.zilberman@tum.de (I. Zilberman).

https://doi.org/10.1016/j.jpowsour.2018.05.052
Received 13 February 2018; Received in revised form 17 April 2018; Accepted 14 May 2018

reversible and irreversible part [1]. Irreversible losses are usually attributed to charge transfer, finite conductivity of the electrolyte, the current collector foil, active materials and cell connectors [2]. The reversible heat losses on the other hand are connected to structural properties of the active materials, which might change during the lithiation and delithiation due to different arrangement of lithium-ions in the host lattice [2].

Thermodynamics of an electrochemical system can be described by Gibbs free energy ΔG, reaction enthalpy ΔH and reaction entropy ΔS. At constant pressure and physical composition, the maximum available electrical energy, the Gibbs free energy ΔG is given by

$$\Delta G = -nFU_0(x) \tag{1}$$

whereas n is the number of electrons participating in the reaction, F is the Faraday constant, $U_0(x)$ is the equilibrium voltage and x is the SOC. The overall energy of the reaction, the Gibbs free energy ΔG can be expressed by

$$\Delta G = \Delta H - T\Delta S \tag{2}$$

whereas T is the absolute temperature. The reaction entropy ΔS, which describes the reversible heat effect is then given by

$$\Delta S = nF\frac{\mathrm{d}U_0(x)}{\mathrm{d}T} \tag{3}$$

where the entropic coefficient for a constant pressure and a certain SOC is proportional to a change of the OCP for a change in temperature. This relationship holds, if ΔS and ΔH do not depend on temperature.

Considering equations (1)–(3) there are two major techniques for the determination of the entropic coefficients. The calorimetric method utilizes reversible heat effects, by separating the reversible and irreversible heat losses for a subsequent charge and discharge of the cell, which is only applicable in case other effects contributing to the energy balance are negligible [3]. The potentiometric method, however, utilizes the relationship from equation (3). A temperature pulse is applied under open circuit conditions and the terminal voltage is measured. Schmidt et al. have shown that both methods deliver results in good accordance to each other [4].

Due to its simplicity, the potentiometric method has been used repeatedly in the battery research. The entropy profiles of different cathode and anode materials have been analyzed in order to investigate theoretically feasible entropy profiles of full cells [5]. Hudak et al. and Osswald et al. have shown that there are trackable entropy changes during the cyclic aging [6] [7]. Forgez et al. have used the potentiometric method to implement a detailed thermal model of a lithium-ion cell [8].

In most cases, a temperature dependent change of the OCP is assumed to be linear, regardless of the positive or negative temperature change and regardless of the initial temperature [9]. However, a non-linear behavior of the entropy has been already observed. Schmidt et al. have shown an entropy hysteresis depending on the direction of the current [4]. Bazinksi et al. observed different entropy coefficients for the same temperature change at the same SOC at different initial temperatures [10].

This work deals with the effect of the temperature path dependent entropy hysteresis, which to the knowledge of the authors has not been reported yet. This paper is organized as follows. After a brief description of the experimental setup, different temperature excitations are specified and their influence on the non-linear behavior of the reaction entropy is discussed. Finally, an optimal temperature excitation is proposed for potentiometric entropy determination method.

2. Experimental

One 2032 coin type lithium-ion cell and three different 18650 type cells comprising different NMC and NCA cathodes and graphite anodes were object of this study. All cells rested for more than six months at different SOCs at room temperature in order to guarantee a most equalized state [11]. Similar to the 18650 cells, the investigated coin cell contains a jelly roll as well. Due to the large surface to volume ratio and the small height of the cell, thermal gradients along the jelly roll are considered to be negligible even during rapid temperature changes. Cylindrical 18650 cells, however, might exhibit a certain temperature gradient along the jelly roll, leading to possible equalization processes, which might interfere with the potentiometric measurement method. All considered cell types and their corresponding properties are summarized in Table 1. The results presented in the discussion section depict the averaged behavior of the considered quantity of each cell type.

Table 1
Overview of tested cells and their respective properties.

Name	Manuf.	Cathode	SOC	ΔS sign	Format	Quantity
A	Moli	NMC111	48%	Positive	18650	3
B	Sanyo	NCA	50%	Positive	18650	3
C	LG	NMC811	30%	Negative	18650	3
D	Varta	NMC111	28%	Negative	Coin	2

During the experiment, all cells were placed in a Binder KT115 climate chamber, which guaranteed isothermal test condition with a temperature accuracy of 15 mK. The temperature was measured on the surface of each cell with mounted PT100 sensors.

The voltage was measured with a self-built, custom measurement unit on the basis of ADS1278 from Texas Instruments, a 24 Bit analog digital converter (ADC) with 8 differential input channels. All channels underwent gain and offset calibration with a high precision voltage source LTC6655 from Linear Technology. The noise level for each channel was under 15 µV for a 10 Hz sampling rate. Due to the high input impedance of 20 GΩ it was insured, that no leakage current of the circuit interfered with the voltage measurement by slowly discharging the cell. The fact, that a potentiometric measurement of the entropic coefficient of a cell is based on the change of the cell's potential for a change in its temperature inevitably comes with a change of the temperature of the sense wires. That might cause a possible interference due to the Seebeck effect. However, by using the same length as well as the same material for the positive and negative sensing wire, the Seebeck effect can be neglected. Since all cell internal junctions between different materials exhibit the same temperature at all times, the Seebeck effect within the cell can be neglected as well.

In order to investigate a possible hysteresis of the reaction entropy, the following temperature profile was applied. The chosen generic temperature excitation was composed of a positive and a consequent negative temperature pulse, both starting at initial temperature of 25°C. Based on this concept two different temperature profiles were deployed.

Profile I, shown in Fig. 1a, was used to investigate the influence of the temperature pulse frequency on the entropic coefficient. The resting time at each temperature level was increased from 2 to 24 h. The amplitude of the temperature pulse was chosen to be 15°C with initial temperature of 25°C. As 2 h resting time showed to be not sufficient to reach a thermally equalized state for each cell, only the results from 4, 8 and 24 h resting time are discussed further. A distinct variation in the gained entropy data for a change in the dynamics of temperature excitation would be an evidence that the entropy measurement is corrupted by charge equalization or self-discharge processes in the cell. Profile II, shown in Fig. 1b, on the other hand investigates the dependency between the amplitude of the temperature pulse and the derived entropy coefficients. This profile verifies the linear characteristic of the entropy. The temperature pulse was increased from 5°C over 10°C to 15°C with 8 h resting time.

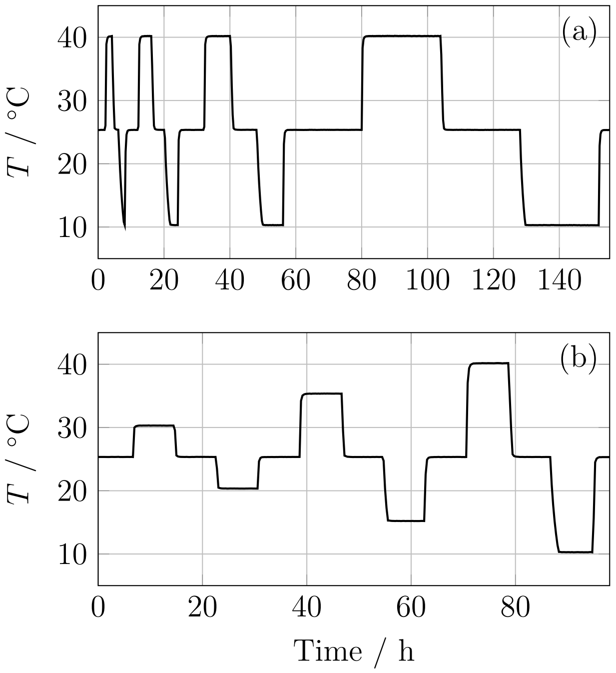

Fig. 1. Profile I with increasing resting time (a), profile II with increasing temperature amplitude (b).

3. Results and discussion

According to equation (3), the same relative change in temperature evokes the same relative change in the terminal voltage of the cell, regardless of the direction of the temperature change and absolute value of the temperature. Additionally, it is assumed that the amplitude of the temperature pulse is irrelevant, since the entropy should behave linearly. Both properties are valid as long as the pressure and lithium-ion concentration in the anode, cathode and electrolyte remain unchanged. Theoretically, there is an infinite amount of possible temperature pulses for determining the entropic coefficients by means of potentiometric measurement method. Fig. 2a shows a temperature profile, which includes a positive and negative pulse of 10°C with a duration of 8 h starting at 25°C. This profile depicts a segment of the profile II in Fig. 1. The corresponding voltage response of cell C is shown in Fig. 2b in gray. Due to self-discharge processes in the cell, the terminal voltage exhibits a negative slope with time. Schmidt et al. have determined the highest self-discharge current of 0.105 mA at 95% SOC for a 2 A h NCA cell [12]. Such self-discharge would evoke a 0.2% SOC change during this experiment. As the entropy does not exhibit a strong dependency on such a small change in degree of lithiation as reported previously [5], the entropic coefficient is assumed not to be affected by SOC changes during the experiment. An adjusted voltage progression without self-discharge effects is shown in Fig. 2b in blue. After the first voltage drop, each voltage change segment is lifted by the value of the previous voltage decrease during the resting time. Due to negative sign of the entropic coefficient, shown in this example, an increase in temperature evokes a drop in the terminal voltage, whereas a drop in temperature results in an increase of the terminal voltage. In comparison to the temperature increase from 25°C to 35°C, the drop from 35°C to 25°C clearly evokes smaller change in the terminal voltage, whereas the difference is becoming larger as the temperature is further decreased by 10°C, to 15°C. As the temperature is increased again to its initial state of 25°C, the self-discharge corrected terminal voltage reaches its initial state prior to the applied temperature profile. In this brief example, four temperature excitations with the same pulse amplitude, resulted in different changes of the terminal voltage, which does not allow for a straightforward determination of the cells's entropic coefficient. It has to be mentioned that the observed difference between the voltage responses is below 1 mV for all investigated cells. Fig. 2c shows the cell's voltage as a function of temperature at the beginning and the end of each temperature change. When looking into the self-discharge corrected voltage response of the cell (see Fig. 2c in blue), the voltage to temperature relationship clearly shows a hysteresis behavior of the voltage, which is highly non-linear. According to equation (3), the voltage response is expected to follow the red dotted line in Fig. 2c. Similar hysteresis-like behavior was observed for all tested cells regardless of the chemistry, SOC or the cell's format. Not each cell type has shown such an ideal hysteresis behavior, in which adjusted voltage starts and ends at the same point after applied profile, however the tendency for the hysteresis was observed for every cell.

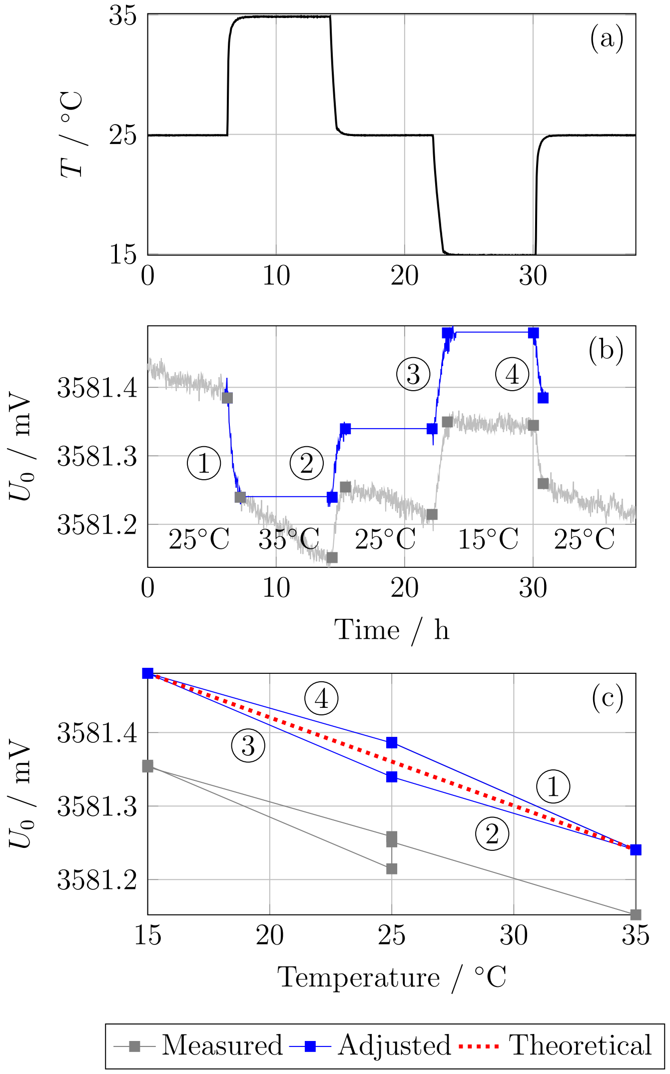

Fig. 2. Applied temperature profile (a), voltage response of cell C (b), temperature-voltage relationship (c). Adjusted curve (blue) depicts the voltage progression without self-discharge, theoretical curve (red) depicts an ideal behavior according to equation (3). (For interpretation of the references to color in this figure legend, the reader is referred to the Web version of this article.)

In order to further investigate this hysteresis-like behavior, the temperature profiles I and II from Fig. 1 were applied to cells A-D listed in Table 1. The influence of frequency and amplitude of the applied temperature pulse on cells A to D is summarized in Fig. 3. The colored dashed lines depict the calculated values of the entropic coefficient for a corresponding temperature change. The black solid line reflects the maximum relative deviation from the mean entropic coefficient. In

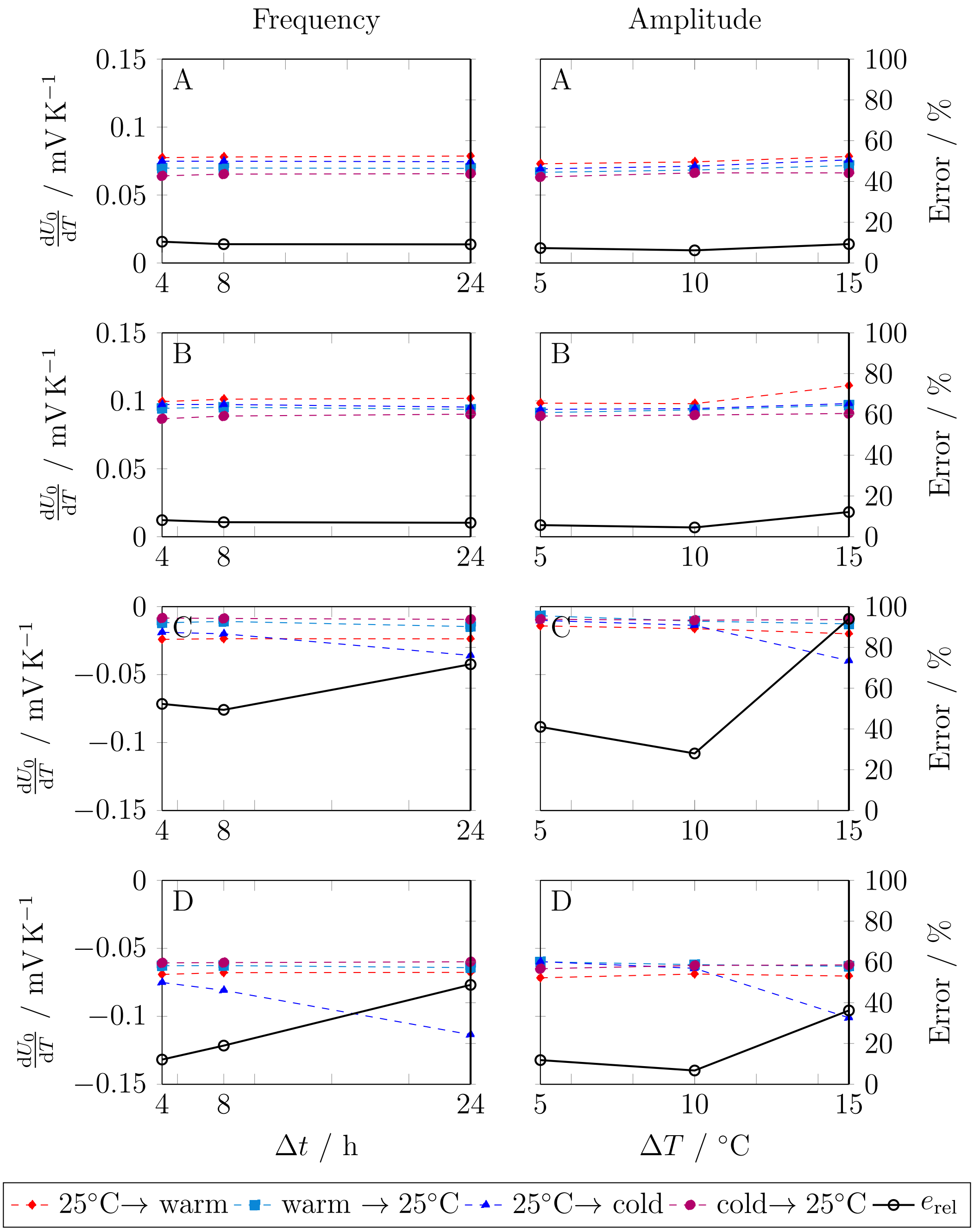

Fig. 3. Calculated entropic coefficients for the cells A-D for the profile I (left) and profile II (right). Each data point represents the averaged value of the considered quantity of each cell type, depicted in Table 1.

theory, the dashed lines would form a single line parallel to x axis for both investigated cases. However, Fig. 3 shows a different behavior for all tested cells.

In the case of frequency dependency, cells A and B, which both exhibit a positive entropic coefficient show a similar behavior. The increasing time interval does not affect the characteristics of the observed hysteresis, nonetheless four different entropic coefficients for the same absolute temperature change could be identified. However, observed relative error of 10% and 7% for cells A and B is comparably small. Cells C and D, which exhibit a negative entropic coefficient show a slightly different behavior. Except for the temperature change from 25°C to 10°C all entropic coefficients remain almost constant with increasing pulse duration and amplitude. Especially, with increasing pulse duration, the calculated absolute entropic coefficient dU_0/dT for the 25°C → 10°C temperature change increases. The authors believe that temperature gradients within the cell based on a sudden change in ambient temperature are not responsible for this phenomenon, as the format varies for cells C and D. The relative errors for 24 h pulse amount to approximately 72% and 49% for cells C and D. These results suggest to limit the ratio of the temperature pulse duration to the thermal equalization time of the cell in order to minimize the uncertainty of the determined entropic coefficient.

The right side of Fig. 3 shows the calculated entropic coefficients when applying profile II with differing amplitudes of the temperature pulse. The results indicate that increasing the amplitude of the temperature pulse amplifies the variance in the calculated entropic coefficients. Similar to profile I, both cells C and D show a non linear increase in the calculated entropic coefficient for the 25°C → cold temperature change with an increase of the temperature pulse amplitude. The relative errors when applying 15°C pulse amount to 94% and 36% for

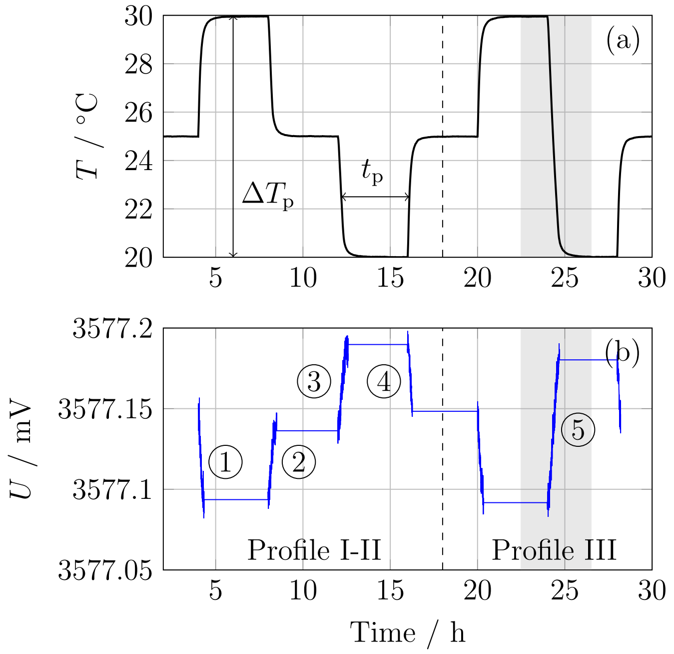

Figure 4. Optimal temperature profile for potentiometric measurement of entropy (a), voltage response of cell C (b).

cells C and D respectively. Contrary to profile I, also cells A and B show a slight increase in the variance of the calculated entropic coefficient. When comparing the influence of frequency and amplitude in Fig. 3 left and right, the previous history of the temperature excitation seems to play an additional role. Data sets from the graphs with varying amplitude at $\Delta T = 15°\mathrm{C}$ and data sets from the graphs with varying frequency at $\Delta t = 8\,\mathrm{h}$ exhibit the exact same temperature excitation. However, the resulting calculated entropic coefficients are not identical. The findings from evaluation of profile II suggest to limit the amplitude of the temperature pulse to a minimum.

In the literature, a certain temperature path dependent voltage hysteresis was previously observed by Jalkanen et al. [13]. However, this effect was not further discussed and was attributed to general measurement uncertainties. Based on the customized measurement equipment applied within this study, the results support the hypothesis of a hysteresis-like behavior in the voltage response of a cell with a change in its temperature. Assuming that self-discharge effects are not able to significantly change the lithium-ion concentration within the electrodes during the course of the experiment, the crystallographic structure of the materials and associated entropy should remain unchanged. Therefore, the authors believe that such behavior might be caused by a certain hysteresis of the thermal expansion of the electrodes which would result in a variance of the overall pressure distribution within the cell. The results from the frequency varying profile in Fig. 3 reveal that the difference between the maximum and minimum coefficients are in the same order of magnitude, independently of the absolute entropy value, SOC or cell chemistry. Due to this fact the reason for this behavior might be connected to mutual properties of all cells. Oh et al. recently showed a hysteresis in the thermal expansion of cell components, which supports this assumption [14]. However, examination of this theory will be subject of the future work. Modelling of this phenomena might support the general understanding of the hysteresis behavior, as it was shown in case of a hysteresis in OCP vs. SOC in lithiated silicone electrodes [15].

Based on the presented results, the authors propose a new temperature profile III in order to minimize errors during potentiometric entropy measurements, which is shown in Fig. 4a. After a sufficient equalization time at the base temperature T_base, a positive temperature pulse with the amplitude of $\Delta T_\mathrm{p}/2$ and duration of time t_p is applied. Immediately afterwards, a second negative pulse with the same amplitude and duration is applied. As shown in Table 2, the calculated entropic coefficient with temperature change ⑤ in profile III is the average of $\frac{\mathrm{d}U_0}{\mathrm{d}T}$ values derived from profile I-II. The authors suggest, that the pulse duration in profile III should not exceed the thermal equalization time of the investigated lithium-ion cell, which depends on the thermal boundary conditions and the size of the cell. During this experiment the minimum pulse duration was 4 h. The change from positive to negative pulse should be used for the calculation of the entropic coefficient, which is highlighted by the gray area in Fig. 4. The authors suggest to minimize the amplitude of the temperature pulse as much as possible, whilst still allowing for an acceptable SNR for the measured voltage response.

Table 2
Comparison between different $\frac{\mathrm{d}U_0}{\mathrm{d}T}$ calculated with profile I-II and profile III.

	①	②	③	④	avg.① -④	⑤
$\frac{\mathrm{d}U_0}{\mathrm{d}T}/mV\ K^{-1}$	−0.0115	−0.0075	−0.0107	−0.0083	−0.0095	−0.009
$e_\mathrm{rel}/\%$	21	21	13	13	–	5

4. Conclusion

In this work, the existence of a temperature path dependent voltage hysteresis was demonstrated. With the aid of low noise voltage measurement equipment, a systematic characteristics of this hysteresis could be proved. This effect leads to uncertainties in determining the entropic coefficient of lithium-ion cells when applying potentiometric measurement techniques. Four different cell types, including different cathode materials and cell formats were subject of this study. Two different temperature profiles were applied consisting of positive and negative temperature pulses with varying amplitude and frequency. The results revealed a highly non-linear behavior of the voltage response and associated calculated entropy coefficients for the same absolute change in the temperature.

In order to minimize possible errors during potentiometric measurements, the authors recommend to use profile III from Fig. 4 for determination of entropic coefficients. Pulse duration at maximum and minimum temperature should be limited to thermal equalization time of the cell. Additionally, the authors suggest to limit the amplitude of the temperature pulse as much as possible, whilst still allowing for an acceptable SNR.

Future work will elaborate on the reasons for the temperature path dependent voltage hysteresis, evaluating the hysteresis in the thermal expansion of lithium-ion cells.

Acknowledgements

This work has received funding from the European Unions Horizon 2020 research and innovation program under the grant ”Electric Vehicle Enhanced Range, Lifetime And Safety Through INGenious battery management” (EVERLASTING 713771).

References

[1] J.-S. Hong, Electrochemical-calorimetric studies of lithium-ion cells, J. Electrochem. Soc. 145 (5) (1998) 1489, http://dx.doi.org/10.1149/1.1838509.
[2] T.M. Bandhauer, S. Garimella, T.F. Fuller, A critical review of thermal issues in lithium-ion batteries, J. Electrochem. Soc. 158 (3) (2011) R1, http://dx.doi.org/10.1149/1.3515880.
[3] D. Bernardi, A general energy balance for battery systems, J. Electrochem. Soc. 132 (1) (1985) 5, http://dx.doi.org/10.1149/1.2113792.
[4] J.P. Schmidt, A. Weber, E. Ivers-Tiffée, A novel and precise measuring method for the entropy of lithium-ion cells: δs via electrothermal impedance spectroscopy, Electrochim. Acta 137 (2014) 311–319, http://dx.doi.org/10.1016/j.electacta.2014.05.153.
[5] V.V. Viswanathan, D. Choi, D. Wang, W. Xu, S. Towne, R.E. Williford, J.-G. Zhang,

J. Liu, Z. Yang, Effect of entropy change of lithium intercalation in cathodes and anodes on li-ion battery thermal management, J. Power Sources 195 (11) (2010) 3720–3729, http://dx.doi.org/10.1016/j.jpowsour.2009.11.103.

[6] N.S. Hudak, L.E. Davis, G. Nagasubramanian, Cycling-induced changes in the entropy profiles of lithium cobalt oxide electrodes, J. Electrochem. Soc. 162 (3) (2014) A315–A321, http://dx.doi.org/10.1149/2.0071503jes.

[7] P.J. Osswald, M. d. Rosario, J. Garche, A. Jossen, H.E. Hoster, Fast and accurate measurement of entropy profiles of commercial lithium-ion cells, Electrochim. Acta 177 (2015) 270–276, http://dx.doi.org/10.1016/j.electacta.2015.01.191.

[8] C. Forgez, D. Vinh Do, G. Friedrich, M. Morcrette, C. Delacourt, Thermal modeling of a cylindrical LiFePO4/graphite lithium-ion battery, J. Power Sources 195 (9) (2010) 2961–2968, http://dx.doi.org/10.1016/j.jpowsour.2009.10.105.

[9] A. Eddahech, O. Briat, J.-M. Vinassa, Thermal characterization of a high-power lithium-ion battery: potentiometric and calorimetric measurement of entropy changes, Energy 61 (2013) 432–439, http://dx.doi.org/10.1016/j.energy.2013.09.028.

[10] S.J. Bazinski, X. Wang, The influence of cell temperature on the entropic coefficient of a lithium iron phosphate (LFP) pouch cell, J. Electrochem. Soc. 161 (1) (2013) A168–A175, http://dx.doi.org/10.1149/2.082401jes.

[11] J. Wilhelm, S. Seidlmayer, P. Keil, J. Schuster, A. Kriele, R. Gilles, A. Jossen, Cycling capacity recovery effect: a coulombic efficiency and post-mortem study, J. Power Sources 365 (2017) 327–338, http://dx.doi.org/10.1016/j.jpowsour.2017.08.090.

[12] J.P. Schmidt, A. Weber, E. Ivers-Tiffée, A novel and fast method of characterizing the self-discharge behavior of lithium-ion cells using a pulse-measurement technique, J. Power Sources 274 (2015) 1231–1238, http://dx.doi.org/10.1016/j.jpowsour.2014.10.163.

[13] K. Jalkanen, T. Aho, K. Vuorilehto, Entropy change effects on the thermal behavior of a LiFePO4/graphite lithium-ion cell at different states of charge, J. Power Sources 243 (2013) 354–360, http://dx.doi.org/10.1016/j.jpowsour.2013.05.199.

[14] K.-Y. Oh, B.I. Epureanu, Characterization and modeling of the thermal mechanics of lithium-ion battery cells, Appl. Energy 178 (2016) 633–646, http://dx.doi.org/10.1016/j.apenergy.2016.06.069.

[15] D.R. Baker, M.W. Verbrugge, X. Xiao, An approach to characterize and clarify hysteresis phenomena of lithium-silicon electrodes, J. Appl. Phys. 122 (16) (2017) 165102, http://dx.doi.org/10.1063/1.4995277.

3.2 Influence of drifting entropic coefficients on pack utilization

3.2.1 Validation of half-cell entropy profiles

The entropy profiles of the positive and negative electrodes were measured using the potentiometric method presented in the previous section. For that purpose, coin cells of both anode and cathode, which were also studied in [104], were utilized. Measured entropy profiles of the anode and cathode are shown in Fig. 3.3a, whereby the balancing and loading ratios of both electrodes were taken from the previous differential voltage analysis in [104]. Fig.3.3b shows the measured full-cell entropy profile and the entropy profile calculated using the half-cell data, which are in good accordance with each other. In order to validate the full-cell entropy data, calorimetric measurements were conducted. For that purpose the heat generation of a pristine MJ1 cell was measured at a 0.2C CC charge- and discharge-rate with an accelerating rate calorimeter (EV-ARC, Thermal Hazard Technology) combined with a cycler (CTS, Basytec). Each charge and discharge step was followed by a CV period with a termination criterion of 0.05 C at 4.2 V and 2.5 V, respectively. After each step the cell was rested for at least 10 h. The total heat capacity of the cell was determined during the adiabatic conditions in the calorimeter. The utilization of the heat measured during the charge and discharge for the calorimetric determination of the cell's entropic coefficient is described in the following.

The heat produced by a cell during the charge or discharge is given by [144]:

$$\dot{Q}_{\mathrm{cell}} = \dot{Q}_{\mathrm{irr}} + \dot{Q}_{\mathrm{rev}} + \dot{Q}_{\mathrm{sr}} + \dot{Q}_{\mathrm{mix}} \tag{3.1}$$

and is composed of reversible and irreversible losses $\dot{Q}_{\mathrm{rev}}$ and $\dot{Q}_{\mathrm{irr}}$, parasitic heat from side reactions $\dot{Q}_{\mathrm{sr}}$ and mixing processes $\dot{Q}_{\mathrm{mix}}$. The heat from side reactions sums up all reactions within the cell which are not a part of the main charge transfer reaction, such as degradation processes. As such processes are usually slow, the absolute values of the heat generation rate are very small [166] and therefore negligible. Heat based on mixing effects is linked to the equalization of the concentration gradients within the cell. This equalization process is accompanied by the change of the reaction entropy, which also results in heat generation. However, since the absolute values are rather low [167], heat based on mixing processes can also be neglected. Thus, the heat flow of a lithium-ion cell is dominated by reversible and irreversible losses.

Irreversible heat is mainly based on Joule heat losses linked to the dynamic voltage drop during the operation and can be expressed by equation 3.2. Under the assumption that electrochemical impedance does not depend on the current and that the difference between the equilibrium and terminal voltage is the same regardless the direction of the current, irreversible heat becomes a product of electrochemical impedance and the load current squared.

$$\dot{Q}_{\mathrm{irr}} = (U_0 - U_{\mathrm{t}}) \cdot i(t) = \mathrm{Re}(Z) \cdot I^2 \tag{3.2}$$

The reversible heat is especially dependent on the entropic coefficients of the cell and can be calculated via

$$\dot{Q}_{\mathrm{rev}} = \frac{T\Delta S}{nF} \cdot I \tag{3.3}$$

From equations 3.2 and 3.3 it can be seen that by adding the cell heat during charge and discharge, the reversible heat is removed from the equation and the sum becomes twice the irreversible heat, if the temperature during charge and discharge is the same. By subtracting the irreversible heat from the overall cell heat during charge or discharge, the reversible heat can be calculated. In that way the entropy profile of the MJ1 cell was obtained via calorimetric method and is shown in Fig. 3.3b. The results reveal that the calorimetrically determined entropy profile is generally in good accordance with voltage based results, however the differences increase as the SOC decreases. Such discrepancy might be linked to the hysteresis effects within electrodes and not equal irreversible heat in charge and discharge direction. It has been shown that insertion batteries suffer from hysteresis of the OCV, depending on the charge or discharge direction [169], which has been linked to the fact that in a multiparticle electrode, the insertion does not proceed coherently in all particles [170]. Further effects, such as concentration gradients within the electrode due to prior charge or discharge, which might last for many hours, impede the determination of the entropy even more. However, since the utilization of the battery pack relies on the full charge of each cell, as discussed in the introduction, the validity of the measurement results in the upper SOC range is particularly important. As the entropy above 20 % SOC is relatively consistent between all measurement methods, half-cell entropy profiles will be used in the further analysis.

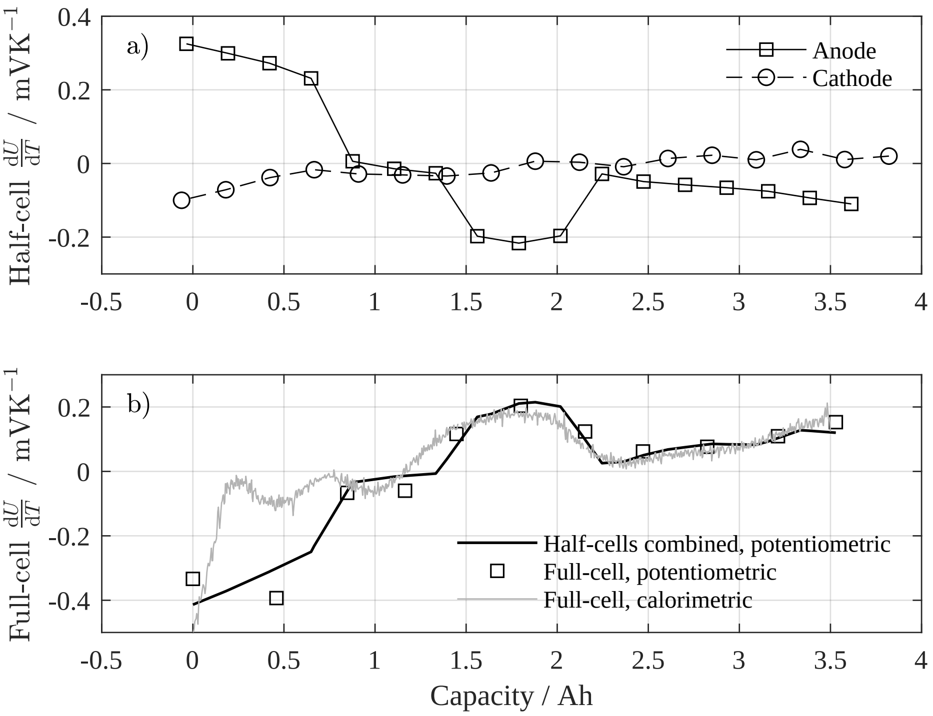

Figure 3.3: (a) Entropy profiles of the anode and cathode. The anode and the cathode half cells were initially set to 10 mV and 4.6 V respectively at 0.1 C with a subsequent CV period and termination criterion of C/1000. Afterwards, the anode was delithiated and the cathode was lithiated with C/30 in steps of 6.25 % SOC. After resting for 6 h a temperature pulse was applied according to [168] with a climate chamber KT115 from Binder. As the half cell voltage was not completely relaxed after 6 h, the voltage response to the temperature profile was corrected using the method presented by Osswald *et al.* [148]. (b) Calorimetrically derived entropy profile of the full-cell, combined full-cell entropy from the half-cell data and full-cell entropy profile measured according to the half-cell measurement sequence (full cell was lithiated to 4.2 V at 0.1 C with a subsequent CV period and termination criterion of C/1000. Afterwards, the full cell was delithiated with C/30 in steps of 10 % SOC).

3.2.2 Voltage imbalance due to changed entropy profiles

As previously stated in section 1.2.3, the influence of the manufacturing tolerances on the part of the cells potential, which is linked to the reaction entropy, is relatively small and can be neglected. The influence of different aging rates on the entropy profiles and therefore the terminal voltage is discussed in the following. Different aging rates in battery packs are often linked to the presence of temperature gradients. As LAM is more dependent on mechanical properties, such as particle expansion during lithiation and delithiation, the electrochemical processes of LLI at the negative electrode is often claimed to be the dominant temperature influenced degradation mechanism [129].

Therefore, it can be assumed that different rates of LLI are responsible for the alterations on full-cell entropy profiles. Furthermore, since the entropy profile of the anode dominates the full-cell entropy it can be assumed that only changes in the anode will be observable on the cell level.

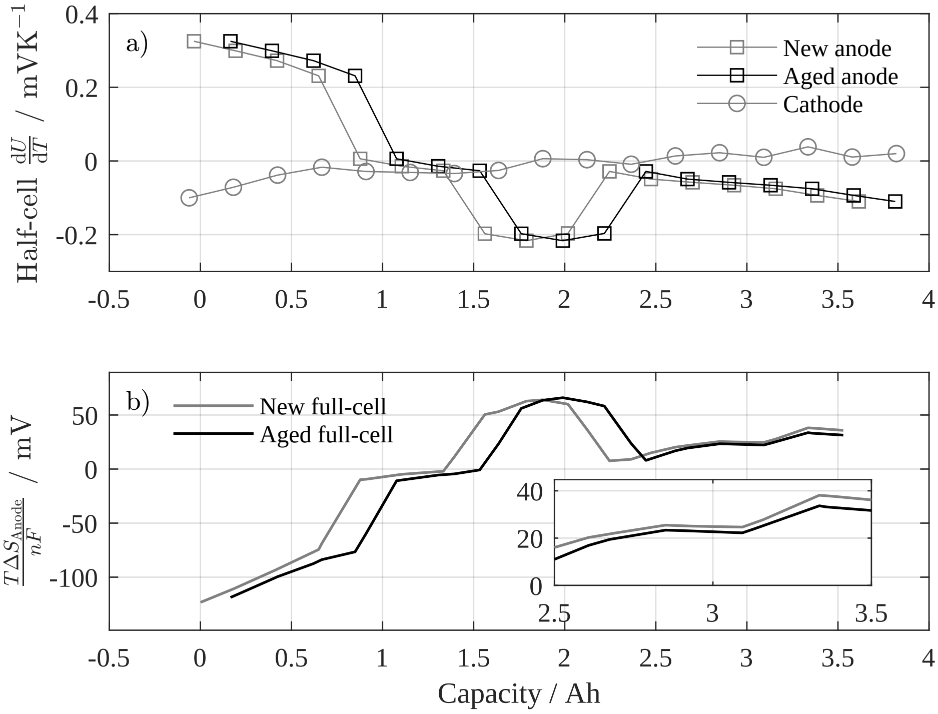

Figure 3.4: (a) Shift of the anode entropy profile by approx. 0.2 Ah, emphasizing the process of LLI to the right, (b) new and aged full-cell entropy profiles.

A shift and compression of the half-cell potentials of both electrodes have been applied in the past in order to imitate LAM and LLI [115]. Using this approach, the influence of a particular degradation mechanism on voltage imbalance between two cells is discussed in the following.

In a similar manner to the OCV, the compression and shift of entropy profiles due to degradation leads to a change in the full cell entropy profile, as already reported in the literature [147][171]. Anodic side reactions, such as growth and repair of the SEI, resulting in LLI, lead to a delithiation of the negative electrode and associated shift of the anode half-cell entropy profile to the right, as shown in Fig.3.4a. The shift amounts to 0.2 Ah, corresponding to approx. 6 % of the initial cell capacity, which emphasizes a change between a pristine and an aged cell. Such high discrepancy in aging rates depicts the worst case scenario in the battery pack. Fig.3.4b shows the corresponding full-cell entropy profiles.

Since the anode is limiting in discharge direction, the overall cell capacity decreases. Due to a change in the full cell entropy profile it can be expected that during charge, the unmodified cell reaches the end-of-charge voltage at 4.2 V first, resulting in a voltage imbalance between two cells with a 4.5 mV difference after 0.2 Ah shift, whereby the influence of the impedance is neglected.

It can be concluded that changes in full-cell entropy profiles can lead to a change of cell terminal voltage. However, since the voltage changes are expected to be very small, the influence of the entropy profiles can be neglected. For this reason, entropy profiles were not included in the holistic battery pack simulation described in the next section.

3.3 Statistical evaluation of the influence of different degradation mechanisms on pack utilization

Up to this point, possible influencing factors on the voltage imbalance, such as differing self-discharge and aging rates have been analyzed individually. This section presents a submitted manuscript, which investigates the influence of overall cell-to-cell variations including differing initial parameters, divergent self-discharge as well as aging rates on the utilization of large lithium-ion battery packs. As previously described in the introduction, the discharge energy has been designated as a suitable measure of the utilization of battery packs. However, this metric seems especially suited for evaluating the progression of single pack utilization. A comparison between several packs would seem to present problems, since, due to parameter variations, initial discharge energies might vary. Therefore, in the following analysis, a normalized discharge energy of the last discharge cycle at the end of life was used. This normalized discharge energy was defined as the quotient between the last discharge energy of the pack, which suffered from non-uniform aging and last discharge energy of a pack, which was subject neither to any temperature gradients nor to cell parameter variations.

For this purpose, a holistic battery pack lifetime simulation was implemented, which was able to emulate voltage drift due to cell parameter variations, temperature distributions within the pack and the applied balancing strategy over the lifetime of the pack. In order to obtain a representative distribution of the normalized pack utilizations, lifetime simulations had to be repeated many times. For each simulation, cell parameters were randomly chosen from a given distribution, whereby the operating conditions such as the balancing strategy, temperature distribution and the current load remained the same. This approach allowed the investigation of the battery pack's performance for a given cell quality, represented by the distribution parameters of the cell batch. However, a simulation based approach such the one presented here also imposes limitation. Due to the number of lifetime simulations required, it was necessary to implement an optimized model of a battery system in order to reduce the simulation time. The principles behind this simulation framework are presented and discussed in the following manuscript.

Degradation mechanisms were simulated via a shift and compression of half-cell OCVs. The presented simulation based study has shown that the loss of lithium inventory is the major contributor to the voltage changes attributable to differences in aging. Its findings were therefore integrated into the Monte Carlo simulation discussed here. The electric behavior of the cell was modeled using an impedance and self-discharge model. In order to exclude the current distributions between cells connected in parallel, which would consume a lot of computational power, cell blocks were treated as large cells. The influence of cell-to-cell variations was, however, considered in the calculation of cell block parameter variations.

The results presented in the following manuscript reveal that the variation of intrinsic aging rates has much more influence on the utilization of the battery pack than variations of capacity or impedance. The latter was linked to the fact that a parallel connection of cells reduced the variation between cell block parameters drastically.

Furthermore, different LLI and self-discharge rates led to rather small voltage drifts, which resulted in $<2\,\%$ less utilization in battery packs without balancing circuits compared to those employing dissipative balancing. Added together, the investigation of the influence of different self-discharge rates, changing entropy and half-cell OCVs on the voltage imbalance within cells connected in series revealed that although all mentioned influencing factors are able to contribute to the voltage imbalance, the reduction of the utilization that these influencing factors evoke is rather low.

Authors contribution Design of the simulation approach was performed by Ilya Zilberman. Implementation and execution of the Monte Carlo simulations was performed by Julius Schmidt. Sebastian Ludwig provided the impedance model. Simulation of the degradation modes was performed by Ilya Zilberman. Andreas Jossen supervised this work, the manuscript was written by Ilya Zilberman and was edited by all authors.

Simulation of Voltage Imbalance in Large Lithium-Ion Battery Packs Influenced by Cell-to-Cell Variations and Balancing Systems

Ilya Zilberman, Julius Schmitt, Sebastian Ludwig, Maik Naumann, Andreas Jossen

Journal of Energy Storage 32, 101828, 2020

Permanent weblink:
`https://doi.org/10.1016/j.est.2020.101828`

Journal of Energy Storage 32 (2020) 101828

Contents lists available at ScienceDirect

Journal of Energy Storage

journal homepage: www.elsevier.com/locate/est

Simulation of voltage imbalance in large lithium-ion battery packs influenced by cell-to-cell variations and balancing systems

I. Zilberman*, J. Schmitt, S. Ludwig, M. Naumann, A. Jossen

Institute for Electrical Energy Storage Technology, Technical University of Munich (TUM), Arcisstr. 21, 80333 Munich

ARTICLE INFO

Keywords:
Lithium-ion
Self-discharge
Voltage imbalance
Battery pack
Balancing
OCV

ABSTRACT

Due to manufacturing tolerances, lithium-ion cells usually suffer from varying capacities, impedances, self-discharge currents and intrinsic aging rates, which are often claimed to be the reason for the voltage imbalance and subsequently deteriorated utilization of the battery pack. However, the true influence of such cell-to-cell variations is still not completely understood. This work presents a lean battery pack modeling approach combined with a holistic Monte Carlo simulation. Using this method, the presented study statistically evaluates how experimentally determined parameters of commercial 18650 nickel-rich/SiC lithium-ion cells influence the voltage drift within a 168s20p battery pack throughout its lifetime. Major degradation mechanisms were represented through the manipulation of the half-cell potentials of the anode and the cathode. A low-DOD cycle profile was used for the aging. Additionally, cell impedance and reversible self-discharge were taken into account. The results obtained in this work reveal that the intrinsic variation of aging rates has the biggest influence on the pack utilization. Furthermore, initial variations of the capacity and impedance of state of the art lithium-ion cells play a rather minor role in the utilization of a battery pack, due to a decrease of the relative variance of cell blocks with cells connected in parallel. Although different self-discharge and aging rates evoked a voltage drift, the utilization of battery packs with and without dissipative balancing remained almost the same, assuming no cells with internal defects were present.

1. Introduction

The rising trend of the decentralized renewable energy production, as well as the growing market for electric vehicles (EVs) has created a demand for economically reasonable, persistent and reliable energy storage. Lithium-ion technology has shown high potential for many applications by overcoming such downsides as high costs, safety hazards and short system life during the last decade [1,2]. However, EV battery packs still remain the most expensive component in an electric vehicle, which makes their maximum utilization indispensable.

In order to reduce load currents and consequently ohmic losses within battery packs and charging infrastructure, system voltage is usually increased by connecting cells in series. State-of-the-art battery packs exhibit system voltages of up to 800V with almost 200 cell blocks in serial configuration [3], whereby the number of cells in parallel is determined by the capacity of the selected cell and power/energy demand of the application. As a consequence, a large number of cells increases the chance of having a negative production outlier in the battery pack, which might deteriorate the operation of the whole energy storage system.

Such outliers are linked to the finite accuracy during the manufacturing process, which leads to minimal differences in the electrode thickness, material compositions, overall component connectivity, etc. among lithium-ion cells produced of the same type [4]. These deviations become apparent in varying cell capacities, impedances and self-discharge rates. Although many studies have been carried out in order to quantify the initial cell-to-cell variations [5–7], it is still not completely understood how these intrinsic variations influence the operation of the battery pack throughout its lifetime.

In order to quantify intrinsic aging variation, Baumhoefer et al. simultaneously cycled 48 pristine lithium-ion cells with the same current load at 25 °C [8]. The results revealed that despite equal operational conditions for each cell, the relative capacity variance increased during the cycling aging. An increase in relative capacity variance was also observed in a calendar aging study, in which 24 pristine lithium-ion cells were stored at 70% SOC and 25 °C for almost a year [9]. Consequently, it can be expected that battery packs experience an aggravated aging behavior, even only due to intrinsic cell parameter variations, since, due to the negative outliers, a serial interconnection of cells or cell blocks usually results in the reduced pack capacity [10,11]. Such

---

* Corresponding author.
E-mail address: ilya.zilberman@tum.de (I. Zilberman).

https://doi.org/10.1016/j.est.2020.101828
Received 15 April 2020; Received in revised form 17 August 2020; Accepted 21 August 2020

behavior was also already observed via battery pack simulations including cell-to-cell variations in [12]. Further studies took extrinsic influence factors such as temperature gradients [13,14] and even balancing systems [15,16] into account, revealing that the presence of the former and the absence of the latter aggravated the available capacity of the battery pack. However, until now there has been no study that statistically evaluates the true origin of the reduced available pack capacity due to voltage imbalance during the course of aging by jointly taking into account measured cell parameter variations, different balancing approaches and temperature gradients.

The majority of the experimental and simulative studies regarding the influence of cell-to-cell variations and extrinsic system factors on the battery performance usually consider only a selective set of cell/system parameters or upper/lower limits of a cell parameter distribution [17,18]. Either way, the results represent only a snapshot of the battery performance given for one set of cell and system parameters. In order to get a statically relevant statement about the battery performance, a simulation or an experiment has to be repeated many times, due to a complex non-linear relationship between the cell parameters. This method, called Monte Carlo simulation, is usually used when the analytical calculation of the statistical result is not possible or at least is very demanding [19].

This work presents a holistic simulation framework, which enables a voltage drift among cells connected in series due to differing aging and self-discharge rates throughout its lifetime. Furthermore, by means of the presented approach shown in Fig. 1, this study investigates how cell and system parameters influence the voltage imbalance and the associated maximum utilization of a 168s20p battery pack. The battery pack model includes 168 separate cell block models, whereby each cell block is represented by an equivalent circuit (EC) model. Based on the measured parameter distributions of the capacity, impedance and reversible self-discharge, three unique battery packs are constructed. First battery pack does not have any cell balancing, second and third battery packs utilize dissipative and ideal balancing systems respectively. After the battery pack lifetime simulation, including the influence of the temperature gradients and balancing circuits, a pack utilization is determined, which is the quotient between the withdrawable energy of the simulated pack and a uniform pack at the end of life (EOL). A uniform pack is a simulated battery pack without temperature gradients, which consists of cells with identical cell parameters and aging rates. Subsequently, by repeating the pack simulation with new cell parameters in each run, the distribution of the pack utilization is derived, which depicts a statistical performance of the battery pack for a given cell parameter variation and system properties, as shown in Fig. 1.

This paper is structured as follows. First, the electrical cell model is described, which consists of the half-cell OCVs of the anode and the cathode, a temperature and SOC-dependent impedance and a temperature and SOC-dependent self-discharge current source. Afterwards, an aging case study, based on the manipulation of the half-cell potentials is presented, aiming to identify the relevant degradation mechanisms on the voltage drift. Subsequently, the simulation procedure is described, including the integration of cell parameter variations into the variability of the 168s20p battery pack. Finally, the results regarding the influence of the cell-to-cell variations, the balancing approach and the temperature gradients on the utilization of the battery pack are presented and discussed.

2. Model description

The object of this Monte Carlo study was a commercial NMC (nickel-rich)/SiC 18650 high energy lithium-ion cell INR18650-MJ1 (MJ1) from LGChem with a nominal capacity of 3.5A h and specific energy of 259.6 Whkg^{-1}. According to the cell manufacturer, the recommended operation window is between 4.2V and 2.5V. Due to the nature of the Monte Carlo approach, which relies on a quick battery pack lifetime simulation, equivalent circuit models were used. EC models have the advantage of the short computational time and fewer model parameters, while remaining almost as accurate as physico-chemical p2D-Newman models [20], in case no internal states of a lithium-ion cell are of interest and no high currents are applied. In the following, the electrical and aging parts of the model are described in detail.

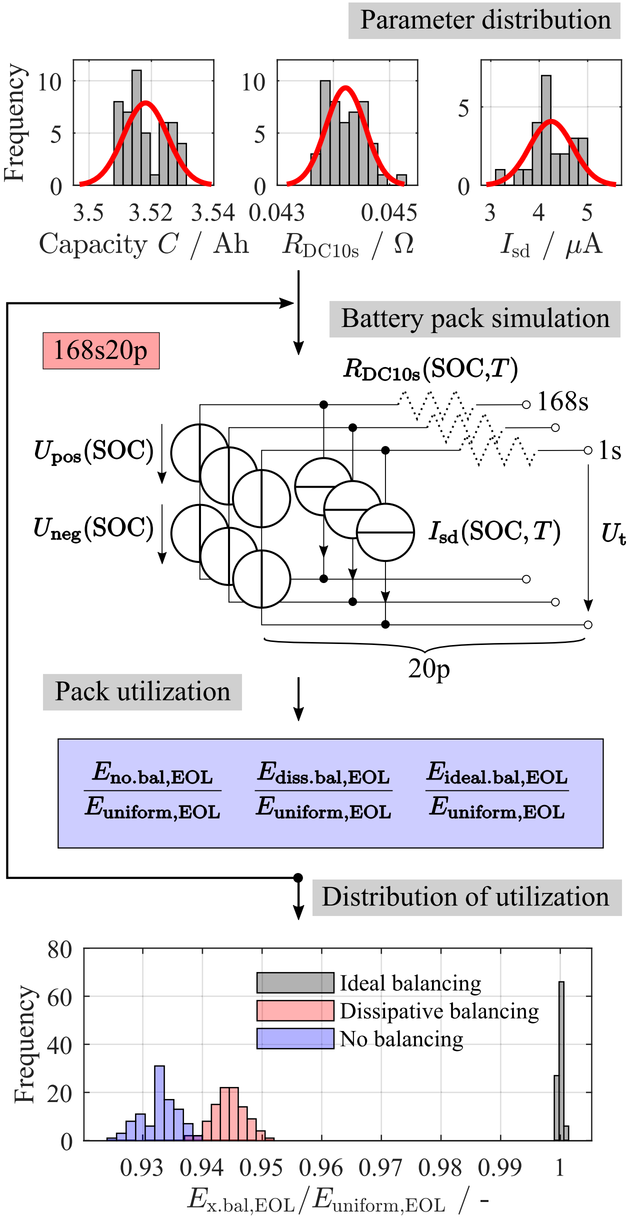

Fig. 1. Overview of the Monte Carlo simulation framework. First, based on the measured parameter distributions of the capacity, impedance and reversible self-discharge, three unique battery packs (no balancing, dissipative and ideal balancing) with 168 single EC cell block models connected in series are constructed. After consecutive lifetime simulations a distribution of the pack utilization with ideal and dissipative balancing and without balancing is derived.

2.1. OCV model

The equilibrium or open circuit voltage (OCV) of a lithium-ion cell is the difference between the potential of the positive and the negative electrode in their thermodynamic equilibrium state [21]. Those equilibrium potentials especially depend on the concentration of lithium-ions within electrodes and to a lesser extent on the temperature [21]. Furthermore, the OCV curve in the full-cell configuration, as a function

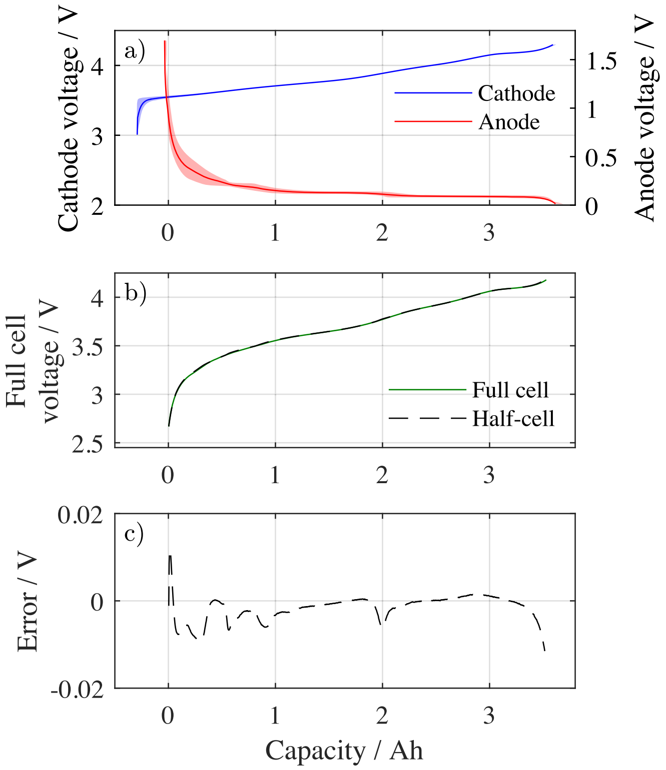

Fig. 2. (a) Charge, discharge and averaged half-cell potentials of the anode and cathode of the MJ1 (filled areas), (b) Averaged full-cell OCV and constructed full-cell OCV from half-cell data. (c) Difference between measured and constructed full-cell OCVs.

of lithium concentration or generally of the SOC, additionally depends on the stoichiometric properties of both electrodes, such as loading ratio and electrode balancing [22]. Additionally, it has been shown that insertion batteries suffer from a hysteresis effect of the OCV, depending on the charge or discharge direction [23], which has been linked to the fact that in a multiparticle electrode, the insertion does not proceed coherently in all particles [24]. Further effects, such as concentration gradients within the electrode due to prior charge or discharge, which might last for many hours, aggravate the determination of the OCV even more [25].

Major degradation mechanisms in lithium-ion cells have an influence on half-cell potentials and consequently on the full-cell OCV [26]. Therefore, the used EC model consists of two voltage sources, one for each electrode, as shown in Fig. 1. Sturm et al. performed an analysis of active materials and measured half-cell potentials for both electrodes of the MJ1 cell vs. lithium-metal in the charge and discharge direction at 25 °C [27]. The stoichiometric properties of both electrodes were derived from fitting the half-cell differential voltages with the full-cell differential voltage in the charge direction [27]. Fig. 2a depicts the results from half-cell measurements. Electrode balancing revealed an oversized cathode ($\sim$ 9.4%) and an almost complete use of the anode ($>$ 99%) [27]. Such extreme utilization of the anode facilitated the high energy density of the cell. While cathode charge and discharge curves showed only a minimal hysteresis behavior, the charge and discharge curves from the anode differed in their characteristics, especially at the lower SOC, as shown with the blue and red filled areas in Fig. 2a. Constructed OCV from half-cell data and obtained full-cell OCV according to Table 1 are in good accordance to each other as shown in Fig. 2b-c.

In general, the terminal voltage of a lithium-ion cell also depends on the temperature [28]. The exact relation between the OCV and the temperature is defined by the entropy. Although it has been shown that entropy exhibits a non-linear, hysteresis-like behavior [29], it can be neglected in this study since differences in terminal voltage before and after the same absolute temperature change amount only to several 100µV. However, as reported in [30,31] temperature still has a major influence on OCV determination, among others due to unavoidable interference of overpotentials with the measurement. Nevertheless, reversible heat effects due to reaction entropy are neglected in the model. The characterization of the overpotentials within the MJ1 cell is described in the following.

Table 1
Full cell OCV measurement sequence with constant current method. For the averaging of charge and discharge curves, the data from the CC phase is used.

ine Step	Parameters	Termination
1. Charge CCCV	I= 0.2C, U= 4.2V	$I <$ 0.001C
2. Pause		$t >$ 6h
3. Discharge CCCV	$-I$= 0.033C, U= 2.5V	$I >$ -0.001C
4. Pause		$t >$ 6h
5. Charge CCCV	I= 0.033C, U= 4.2V	$I <$ 0.001C

2.2. Impedance model

Due to the main reaction, the finite conductivity of the cell components and mass transport limitations of the electrolyte and active materials, lithium-ion cells are exposed to overpotentials during the operation [32]. The ionic conductivity of the electrolyte and the electronic conductivity of the electrode materials and current collectors cause an instant voltage drop in case of a current flow. Double-layer effects, in combination with charge transfer reaction and, subsequently, mass transport effects in solid and liquid phases evoke further overpotentials [33]. Additionally, the overall dynamic behavior depends on the SOC, temperature and age of a lithium-ion cell [34,35].

Generally, the dynamic response can be measured in the frequency domain via electrochemical impedance spectroscopy (EIS) [36,37] or in the time domain among others via the galvanostatic intermittent titration technique (GITT) [38,39]. For the particular operating point (SOC, temperature, etc.), the former approach provides a complex impedance spectrum and the latter provides a voltage response to a current step. Both outcomes are usually used for the parameter fitting of RC networks, which can be used for the representation of the dynamic behavior of the cell [40]. Since this work focuses on the long-term behavior of a battery pack, rather than on the short-term response, a simple resistor was used to model the overpotentials. Different current steps regarding the current intensity and direction were applied at 10 °C, 20 °C, 30 °C and 40 °C on three pristine MJ1 cells over the whole SOC range in the charge and discharge direction. For the sake of integrity, current pulses were applied after voltage equalization processes almost decayed, which was defined as the moment after which the slope of the terminal voltage was lower than 5 mVh^{-1}. Depending on the current intensity, pulses were applied for 10s or 20s, whereby a voltage rise or drop after 10s was evaluated for calculation of the R_{DC10s} value. Sturm et al. used 10s pulses for fitting of an EC model for the MJ1 cell consisting of internal resistance and RC element in series. The results revealed that voltage errors from CC charge and discharge below 0.5C did not exceed 20 mV [20]. The exact measurement sequence is summarized in Table 2. Fig. 3a shows averaged R_{DC10s} for different pulses, temperatures and SOCs. Especially due to slowed down reaction kinetics and diffusion, overpotentials increased with lower temperatures, as has already been reported in [41,42]. Also a high impedance increase towards lower SOCs was presented in the literature [35] and was linked to an increase of the cathode impedance [43]. In order to use the presented measurement results in the EC model, the measurement results were fitted with a polynomial function $R_{\mathrm{DC10s}}(\mathrm{SOC}, T)$, which is described in the Appendix A.

Table 2
Impedance measurement sequence using GITT method. Discharge pulses at step 3 and 7 are not applied after the initial discharge.

Step	Parameters	Termination
1. Discharge CCCV	$-I = 0.2$C, $U = 2.5$V	$I >$ -0.014C
2. Pause		$\mathrm{d}V/dt <$ 5 mVh^{-1}
3. Pulse	$-I = 0.5$C,	$t >$ 20s
4. Pause		$t >$ 1h
5. Pulse	$I = 0.5$C,	$t >$ 20s
6. Pause		$t >$ 1h
7. Pulse	$-I = 1$C,	$t >$ 10s
8. Pause		$t >$ 1h
9. Pulse	$I = 1$C,	$t >$ 10s
10. Pause		$t >$ 1h
11. Charge	$I = 0.2$C,	$Q > C_\mathrm{N}$ / 10
12. Goto 2		Count > 10

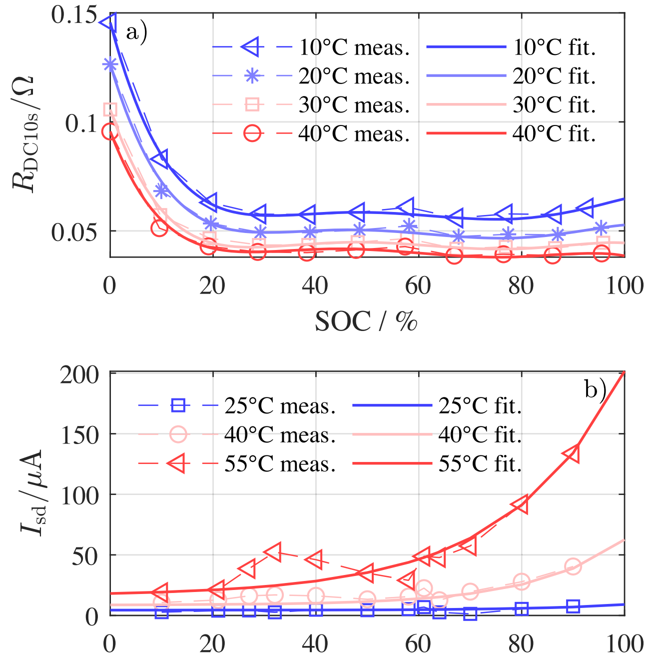

Fig. 3. (a) Measured self-discharge and fitting results of the presented self-discharge model, (b) measured R_{DC10s} values and fitting results of the presented impedance model.

2.3. Self-discharge model

In order to mimic the long-term behavior of the lithium-ion cell, self-discharge was modeled via a current sink in parallel to the voltage sources. Self-discharge current slowly discharges the cell, which consequently leads to a voltage decay, without any change in the cell's capacity. Therefore, variation of self-discharge rates within an in-series connection of cells might lead to a voltage imbalance. In our previous study, it was shown, that the reversible self-discharge of the MJ1 was most likely linked to coupled side reactions between the anode and the cathode [44]. In this study, self-discharge currents for 13 SOCs between 10% and 90% at 25 °C, 40 °C and 55 °C were determined via the voltage-based measurement method, which evaluated the voltage decay $\mathrm{d}U/\mathrm{d}t$ after all equalization processes were finished [44]. Combined with the derivative of the open circuit voltage (OCV) $\mathrm{d}Q/\mathrm{d}U$, which was determined by a small discharge pulse (0.033C), the self-discharge current was calculated as follows:

$$\frac{\mathrm{d}Q}{\mathrm{d}U}\cdot\frac{\mathrm{d}U}{\mathrm{d}t} = \frac{\mathrm{d}Q}{\mathrm{d}t} = \sum I_{\mathrm{sd}} \tag{1}$$

where $\sum I_{\mathrm{sd}}$ is the sum of all side reaction currents which have an influence on half-cell potentials of both electrodes. In our further study, a simple mathematical model for the self-discharge current was proposed [9]. The model is based on the exponential function with an offset and depends on the SOC (between 0 and 1) and temperature T in K [9]:

Table 3
Overview of fitting parameters for the Eq. (2), which results in a self-discharge current in ampere.

Parameter	Function
$a(T)$	$2.753\cdot10^{-141}\cdot T^{53.6}$
$b(T)$	$-\,4.275\cdot10^{-19}\cdot e^{0.1301T} + 6.015$
$c(T)$	$1.033\cdot10^{-39}\cdot T^{13.59}$

$$I_{\mathrm{sd}}(\mathrm{SOC},\,T) = a(T)\cdot e^{b(T)\cdot\mathrm{SOC}} + c(T) \tag{2}$$

Model parameters are summarized in Table 3. As shown in Fig. 3b, the fitted model is in good accordance with measurement results except for the SOC range between 20% and 50%. However, the model is considered to be sufficient for the Monte Carlo study.

2.4. OCV changes due to different degradation mechanisms

Over the lifetime of a battery pack, lithium-ion cells usually exhibit power fade and deteriorating energy storage ability [45,46], which are often linked to side reactions and a loss of active materials (LAM) on both electrodes [26,47]. In the following, a case study is presented that evaluates an influence of each separate degradation mechanism on the OCV and subsequently on a possible voltage drift within an in-series connection of cells. The influence of each degradation mechanism is evaluated by the change of the OCV at 100% SOC, which indicates whether all cells connected in series can be theoretically fully charged.

LAM is usually attributed to particle cracking and loss of electrical contact [26]. In that way, a part of the electrode's active mass is no longer available for the intercalation and deintercalation of lithium, which can be observed in compression of the half-cell potential [48]. Anodic side reactions, such as the growth and repair of the SEI, result in the loss of lithum inventory (LLI), which leads to a delithiation of the negative electrode and an associated shift of the anode half-cell potential, resulting in the capacity decrease [49]. Cathodic side reactions, such as electrolyte oxidation and transition-metal dissolution, provoke a reinsertion of lithium into the positive electrode that can be observed in the form of a potential decrease and might even lead to an increase of cell capacity [50]. The mechanism of lithium plating was omitted in this analysis, since it usually depicts an extreme case of the operation. However, it has to be stated that temperature differences within an in-series connection during plating might lead to voltage imbalance, due to different relaxation voltages after the stripping reaction [51,52].

A shift and compression of the half-cell potentials of both electrodes have been applied in the past in order to imitate LAM and LLI [22]. Using this approach, the influence of a particular degradation mechanism on voltage imbalance between two cells is discussed in the following, assuming both cells are connected in series.

Fig. 4 a depicts the effect of the anodic side reactions, which lead to the discharge of the anode. As a consequence thereof, a change in the electrode balancing occurs by shifting the anode half-cell potential of the aged cell to the right. In Fig. 4, the shift amounts to 0.2Ah, corresponding to approx. 6% of the initial cell capacity, which emphasizes a change between a pristine and an aged cell. Such high discrepancy in aging rates depicts the worst case scenario in the battery pack. The resulting OCVs of a new (gray) and aged cell (black) are shown in Fig. 4d. The red areas represent the cut-off voltages. The aged cell limits the capacity of 2s1p cell string at low SOC. Despite an almost flat half-cell potential of the anode, a shift of the negative electrode results in a small drop of the full cell voltage. Therefore, the newer cell limits the

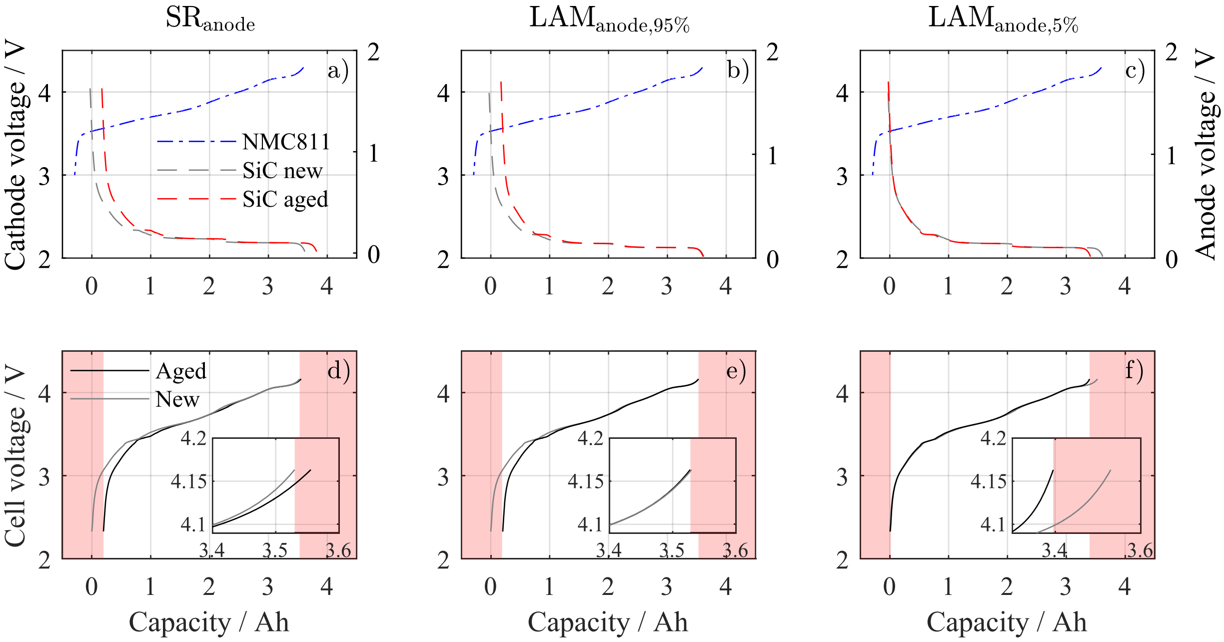

Fig. 4. Case study of the influence of the anode degradation effects on the voltage imbalance of two cells connected in series. (a)(d) Side reactions, LLI (b)(e) LAM at 95% SOC, (c)(f) LAM at 5% SOC.

capacity of 2s1p cell string at high SOC, resulting in a voltage imbalance between two cells with a 18 mV difference after 0.2Ah shift.

The SOC of the LAM-induced compression of the half-cell potential has a crucial role for the voltage imbalance of a cell string. Usually, a distinction is made between LAM at high and low SOCs. Fig. 4b depicts LAM of the anode at high SOC. The half-cell potential is compressed around 95% SOC with the resulting capacity reduction of the anode by 0.2Ah, which leads to a reduction of full cell capacity as shown in Fig. 4e. The aged cell limits the capacity of the 2s1p cell string at low SOC. However, at high SOC, there is almost no voltage imbalance between two cells.

Due to an unusual, almost full utilization of the anode, LAM at the low SOC also results in a capacity loss of the cell, as shown in Fig. 4c. In contrast to LAM at the high SOC, the OCV difference between an aged and new cell results in a voltage imbalance of −52 mV. In this scenario the aged cell limits the capacity of the 2s1p string at high SOC.

From Fig. 4d and f it can be seen that side reactions on the anode and LAM at the high SOC have an opposing effect on the voltage imbalance. Several studies have shown that both degradation mechanisms might occur simultaneously in cells with a pure graphite anode [53] and silicon-graphite blend anode [54,55]. Furthermore, LAM at low SOCs was made responsible for the degradation of the negative electrode due to high mechanical stress during lithiation [56,57]. However, the exact implication for the voltage imbalance is not clear yet, since there is no information about the share of each degradation mechanism on the overall aging. Nevertheless, LLI at the negative electrode is often claimed to be the dominant degradation mechanism [58–61]. Additionally, it can be assumed that temperature has a higher influence on the LLI [62], since it is an electrochemical process, than on LAM, which depends more on the mechanical properties. Furthermore, assuming that cells are not completely discharged during the operation, LAM at low SOCs is considered unlikely and therefore negligible.

Similar to the degradation mechanisms of the anode, the influence of the cathode aging on the voltage imbalance is discussed in the following. Fig. 5a shows the influence of cathodic side reactions on half-cell potential and subsequently on the full cell voltage. As shown in Fig. 5d, a 0.2Ah shift of the cathode half-cell potential evokes a drop of the cell voltage, resulting in the voltage imbalance of 61 mV. Due to the voltage drop of the aged cell, the new cell limits the available capacity of the 2s1p cell string at high SOC.

Owing to an oversized cathode, a LAM at the high SOC does not evoke any capacity loss, despite a slightly changed full-cell OCV, as shown in Fig. 5b for a compression by 0.2Ah. Small differences in OCVs at high SOC are considered being negligible.

Due to the compressed cathode half-cell potential in the combination with a flat anode curve, LAM at the low SOC at the cathode results in capacity loss as shown in Fig. 5c and f. The aged cell limits the capacity of the 2s1p cell string at high SOC and evokes a voltage imbalance of −68 mV.

Since such cathodic side reactions as electrolyte oxidation and transition metal dissolution evoke a voltage decay without any capacity loss [63,64], they are included in the self-discharge model per definition. However, transition metal dissolution might also lead to LAM, whereby it has been shown that increased NMC cathode potential accelerated the degradation of the electrode [65,66]. Furthermore, nickel-rich cathodes suffered from cycling at high potentials even more [67]. Therefore, it can be assumed that LAM at the high SOC is a dominant degradation mechanism at a positive electrode. However, since LAM at the high SOC does not provoke the voltage imbalance of a cell string, it won't be included in the aging model.

The analysis of the single degradation mechanisms at the positive and negative electrode showed that both side reactions and the LAM at low SOCs at the anode might be responsible for the voltage imbalance in cell strings. Assuming that the battery pack is not operated at low SOCs most of the time, solely LLI will be included in the aging model as the major degradation mechanism.

2.5. Aging model

LLI is implemented as a shift of the anode half-cell potential to the right, according to the Fig. 4a, which occurs after each load cycle. As a result, a new OCV curve, the actual capacity and the terminal voltage of each cell block are updated. Such approach was validated by Birkl et al. [26]. However, due to the lack of aging model validation for the MJ1 cell, no quantitative statements are aimed in this work. The calculation of the aforementioned shift is presented in the following.

Despite the passivation nature of the LLI, it is assumed that the aging rate remains constant over the course of aging. The temperature

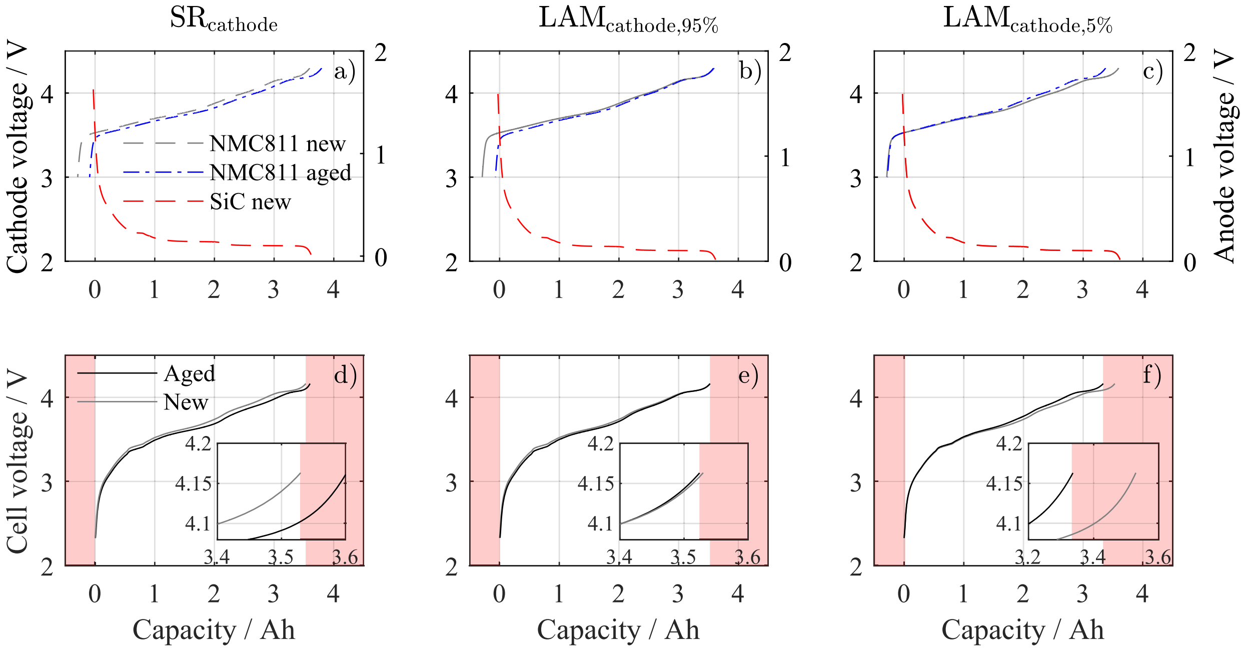

Fig. 5. Case study of the influence of the cathode degradation effects on the voltage imbalance of two cells connected in series. (a)(d) Side reactions, (b)(e) LAM at 95% SOC, (c)(f) LAM at 5% SOC.

dependency of the side-reaction is modeled with an Arrhenius-like relation. The amount of LLI lost during one cycle Q_{LLI} is therefore modeled with an exponential dependency on the cell block temperature T and is calculated by Eq. (3).

$$Q_{\mathrm{LLI}} = \frac{e^{\beta \cdot T}}{\alpha} \cdot \frac{Q_{\mathrm{LLI,EOL}}}{N_{\mathrm{EOL}}} \tag{3}$$

Here, β equals $0.06931\mathrm{K}^{-1}$ which is the exponential factor that leads to a doubling of the reaction rate for a 10K temperature increase, compared to the reaction rate at the reference temperature of 25 °C. Further, $\alpha = e^{\beta \cdot 298.15\mathrm{K}}$ is the Arrhenius factor at the reference temperature. The amount of LLI at the EOL $Q_{\mathrm{LLI,EOL}}$ is chosen in the way that a cell at the reference temperature 25 °C reaches a remaining capacity of 80% of the initial capacity after 400 full cycles, which is specified in the MJ1 datasheet. In the chosen scenario, $Q_{\mathrm{LLI,EOL}}$ equals 21.548%, which evokes a loss of the initial capacity C_{init} by 20% and N_{EOL} is the number of partial cycles until the EOL. Therefore, assuming a constant usage of the battery pack during the operation life, $Q_{\mathrm{LLI,EOL}}$ is closely linked to a capacity loss per amount of time. For the sake of simplicity, no dependency of the DOD on the aging is assumed. The new full-cell OCV curve is calculated as the difference between the cathode half-cell OCV and the shifted anode half-cell OCV, with the respective full cell voltage limits, amounting to 2.5V and 4.2V.

In order to evaluate the progression of the available energy as stated in the introduction, an inclusion of the impedance is crucial. Several studies have shown that there is an almost linear correlation between capacity loss and impedance increase during cycle aging [68,69]. In our previous study, the cycle aging of an MJ1 cell at different temperatures between 25 °C and 30 °C also revealed a strong linear correlation between the capacity loss and impedance increase [70]. In order to model this impedance increase, the impedance R_{DC10s} is multiplied by an aging factor γ which is calculated by Eq. (4), where C_{init} is the initial capacity, C_{act} the actual block capacity and ζ an empirically derived correlation parameter that amounts to approx. 1.5 [70]. This number implies that impedance increases by 30% in case of 20% capacity loss.

$$\gamma_i = \zeta \cdot \frac{C_{\mathrm{init}} - C_{\mathrm{act}}}{C_{\mathrm{init}}} \tag{4}$$

2.6. Cell block parameter distribution

In order to comply with the energy/power demand of the application and in order to increase the reliability of the overall battery pack, lithium-ion cells are usually connected in parallel. Due to slightly different OCV characteristics, cell capacities and impedances, short-term and long-term load deviations along the parallel connection might occur, as reported in [71,72]. Even cell connectors and their placing in regard to the load point play an important role in current distribution among the cells in parallel [73]. In the literature, there are contradictory statements regarding whether such load deviations enable a convergence of the cell parameters [5,74] and therefore homogeneous aging of cells within the cell block or whether the deviations facilitate the parameter drift [14]. However, assuming that the load current is rather smooth and there is no temperature gradient along the parallel connection and there are no manufacturing outliers, homogeneous aging among cells in parallel is further considered. Therefore, within the scope of this Monte Carlo study, a cell block is modelled as a large lithium-ion cell. However, in order to consider cell-to-cell variations on the cell block level, the relationship between the initial parameter variations of single cells and initial parameter variations of cell blocks is derived in the following.

Rumpf et al. statistically analyzed the initial cell parameter distribution of 1100 mass-produced lithium-ion cells [75]. The results revealed that cell parameters were normally distributed, which is a sign for a random and not for a systematic deviation during the cell manufacturing. Therefore, the initial variations of the capacity, impedance and self-discharge of 24 pristine MJ1 cells presented in our previous work [9] and shown in Fig. 1, were fitted with a normal distribution. The mean values μ and the standard deviations σ are summarized in Table 4.

Table 4
Fitted μ and σ values of the measured capacity, impedance and self-discharge rates of 24 pristine MJ1 cells [9].

Parameter	C / Ah	R_{DC10s} / Ω	I_{sd} /µA
μ	3.518	0.0442	4.248
σ	0.007	3.49E-04	0.447
σ/μ	0.2%	0.79%	10.52%

Since the proposed OCV model is based on charge-controlled voltage sources, the overall charge, which is stored in a parallel connection, is the sum of charges stored in cells in parallel. Consequently, due to the Kirchhoff mesh rule, which implies that the voltage in a parallel connection is equal, the overall capacity of the parallel connection is the sum of single cell capacities. Assuming that the cell capacities are normally distributed and independent random variables, cell block capacity consisting of p cells in parallel amounts to [76]:

$$C_{\text{block}} = \sum_{i=1}^{p} C_{\text{cell,i}} \sim \mathcal{N}\Big(\underbrace{p\cdot\mu_{C_{\text{cell}}}}_{\mu_{C_{\text{block}}}}, \underbrace{\sqrt{p}\cdot\sigma_{C_{\text{cell}}}}_{\sigma_{C_{\text{block}}}}\Big), \tag{5}$$

In our previous study, investigated MJ1 cells showed a negative moderate correlation between the distribution of the capacity and the impedance, which implied a lower impedance with a higher capacity [9]. This result was linked to the fact that impedance was measured with a 1C pulse, whereby C referred to 3.35Ah and not to the actual capacity of the cell. Assuming that the cell capacity variation is linked to the accessibility of the active material, the same discharge pulse created a higher current density in a cell with less active material and thus a cell with the smaller capacity seemed to exhibit a higher impedance. Similar results were presented in [75]. Therefore, a linear correlation between the initial cell block impedance and cell block capacity was considered in the Monte Carlo simulation, which produced a similar impedance distribution, as in Table 4:

$$R_{\text{DC10s,block}} = \left(-0.0325\cdot\frac{C_{\text{block}}}{p} + 0.1586\right)\cdot\frac{1}{p}\,\frac{\Omega}{\text{Ah}} \tag{6}$$

The distribution of the self-discharge did not show any correlation with either the capacity or the impedance and is thus assumed to be independent. Therefore, the resulting self-discharge currents of cell blocks can be calculated in a similar way to cell block capacities. According to the proposed EC model, the parallel connection of cells leads to a parallel connection of different current and voltage sources. Since the voltage in a parallel connection is always the same, it can be represented by a single voltage source. Applying the junction law of Kirchhoff, the entire self-discharge current of a cell-block is the sum of self-discharge currents of cells in parallel. Assuming that self-discharge rates are normally distributed and are independent random variables, self-discharge rates of cell-blocks consisting of p cells in parallel amount to [76]:

$$I_{\text{sd,block}} = \sum_{i=1}^{p} I_{\text{sd,cell,i}} \sim \mathcal{N}\Big(\underbrace{p\cdot\mu_{I_{\text{sd,cell}}}}_{\mu_{I_{\text{sd,block}}}}, \underbrace{\sqrt{p}\cdot\sigma_{I_{\text{sd,cell}}}}_{\sigma_{I_{\text{sd,block}}}}\Big), \tag{7}$$

Overall, a parallel connection of lithium-ion cells reduces the initial relative cell block parameter variance σ/μ by the factor of $1/\sqrt{p}$, which confirms the results from Fill et al. [77]. However, in addition to initial cell parameter variations, lithium-ion cells also suffer from the intrinsic cycle and calendar aging differences. In general, it implies that the relative variance of the final distribution of the capacity and impedance at the EOL is higher than the initial one. The empirically derived factor between the initial and final relative variance of the cell capacity, based on the study from Baumhoefer et al. [8] and Schuster et al. [7], amounted to 6.8 and 4.2, respectively. Based on this range, the factor used in this study was set to 5. This factor implies that due to intrinsic variation of aging rates, the final relative variance of the capacity is five times higher than the initial one. This relation was implemented with a random factor Γ_{LLI}, which was assigned to each cell block and multiplied with $p\cdot Q_{\text{LLI}}$ (Eq. (3)), resulting in intrinsically varying aging. Γ_{LLI} is a random number from a normal distribution with a mean value amounting to 1 and standard deviation amounting to 0.04. The standard deviation was chosen in the way, the cells would intrinsically reach a five times higher relative variance of the capacity at the EOL.

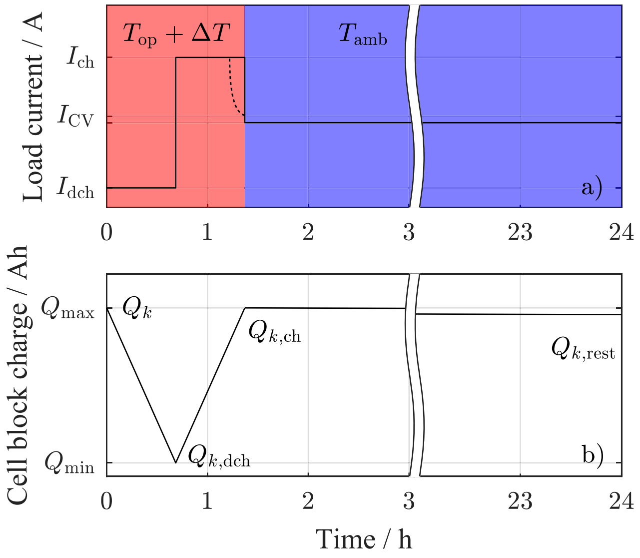

Fig. 6. (a) Simplified load profile including the temperature progression, (b) schematic progression of the cell block charge within one cycle.

3. Simulation of the battery pack

3.1. Generic load and temperature profile

The generic load profile for the simulation consists of three phases and is shown in Fig. 6a. The profile depicts a simplified one day load cycle of an EV. The first two phases are the operation phases, in which the battery pack undergoes a discharge and a subsequent charge. Usually, the actual charge and discharge currents, as well as the voltage limits are set by the application. In this study, the battery pack is discharged by 13.7% of the initial capacity of the reference pack ($C_{\text{ref,init}}$) with 0.2C. This cycle depth is chosen to resemble a typical trip of an EV with the average travel distance of 38km per day, taking about one hour in total [78].

In order to maximize the energy content of the battery pack, often a constant voltage (CV) phase is added after a constant current (CC) charge. By keeping the cell block voltage at its maximum value, the current decreases until the current cut-off criterion is reached. Such a charging protocol reduces the influence of the internal resistance of the cell. The CV phase is considered in the simulation with the cut-off current of 1A, which corresponds to recommended 50mA on the cell level according to the MJ1 datasheet.

In the third phase, the battery pack rests for a certain amount of time until the overall duration of the cycle is 24 h. The simulation is run for 400 equivalent full cycles, which is the expected lifetime of the cell. For the chosen DOD per cycle, it implies that the simulation is run for 2920 partial cycles (N_{EOL}), which results in 8 years of operation until reaching the 80% of the initial capacity.

The temperature within a single cell block is assumed to be homogeneously distributed at all times. However, due to the spatial location of each cell block in the battery pack, it is almost impossible to provide the same cooling power and thermal condition to each cell block [79,80], which usually leads to temperature gradients during the operation [81,82]. Therefore, in addition to the operation temperature T_{op}, a linear temperature gradient within the battery pack was implemented. Starting with the temperature T_{op} of the first cell block, the temperature linearly increases until it reaches its maximum at the last cell block. Such temperature distribution is rather unusual for a battery pack with 168 cell blocks in series. However, since the goal of the modeled temperature gradient is to provide different aging conditions for in series connection of cell blocks and not to reflect geometrical

Table 5
Overview of the simulation profile parameters. Monte Carlo simulations were performed with and without temperature gradient.

Step	Parameters	Termination
1. Discharge CC	$-I = 0.2\text{C}$, $T_{\text{op}} = 25\ ^{\circ}\text{C}$, $\Delta T = 0\text{K}/5\text{K}$	DOD $>$ 13.7% $C_{\text{ref,init}}$
2. Charge CCCV	$I = 0.2\text{C}$, $U = 4.2\text{V}$, $T_{\text{op}} = 25\ ^{\circ}\text{C}$, $\Delta T = 0\text{K}/5\text{K}$	$I <$ 1A
4. Pause	$T_{\text{amb}} = 10\ ^{\circ}\text{C}$, $\Delta T = 0\text{K}$	$t_{\text{cycle}} >$ 24h

properties of the battery pack, such simplified temperature distribution seems to be acceptable. The temperature of the cell blocks connected in series is given by Eq. (8), where T_i is the temperature of the cell block number i, ΔT is the difference between the highest and the lowest temperature in the battery pack during the operation phase and s is the overall number of in-series connected cell blocks.

$$T_i = T_{\text{op}} + \frac{i-1}{s-1} \cdot \Delta T \tag{8}$$

During the resting phase, the pack exhibits the ambient temperature T_{amb} without any temperature difference between the cell blocks. The temperature transition between both cycle phases is assumed to be immediate, as shown in Fig. 6a. The simulation profile parameters are summarized in Table 5.

3.2. Simplified cycling model and balancing techniques

Due to the nature of the used load profile without many changes in the load current, the cycle simulation was optimized in terms of speed, which was favorable for the Monte Carlo approach with many lifetime runs. Instead of using infinitesimal simulation time steps, the internal state of each cell block, which is the charge Q_k, was calculated only at the end-of-discharge, the end-of-charge and at the end of the resting phase, as shown in a simplified progression of the cell block charges within one cycle in Fig. 6b. The idea behind this simplified simulation approach was to pre-calculate the maximum and minimum charges Q_{dch} and Q_{ch}, which can be withdrawn after the discharge and be stored after the charge in each cell block based on the actual capacity, OCV, impedance, load current, self-discharge and the state of charge. Subsequently, by identifying the limiting cell blocks in the pack, the charge $Q_{\text{pack,dch}}$ and $Q_{\text{pack,ch}}$, which can be withdrawn after the discharge and be stored after the charge in the pack was determined. This procedure is described in more detail in the following.

Due to the relatively small DOD of the used load profile, the discharging phase is never limited by the lower cut-off voltage and therefore, besides the last cycle, the withdrawable charge $Q_{\text{dch}} = C_{\text{init}} \cdot \text{DOD}$ remains constant during the entire simulation. In the case of a full discharge, which was applied only during the last cycle of the lifetime simulation in order to compare the withdrawable energies, the withdrawable charge for each cell block was calculated according to:

$$Q_{\text{dch}} = Q_k - Q_{\min} - Q_{\text{sd}} \tag{9}$$

where Q_k is the charge in each cell block before the cycle according to Fig. 6b, Q_{sd} is the amount of charge loss due to self-discharge during the discharging step and $Q_{\min}$ is the minimum charge in the cell block according to the actual cell block OCV ($U_{\text{pos,act}} - U_{\text{neg,act}}$), impedance and the negative discharge current I_{dch}. At the first cycle, Q_k depicts the capacity of the cell block. $Q_{\min}$, which is the minimum possible charge in each cell block with respect to the lower cut-off voltage and the voltage drop caused by the discharge current, is calculated as follows:

$$Q_{\min} := Q \;\middle|\; U_{\text{pos,act}}\left(\frac{Q}{C_{\text{act}}}\right) - U_{\text{neg,act}}\left(\frac{Q}{C_{\text{act}}}\right) + I_{\text{dch}} \cdot R_{\text{act}}\left(\frac{Q}{C_{\text{act}}}, T\right) = 2.5\text{V} \tag{10}$$

After the discharge step, the storable charge for each cell block is calculated as follows:

$$Q_{\text{ch}} = Q_{\max} - Q_{k,\text{dch}} + Q_{\text{sd}} \tag{11}$$

where $Q_{k,\text{dch}}$ depicts the charge in each cell block before the charging step, Q_{sd} is the amount of charge loss due to the self discharge during the charging step and $Q_{\max}$ is the maximum charge according to the actual cell block OCV ($U_{\text{pos,act}} - U_{\text{neg,act}}$), impedance and the positive termination current of the CV phase I_{CV}. $Q_{\max}$ is calculated as follows:

$$Q_{\max} := Q \;\middle|\; U_{\text{pos,act}}\left(\frac{Q}{C_{\text{act}}}\right) - U_{\text{neg,act}}\left(\frac{Q}{C_{\text{act}}}\right) + I_{\text{CV}} \cdot R_{\text{act}}\left(\frac{Q}{C_{\text{act}}}, T\right) = 4.2\text{V} \tag{12}$$

The actual amount of charge during the discharging and charging step for each cell block depends on the application of the balancing systems. Balancing circuits are usually used in order to counteract the voltage drift in battery packs. The distinction is made between dissipative and non-dissipative (ideal) balancing systems and battery packs without any voltage equalization. In this study, all three options are considered and integrated into the simulation by manipulating the actual charges $Q_{\text{pack,dch}}$ and $Q_{\text{pack,ch}}$ in the discharging and charging steps according to Table 6.

In case of no balancing, both the charge and the discharge are limited by the upper and the lower cut-off voltages of the limiting cell block. Therefore, only the smallest of the calculated possible charges Q_{ch} and Q_{dch} can be applied to the battery pack. Dissipative balancing systems are able to equalize the voltage by dissipating the excessive charge. Hardware realization of the dissipative balancing is usually a parallel resistor and an active switch [83]. The goal of the dissipative balancing is to allow each cell block to exhibit the same voltage at the end of the charging procedure. Cell blocks that exhibit a higher voltage are discharged. Therefore, dissipative balancing theoretically allows every cell block to reach its end-of-charge voltage, as listed in Table 6. However, the discharge is still limited by the cell, which reaches the lower cut-off voltage first. Non-dissipative (ideal) balancing systems are usually more complex and consist of power electronics and control networks. In contrast to dissipative circuits, different topologies, such as cell-to-cell, cell-to-stack or stack-to-cell configurations have high energy transfer efficiencies in common [84]. Such balancing systems also perform voltage equalization during the discharge, allowing all cell blocks to reach the same end-of-discharge voltage, as reflected by the $Q_{\text{pack,ch}}$ and $Q_{\text{pack,dch}}$ in Table 6.

With the manipulated charges during the charging and the discharging phase for each battery pack without balancing and with dissipative/ideal balancing, the simulation steps for the cycle in accordance with Fig. 6b are listed in the following:

$$Q_{k,\text{dch}} = Q_k - Q_{\text{pack,dch}} - Q_{\text{sd,dch}} \tag{13}$$

$$Q_{k,\text{ch}} = Q_{k,\text{dch}} + Q_{\text{pack,ch}} - Q_{\text{sd,ch}} \tag{14}$$

$$Q_{k,\text{rest}} = Q_{k,\text{ch}} - Q_{\text{sd,rest}} \tag{15}$$

$$Q_{k+1} = f_{\text{LLI}}(Q_{k,\text{rest}}, T_i) \tag{16}$$

The individual self-discharge charges $Q_{\text{sd,dch}}$, $Q_{\text{sd,ch}}$ and $Q_{\text{sd,rest}}$ are calculated according to the cell block SOC, temperature and the duration of the cycle phase. Based on the actual charge after the resting

Table 6
Influence of the ideal balancing systems on the charging and discharging charges. Discharging charges are only valid during the last full discharge at the end of life.

Balancing system	$Q_{\text{pack,ch}}$	$Q_{\text{pack,dch}}$
No balancing	$\min(Q_{\text{ch}})$	$\min(Q_{\text{dch}})$
Dissipative	Q_{ch}	$\min(Q_{\text{dch}})$
Ideal	Q_{ch}	Q_{dch}

Table 7
Variation of relative parameter variances for the Monte Carlo simulation.

Scaling factor	0	0.5	1	1.5	2
Capacity σ_C/μ_C	0	0.001	0.002	0.003	0.004
Self-discharge $\sigma_{I_{SD}}/\mu_{I_{SD}}$	0	0.05	0.1	0.15	0.2
Aging rate σ_{LLI}/μ_{LLI}	0	0.0075	0.0150	0.0225	0.0300

phase $Q_{k,\text{rest}}$ and the cell block temperature during operation T_i, new actual charge before the next cycle Q_{k+1} is calculated according to the aging model.

3.3. Simulation parameters

In order to separate the possible influence of the cell parameters on the simulation results, the relative variance of the capacity, self-discharge and LLI was changed individually in the simulation. Based on the statistical data from Table 4, the parameters were scaled by the factor of 0, 0.5, 1, 1.5 and 2 of the initial value and are listed in Table 7. Only one scaling factor was changed at a time, while other parameters were scaled by the factor of 1. The energy content of the battery pack with the varying cell parameters was compared with the discharge energy of the battery pack with uniform cell parameter distribution at the EOL, $E_{\text{act}}/E_{\text{uniform}}$. Additionally, ΔU_{EOL} the voltage difference between the maximum and minimum voltage in the battery pack after the last charge was evaluated. The outcome of each Monte Carlo simulation depicted the distributions of both measures.

The number of simulation runs per one set of parameters was set to 207, which allowed for an absolute error of the normalized mean value of approx. 2‰. The absolute error e with the confidence level γ of the mean value of a normal distributed quantity is

$$e = \frac{z_{(1+\gamma)/2}\cdot\sigma}{\sqrt{n}} \tag{17}$$

where $z_{(1+\gamma)/2}$ is the $((1+\gamma)/2)$-quantile of the standard normal distribution and n the number of samples [85]. The maximum observed standard deviation of the pack energy at the EOL in this study amounted to σ= 484W h. Therefore, by setting the confidence level to $z_{(1+\gamma)/2} = 1.96$ (2σ), the absolute error of the resulting mean value yielded an upper bound of $e = 65.8$W h, which, in combination with the smallest observed value for E_{uniform} amounting to 31656W h, resulted in the aforementioned absolute error of the normalized mean value.

4. Results and discussion

In the following, the results of the Monte Carlo simulation are presented and discussed. Fig. 7 shows the results from the parameter study without the temperature gradient. Since the outcome of each Monte Carlo simulation is a distribution, the mean values are depicted as a solid line Fig. 7, whereas filled areas reflect $+ -1\sigma$, which represents 68.2% of the whole distribution. As shown in Fig. 7a, even the doubling of the relative variance of the capacity has no noticable influence on the energy content. Due to the high amount of cells in parallel, the relative capacity and impedance variance of cell blocks is negligible. These results suggest that cell matching before the pack assembly for the investigated 168s20p pack is not necessary, leaving out the possible influence on the parallel connection of cells. Whereas the ideal balancing performs exactly the same as battery packs with uniform parameter distribution, battery packs with and without dissipative balancing reach 97.8% and 97.3% of the ideal discharge energy at the EOL, respectively. Such high utilization values are due to the absence of the temperature gradients, which imply a homogeneous aging and low absolute self-discharge currents, resulting in the voltage drift below 20 mV, shown in Fig. 7d.

As depicted in Fig. 7b, the battery pack without balancing performs as well as the one with dissipative balancing in case of no self-discharge variation. However, an increase in relative variance of the self-discharge deteriorates the overall discharge energy of the battery pack without balancing, reaching 96.8% for doubling the relative variance. Since the dissipative balancing is theoretically able to equalize any voltage drift, which is shown in Fig. 7e and amounts to 32 mV in the worst case without balancing, different self-discharge rates have no effect on the battery pack with dissipative balancing. On the other hand, different capacities cannot be utilized with dissipative balancing, since the limiting cell block confines the available capacity of the pack during the discharge. This relation is also highlighted in the Fig. 7c, which shows that in case all cells exhibit uniform aging with no variation of LLI, dissipative balancing performs as well as the ideal balancing, since there are no different capacities that can be left unutilized. However, increasing the variation of aging deteriorates the performance of both packs with and without dissipative balancing. Due to almost no influence on the voltage drift (Fig. 7f), caused by low intrinsic aging differences and low absolute value of the self-discharge, the battery pack without balancing performs almost as well as the one with dissipative balancing.

The minor influence of the capacity and impedance variations on the pack utilization without temperature gradients is only valid under the assumption that a parallel connection within a cell block behaves as a large-format lithium-ion cell. Despite the fact that large electrodes can be treated as a parallel connection [86], due to spatial properties, large-format cells usually suffer from larger internal temperature gradients [87,88], which might lead to inhomogeneous aging within the electrode [27]. However, it stands to reason that initial variations of the impedance and the capacity play a rather minor part in the final utilization of the battery pack. On the other hand, the variation of the intrinsic aging rates revealed the largest influence on the pack utilization. Despite the fact that in battery packs without temperature gradients, the voltage drift was solely caused by the different self-discharge rates, the absolute value of the drift remained low. Therefore, no major difference between the packs with and without dissipative balancing was observed.

Fig. 8 depicts the results of the Monte Carlo simulation with the same intrinsic cell-to-cell variation parameters, but with an additional 5K temperature gradient along the in-series connection of cell blocks. Similar to previous results, any change in the relative capacity variance has no effect on the available pack energy at the EOL, as shown in Fig. 8a. However, the presence of the temperature gradient deteriorates the energy utilization severely for battery packs with and without dissipative balancing and amounts to 93% and 91.9%, respectively. The actual utilization is directly linked to the implemented temperature dependancy of the aging rate and therefore has to be treated with caution. However, despite the presence of the temperature gradient, the difference in the utilization of the battery pack with and without balancing amounts to approx. 1%. Such little difference is especially linked to the fact that even in the presence of the temperature gradient, the voltage drift only increased to 24.5 mV. The battery pack without balancing reveals decreased utilization with increasing relative self-discharge variance, whereas the pack with dissipative balancing is not influenced, as shown in Fig. 8b. Fig. 8e depicts the increasing voltage drift with the increasing variation of self-discharge rates. In case of no variation, the voltage drift is caused solely by different aging rates and amounts to 16.7 mV, which is in the same magnitude as the voltage drift evoked by different self-discharge rates. Therefore it stands to reason that self-discharge rates are not solely responsible for the voltage imbalance in battery packs, as already discussed in [9]. Furthermore, in case of an increasing variation of the LLI (Fig. 8c), both battery packs with and without dissipative balancing experience deteriorated utilization, amounting to 90% and 89%, respectively, with increasing variance in the pack performance. The deteriorated utilization was linked to the limiting cell during the discharge rather than the voltage drift,

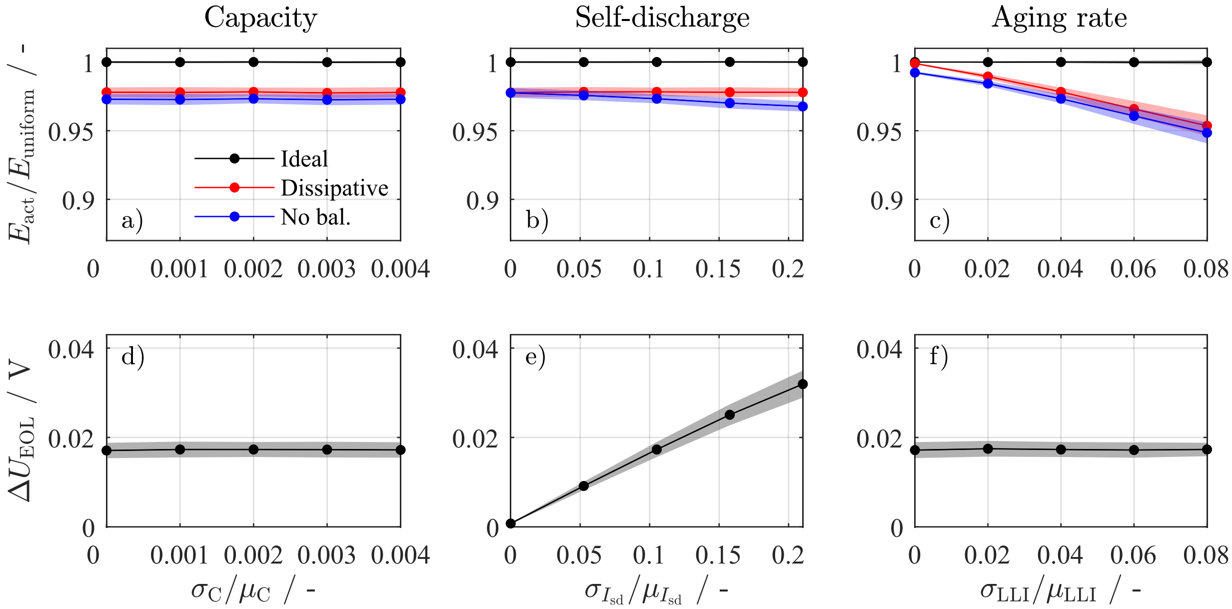

Fig. 7. Monte Carlo results for battery packs without temperature gradients and with different balancing approaches (ΔT= 0K, T_{op}= 25 °C, T_{op}= 10 °C). (a)(d) The utilization of the pack and the maximum voltage drift at the EOL for different capacity variations, (b)(e) the utilization of the pack and the maximum voltage drift at the EOL for different self-discharge variations, (c)(f) the utilization of the pack and the maximum voltage drift at the EOL for different LLI variations.

which remained constant at 25 mV.

Despite the fact that the ideal balancing was able to utilize the available cell block capacities in all simulation scenarios, real non-dissipative balancing circuits exhibit energy transfer efficiencies lower than 100%. Depending on the circuit topology and the position of the cell blocks, the overall energy transfer efficiency might drastically fall, making this technique not applicable for commercial applications. Moreover, for the investigated battery pack with and without dissipative balancing it can be concluded that initial cell parameter variations of the MJ1 cell have a minor influence on the final utilization of the pack. In general, temperature gradients within battery packs should be avoided; however, since the influence of the temperature highly depends on the aging model, no quantitative statements are possible. Nevertheless, intrinsic variation of aging rates could be identified as a major influence factor on the pack utilization, which confirms the experimental results from Schuster et al. [7]. Although different self-discharge and aging rates evoked voltage drift, due to low absolute value, the performance of packs with and without balancing differed by a maximum of 1%. Therefore, it stands to reason that some energy storage applications might operate without balancing circuits, as long as load profiles remain moderate and cell blocks do not exhibit any extreme degradation behavior. For instance, full-DOD cycles, which were not used in this study, could lead to a non-linear aging behavior and therefore increase possible voltage drifts.

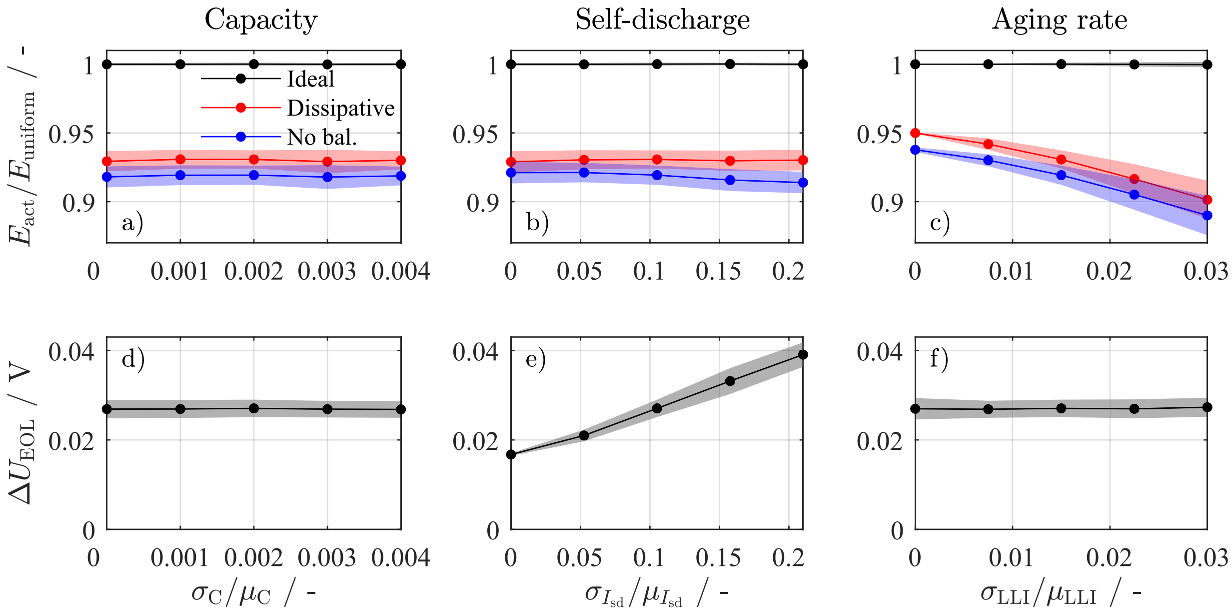

Fig. 8. Monte Carlo results for battery packs with temperature gradients and with different balancing approaches (ΔT= 5K, T_{op}= 25 °C, T_{op}= 10 °C). (a)(d) The utilization of the pack and the maximum voltage drift at the EOL for different capacity variations, (b)(e) the utilization of the pack and the maximum voltage drift at the EOL for different self-discharge variations, (c)(f) the utilization of the pack and the maximum voltage drift at the EOL for different LLI variations.

5. Summary and conclusion

In this work, the influence of the balancing circuits and cell-to-cell variations of the MJ1 lithium-ion cell on the utilization of a 168s20p battery pack was investigated via Monte Carlo simulation. The MJ1 cell was represented using an EC model with two voltage sources reflecting the OCVs of the anode and the cathode, an impedance R_{DC10s} and a self-discharge current source. The EC cell model was scaled up to a cell block representing the parallel connection of cells. The battery pack model consisted of 168 cell blocks connected in series. Based on the measured cell parameter distributions of the capacity, impedance and the self-discharge, a new battery pack was constructed each time before a lifetime simulation. For each parameter set, 207 lifetime simulations were conducted, which resulted in distributions of pack utilization and possible voltage drift, providing a statistically relevant statement about the pack performance. The main findings, which are limited to systems with low-DOD cycling and linear aging of cell blocks are summarized in the following:

1. Intrinsic aging variations depict a major influence on the utilization of the battery pack. An extension of cell testing with a suitable technology for classification of the intrinsic aging behavior would be highly beneficial for battery pack manufacturers.
2. Initial variations of the cell capacity and impedance play a rather minor role in the utilization of a battery pack, due to a decrease of the relative variance of cell blocks with cells connected in parallel. Therefore, cell matching for similar battery packs seems to be dispensable, assuming only a minor influence of possible temperature gradients along the parallel connection of cells.
3. Different self-discharge rates, as well as different aging rates contribute to the voltage drift within the in-series connection of cells. However, due to low absolute values, there is no major difference in the utilization of battery packs with and without balancing.

CRediT authorship contribution statement

I. Zilberman: Writing - original draft, Validation, Writing - review & editing. **J. Schmitt:** Writing - review & editing, Visualization. **S. Ludwig:** Methodology. **M. Naumann:** Writing - review & editing. **A. Jossen:** Writing - original draft.

Declaration of Competing Interest

The authors declare that they have no known competing financial interests or personal relationships that could have appeared to influence the work reported in this paper.

Acknowledgements

This work has received funding from the European Unions Horizon 2020 research and innovation program under the grant ”Electric Vehicle Enhanced Range, Lifetime And Safety Through INGenious battery management” (EVERLASTING 713771).

Appendix A. Fitting of the impedance model

The measurement results from Fig. 3b were fitted with the following polynomial surface using linear least squares method.

$$\begin{aligned}R_{\mathrm{DC10s}}(\mathrm{SOC},T) = {} & p_{00} + p_{10}\cdot\mathrm{SOC} + p_{01}\cdot T + p_{20}\cdot\mathrm{SOC}^2 + p_{11}\cdot\mathrm{SOC}\cdot T\\ & + p_{02}\cdot T^2 + p_{30}\cdot\mathrm{SOC}^3 + p_{21}\cdot\mathrm{SOC}^2\cdot T + p_{12}\cdot\mathrm{SOC}\cdot T^2\\ & + p_{03}\cdot T^3 + p_{40}\cdot\mathrm{SOC}^4 + p_{31}\cdot\mathrm{SOC}^3\cdot T + p_{22}\cdot\mathrm{SOC}^2\cdot T^2\\ & + p_{13}\cdot\mathrm{SOC}\cdot T^3 + p_{50}\cdot\mathrm{SOC}^5 + p_{41}\cdot\mathrm{SOC}^4\cdot T\\ & + p_{32}\cdot\mathrm{SOC}^3\cdot T^2 + p_{23}\cdot\mathrm{SOC}^2\cdot T^3\end{aligned} \tag{A.1}$$

The corresponding coefficients are summarized in Table A.8.

Table A1
Coefficients for the polynomial surface $R_{\mathrm{DC10s}}(\mathrm{SOC}, T)$.

Coefficient	Value
p_{00}	0.04733
p_{10}	−0.0005173
p_{01}	−0.006342
p_{20}	−0.009436
p_{11}	0.001053
p_{02}	0.001543
p_{30}	0.0009925
p_{21}	−0.0006121
p_{12}	−0.0002329
p_{03}	−1.453e-05
p_{40}	0.009418
p_{31}	0.001663
p_{22}	0.0003376
p_{13}	−0.001086
p_{50}	−0.003839
p_{41}	−0.001331
p_{32}	−3.572e-05
p_{23}	0.0005283

References

[1] B. Scrosati, J. Garche, Lithium batteries: status, prospects and future, J. Power Sources 195 (9) (2010) 2419–2430, https://doi.org/10.1016/j.jpowsour.2009.11.048.

[2] George E. Blomgren, The development and future of lithium ion batteries, J. Electrochem. Soc. 164 (1) (2017) A5019–A5025, https://doi.org/10.1149/2.0251701jes.

[3] Volker Reber, Neue mnglichkeiten durch laden mit 800 volt, 2016(accessed March

15, 2019) https://www.porscheengineering.com/filestore/download/peg/de/pemagazin-01-2016-artikel-e-power/default/047e5361-3dfb-11e6-8697-0019999cd470/e-power-g-Magazin-01-2016.pdf.

[4] J. Schnell, C. Nentwich, F. Endres, A. Kollenda, F. Distel, T. Knoche, G. Reinhart, Data mining in lithium-ion battery cell production, J. Power Sources 413 (2019) 360–366, https://doi.org/10.1016/j.jpowsour.2018.12.062.

[5] C. Campestrini, P. Keil, S.F. Schuster, A. Jossen, Ageing of lithium-ion battery modules with dissipative balancing compared with single-cell ageing, J. Energy Storage 6 (2016) 142–152, https://doi.org/10.1016/j.est.2016.03.004.

[6] F. An, L. Chen, J. Huang, J. Zhang, P. Li, Rate dependence of cell-to-cell variations of lithium-ion cells, Sci. Rep. 6 (2016) 35051, https://doi.org/10.1038/srep35051.

[7] S.F. Schuster, M.J. Brand, P. Berg, M. Gleissenberger, A. Jossen, Lithium-ion cell-to-cell variation during battery electric vehicle operation, J. Power Sources 297 (2015) 242–251, https://doi.org/10.1016/j.jpowsour.2015.08.001.

[8] T. Baumhöfer, M. Brühl, S. Rothgang, D.U. Sauer, Production caused variation in capacity aging trend and correlation to initial cell performance, J. Power Sources 247 (2014) 332–338, https://doi.org/10.1016/j.jpowsour.2013.08.108.

[9] I. Zilberman, S. Ludwig, A. Jossen, Cell-to-cell variation of calendar aging and reversible self-discharge in 18650 nickel-rich, silicon–graphite lithium-ion cells, J. Energy Storage 26 (2019) 100900, https://doi.org/10.1016/j.est.2019.100900.

[10] B. Kenney, K. Darcovich, D.D. MacNeil, I.J. Davidson, Modelling the impact of variations in electrode manufacturing on lithium-ion battery modules, J. Power Sources 213 (2012) 391–401, https://doi.org/10.1016/j.jpowsour.2012.03.065.

[11] D. Shin, M. Poncino, E. Macii, N. Chang, A statistical model-based cell-to-cell variability management of li-ion battery pack, IEEE Trans. Comput. Aided Des. Integr. Circuits Syst. 34 (2) (2015) 252–265, https://doi.org/10.1109/TCAD.2014.2384506.

[12] M. Dubarry, C. Pastor-Fernández, G. Baure, T.F. Yu, W.D. Widanage, J. Marco, Battery energy storage system modeling: investigation of intrinsic cell-to-cell variations, J. Energy Storage 23 (2019) 19–28, https://doi.org/10.1016/j.est.2019.02.016.

[13] S. Paul, C. Diegelmann, H. Kabza, W. Tillmetz, Analysis of ageing inhomogeneities in lithium-ion battery systems, J. Power Sources 239 (2013) 642–650, https://doi.org/10.1016/j.jpowsour.2013.01.068.

[14] M. Baumann, L. Wildfeuer, S. Rohr, M. Lienkamp, Parameter variations within li-ion battery packs – theoretical investigations and experimental quantification, J. Energy Storage 18 (2018) 295–307, https://doi.org/10.1016/j.est.2018.04.031.

[15] L. Zhou, Y. Zheng, M. Ouyang, L. Lu, A study on parameter variation effects on battery packs for electric vehicles, J. Power Sources 364 (2017) 242–252, https://doi.org/10.1016/j.jpowsour.2017.08.033.

[16] D. Oeser, A. Ziegler, A. Ackva, Single cell analysis of lithium-ion e-bike batteries aged under various conditions, J. Power Sources 397 (2018) 25–31, https://doi.org/10.1016/j.jpowsour.2018.06.101.

[17] K.-C. Chiu, C.-H. Lin, S.-F. Yeh, Y.-H. Lin, C.-S. Huang, K.-C. Chen, Cycle life analysis of series connected lithium-ion batteries with temperature difference, J. Power Sources 263 (2014) 75–84, https://doi.org/10.1016/j.jpowsour.2014.04.034.

[18] X. Wang, Z. Wang, L. Wang, Z. Wang, H. Guo, Dependency analysis and degradation process-dependent modeling of lithium-ion battery packs, J. Power Sources 414 (2019) 318–326, https://doi.org/10.1016/j.jpowsour.2019.01.021.

[19] S. Santhanagopalan, R.E. White, Quantifying cell-to-cell variations in lithium ion batteries, Int. J. Electrochem. 2012 (12) (2012) 1–10, https://doi.org/10.1155/2012/395838.

[20] J. Sturm, S. Ludwig, J. Zwirner, C. Ramirez-Garcia, B. Heinrich, M.F. Horsche, A. Jossen, Suitability of physicochemical models for embedded systems regarding a nickel-rich, silicon-graphite lithium-ion battery, J. Power Sources 436 (2019) 226834, https://doi.org/10.1016/j.jpowsour.2019.226834.

[21] J.S. Newman, K.E. Thomas-Alyea, Electrochemical Systems, third ed., Electrochemical Society series, Wiley, Hoboken, N.J., 2004.

[22] M. Dubarry, C. Truchot, B.Y. Liaw, Synthesize battery degradation modes via a diagnostic and prognostic model, J. Power Sources 219 (2012) 204–216, https://doi.org/10.1016/j.jpowsour.2012.07.016.

[23] F. Baronti, N. Femia, R. Saletti, C. Visone, W. Zamboni, Preisach modelling of lithium-iron-phosphate battery hysteresis, J. Energy Storage 4 (2015) 51–61, https://doi.org/10.1016/j.est.2015.09.004.

[24] W. Dreyer, J. Jamnik, C. Guhlke, R. Huth, J. Moskon, M. Gaberscek, The thermodynamic origin of hysteresis in insertion batteries, Nat. Mater. 9 (5) (2010) 448–453, https://doi.org/10.1038/nmat2730.

[25] M.A. Roscher, D.U. Sauer, Dynamic electric behavior and open-circuit-voltage modeling of lifepo4-based lithium ion secondary batteries, J. Power Sources 196 (1) (2011) 331–336, https://doi.org/10.1016/j.jpowsour.2010.06.098.

[26] C.R. Birkl, M.R. Roberts, E. McTurk, P.G. Bruce, D.A. Howey, Degradation diagnostics for lithium ion cells, J. Power Sources 341 (2017) 373–386, https://doi.org/10.1016/j.jpowsour.2016.12.011.

[27] J. Sturm, A. Rheinfeld, I. Zilberman, F.B. Spingler, S. Kosch, F. Frie, A. Jossen, Modeling and simulation of inhomogeneities in a 18650 nickel-rich, silicon-graphite lithium-ion cell during fast charging, J. Power Sources 412 (2019) 204–223, https://doi.org/10.1016/j.jpowsour.2018.11.043.

[28] V.V. Viswanathan, D. Choi, D. Wang, W. Xu, S. Towne, R.E. Williford, J.-G. Zhang, J. Liu, Z. Yang, Effect of entropy change of lithium intercalation in cathodes and anodes on li-ion battery thermal management, J. Power Sources 195 (11) (2010) 3720–3729, https://doi.org/10.1016/j.jpowsour.2009.11.103.

[29] I. Zilberman, A. Rheinfeld, A. Jossen, Uncertainties in entropy due to temperature path dependent voltage hysteresis in li-ion cells, J. Power Sources 395 (2018) 179–184, https://doi.org/10.1016/j.jpowsour.2018.05.052.

[30] C. Campestrini, S. Kosch, A. Jossen, Influence of change in open circuit voltage on the state of charge estimation with an extended Kalman filter, J. Energy Storage 12 (2017) 149–156, https://doi.org/10.1016/j.est.2017.04.011.

[31] A. Farmann, D.U. Sauer, A study on the dependency of the open-circuit voltage on temperature and actual aging state of lithium-ion batteries, J. Power Sources 347 (2017) 1–13, https://doi.org/10.1016/j.jpowsour.2017.01.098.

[32] M. Park, X. Zhang, M. Chung, G.B. Less, A.M. Sastry, A review of conduction phenomena in li-ion batteries, J. Power Sources 195 (24) (2010) 7904–7929, https://doi.org/10.1016/j.jpowsour.2010.06.060.

[33] A. Jossen, Fundamentals of battery dynamics, J. Power Sources 154 (2) (2006) 530–538, https://doi.org/10.1016/j.jpowsour.2005.10.041.

[34] M.D. Levi, D. Aurbach, Diffusion coefficients of lithium ions during intercalation into graphite derived from the simultaneous measurements and modeling of electrochemical impedance and potentiostatic intermittent titration characteristics of thin graphite electrodes, J. Phys. Chem. B 101 (23) (1997) 4641–4647, https://doi.org/10.1021/jp9701911.

[35] W. Waag, S. Käbitz, D.U. Sauer, Experimental investigation of the lithium-ion battery impedance characteristic at various conditions and aging states and its influence on the application, Appl. Energy 102 (2013) 885–897, https://doi.org/10.1016/j.apenergy.2012.09.030.

[36] E. Barsoukov, J.R. Macdonald, Impedance Spectroscopy, John Wiley & Sons, Inc, Hoboken, NJ, USA, 2005, https://doi.org/10.1002/0471716243.

[37] A.A. Pilla, A transient impedance technique for the study of electrode kinetics, J. Electrochem. Soc. 117 (4) (1970) 467, https://doi.org/10.1149/1.2407544.

[38] W. Weppner, Determination of the kinetic parameters of mixed-conducting electrodes and application to the system Li[sub 3]Sb, J. Electrochem. Soc. 124 (10) (1977) 1569, https://doi.org/10.1149/1.2133112.

[39] J. Illig, J.P. Schmidt, M. Weiss, A. Weber, E. Ivers-Tiffée, Understanding the impedance spectrum of 18650 LiFePO4-cells, J. Power Sources 239 (2013) 670–679, https://doi.org/10.1016/j.jpowsour.2012.12.020.

[40] A. Farmann, W. Waag, A. Marongiu, D.U. Sauer, Critical review of on-board capacity estimation techniques for lithium-ion batteries in electric and hybrid electric vehicles, J. Power Sources 281 (2015) 114–130, https://doi.org/10.1016/j.jpowsour.2015.01.129.

[41] G. Liu, M. Ouyang, L. Lu, J. Li, X. Han, Analysis of the heat generation of lithium-ion battery during charging and discharging considering different influencing factors, J. Therm. Anal. Calorim. 116 (2) (2014) 1001–1010, https://doi.org/10.1007/s10973-013-3599-9.

[42] R. Srinivasan, A. Carson Baisden, B.G. Carkhuff, M.H. Butler, The five modes of heat generation in a li-ion cell under discharge, J. Power Sources 262 (2014) 93–103, https://doi.org/10.1016/j.jpowsour.2014.03.062.

[43] S.R. Gowda, D.W. Dees, A.N. Jansen, K.G. Gallagher, Examining the electrochemical impedance at low states of charge in lithium- and manganese-rich layered transition-metal oxide electrodes, J. Electrochem. Soc. 162 (7) (2015) A1374–A1381, https://doi.org/10.1149/2.0931507jes.

[44] I. Zilberman, J. Sturm, A. Jossen, Reversible self-discharge and calendar aging of 18650 nickel-rich, silicon-graphite lithium-ion cells, J. Power Sources 425 (2019) 217–226, https://doi.org/10.1016/j.jpowsour.2019.03.109.

[45] M. Ecker, N. Nieto, S. Käbitz, J. Schmalstieg, H. Blanke, A. Warnecke, D.U. Sauer, Calendar and cycle life study of Li(NiMnCo)O2-based 18650 lithium-ion batteries, J. Power Sources 248 (2014) 839–851, https://doi.org/10.1016/j.jpowsour.2013.09.143.

[46] M. Naumann, M. Schimpe, P. Keil, H.C. Hesse, A. Jossen, Analysis and modeling of calendar aging of a commercial LiFePO4/graphite cell, J. Energy Storage 17 (2018) 153–169, https://doi.org/10.1016/j.est.2018.01.019.

[47] J. Vetter, P. Novák, M.R. Wagner, C. Veit, K.-C. Möller, J.O. Besenhard, M. Winter, M. Wohlfahrt-Mehrens, C. Vogler, A. Hammouche, Ageing mechanisms in lithium-ion batteries, J. Power Sources 147 (1–2) (2005) 269–281, https://doi.org/10.1016/j.jpowsour.2005.01.006.

[48] K. Kleiner, P. Jakes, S. Scharner, V. Liebau, H. Ehrenberg, Changes of the balancing between anode and cathode due to fatigue in commercial lithium-ion cells, J. Power Sources 317 (2016) 25–34, https://doi.org/10.1016/j.jpowsour.2016.03.049.

[49] I. Bloom, A.N. Jansen, D.P. Abraham, J. Knuth, S.A. Jones, V.S. Battaglia, G.L. Henriksen, Differential voltage analyses of high-power, lithium-ion cells, J. Power Sources 139 (1–2) (2005) 295–303, https://doi.org/10.1016/j.jpowsour.2004.07.021.

[50] P. Keil, A. Jossen, Calendar aging of NCA lithium-ion batteries investigated by differential voltage analysis and coulomb tracking, J. Electrochem. Soc. 164 (1) (2017) A6066–A6074, https://doi.org/10.1149/2.0091701jes.

[51] C. von Lüders, V. Zinth, S.V. Erhard, P.J. Osswald, M. Hofmann, R. Gilles, A. Jossen, Lithium plating in lithium-ion batteries investigated by voltage relaxation and in situ neutron diffraction, J. Power Sources 342 (2017) 17–23, https://doi.org/10.1016/j.jpowsour.2016.12.032.

[52] C. Uhlmann, J. Illig, M. Ender, R. Schuster, E. Ivers-Tiffée, In situ detection of lithium metal plating on graphite in experimental cells, J. Power Sources 279 (2015) 428–438, https://doi.org/10.1016/j.jpowsour.2015.01.046.

[53] X. Han, M. Ouyang, L. Lu, J. Li, Y. Zheng, Z. Li, A comparative study of commercial lithium ion battery cycle life in electrical vehicle: aging mechanism identification, J. Power Sources 251 (2014) 38–54, https://doi.org/10.1016/j.jpowsour.2013.11.029.

[54] M. Wetjen, D. Pritzl, R. Jung, S. Solchenbach, R. Ghadimi, H.A. Gasteiger, Differentiating the degradation phenomena in silicon-graphite electrodes for lithium-ion batteries, J. Electrochem. Soc. 164 (12) (2017) A2840–A2852, https://doi.org/10.1149/2.1921712jes.

[55] M. Klett, J.A. Gilbert, S.E. Trask, B.J. Polzin, A.N. Jansen, D.W. Dees, D.P. Abraham, Electrode behavior re-visited: monitoring potential windows, capacity loss, and impedance changes in li 1.03 (ni 0.5 co 0.2 mn 0.3) 0.97 o 2 /silicon-graphite full cells, J. Electrochem. Soc. 163 (6) (2016) A875–A887, https://doi.org/10.1149/2.

0271606jes.

[56] M. Wetjen, S. Solchenbach, D. Pritzl, J. Hou, V. Tileli, H.A. Gasteiger, Morphological changes of silicon nanoparticles and the influence of cutoff potentials in silicon-graphite electrodes, J. Electrochem. Soc. 165 (7) (2018) A1503–A1514, https://doi.org/10.1149/2.1261807jes.

[57] S. Müller, P. Pietsch, B.-E. Brandt, P. Baade, V. de Andrade, F. de Carlo, V. Wood, Quantification and modeling of mechanical degradation in lithium-ion batteries based on nanoscale imaging, Nat. Commun. 9 (1) (2018) 2340, https://doi.org/10.1038/s41467-018-04477-1.

[58] O. Dolotko, A. Senyshyn, M.J. Mühlbauer, K. Nikolowski, F. Scheiba, H. Ehrenberg, Fatigue process in li-ion cells: an in situ combined neutron diffraction and electrochemical study, J. Electrochem. Soc. 159 (12) (2012) A2082–A2088, https://doi.org/10.1149/2.080212jes.

[59] W.M. Dose, V.A. Maroni, M.J. Piernas-Muñoz, S.E. Trask, I. Bloom, C.S. Johnson, Assessment of li-inventory in cycled Si-graphite anodes using LiFePO4 as a diagnostic cathode, J. Electrochem. Soc. 165 (10) (2018) A2389–A2396, https://doi.org/10.1149/2.1271810jes.

[60] S. Shiotani, T. Naka, M. Morishima, M. Yonemura, T. Kamiyama, Y. Ishikawa, Y. Ukyo, Y. Uchimoto, Z. Ogumi, Degradation analysis of 18650-type lithium-ion cells by operando neutron diffraction, J. Power Sources 325 (2016) 404–409, https://doi.org/10.1016/j.jpowsour.2016.06.026.

[61] N. Paul, J. Keil, F.M. Kindermann, S. Schebesta, O. Dolotko, M.J. Mühlbauer, L. Kraft, S.V. Erhard, A. Jossen, R. Gilles, Aging in 18650-type li-ion cells examined with neutron diffraction, electrochemical analysis and physico-chemical modeling, J. Energy Storage 17 (2018) 383–394, https://doi.org/10.1016/j.est.2018.03.016.

[62] T. Waldmann, M. Wilka, M. Kasper, M. Fleischhammer, M. Wohlfahrt-Mehrens, Temperature dependent ageing mechanisms in lithium-ion batteries – a post-mortem study, J. Power Sources 262 (2014) 129–135, https://doi.org/10.1016/j.jpowsour.2014.03.112.

[63] N.N. Sinha, A.J. Smith, J.C. Burns, G. Jain, K.W. Eberman, E. Scott, J.P. Gardner, J.R. Dahn, The use of elevated temperature storage experiments to learn about parasitic reactions in wound LiCoO2 graphite cells, J. Electrochem. Soc. 158 (11) (2011) A1194, https://doi.org/10.1149/2.007111jes.

[64] J. Xu, R.D. Deshpande, J. Pan, Y.-T. Cheng, V.S. Battaglia, Electrode side reactions, capacity loss and mechanical degradation in lithium-ion batteries, J. Electrochem. Soc. 162 (10) (2015) A2026–A2035, https://doi.org/10.1149/2.0291510jes.

[65] I. Buchberger, S. Seidlmayer, A. Pokharel, M. Piana, J. Hattendorff, P. Kudejova, R. Gilles, H.A. Gasteiger, Aging analysis of graphite/LiNi 1/3 Mn 1/3 Co 1/3 O2 cells using XRD, PGAA, and AC impedance, J. Electrochem. Soc. 162 (14) (2015) A2737–A2746, https://doi.org/10.1149/2.0721514jes.

[66] L.M. Thompson, W. Stone, A. Eldesoky, N.K. Smith, C.R.M. McFarlane, J.S. Kim, M.B. Johnson, R. Petibon, J.R. Dahn, Quantifying changes to the electrolyte and negative electrode in aged NMC532/graphite lithium-ion cells, J. Electrochem. Soc. 165 (11) (2018) A2732–A2740, https://doi.org/10.1149/2.0721811jes.

[67] J. Li, L.E. Downie, L. Ma, W. Qiu, J.R. Dahn, Study of the failure mechanisms of LiNi 0.8 Mn 0.1 Co 0.1 O 2 cathode material for lithium ion batteries, J. Electrochem. Soc. 162 (7) (2015) A1401–A1408, https://doi.org/10.1149/2.1011507jes.

[68] S.F. Schuster, T. Bach, E. Fleder, J. Müller, M. Brand, G. Sextl, A. Jossen, Nonlinear aging characteristics of lithium-ion cells under different operational conditions, J. Energy Storage 1 (2015) 44–53, https://doi.org/10.1016/j.est.2015.05.003.

[69] S.F. Schuster, M.J. Brand, C. Campestrini, M. Gleissenberger, A. Jossen, Correlation between capacity and impedance of lithium-ion cells during calendar and cycle life, J. Power Sources 305 (2016) 191–199, https://doi.org/10.1016/j.jpowsour.2015.11.096.

[70] I. Zilberman, S. Ludwig, M. Schiller, A. Jossen, Online aging determination in lithium-ion battery module with forced temperature gradient, J. Energy Storage 28 (2020) 101170, https://doi.org/10.1016/j.est.2019.101170.

[71] M.J. Brand, M.H. Hofmann, M. Steinhardt, S.F. Schuster, A. Jossen, Current distribution within parallel-connected battery cells, J. Power Sources 334 (2016) 202–212, https://doi.org/10.1016/j.jpowsour.2016.10.010.

[72] M.H. Hofmann, K. Czyrka, M.J. Brand, M. Steinhardt, A. Noel, F.B. Spingler, A. Jossen, Dynamics of current distribution within battery cells connected in parallel, J. Energy Storage 20 (2018) 120–133, https://doi.org/10.1016/j.est.2018.08.013.

[73] K. Rumpf, A. Rheinfeld, M. Schindler, J. Keil, T. Schua, A. Jossen, Influence of cell-to-cell variations on the inhomogeneity of lithium-ion battery modules, J. Electrochem. Soc. 165 (11) (2018) A2587–A2607, https://doi.org/10.1149/2.0111811jes.

[74] C. Pastor-Fernández, T. Bruen, W.D. Widanage, M.A. Gama-Valdez, J. Marco, A study of cell-to-cell interactions and degradation in parallel strings: implications for the battery management system, J. Power Sources 329 (2016) 574–585, https://doi.org/10.1016/j.jpowsour.2016.07.121.

[75] K. Rumpf, M. Naumann, A. Jossen, Experimental investigation of parametric cell-to-cell variation and correlation based on 1100 commercial lithium-ion cells, J. Energy Storage 14 (2017) 224–243, https://doi.org/10.1016/j.est.2017.09.010.

[76] M. Sachs, Wahrscheinlichkeitsrechnung und Statistik: Für Ingenieurstudierende an Hochhochschulen, fifth auflage, Mathematik - Studienhilfen, Carl Hanser Verlag, München, 2018, https://doi.org/10.3139/9783446456204.

[77] A. Fill, S. Koch, K.P. Birke, Analytical model of the current distribution of parallel-connected battery cells and strings, J. Energy Storage 23 (2019) 37–43, https://doi.org/10.1016/j.est.2019.02.031.

[78] Duetschke E., Globisch J., Gnann T., Haendel M., Ploetz P., Ullrich S., Wietschel M., Held M., Elektromobilitaet in gewerblichen Flotten, 2014 (accessed March 1, 2020), URL: https://www.isi.fraunhofer.de/content/dam/isi/dokumente/cce/2014/Get_eReady.pdf.

[79] A. Tang, J. Li, L. Lou, C. Shan, X. Yuan, Optimization design and numerical study on water cooling structure for power lithium battery pack, Appl. Therm. Eng. 159 (2019) 113760, https://doi.org/10.1016/j.applthermaleng.2019.113760.

[80] C. Zhao, W. Cao, T. Dong, F. Jiang, Thermal behavior study of discharging/charging cylindrical lithium-ion battery module cooled by channeled liquid flow, Int. J. Heat Mass Transf. 120 (2018) 751–762, https://doi.org/10.1016/j.ijheatmasstransfer.2017.12.083.

[81] B. Wu, V. Yufit, M. Marinescu, G.J. Offer, R.F. Martinez-Botas, N.P. Brandon, Coupled thermal–electrochemical modelling of uneven heat generation in lithium-ion battery packs, J. Power Sources 243 (2013) 544–554, https://doi.org/10.1016/j.jpowsour.2013.05.164.

[82] X.M. Xu, R. He, Research on the heat dissipation performance of battery pack based on forced air cooling, J. Power Sources 240 (2013) 33–41, https://doi.org/10.1016/j.jpowsour.2013.03.004.

[83] Y. Zheng, M. Ouyang, L. Lu, J. Li, X. Han, L. Xu, On-line equalization for lithium-ion battery packs based on charging cell voltages: part 1. Equalization based on remaining charging capacity estimation, J. Power Sources 247 (2014) 676–686, https://doi.org/10.1016/j.jpowsour.2013.09.030.

[84] F. Baronti, R. Roncella, R. Saletti, Performance comparison of active balancing techniques for lithium-ion batteries, J. Power Sources 267 (2014) 603–609, https://doi.org/10.1016/j.jpowsour.2014.05.007.

[85] H.G. J., Sample sizes for Monte Carlo simulation, IEEE Trans. Syst. Man Cybern. SMC-2 (1972) 678–680, https://doi.org/10.1109/TSMC.1972.4309200.

[86] S.V. Erhard, P.J. Osswald, P. Keil, E. Höffer, M. Haug, A. Noel, J. Wilhelm, B. Rieger, K. Schmidt, S. Kosch, F.M. Kindermann, F. Spingler, H. Kloust, T. Thoennessen, A. Rheinfeld, A. Jossen, Simulation and measurement of the current density distribution in lithium-ion batteries by a multi-tab cell approach, J. Electrochem. Soc. 164 (1) (2017) A6324–A6333, https://doi.org/10.1149/2.0551701jes.

[87] G. Zhang, L. Cao, S. Ge, C.-Y. Wang, C.E. Shaffer, C.D. Rahn, In situ measurement of radial temperature distributions in cylindrical li-ion cells, J. Electrochem. Soc. 161 (10) (2014) A1499–A1507, https://doi.org/10.1149/2.0051410jes.

[88] A. Rheinfeld, J. Sturm, A. Frank, S. Kosch, S.V. Erhard, A. Jossen, Impact of cell size and format on external short circuit behavior of lithium-ion cells at varying cooling conditions: modeling and simulation, J. Electrochem. Soc. 167 (1) (2020) 013511, https://doi.org/10.1149/2.0112001JES.

4 Influence of lithium plating on the voltage imbalance

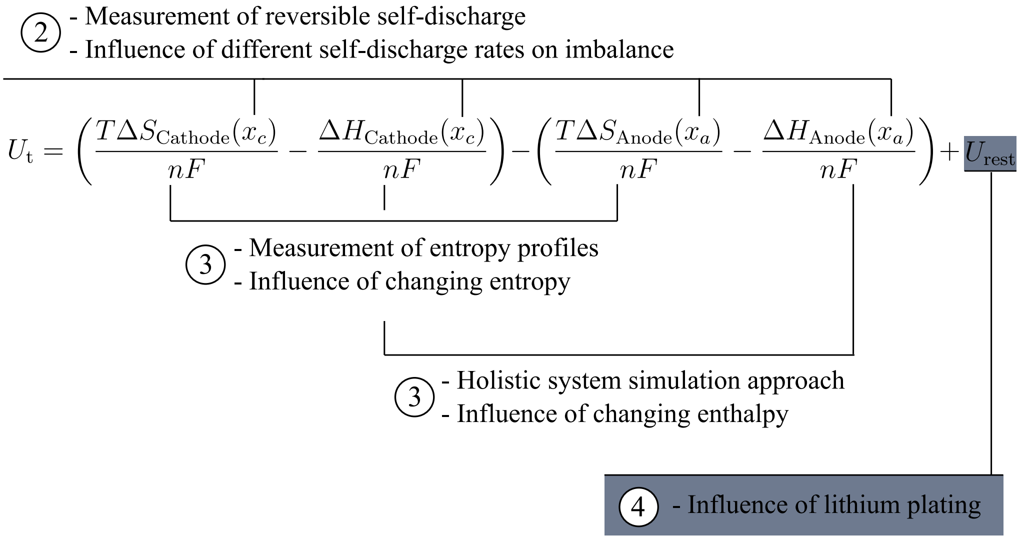

Figure 4.1: Outline of chapter 4.

Based on the results from previous sections, cell-to-cell variations and different rates of LLI and self-discharge are unlikely to induce major voltage imbalances within the battery packs. Therefore, this chapter evaluates the remaining possible influencing factors. In order to verify this outcome, several module aging experiments were conducted. First of all, for that purpose a 6s1p module with a controllable forced temperature gradient along the serial connection was constructed. This apparatus is described in detail in the following article. After the initial checkup measurement, the module was equalized by charging each cell at 25 °C to 4.2 V using the CCCV protocol, with a termination current of 0.001 C. Subsequently, a temperature gradient of $\Delta T = 5\,\text{K}$ at 25 °C was applied with a thermal equalization time of 2 h, in order to establish a homogeneous temperature distribution of between 25 °C and 30 °C between the first and the last cell within the serial connection. The cycling routine included 20 CC cycles with 1 C, and cell-level charge and discharge termination at 4.2 V and 2.5 V. After each cycling sequence, the temperature of each cell was set back to 25 °C. All cells were rested for at least 12 h after the last 1 C charge, so that most overpotentials had decayed. Subsequently, the clipboard wiring was changed to a single cell configuration and each cell underwent capacity and impedance measurements. At the end, each cell was charged to the target voltage before the checkup measurement at 25 °C using a CCCV protocol, with a termination current of 0.001 C. This approach allowed voltage drift of the 6s1p module, whilst conducting checkup measurement on the cell level.

The results, which are shown in Fig. 4.2, revealed that due to different aging rates there was a detectable voltage drift within the module after the 12 h relaxation periods. After only 100 cycles, the voltage difference between the maximum and minimum cell voltages in the charged state amounted to 30 mV, as depicted in Fig. 4.2b. The forced temperature gradient evoked different aging rates

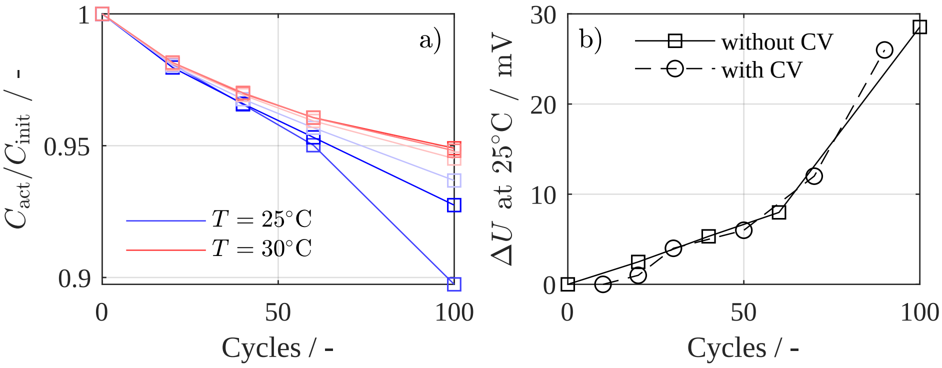

Figure 4.2: (a) Progression of the relative capacity of each cell in the 6s1p module. (b) Increased difference between the maximum and minimum cell voltage within the 6s1p module during cycling with and without CV phase.

within the 6s1p module, whereby the coldest cell showed the largest degradation. In order to exclude different impedances as the cause of the voltage imbalance, a further experiment was conducted. Instead of the previous 1 C charge, the module was charged with 1 C and a subsequent CV phase with a termination current amounting to C/70, minimizing the influence of the impedance. The cumulative voltage difference between the maximum and minimum cell voltage within the 6s1p module after 12 h of relaxation is shown Fig. 4.2b. As the voltage differences are almost identical, regardless of the CV phase, the influence of impedances was considered to be negligible.

In the following article, the observed voltage imbalance was further investigated. The idea behind this study was to repeat the module aging experiments, while including the effects of dissipative balancing. Furthermore, DVA and post-mortem analysis were used for more precise identification of the causes of cell degradation. The results of the presented study were in accordance with the preliminary tests. It could be shown that the degradation of colder cells was linked to lithium plating, possibly due to deeper cycling and the concomitantly increased mechanical stress on the negative electrode. Furthermore, the plating reaction was responsible for the majority of the voltage drift, which in sum amounted to >75 mV. Voltage drift limited the module's energy, whereby dissipative balancing improved the module utilization. Finally, cumulative balancing charge showed a strong correlation with capacity differences between the limiting and remaining cells and could be therefore used for the identification of lithium plating in battery packs.

Authors contribution Design and execution of the experiment were performed by Ilya Zilberman. Sebastian Ludwig supported the design of the cycling procedure and performed post-mortem analysis. Martin Schiller was involved in the preliminary tests. Andreas Jossen supervised this work, the manuscript was written by Ilya Zilberman and was edited by all authors.

Online aging determination in lithium-ion battery module with forced temperature gradient

Ilya Zilberman, Sebastian Ludwig, Martin Schiller, Andreas Jossen

Journal of Energy Storage 28, 101170, 2020

Permanent weblink:
`https://doi.org/10.1016/j.est.2019.101170`

Journal of Energy Storage 28 (2020) 101170

Contents lists available at ScienceDirect

Journal of Energy Storage

journal homepage: www.elsevier.com/locate/est

Online aging determination in lithium-ion battery module with forced temperature gradient

I. Zilberman[*], S. Ludwig, M. Schiller, A. Jossen

Institute for Electrical Energy Storage Technology, Technical University of Munich (TUM), Arcisstr. 21, Munich 80333, Germany

A R T I C L E I N F O

Keywords:
Aging
Voltage drift
Lithium plating
Battery pack
Balancing

A B S T R A C T

Voltage imbalance in lithium-ion battery packs, which leads to impaired utilization of the whole energy-storage system, is often linked to different self-discharge rates. Despite the established use of balancing circuits, neither the true origin of voltage imbalance nor the benefits of cell balancing are as yet completely understood. In this study, a forced temperature gradient along six in-series connected, commercial 18650 nickel-rich/SiC cells was applied during cycles resulting in cell temperatures of between 25 °C and 30 °C. Every 20 cycles, the 6s1p module was equalized using dissipative balancing. Aging behavior was analyzed using checkup measurements, differential voltage analysis (DVA) and conclusive scanning electron microscope (SEM) imaging of negative electrodes. The results obtained in this work reveal that the forced temperature gradient caused different degradation rates, whereas the colder cells exhibited aggravated aging behavior, which was linked to lithium plating. Furthermore, the lithium plating caused the majority of the voltage drift within the module. The application of dissipative balancing enabled an improved utilization of the module, and increased the discharge energy. Finally, the cumulative balancing charge reflected the capacity differences between the cells, and could therefore be used for the online determination of relative aging of single cells or cell blocks in lithium-ion battery packs..

1. Introduction

Over the past decade lithium-ion technology has overcome several downsides such as high costs, safety hazards and short system life [1,2]. Now, the wide field of applications ranges from mobile devices to decentralized energy storage and electric vehicles (EVs). In order to cover the high energy demand, battery packs usually consist of up to thousands of single lithium-ion cells connected in series and in parallel. A serial connection of cells increases the system voltage, which, due to lower current loads, reduces ohmic losses within the battery pack and charging infrastructure. State-of-the-art battery packs exhibit system voltages of up to 800V with almost 200 cell blocks in series [3], whereas each cell block contains cells in parallel. As a consequence, there is a higher chance for cell block voltages to drift apart, limiting the available capacity of the battery pack. Deployment of balancing circuits usually solves this issue [4], however the true origin of voltage imbalance is still not completely understood. Different self-discharge rates, which evoke voltage decay without any irreversible capacity loss, are often stated for being the major reason behind the voltage drift [5,6]. However, recent studies of state-of-the-art lithium-ion cells with nickel-rich cathodes and silicon-graphite anodes revealed that differing self-discharge rates had almost no influence on possible voltage imbalance, due to low self-discharge currents [7,8].

Due to finite accuracy during the manufacturing processes, cells vary in their characteristics even immediately after the production stage. In general, cell parameter variations are usually linked to minimal differences in the electrode thickness, material composition, overall component connectivity, etc. among same type produced lithium-ion cells [9]. Rumpf et al. showed that initial cell parameters of mass-produced lithium-ion cells are usually normally distributed, which is symptomatic of random - and not systematic - deviation during cell manufacturing [10]. Subsequently, due to negative outliers, it is inevitable that a serial interconnection of cells or cell blocks results in reduced pack capacity [11,12]. However, in addition to initial parameter variation, lithium-ion cells exhibit intrinsically varying aging rates, even under the same operational conditions [13], although the absolute differences remain rather low [7]. Due to spatial location of each cell in the battery pack it is almost impossible to provide the same cooling power and thermal condition to each cell [14,15], which leads to temperature gradients during operation [16,17]. Several studies reported that major degradation mechanisms are influenced by temperature [18,19]. Furthermore, it has been shown that temperature gradients deteriorate the capacity spread among the cells in battery packs [20–22].

---

[*] Corresponding author.
E-mail address: ilya.zilberman@tum.de (I. Zilberman).

https://doi.org/10.1016/j.est.2019.101170
Received 30 September 2019; Received in revised form 19 November 2019; Accepted 18 December 2019
2352-152X/

A forced temperature gradient was applied by Klein et al. in order to investigate the influence of non-uniform temperature conditions on current distributions among cells in parallel [23]. In that investigation, all cells were placed in an enclosing aluminum casing, while Peltier elements on each side of the aluminum block controlled the non-uniform temperature distribution. Using two lithium-ion cells in series, one of which was placed in a climate chamber at 55 °C and another at 25 °C, Chiu et al. showed that temperature gradients have a negative impact on pack performance and can induce safety issues, if cell voltage supervision is neglected [24]. However, no detailed information on voltage imbalance was presented. Cordoba et al. demonstrated via simulation that the lifetime of a battery pack depends on the topology, thermal properties, cell balancing and intrinsic cell parameter variations, whereas the latter were not significant for the aging progression of the pack [25]. Unfortunately, voltage-drift progression was not also presented. Wang et al. compared the aging behaviors of four different battery pack typologies, including serial connection with uniform temperature distribution among all cells [26]. The presented empirical study revealed a higher degradation rate of battery packs compared to single cell aging. More details on possible roots of such behavior were provided by Zheng et al. [27]. Reduced capacity of a battery pack consisting of two cells at 30 °C and 45 °C connected in series was linked to voltage imbalance, which was induced by different rates of loss of lithium inventory. However, no cell balancing during the cycling was applied. A comprehensive aging study of two 8s14p modules with dissipative balancing and naturally emerged temperature gradients was carried out by Campestrini et al. [28]. Results revealed no considerable deviations between single cell and battery pack aging. Owing to the fact that dissipative balancing was active during the entire time and not only during the idle phases, no statement regarding balancing charges and voltage imbalance could be made, since the influence of impedances was more dominant than the influence of different capacities.

To date, there has been no study investigating module aging with forced temperature gradients for in-series connections, while evaluating the root of the voltage imbalance and balancing effort. The goal of this work is to investigate whether balancing charges can be used for the online determination of cell aging. In order to isolate the influence of serial connection, no cells in parallel were considered.

This paper is organized as follows. First, the investigated cells, experimental setup and all test sequences are described. After that, the aging progressions of each cell are evaluated and the roots of the aging are discussed using differential voltage analysis (DVA) and scanning electron microscope (SEM) imaging. Subsequently, the aging progression of the module is presented with corresponding energy, voltage drift and balancing charge progressions. Finally, the results are concluded.

2. Experimental

2.1. Cell and experimental setup

The object of this study was a commercial NMC(nickel-rich)/SiC 18650 high energy lithium-ion cell INR18650-MJ1 from LGChem with a nominal capacity of 3.5 Ah and a specific energy of 259.6 Wh kg^{-1}. According to the cell manufacturer, the recommended operation window is between 4.2 V and 2.5 V. Sturm et al. performed an analysis of active materials and measured half-cell open circuit voltage (OCV) curves for both electrodes of the same MJ1 cell [29]. Electrode balancing revealed an oversized cathode ($\sim$ 9.4%) and an almost complete use of the anode ($>$ 99%) [29]. Such extreme utilization of the anode facilitated the high energy density of the cell. The amount of silicon in graphite was measured via inductively coupled plasma-optical emission spectroscopy (ICP-OES) and amounted to $\sim$ 3.5 wt % [29]. The ratio of nickel, manganese and cobalt in the active material of the cathode, determined via ICP-OES, amounted to 82%-6.3%-11.7% respectively, indicating the dominance of nickel in the cathode.

For this experiment, six pristine cells were selected with constant current (CC) discharge capacities at 25 °C of between 3.461 Ah and 3.47 Ah. The R_{DC10s} value, which is a DC resistance, calculated after a 10 s discharge pulse with 1 C at 50% SOC, ranged from 42.0 mΩ to 43.0 mΩ. Details of each cell, including mean and standard deviation values, are summarized in Table 1.

Table 1
Overview of parameters of six cells used in the experiment, including the capacity of the cell and the internal resistance.

Parameter	1	2	3	4	5	6	μ	σ
C / Ah	3.461	3.469	3.461	3.47	3.462	3.463	3.464	0.004
R_{DC10s} / mΩ	42.3	42.7	42.3	43.0	42.4	42.0	42.45	0.3507

Fig. 1a shows the test setup for 6s1p module aging with a forced temperature gradient. Each cell was encapsulated in a copper block, in order to allow a thermal contact via heat conduction. The cylinder wall within the cell block was covered with the high thermal conductivity foil Softtherm 86/600 with a thermal resistance of 0.2 K W^{-1} and a foil thickness of 0.5 mm. Additionally, an increase in cell pressure due to the mechanical expansion of the cell during lithiation was prevented thanks to the low Young modulus of the foil material, which amounted to 77 N cm^{-2}. PT100 temperature sensors were integrated into copper blocks and were mounted onto the surface of each cell. The sensors were logged with the Cell Measurement Unit (CMU) from Basytec during the experiment. All temperature sensors in the experimental set up underwent offset correction at 25 °C. Each cell block was screwed to a copper flat rail, whereby the contact areas were lubricated with a heat paste, in order to minimize the thermal transfer resistance. Two Peltier elements MCTE1-19913L-S from Multicomp with attached heat sinks were mounted onto each side of the flat bar. Each Peltier element was separately controlled via a custom-made H-bridge circuit allowing a maximum output power of 200 W. For the temperature control, two additional temperature sensors were used, which were placed in small drill holes beneath the Peltier elements. Fig. 1b shows temperature settling with a temperature gradient $\Delta T = 5$ K at 25 °C without any current load. All temperatures became and remained constant after approx. 20 min, although the temperatures were not completely equidistantly distributed. Such discrepancy was due to the fact that the copper set-up was not thermally isolated, which implied a loss heat flow proportional to the temperature difference between the cell block and the environment. All cells, including cell blocks, were placed into an assembly with six clipboards, which connected the positive and negative tabs of the cells with gold contact pins in a 4-wire connection. During cycling, each cell voltage was logged with a CMU. Resolution of the CMU voltage measurement amounted to 0.2 mV with an accuracy of 2.5 mV. The clipboard wiring allowed the connection of all six cells in series. The cycling of the 6s1p module was accomplished with a High Power System (HPS) from Basytec with a maximum current of 5 A and maximum voltage of 60 V. Checkup measurements were performed on the cell level with the Cell Testing System (CTS) from Basytec with a precision of +/- 0.3 mV and +/- 0.5 µA in the smallest range for the voltage and current measurement respectively. For checkup sequences, the wiring of the clipboard assembly was changed to single-cell configuration. Fig. 1c shows cell temperature progression during module cycling with 1 C discharge, 10 min pause and subsequent 1 C charge, while applying a temperature gradient $\Delta T = 5$ K between 25 °C and 30 °C. All cells managed to maintain a quasi-isothermal condition with a maximum deviation of +/- 0.4 °C, which was sufficient for the experiment.

After the aging experiment, SEM images of the anode of a pristine cell, of the cell, which aged at 25 °C and of the cell, which aged at 30 °C were taken. All cells were discharged at 0.5 C–2.5 V using CCCV protocol with the termination current amounting to 50 mA. Afterwards, all cells were opened in a glovebox under argon atmosphere and several samples from each negative electrode were punched out. Finally, SEM images were taken using a JEOL JCM-6000 in high vacuum mode, with an acceleration voltage of 15 kV and a high filament and probe current.

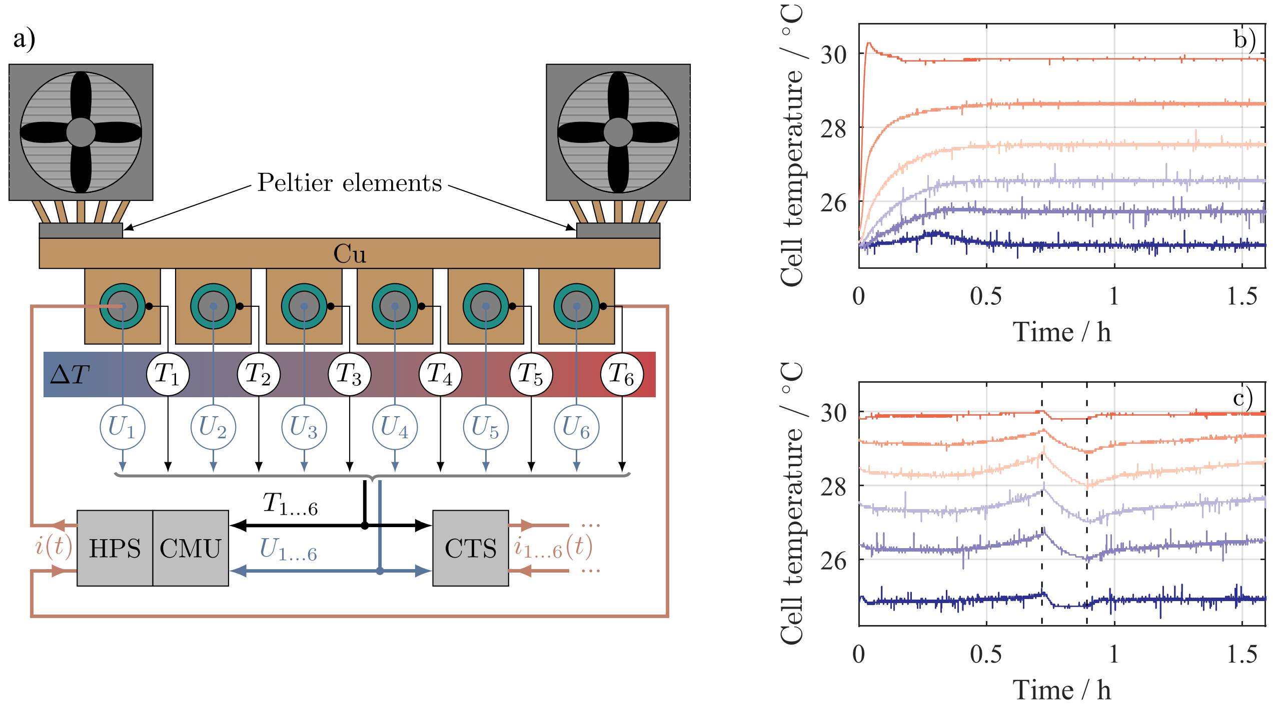

Fig. 1. (a) Overview of the test setup for 6s1p module aging with forced temperature gradient, (b) cell surface temperature while applying a temperature gradient ΔT = 5 K without current load, (c) cell surface temperature during 1 C discharge, 10 min pause and subsequent 1 C charge, while applying a temperature gradient ΔT = 5 K.

2.2. *Test sequence*

In the following, the checkup routine and overall test sequence are described. Each checkup measurement included a slow constant current (CC) discharge at 0.033 C for the purpose of differential voltage analyses (DVA) and subsequent R_{DC10s} determination at 50% SOC. DVA is an established method in order to analyze degradation mechanisms as loss of lithium inventory (LLI) and loss of active materials (LAM) and was successfully applied in the past [8,30,31]. At the same time, the CC discharge capacity was used for the evaluation of the degradation behavior and the determination of the absolute irreversible capacity loss. In order to guarantee a fixed starting point for a discharge, each cell was charged to 4.2 V via the constant current constant voltage protocol (CCCV). A detailed description of the checkup sequence is given in the Table 2. During the checkup measurements, all cells exhibited 25 °C and were rested at this temperature for at least 2h before the start of the measurement.

Fig. 2 gives an overview of all test sequences during the experiment. After the initial checkup measurement, the module was equalized by charging each cell at 25 °C to 4.2 V using the CCCV protocol, with a termination current of 0.001 C. Subsequently a temperature gradient ΔT = 5 K at 25 °C was applied with a thermal equalization time of 2h, in order to establish a homogeneous temperature distribution of between 25 °C and 30 °C. The cycling routine included four CC cycles with 1 C, and charge and discharge termination at the cell level at 4.2 V and 2.5 V respectively. For further investigations, which are not discussed in this work, a concatenation of randomly chosen load profiles from the database presented in [32] was applied with the same discharge termination criteria. A dynamic cycle was deemed to be a single CC cycle, despite the higher charge throughput. Subsequently, the module was CC charged to 4.2 V. Combined with CC cycles, the whole sequence was repeated four times, resulting in 20 consecutive cycles. After each cycling sequence, the temperature distribution was set back to 25 °C. All cells rested for at least 12 h after the last 1 C charge, so that most overpotentials were decayed [33]. Subsequently, clipboard wiring was changed to single cell configuration and each cell was connected to the CTS. Dissipative balancing was performed by discharging each cell to the lowest cell voltage U_{bal} (see Fig. 2) within the module using a CCCV protocol, with the termination current of 0.001 C. After that, the aforementioned checkup sequence from Table 2 took place, with conclusive 0.33 C, 0.66 C, 1 C charge and discharge pulses at 50% SOC, whereas a 1 C discharge pulse was used for R_{DC10s} determination. At the end, each cell was charged to the latest U_{bal} using a CCCV protocol, with a termination current of 0.001 C. This approach reduced the possible influence of checkup measurement on the voltage drift within the module. During the experiment, 200 cycles and 11 checkup measurements were conducted.

Table 2
Checkup sequence consists cycles for cell capacity determination (steps 3-4) and determination of internal impedance R_{DC10s} (steps 5-7).

Step	Parameters	Termination
1. Charge CCCV	I= 0.5 C, U= 4.2 V	I < 0.001 C
2. Pause		t > 30 min
3. Discharge CC	I= -0.033 C	U < 2.5 V
4. Pause		t > 30 min
5. Charge CC	I= 0.5 C	SOC >50%
6. Pause		t > 10 min
7. Discharge CC	I= -1 C	t > 10 s

3. Results and discussion

3.1. *Cell level*

In the following, the evaluation of checkup measurements during the experiment is presented and discussed. Fig. 3a depicts the progression of relative capacity for each cell over 200 cycles. The colors in Fig. 3 represent the position of each cell along the temperature gradient, whereby blue represents the coldest cell at 25 °C, and red represents the hottest cell at 30 °C. The results reveal that the forced temperature gradient facilitated different aging rates within in-series connection. During the first 40 cycles, all cells exhibited similar aging rates. Afterwards, the cell at 25 °C started to show an aggravated aging behavior, which continued till the end of the experiment, when it reached almost 80% of the initial capacity. The cell at 26 °C also exhibited an aggravated capacity loss, however the aging rate

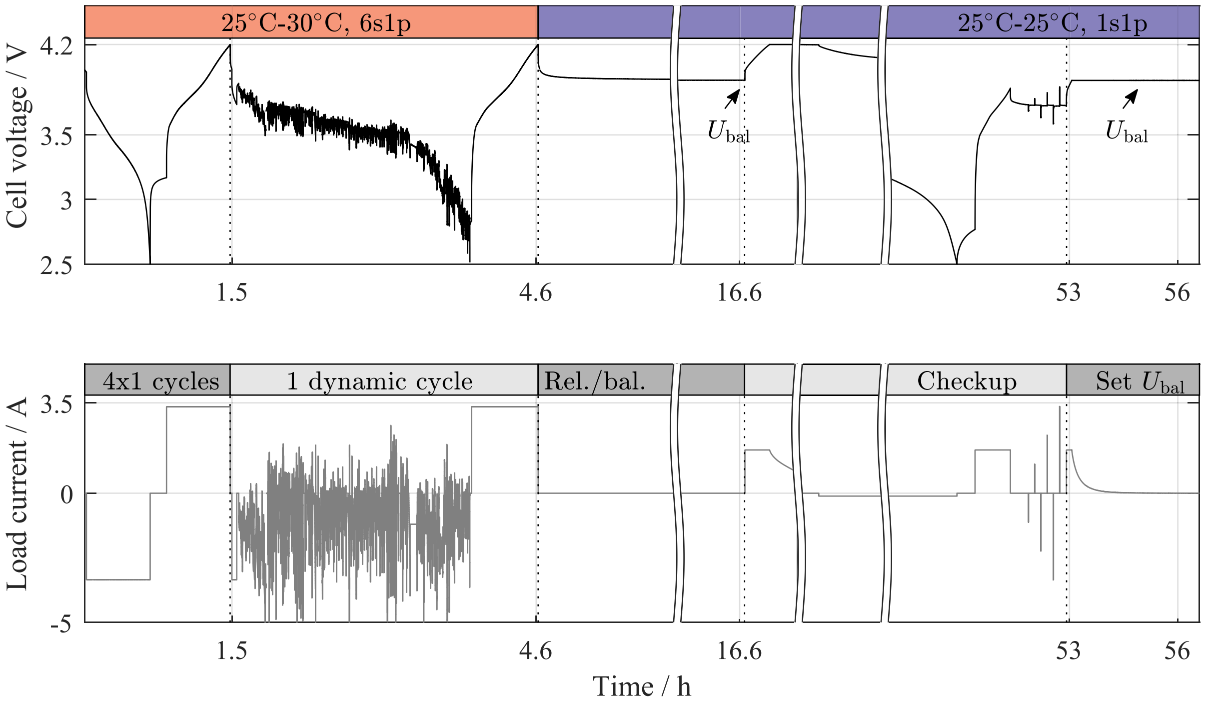

Fig. 2. Overview of all test sequences used in the aging experiment. Figure at the bottom depicts different current loads, whereas the figure at the top depicts the corresponding voltage response.

seemed to decelerate towards the end of the experiment, when it finally reached approx. 90% of the initial capacity. Cells above 26 °C all showed similar aging behavior, reaching approx. 94% of their initial capacities after 200 cycles. The progression of the impedance increase is depicted in Fig. 3b. The cell at 25 °C showed the highest increase, resulting in approx. 130% of the initial impedance at the end of the experiment. Similar to capacity progression, the cell at 26 °C also showed an additional impedance increase, whereas cells above 26 °C exhibited the least impedance increase. Furthermore, Fig. 3c presents the correlation between the relative capacity loss and impedance increase, which is similar for all cells in the module. It stands to reason that impedance could be used for the online determination of aging inhomogeneities within the scope of the presented 6s1p MJ1 module aging. However, not all lithium-ion cells exhibit such a consistent correlation between capacity loss and impedance increase [34], which makes this method not generally applicable.

The aforementioned aging behavior might be linked to the fact, that the charge throughput of a serial connection of cells is usually determined by the cell, which reaches the end of charge and discharge voltages first. It results in maximum depth of discharge (DOD) for the limiting cell and decreasing DOD for other cells during the course of aging. Furthermore, temperature dependency on degradation behavior during cycling and in particular improved capacity retention at elevated temperatures, were already reported in literature [35–37]. Such behavior was linked to irreversible capacity loss due to lithium plating at lower temperatures.

In general, power fade and deteriorating energy storage ability are often linked to side reactions and the loss of active materials (LAM) on both electrodes [30,38]. LAM is usually attributed to the particle cracking and loss of electrical contact [30]. In that way, a part of the electrode's active mass is no longer available for the intercalation and deintercalation of lithium, which can be observed in the compression of the half-cell potential [39]. Anodic side reactions, such as the growth and repair of the solid electrolyte interface (SEI), result in LLI, which leads to a delithiation of the negative electrode and an associated shift of the anode half-cell potential, resulting in capacity decrease [40]. Several studies have shown that both degradation mechanisms might occur simultaneously in cells with a pure graphite anode [41] and with a silicon-graphite blend anode [42,43]. Furthermore, LAM at low SOCs was deemed to be responsible for degradation of the silicon-graphite electrode due to high mechanical stress during lithiation [44,45].

Cathodic side reactions, such as electrolyte oxidation and transition-metal dissolution, provoke a reinsertion of lithium into the positive electrode, which can be observed in form of a potential decrease without any capacity loss [46,47], and might even lead to an increase in cell capacity [31]. Similarly to anodic side reactions, cathodic side reactions also result in an associated shift of the cathode half-cell potential. However, side reactions, such as transition metal dissolution, might also lead to LAM. It has been shown that increased NMC cathode

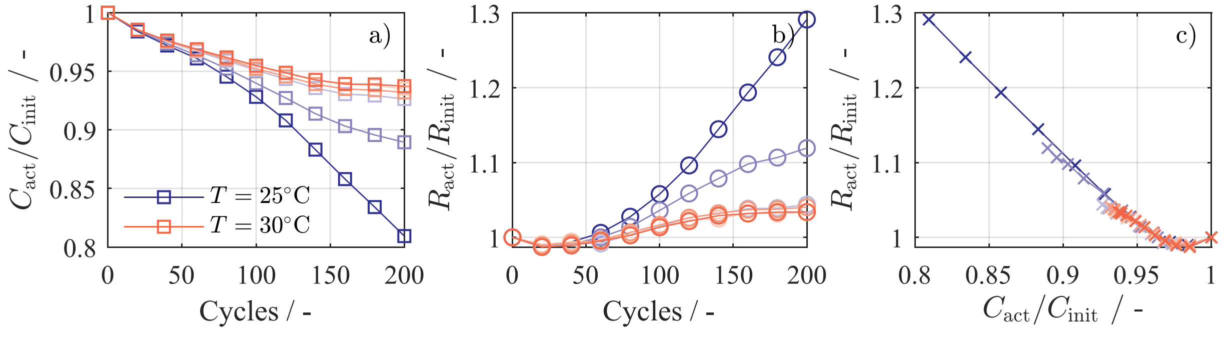

Fig. 3. (a) Relative capacity loss of each cell, (b) relative impedance increase of each cell, (c) correlation between capacity loss and impedance increase.

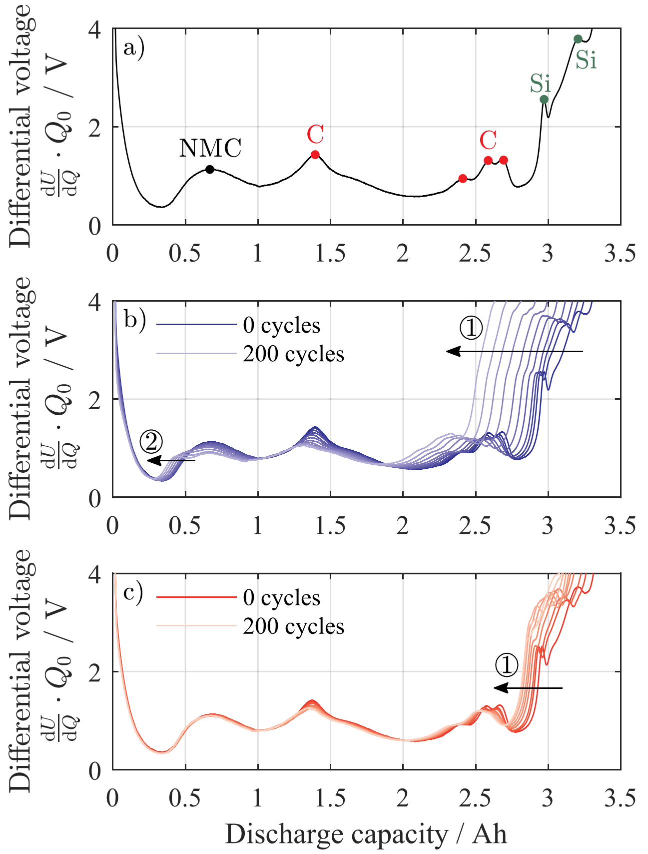

Fig. 4. (a) Measured differential voltage of the full cell for a 0.033 C discharge with assigned characteristic material markers, (b) differential voltage progression of the cell cycled at 25 °C, (c) differential voltage progression of the cell cycled at 30 °C.

potential accelerated the degradation of active materials [48,49], especially in the case of nickel rich cathodes [50].

Due to the shift and compression of half-cell potentials, the described degradation mechanisms can be observed via differential voltage analysis (DVA), which has been already successfully applied in the past [51]. Fig. 4a depicts the differential voltage in the discharge direction of the MJ1 cell, with accordingly distinctive material markers. Graphite electrodes usually exhibit a steep ascent of the potential towards delithiation [52]. Silicon-graphite composite electrodes, on the other hand, exhibit a smoother increase [53]. A smooth increase of this type results in two distinctive peaks in the differential voltage of the negative electrode and can be also observed in the full-cell characteristic between 2.9 Ah and 3.4 Ah in Fig. 4a. The distance between those two peaks is attributed to the storage capability of silicon. The peak at ca. 1.4 Ah indicates the phase transition between LiC_{12} and LiC_6 [54]. Further phase transition peaks of graphite are located between 2.4 Ah and 2.7 Ah. Finally, the nickel-rich cathode is represented only with one peak at ca. 0.7 Ah [29].

Fig. 4b shows the evolution of differential voltages of the cell at 25 °C during cycling, whereby all curves are aligned at the left side. Over the course of aging, the distance between Si distinctive peaks decreased, such that no part of either peak was noticeable, which is a sign for the loss of storage capability of silicon in the anode. However, the overall cell capacity loss was much higher and bore no relation to the loss of silicon, as depicted by ① in Fig. 4b. Furthermore, a shift of the NMC peak was observed ②. Previously, a case study was conducted, which investigated how different degradation mechanisms influence the differential voltage of the full cell through the compression and shifting of the half-cell potentials of the MJ1 cell [8]. The results revealed that the shift in the NMC peak as in ② is a sign of LAM at the negative electrode, which occurred at low SOC. Despite a small shift in the main graphite peak, no statement regarding the LLI can be made, since the negative electrode suffered from LAM according to DVA. The cell at 30 °C did not exhibit such severe degradation, as shown in the evolution of differential voltages during cycling in Fig. 4c. It can be seen that the presence of silicon faded ① over the course of aging, however, in contrast to the cell at 25 °C, the remainder of the differential voltage characteristics stayed almost the same.

From DVA it can be concluded that both cells suffered from a loss of silicon in the anode during cycle aging, which has been already reported in literature [44,45]. Such behavior was linked to the high volumetric expansion of silicon particles during the lithiation, which facilitated the separation of the electrical contact between particles. The cell at 25 °C suffered additionally from LAM at low SOC, which most likely led to the observed capacity decrease.

Deteriorated aging behavior is often linked to the deposition of metallic lithium, also referred to as lithium plating, which occurs on the negative electrode during charging [55]. Triggered by cell operation at high charge rates and/or low temperatures, lithium plating leads to severe capacity loss due to the formation of passivating surface films and due to the consumption of lithium [56,57]. Lithium plating occurs if the potential at the graphite electrode-electrolyte interface falls below 0V vs. Li/Li+. Under certain circumstances a reverse reaction - lithium stripping - can be observed, however this process is not completely reversible [58,59]. The presence of lithium stripping is usually a clear evidence for occurred plating reaction. A striping reaction is evident in the relaxation voltage, which exhibits a slower relaxation, sometimes even a plateau and is usually lower than normal relaxation voltage [60,61].

Fig. 5a depicts cell voltages and Fig. 5b temperatures during the 140th cycle and the subsequent relaxation phase at 25 °C before the balancing routine. After the cycling, the temperature control automatically switched to 25 °C for each cell and reached its set temperature

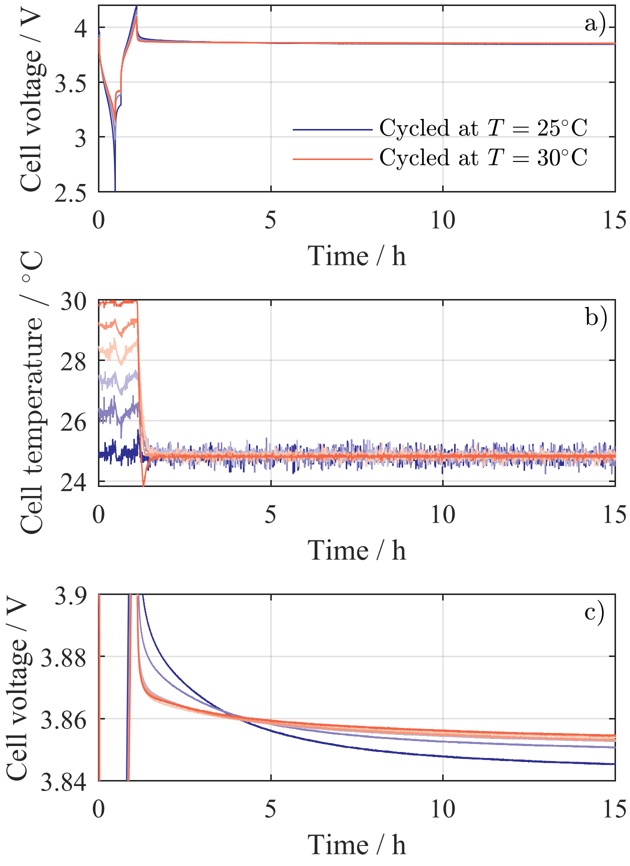

Fig. 5. (a) Cell voltages and (b) temperature during the 140th cycle and subsequent relaxation phase at 25 °C, (c) enlarged view of cell voltages during the relaxation phase.

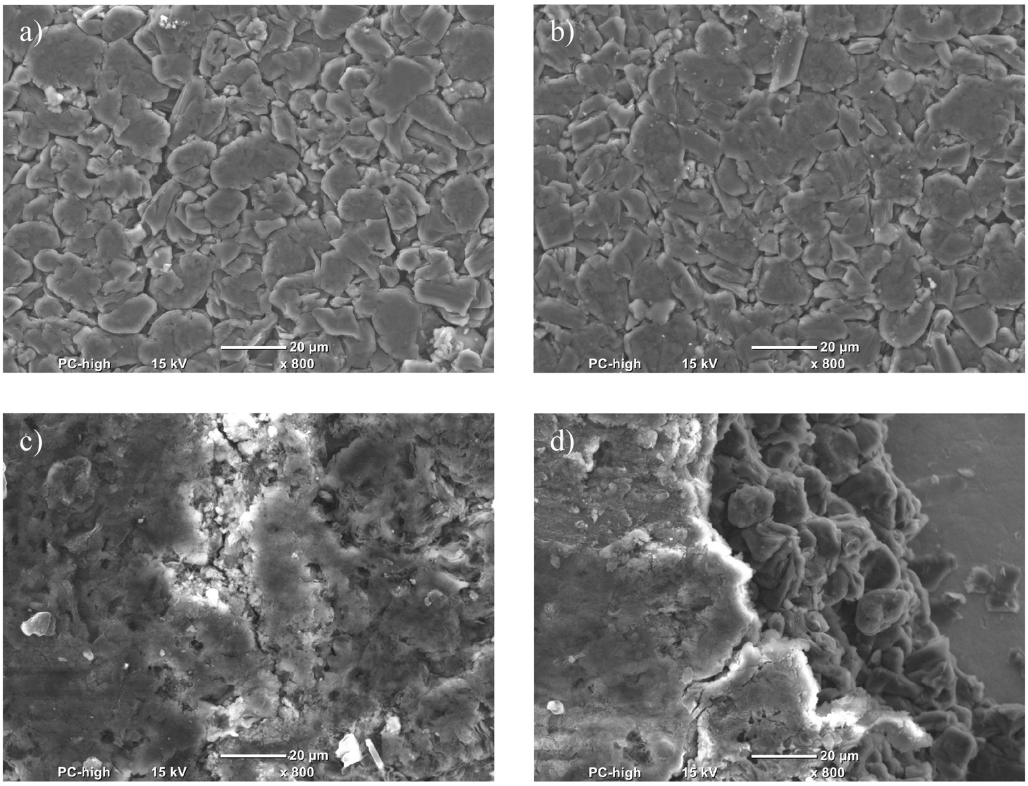

Fig. 6. SEM images of the negative electrode of (a) pristine cell, (b) cell aged at 30 °C, (c) cell aged at 25 °C, (d) cell aged at 25 °C with a provoked crack.

after 20 min, as shown in Fig. 5b. Therefore, during the relaxation process, all cells exhibited 25 °C. Fig 5c depicts an enlarged view of Fig. 5a. It can be seen that cells aged at 25 °C and 26 °C, which also showed deteriorated aging behavior, differed in voltage relaxation. The cell aged at 25 °C in particular exhibited the aforementioned stripping behavior, whereas cells above 26 °C exhibited a normal voltage relaxation behavior. Severe aging behavior of the cell at 25 °C was therefore most likely due to lithium plating. However, since it has been shown that voltage-plateau technique might be misleading due to concentration gradients within the cell [62], a post-mortem analysis was carried out and is described in the following.

In order to verify the presence of lithium plating, SEM images of the negative electrode were taken, whereby a pristine cell, the cell aged at 25 °C and the cell aged at 30 °C were compared. In the case of the inhomogeneous texture of the electrode, the probes were taken from areas which were the majority of the electrodes surface. Fig. 6a shows the anode particles of the pristine cell. The structure of the anode in Fig. 6b, which belongs to the cell aged at 30 °C, is not entirely altered, however, the arrangement of particles seems to be more dense. Such slight electrode degradation is in accordance with results from the DVA. In contrast, Fig. 6c, which represents the anode of the cell aged at 25 °C, shows severe structural differences. Individual graphite particles are no longer visible due to the inhomogeneous surface film near the separator. A provoked crack of the graphite electrode, which is shown in Fig. 6d, confirms that the observed film is confined to the surface layer, since intact particles are visible beneath it. Combined with results from DVA and voltage relaxation, the observed surface film is most likely a deposition of metallic lithium. Several simulative investigation of lithium plating revealed that such films initially occur near the separator [58,63], which is in accordance with the findings from the evaluation of SEM images.

Despite the use of easily deformed heat foil in the cell holder, the compression of cells can not be completely ruled out. It has been reported, that compression might facilitate lithium plating [64]. However, since all cells from the 6s1p module were placed in cell holders, and a clear temperature dependency regarding the aging behavior was observed, compression was most likely not the major reason for lithium plating.

The evaluation of single cell aging behavior revealed that the forced temperature gradient was able to cause different aging rates within a

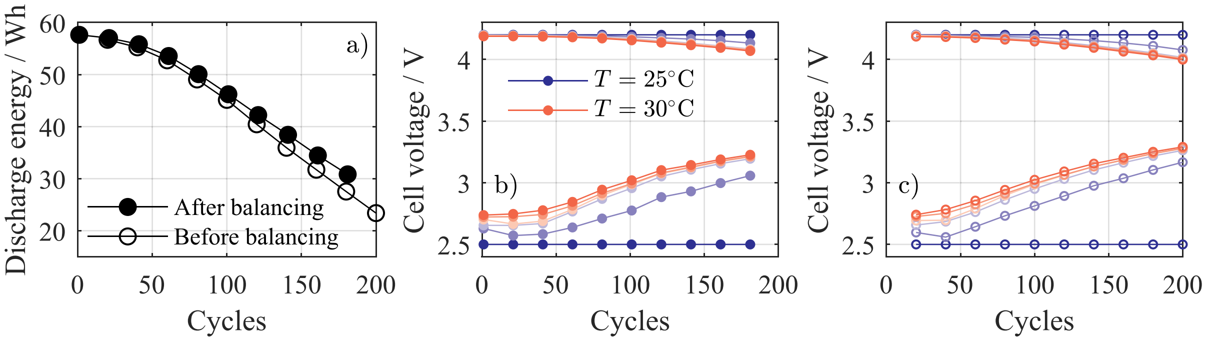

Fig. 7. (a) Progression of the module CC discharge energy before and after balancing, (b) end of charge and discharge voltages of each cell in the first cycle after balancing, (c) end of charge and discharge voltages of each cell in the last cycle before balancing.

6s1p module. During cycle aging, all cells suffered from the loss of storage capability of the silicon. Cells aged at 25 °C and 26 °C additionally experienced lithium plating, which led to severe capacity loss due to the loss of active materials of the anode at low SOC. Furthermore, the limiting cell experienced the highest DOD and therefore the highest mechanical stress, which could increase overpotentials and facilitate lithium plating.

3.2. Module level

In the following, the influence of different cell degradation rates on module aging behavior is described and progressions of module discharge energy, voltage imbalance and balancing charges are presented. Fig. 7a shows the progression of module discharge energy, which was withdrawn in the last cycle before and at the second cycle after the balancing procedure. The second discharge cycle was used for comparison due to the application of the dissipative equalization technique, which deteriorated the discharge energy of the first cycle after balancing. The results reveal that the discharge energy decreased almost by half after 200 cycles, despite the positive influence of cell balancing.

The origin of such behavior lay in the progression of cell voltages, which are shown in Fig. 7b and c. Fig. 7b depicts the end-of-charge and end-of-discharge voltages after - and Fig. 7c before - the balancing routine. From the beginning of the experiment, the cell at 25 °C remained the limiting cell, reaching the end-of-charge and discharge voltages first, whereas the cell at 30 °C exhibited the highest end-of-discharge voltage as early as the first cycle. Such behavior was linked to reduced overpotentials of lithium-ion cells at higher temperatures [65]. The combination of aggravated capacity loss and impedance increase of the cell at 25 °C, and steep slope of the OCV in the low SOC region resulted in an increasing difference between the end-of-charge voltages. Such behavior is not unusual, since the goal of dissipative balancing is to maximize the available energy by equalizing cell voltages at the upper area of the SOC. In that way, cells would exhibit higher voltage during the discharge, resulting in a higher voltage discrepancy towards the end-of-discharge, as confirmed by the presented results.

Despite the application of dissipative balancing, the differences between single end-of-charge voltages also increased during the module aging. Due to the lack of a CV phase after CC charging and the high impedance of the limiting cell, the relaxation voltage was several hundred mV lower than the end-of-charge voltage at 4.2 V. Equalization at the relaxation voltage and increasing capacity difference consequently led to a voltage drift at the end of charge. Such balancing strategy would not be applicable for industrial applications, since the module was not optimally utilized, however, it demonstrated that dissipative balancing was able to improve overall energy content. The influence of balancing can be also seen in Fig. 7b, in which the end-of-charge voltages are slightly higher than in Fig. 7c, which allowed a longer discharge, resulting in increased energy.

The dissipated balancing charges for each cell after every 20 cycles are shown in Fig. 8a. The limiting cell at 25 °C exhibited the lowest voltage before the balancing routine. Therefore its balancing charge remained zero over the course of the experiment. Even after the first 20 cycles, the balancing charge started to increase, whereas the cell at 30 °C remained the cell with the highest balancing effort. Since the differences between single balancing charges were not clearly separable, the cumulative balancing charge was additionally evaluated, which is shown in Fig. 8b. The progressions of cumulative balancing charges reveal a finer resolution of the temperature dependency, whereas the higher temperature during cycling resulted in a higher cumulative balancing charge. Fig. 8c depicts differences between the capacity of the limiting and the remaining cells during the experiment. A correlation plot between the cumulative balancing charge and capacity differences, shown in Fig. 8f, reveals a strong correlation (Pearson = 0.995) between the two parameters. It can be therefore deduced that within the scope of the presented experiment, a cumulative balancing charge might be used for online aging determination, or at least for the recognition of lithium plating.

Fig. 8 d depicts voltage differences between the limiting and the remaining cells immediately before the balancing procedure, and after 12 h of voltage relaxation at 25 °C. The voltage differences increased during the aging, despite the application of dissipative balancing every 20 cycles. At the end of the experiment, the voltage difference between the limiting and remaining cells amounted to almost 20 mV. Assuming that changes in OCV during aging are negligible and that all cells exhibit almost the same self-discharge rates, an equal charge and discharge of the in-series connection of cells would not lead to any voltage drift, since all cell blocks would exhibit the same charge throughput. Even altering capacities and impedances would not cause a voltage drift, as long as the charge throughput were the

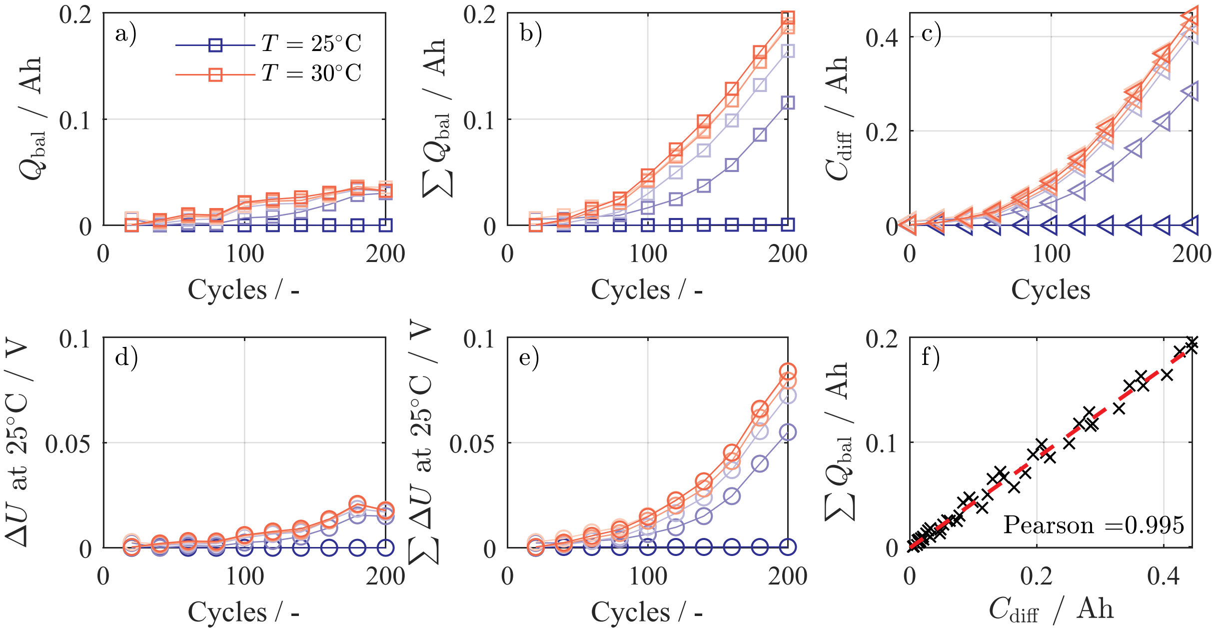

Fig. 8. (a) Progression of balancing charge of each cell, (b) cumulative balancing charge of each cell, (c) capacity differences between the limiting and remaining cells, (d) progression of voltage differences between cells with the lowest and remaining voltages at the end of the relaxation phase, (e) cumulative voltage differences between cells with the lowest and remaining voltages at the end of the relaxation phase, (f) correlation between cumulative balancing charge and capacity differences with the corresponding Pearson coefficient.

same for all cell blocks. In contrast to that, in the case of lithium plating, the charge would not only participate in the main intercalation reaction but also in parasitic plating reaction, resulting in the formation of passivating surface films. In that way, cells, which experienced lithium plating would exhibit lower charge throughput, resulting in lower SOC. Therefore, in combination with the asymmetric characteristic of the reversed stripping reaction [60], the observed high voltage drift within the 6s1p module is most likely linked to lithium plating.

The cumulative voltage differences, as shown in Fig. 8e reveal similar dependency in comparison to cumulative balancing charges. However, this outcome is due to the linear relationship between the OCV and SOC, where the evaluation of relaxation voltages took place. If the OCV characteristic exhibited a high curvature or, in general, a non-linear behavior, the cumulative voltage differences would be misleading.

Despite the fact that the complete potential of the 6s1p module was not utilized during cycling, dissipative balancing accomplished to increase the energy of the module. Voltage drift was most likely brought about by the lithium-plating reaction of colder cells and cumulative balancing charge was able to reflect differences in the capacity and aging behavior of single cells.

4. Summary and conclusion

In this work, cycle aging behavior of a 6s1p battery module with dissipative balancing and forced temperature distribution was investigated. The temperature gradient amounted to 5 K, ranging from 25 °C to 30 °C during cycling. After every 20 cycles the temperature of all cells was set to 25 °C, after which the balancing routine and checkup measurements were conducted. Degradation mechanisms were analyzed using differential voltages over the course of the experiment. Additionally, SEM images of negative electrodes were taken as a part of post-mortem analysis. The main findings are summarized below:

1. Temperature gradient during cycling led to differing aging rates, whereas the colder cells showed aggravated aging behavior. DVA revealed that all cells suffered from the loss of storage capabilities of silicon. However, the severe degradation of colder cells was linked to lithium plating, possibly due to deeper cycling and therefore the increased mechanical stress of the negative electrode.
2. Plating reaction caused the majority of the voltage drift within the in-series configuration of cells, limiting the module's available energy. The application of dissipative balancing allowed an improved utilization of the module.
3. The cumulative balancing charge showed a strong correlation with capacity differences between the limiting and remaining cells.

The results of this experimental study suggest, that the evaluation of the cumulative balancing charge might be used for the online detection of lithium plating in MJ1 battery packs. However, there are some limitations to this approach. The equalization must take place in an idle state, in order to ensure that the terminal voltage is not disturbed by high load currents. Additionally, a homogeneous temperature distribution must be provided during the balancing procedure. Furthermore, a sufficient voltage measurement accuracy, low tolerance balancing resistors and stable clock source for numerical current integration have to be considered in the BMS design. Therefore, further validation must be performed in order to ensure the applicability of the presented balancing strategy with different lithium-ion chemistries, battery pack configurations and different thermal gradients. Future work will address how different aging mechanisms affect the OCV and the terminal voltage, and subsequently the state of inhomogeneity of the battery pack.

CRediT authorship contribution statement

I. Zilberman: Conceptualization, Methodology, Software, Validation, Visualization, Investigation, Writing - original draft, Writing - review & editing. **S. Ludwig:** Writing - review & editing, Methodology, Investigation. **M. Schiller:** Validation. **A. Jossen:** Resources, Writing - review & editing.

Declaration of Competing Interest

The authors declare that they have no known competing financial interests or personal relationships that could have appeared to influence the work reported in this paper.

Acknowledgements

This work has received funding from the European Union's Horizon 2020 research and innovation program under the grant "Electric Vehicle Enhanced Range, Lifetime And Safety Through INGenious battery management" (EVERLASTING 713771). The presented data of this work is available under [http://doi.org/10.4121/uuid:f4575140-b2cf-4aa2-a6d5-e48d60dc0f8f]

The authors would like to thank Korbinian Schmidt for supporting with the design and assembly of the experimental setup.

References

[1] B. Scrosati, J. Garche, Lithium batteries: Status, prospects and future, J. Power Sources 195 (9) (2010) 2419–2430, https://doi.org/10.1016/j.jpowsour.2009.11.048.
[2] G.E. Blomgren, The development and future of lithium ion batteries, J. Electrochem. Soc. 164 (1) (2017) A5019–A5025, https://doi.org/10.1149/2.0251701jes.
[3] V. Reber, Neue Möglichkeiten Durch Laden mit 800 Volt, 2016(accessed March 15, 2019), URL: https://www.porscheengineering.com/filestore/download/peg/de/pemagazin-01-2016-artikel-e-power/default/047e5361-3dfb-11e6-8697-0019999cd470/e-power-%E2%80%93-Neue-M%C3%B6glichkeiten-durch-Laden-mit-800-Volt-Porsche-Engineering-Magazin-01-2016.pdf.
[4] M.M. Hoque, M.A. Hannan, A. Mohamed, A. Ayob, Battery charge equalization controller in electric vehicle applications: a review, Renew. Sustain. Energy Rev. 75 (2017) 1363–1385, https://doi.org/10.1016/j.rser.2016.11.126.
[5] L. Zhou, Y. Zheng, M. Ouyang, L. Lu, A study on parameter variation effects on battery packs for electric vehicles, J. Power Sources 364 (2017) 242–252, https://doi.org/10.1016/j.jpowsour.2017.08.033.
[6] L. Lu, X. Han, J. Li, J. Hua, M. Ouyang, A review on the key issues for lithium-ion battery management in electric vehicles, J. Power Sources 226 (2013) 272–288, https://doi.org/10.1016/j.jpowsour.2012.10.060.
[7] I. Zilberman, S. Ludwig, A. Jossen, Cell-to-cell variation of calendar aging and reversible self-discharge in 18650 nickel-rich, silicon–graphite lithium-ion cells, J. Energy Storage 26 (2019) 100900, https://doi.org/10.1016/j.est.2019.100900.
[8] I. Zilberman, J. Sturm, A. Jossen, Reversible self-discharge and calendar aging of 18650 nickel-rich, silicon-graphite lithium-ion cells, J. Power Sources 425 (2019) 217–226, https://doi.org/10.1016/j.jpowsour.2019.03.109.
[9] J. Schnell, C. Nentwich, F. Endres, A. Kollenda, F. Distel, T. Knoche, G. Reinhart, Data mining in lithium-ion battery cell production, J. Power Sources 413 (2019) 360–366, https://doi.org/10.1016/j.jpowsour.2018.12.062.
[10] K. Rumpf, M. Naumann, A. Jossen, Experimental investigation of parametric cell-to-cell variation and correlation based on 1100 commercial lithium-ion cells, J. Energy Storage 14 (2017) 224–243, https://doi.org/10.1016/j.est.2017.09.010.
[11] B. Kenney, K. Darcovich, D.D. MacNeil, I.J. Davidson, Modelling the impact of variations in electrode manufacturing on lithium-ion battery modules, J. Power Sources 213 (2012) 391–401, https://doi.org/10.1016/j.jpowsour.2012.03.065.
[12] D. Shin, M. Poncino, E. Macii, Naehyuck Chang, A statistical model-based cell-to-cell variability management of li-ion battery pack, IEEE Trans. Computer-Aided Des.Integr. Circuits Syst. 34 (2) (2015) 252–265, https://doi.org/10.1109/TCAD.2014.2384506.
[13] T. Baumhöfer, M. Brühl, S. Rothgang, D.U. Sauer, Production caused variation in capacity aging trend and correlation to initial cell performance, J. Power Sources 247 (2014) 332–338, https://doi.org/10.1016/j.jpowsour.2013.08.108.
[14] A. Tang, J. Li, L. Lou, C. Shan, X. Yuan, Optimization design and numerical study on water cooling structure for power lithium battery pack, Appl. Thermal Eng. 159 (2019) 113760, https://doi.org/10.1016/j.applthermaleng.2019.113760.
[15] C. Zhao, W. Cao, T. Dong, F. Jiang, Thermal behavior study of discharging/charging cylindrical lithium-ion battery module cooled by channeled liquid flow, Int. J. Heat Mass Transf. 120 (2018) 751–762, https://doi.org/10.1016/j.ijheatmasstransfer.2017.12.083.
[16] B. Wu, V. Yufit, M. Marinescu, G.J. Offer, R.F. Martinez-Botas, N.P. Brandon, Coupled thermal–electrochemical modelling of uneven heat generation in lithium-ion battery packs, J. Power Sources 243 (2013) 544–554, https://doi.org/10.1016/j.jpowsour.2013.05.164.
[17] X.M. Xu, R. He, Research on the heat dissipation performance of battery pack based on forced air cooling, J. Power Sources 240 (2013) 33–41, https://doi.org/10.1016/j.jpowsour.2013.03.004.
[18] M. Ecker, N. Nieto, S. Käbitz, J. Schmalstieg, H. Blanke, A. Warnecke, D.U. Sauer, Calendar and cycle life study of li(nimnco)o2-based 18650 lithium-ion batteries, J. Power Sources 248 (2014) 839–851, https://doi.org/10.1016/j.jpowsour.2013.09.143.

[19] M. Naumann, M. Schimpe, P. Keil, H.C. Hesse, A. Jossen, Analysis and modeling of calendar aging of a commercial lifepo4/graphite cell, J. Energy Storage 17 (2018) 153–169, https://doi.org/10.1016/j.est.2018.01.019.

[20] M. Baumann, L. Wildfeuer, S. Rohr, M. Lienkamp, Parameter variations within li-ion battery packs – theoretical investigations and experimental quantification, J. Energy Storage 18 (2018) 295–307, https://doi.org/10.1016/j.est.2018.04.031.

[21] S.F. Schuster, M.J. Brand, P. Berg, M. Gleissenberger, A. Jossen, Lithium-ion cell-to-cell variation during battery electric vehicle operation, J. Power Sources 297 (2015) 242–251, https://doi.org/10.1016/j.jpowsour.2015.08.001.

[22] S. Paul, C. Diegelmann, H. Kabza, W. Tillmetz, Analysis of ageing inhomogeneities in lithium-ion battery systems, J. Power Sources 239 (2013) 642–650, https://doi.org/10.1016/j.jpowsour.2013.01.068.

[23] M.P. Klein, J.W. Park, Current distribution measurements in parallel-connected lithium-ion cylindrical cells under non-uniform temperature conditions, J. Electrochem. Soc. 164 (9) (2017) A1893–A1906, https://doi.org/10.1149/2.0011709jes.

[24] K.-C. Chiu, C.-H. Lin, S.-F. Yeh, Y.-H. Lin, C.-S. Huang, K.-C. Chen, Cycle life analysis of series connected lithium-ion batteries with temperature difference, J. Power Sources 263 (2014) 75–84, https://doi.org/10.1016/j.jpowsour.2014.04.034.

[25] A. Cordoba-Arenas, S. Onori, G. Rizzoni, A control-oriented lithium-ion battery pack model for plug-in hybrid electric vehicle cycle-life studies and system design with consideration of health management, J. Power Sources 279 (2015) 791–808, https://doi.org/10.1016/j.jpowsour.2014.12.048.

[26] X. Wang, Z. Wang, L. Wang, Z. Wang, H. Guo, Dependency analysis and degradation process-dependent modeling of lithium-ion battery packs, J. Power Sources 414 (2019) 318–326, https://doi.org/10.1016/j.jpowsour.2019.01.021.

[27] Y. Zheng, M. Ouyang, L. Lu, J. Li, Understanding aging mechanisms in lithium-ion battery packs: From cell capacity loss to pack capacity evolution, J. Power Sources 278 (2015) 287–295, https://doi.org/10.1016/j.jpowsour.2014.12.105.

[28] C. Campestrini, P. Keil, S.F. Schuster, A. Jossen, Ageing of lithium-ion battery modules with dissipative balancing compared with single-cell ageing, J. Energy Storage 6 (2016) 142–152, https://doi.org/10.1016/j.est.2016.03.004.

[29] J. Sturm, A. Rheinfeld, I. Zilberman, F.B. Spingler, S. Kosch, F. Frie, A. Jossen, Modeling and simulation of inhomogeneities in a 18650 nickel-rich, silicon-graphite lithium-ion cell during fast charging, J. Power Sources 412 (2019) 204–223, https://doi.org/10.1016/j.jpowsour.2018.11.043.

[30] C.R. Birkl, M.R. Roberts, E. McTurk, P.G. Bruce, D.A. Howey, Degradation diagnostics for lithium ion cells, J. Power Sources 341 (2017) 373–386, https://doi.org/10.1016/j.jpowsour.2016.12.011.

[31] P. Keil, A. Jossen, Calendar aging of nca lithium-ion batteries investigated by differential voltage analysis and coulomb tracking, J. Electrochem. Soc. 164 (1) (2017) A6066–A6074, https://doi.org/10.1149/2.0091701jes.

[32] C. Campestrini, M.F. Horsche, I. Zilberman, T. Heil, T. Zimmermann, A. Jossen, Validation and benchmark methods for battery management system functionalities: State of charge estimation algorithms, J. Energy Storage 7 (2016) 38–51, https://doi.org/10.1016/j.est.2016.05.007.

[33] F.M. Kindermann, A. Noel, S.V. Erhard, A. Jossen, Long-term equalization effects in li-ion batteries due to local state of charge inhomogeneities and their impact on impedance measurements, Electrochimica Acta 185 (2015) 107–116, https://doi.org/10.1016/j.electacta.2015.10.108.

[34] N. Omar, M.A. Monem, Y. Firouz, J. Salminen, J. Smekens, O. Hegazy, H. Gaulous, G. Mulder, P. van den Bossche, T. Coosemans, J. van Mierlo, Lithium iron phosphate based battery – assessment of the aging parameters and development of cycle life model, Appl. Energy 113 (2014) 1575–1585, https://doi.org/10.1016/j.apenergy.2013.09.003.

[35] M. Ecker, P. Shafiei Sabet, D.U. Sauer, Influence of operational condition on lithium plating for commercial lithium-ion batteries – electrochemical experiments and post-mortem-analysis, Appl. Energy 206 (2017) 934–946, https://doi.org/10.1016/j.apenergy.2017.08.034.

[36] S.F. Schuster, T. Bach, E. Fleder, J. Müller, M. Brand, G. Sextl, A. Jossen, Nonlinear aging characteristics of lithium-ion cells under different operational conditions, J. Energy Storage 1 (2015) 44–53, https://doi.org/10.1016/j.est.2015.05.003.

[37] T. Waldmann, M. Wilka, M. Kasper, M. Fleischhammer, M. Wohlfahrt-Mehrens, Temperature dependent ageing mechanisms in lithium-ion batteries – a post-mortem study, J. Power Sources 262 (2014) 129–135, https://doi.org/10.1016/j.jpowsour.2014.03.112.

[38] J. Vetter, P. Novák, M.R. Wagner, C. Veit, K.-C. Möller, J.O. Besenhard, M. Winter, M. Wohlfahrt-Mehrens, C. Vogler, A. Hammouche, Ageing mechanisms in lithium-ion batteries, J. Power Sources 147 (1–2) (2005) 269–281, https://doi.org/10.1016/j.jpowsour.2005.01.006.

[39] K. Kleiner, P. Jakes, S. Scharner, V. Liebau, H. Ehrenberg, Changes of the balancing between anode and cathode due to fatigue in commercial lithium-ion cells, J. Power Sources 317 (2016) 25–34, https://doi.org/10.1016/j.jpowsour.2016.03.049.

[40] I. Bloom, A.N. Jansen, D.P. Abraham, J. Knuth, S.A. Jones, V.S. Battaglia, G.L. Henriksen, Differential voltage analyses of high-power, lithium-ion cells, J. Power Sources 139 (1–2) (2005) 295–303, https://doi.org/10.1016/j.jpowsour.2004.07.021.

[41] X. Han, M. Ouyang, L. Lu, J. Li, Y. Zheng, Z. Li, A comparative study of commercial lithium ion battery cycle life in electrical vehicle: Aging mechanism identification, J. Power Sources 251 (2014) 38–54, https://doi.org/10.1016/j.jpowsour.2013.11.029.

[42] M. Wetjen, D. Pritzl, R. Jung, S. Solchenbach, R. Ghadimi, H.A. Gasteiger, Differentiating the degradation phenomena in silicon-graphite electrodes for lithium-ion batteries, J. Electrochem. Soc. 164 (12) (2017) A2840–A2852, https://doi.org/10.1149/2.1921712jes.

[43] M. Klett, J.A. Gilbert, S.E. Trask, B.J. Polzin, A.N. Jansen, D.W. Dees, D.P. Abraham, Electrode behavior re-visited: Monitoring potential windows, capacity loss, and impedance changes in li 1.03 (ni 0.5 co 0.2 mn 0.3) 0.97 o 2 /silicon-graphite full cells, J. Electrochem. Soc. 163 (6) (2016) A875–A887, https://doi.org/10.1149/2.0271606jes.

[44] M. Wetjen, S. Solchenbach, D. Pritzl, J. Hou, V. Tileli, H.A. Gasteiger, Morphological changes of silicon nanoparticles and the influence of cutoff potentials in silicon-graphite electrodes, J. Electrochem. Soc. 165 (7) (2018) A1503–A1514, https://doi.org/10.1149/2.1261807jes.

[45] S. Müller, P. Pietsch, B.-E. Brandt, P. Baade, V. de Andrade, F. de Carlo, V. Wood, Quantification and modeling of mechanical degradation in lithium-ion batteries based on nanoscale imaging, Nature Commun. 9 (1) (2018) 2340, https://doi.org/10.1038/s41467-018-04477-1.

[46] N.N. Sinha, A.J. Smith, J.C. Burns, G. Jain, K.W. Eberman, E. Scott, J.P. Gardner, J.R. Dahn, The use of elevated temperature storage experiments to learn about parasitic reactions in wound licoo2 graphite cells, J. Electrochem. Soc. 158 (11) (2011) A1194, https://doi.org/10.1149/2.007111jes.

[47] J. Xu, R.D. Deshpande, J. Pan, Y.-T. Cheng, V.S. Battaglia, Electrode side reactions, capacity loss and mechanical degradation in lithium-ion batteries, J. Electrochem. Soc. 162 (10) (2015) A2026–A2035, https://doi.org/10.1149/2.0291510jes.

[48] I. Buchberger, S. Seidlmayer, A. Pokharel, M. Piana, J. Hattendorff, P. Kudejova, R. Gilles, H.A. Gasteiger, Aging analysis of graphite/lini 1/3 mn 1/3 co 1/3 o 2 cells using xrd, pgaa, and ac impedance, J. Electrochem. Soc. 162 (14) (2015) A2737–A2746, https://doi.org/10.1149/2.0721514jes.

[49] L.M. Thompson, W. Stone, A. Eldesoky, N.K. Smith, C.R.M. McFarlane, J.S. Kim, M.B. Johnson, R. Petibon, J.R. Dahn, Quantifying changes to the electrolyte and negative electrode in aged nmc532/graphite lithium-ion cells, J. Electrochem. Soc. 165 (11) (2018) A2732–A2740, https://doi.org/10.1149/2.0721811jes.

[50] J. Li, L.E. Downie, L. Ma, W. Qiu, J.R. Dahn, Study of the failure mechanisms of lini 0.8 mn 0.1 co 0.1 o 2 cathode material for lithium ion batteries, J. Electrochem. Soc. 162 (7) (2015) A1401–A1408, https://doi.org/10.1149/2.1011507jes.

[51] K. Honkura, T. Horiba, Study of the deterioration mechanism of licoo2/graphite cells in charge/discharge cycles using the discharge curve analysis, J. Power Sources 264 (2014) 140–146, https://doi.org/10.1016/j.jpowsour.2014.04.036.

[52] P. Keil, S.F. Schuster, J. Wilhelm, J. Travi, A. Hauser, R.C. Karl, A. Jossen, Calendar aging of lithium-ion batteries, J. Electrochem. Soc. 163 (9) (2016) A1872–A1880, https://doi.org/10.1149/2.0411609jes.

[53] V.G. Khomenko, V.Z. Barsukov, J.E. Doninger, I.V. Barsukov, Lithium-ion batteries based on carbon–silicon–graphite composite anodes, J. Power Sources 165 (2) (2007) 598–608, https://doi.org/10.1016/j.jpowsour.2006.10.059.

[54] T. Ohzuku, I. Yasunobi, S. Keijiro, Formation of lithium-graphite intercalation compunds in nonaqueous electrolytes and their application as a negative electrode for a lithium ion (shuttlecock) cell, J. Electrochem. Soc. 140 (9) (1993) 2490–2498, https://doi.org/10.1149/1.2220849jes.

[55] T. Waldmann, B.-I. Hogg, M. Wohlfahrt-Mehrens, Li plating as unwanted side reaction in commercial li-ion cells – a review, J. Power Sources 384 (2018) 107–124, https://doi.org/10.1016/j.jpowsour.2018.02.063.

[56] M. Ouyang, Z. Chu, L. Lu, J. Li, X. Han, X. Feng, G. Liu, Low temperature aging mechanism identification and lithium deposition in a large format lithium iron phosphate battery for different charge profiles, J. Power Sources 286 (2015) 309–320, https://doi.org/10.1016/j.jpowsour.2015.03.178.

[57] M. Petzl, M. Kasper, M.A. Danzer, Lithium plating in a commercial lithium-ion battery – a low-temperature aging study, J. Power Sources 275 (2015) 799–807, https://doi.org/10.1016/j.jpowsour.2014.11.065.

[58] C. von Lüders, J. Keil, M. Webersberger, A. Jossen, Modeling of lithium plating and lithium stripping in lithium-ion batteries, J. Power Sources 414 (2019) 41–47, https://doi.org/10.1016/j.jpowsour.2018.12.084.

[59] D. Ren, K. Smith, D. Guo, X. Han, X. Feng, L. Lu, M. Ouyang, J. Li, Investigation of lithium plating-stripping process in li-ion batteries at low temperature using an electrochemical model, J. Electrochem. Soc. 165 (10) (2018) A2167–A2178, https://doi.org/10.1149/2.0661810jes.

[60] C. von Lüders, V. Zinth, S.V. Erhard, P.J. Osswald, M. Hofmann, R. Gilles, A. Jossen, Lithium plating in lithium-ion batteries investigated by voltage relaxation and in situ neutron diffraction, J. Power Sources 342 (2017) 17–23, https://doi.org/10.1016/j.jpowsour.2016.12.032.

[61] S. Schindler, M. Bauer, M. Petzl, M.A. Danzer, Voltage relaxation and impedance spectroscopy as in-operando methods for the detection of lithium plating on graphitic anodes in commercial lithium-ion cells, J. Power Sources 304 (2016) 170–180, https://doi.org/10.1016/j.jpowsour.2015.11.044.

[62] I.D. Campbell, M. Marzook, M. Marinescu, G.J. Offer, How observable is lithium plating? Differential voltage analysis to identify and quantify lithium plating following fast charging of cold lithium-ion batteries, J. Electrochem. Soc. 166 (4) (2019) A725–A739, https://doi.org/10.1149/2.0821904jes.

[63] P. Arora, Mathematical modeling of the lithium deposition overcharge reaction in lithium-ion batteries using carbon-based negative electrodes, J. Electrochem. Soc. 146 (10) (1999) 3543, https://doi.org/10.1149/1.1392512.

[64] T.C. Bach, S.F. Schuster, E. Fleder, J. Müller, M.J. Brand, H. Lorrmann, A. Jossen, G. Sextl, Nonlinear aging of cylindrical lithium-ion cells linked to heterogeneous compression, J. Energy Storage 5 (2016) 212–223, https://doi.org/10.1016/j.est.2016.01.003.

[65] W. Waag, S. Käbitz, D.U. Sauer, Experimental investigation of the lithium-ion battery impedance characteristic at various conditions and aging states and its influence on the application, Appl. Energy 102 (2013) 885–897, https://doi.org/10.1016/j.apenergy.2012.09.030.

5 Summary and Conclusion

It is indisputable, that reliable and efficient energy storage solutions are one of the most important keys to a sustainable future. Despite the fact that lithium-ion technology has overcome many shortcomings in the past decade, a widespread use of the technology, especially in field of transportation, has still not been achieved. As the competitiveness of a mass produced technology is often linked to its cost, the widespread adoption of EVs cannot be expected, until the average EV prices match those of an ICE vehicle. Due to the fact that the main EV cost driver remains the powertrain and the battery pack in particular, a full utilization of battery pack capacity is indispensable for avoiding the overdimensioning and therefore for cost reduction.

Due to manufacturing tolerances, produced lithium-ion cells vary slightly in capacity, impedance and self-discharge rate. Furthermore, even under the same operational conditions, cells exhibit slightly different aging behaviors, aggravating the parameter variations even more. In series connection of cells is usually limited by the performance of the weakest cell, while the remaining capacity of the other cells stays unused. The phenomenon, of voltage imbalance in cells connected in series is generally well-known. In order to mitigate the performance limitations caused by the voltage imbalance, balancing systems are usually used. However, the true origin of the voltage imbalance is still not completely understood, which results in the design of battery packs with diminished utilization, requiring significant overdimensioning.

Therefore, within the scope of this thesis possible influencing factors on the voltage imbalance were investigated. For this purpose an analytical representation of the terminal voltage was derived, which aimed to identify the relevant influencing factors. The effects responsible were identified as differently changing stoichiometric properties and emerging differences in the lithium-ion concentration within the electrodes among the cells, whereby the causes were linked to varying self-discharge and aging rates between the cells. Further possible causes, such as lithium plating were also included in the analysis. Finally, the goals of this thesis were set to investigate the influence of different self-discharge rates, varying reaction entropies and enthalpies induced through non-identical aging and the influence of lithium plating on the voltage imbalance. For the purpose of the experimental evaluation, a new flexible prototyping platform for battery management systems (EES-BMS) was developed. Since lithium-ion cells containing nickel-rich cathodes and SiC anodes are expected to be deployed in the next generation of EVs, the object of this work was a commercial NMC(nickel-rich)/SiC 18650 high energy lithium-ion cell INR18650-MJ1 from LGChem.

In order to quantify the reversible self-discharge, a new voltage based measurement method was developed. In the presented study, the capacity fade of commercial 18650 nickel-rich/SiC cells after 11 months of storage in a climate chamber was analyzed using DVA. Reversible self-discharge losses were determined via capacity measurements before and after the storage and via the decay of cell voltages, which were monitored throughout the experiment. The results obtained in this work revealed that capacity fade during the storage was mainly caused by the LAM from the anode, which was linked to the presence of silicon. The calculated reversible self-discharge current ranged between 2 µA and

4.5 µA at 25 °C and was most likely caused by coupled side reactions between the negative and positive electrodes, triggered by LLI at the anode. Anode overhang impeded the capacity based self-discharge measurement, caused long-term voltage relaxation and induced capacity recovery effect during cycling after the storage. The overall influence of the anode overhang was non-negligible and had to be taken into account in further voltage-based self-discharge measurements.

This voltage-based measurement method was applied in order to investigate self-discharge variations and their influence on voltage imbalance. In the presented study, initial cell parameter distributions were analyzed via DVA and variations of calendar aging and reversible self-discharge rates of 24 MJ1 cells were statistically evaluated. After initial characterization, all cells were stored for 10 months at a 70 % SOC and at a temperature of 25 °C, whereby the final two weeks of storage were used for reversible self-discharge determination via voltage decay. The results obtained in this work revealed that initial capacity and impedance variations depend neither on electrode balancing, nor the storage capabilities of NMC, silicon or graphite. Relative variance of initial capacity and impedance distributions amounted to 0.2 % and 0.68 % respectively. Besides a moderate correlation between the capacity and silicon to graphite ratio in the anode, no further dependencies on material markers in differential voltage were found. Statistical evaluation of calendar aging revealed, that examined cells exhibited constant aging rates. Relative capacity variance doubled during the storage, whereas the relative variance of the impedance remained almost the same. Further analysis revealed that after the manufacturing process all cells were most likely matched by capacity. Relative variance of self-discharge currents amounted to 10 %. Furthermore, no correlations between self-discharge and remaining cell parameters were observed. Using a proposed self-discharge model, it was shown, that the maximum voltage difference within the battery pack caused by differences in self-discharge remained under the typical cell balancing activation threshold of 5 mV.

In order to investigate the influence of different aging rates on full-cell entropy profiles and therefore the terminal voltage, new precise entropy determination method was developed. In the presented study, the potentiometric method was more closely investigated regarding the often assumed linear relationship between the OCV and temperature and possible associated measurement inaccuracies. Four different, completely equalized lithium-ion cells comprising different chemistries and cell formats were object of this study. Two different temperature profiles with varying frequency and amplitude components were applied and according entropic coefficients were calculated based on the preceding data. The results obtained in this work clearly revealed a non-linear behavior of the voltage to temperature relationship regardless of the cell format, SOC, cell chemistry or sign of the derived entropic coefficient. This non-linearity manifested itself in a certain hysteresis of the OCV depending on the temperature history of the cells. The results suggested to minimize the temperature pulse duration whilst still allowing for a thermal equalization of the cell. Additionally, it was suggested to minimize the amplitude of the temperature pulse as much as possible, whilst still allowing for an acceptable SNR for the measured voltage response. This method was applied to determine the half-cell entropy profiles, which were then validated via calorimetric measurements. Using a shift of the anode half-cell entropy profile in order to mimic the mechanism of LLI, it could be shown, that entropy induced voltage imbalance accounted for less than 5 mV in this work.

Individually analyzed influencing factors regarding the voltage imbalance were integrated into a holistic battery pack (168s20p) lifetime simulation framework, which included cell-to-cell parameter variations, differing aging and self-discharge rates, temperature gradients among the cells and various balancing strategies. A Monte Carlo simulation using this framework was performed in order to investigate the possible interaction of the influencing factors on the voltage imbalance. The results obtained in this study revealed that intrinsic aging variations represented a major influence on the utilization of the battery pack. On the other hand, initial variations of the cell capacity and impedance played a rather minor role in the utilization of the battery pack, due to a decrease in the relative variance of cells connected in parallel. Therefore, cell matching for similar battery packs seemed to be dispensable, assuming only a minor influence of possible temperature gradients along the parallel connection of cells. Different self-discharge rates, as well as different aging rates contributed to a voltage drift within the in-series connection of cells. However, simulated maximum voltage differences did not exceed 25 mV at the end of life, even in the presence of temperature gradients.

In order to verify the outcome of the four studies, the final presented work experimentally evaluated the influence of differing operational conditions within a 6s1p module on voltage imbalance. In this study, a forced temperature gradient along six in-series connected MJ1 cells was applied during cycles resulting in cell temperatures of between 25 °C and 30 °C. The 6s1p module was equalized using dissipative balancing after every 20 cycles. Aging behavior was analyzed using checkup measurements, DVA and conclusive scanning electron microscope (SEM) imaging of the negative electrodes. The results obtained in this work revealed that the forced temperature gradient caused different degradation rates, with the colder cells exhibiting aggravated aging behavior, which was linked to lithium plating. Furthermore, this lithium plating caused the majority of the voltage drift within the module, which amounted to >75 mV. Finally, the cumulative balancing charge showed a strong correlation with capacity differences between the limiting and remaining cells.

The results presented in this thesis suggest that the use of dissipative balancing can generally improve the utilization of large battery packs, however the required investment in extra hardware, wiring and control methods is rather doubtful, since the absolute improvement shown by the simulated 168s20p battery pack is under 2 %. The validity of such recommendation is closely linked to the operational conditions of the battery pack and to the quality of the lithium-ion cells deployed. If the battery system is operated far below the absolute maximum ratings set by the cell manufacturer and the lithium-ion cells exhibit low intrinsic aging variations, balancing circuits can be omitted. On the other hand, battery systems, which are already equipped with balancing hardware or with to retain cell balancing might profit from utilizing an extra signal, since cumulated balancing charge could be used as an indicator for lithium plating. However, in order to increase the general validity of the above mentioned statements, more cell chemistries and formats have to be investigated regarding the causes of voltage imbalance. Furthermore, due to almost full utilization of the anode, the MJ1 cell was highly prone to lithium plating. Therefore, the experimental studies should be repeated using cells with incomplete utilization of the anode. Finally, more attention should be payed to the influence of the parallel connection, which was highly simplified in this work.

List of Figures

List of Tables

List of References

[1] B. Scrosati and J. Garche. “Lithium batteries: Status, prospects and future”. In: *Journal of Power Sources* 195.9 (2010), pp. 2419–2430. ISSN: 03787753. DOI: `10.1016/j.jpowsour.2009.11.048`.

[2] George E. Blomgren. “The Development and Future of Lithium Ion Batteries”. In: *Journal of The Electrochemical Society* 164.1 (2017), A5019–A5025. ISSN: 0013-4651. DOI: `10.1149/2.0251701jes`.

[3] B. G. Pollet, S. S. Kocha, and I. Staffell. “Current status of automotive fuel cells for sustainable transport”. In: *Current Opinion in Electrochemistry* 16 (2019), pp. 90–95. ISSN: 24519103. DOI: `10.1016/j.coelec.2019.04.021`.

[4] A. Gissler, C. Raab, M. Tix, and S. Merk. *Electric Vehicle Market Attractiveness. Unraveling Challenges and Opportunities.* 2016 (accessed March 11, 2020). URL: `https://www.accenture.com/_acnmedia/pdf-37/accenture-electric-vehicle-market-attractiveness.pdf`.

[5] S. M. Knupfer, R. Hensley, P. Hertzke, and P. Schaufuss. *Electrifying insights: How automakers can drive electrified vehicle sales and profitability.* 2017 (accessed March 11, 2020). URL: `https://www.mckinsey.com/industries/automotive-and-assembly/our-insights/electrifying-insights-how-automakers-can-drive-electrified-vehicle-sales-and-profitability`.

[6] Xavier Mosquet, Hadi Zablit, Andreas Dinger, Gang Xu, Michelle Andersen, and and Kazutoshi Tominaga. *The Electric Car Tipping Point.* 2018 (accessed March 11, 2020). URL: `https://www.bcg.com/de-de/publications/2018/electric-car-tipping-point.aspx`.

[7] H. Wu, G. Alberts, J. Hooper, and B. Walton. *New market. New entrants. New challenges. Battery Electric Vehicles.* 2019 (accessed March 11, 2020). URL: `https://www2.deloitte.com/content/dam/Deloitte/uk/Documents/manufacturing/deloitte-uk-battery-electric-vehicles.pdf`.

[8] J. Sieg, J. Bandlow, T. Mitsch, D. Dragicevic, T. Materna, B. Spier, H. Witzenhausen, M. Ecker, and D. U. Sauer. “Fast charging of an electric vehicle lithium-ion battery at the limit of the lithium deposition process”. In: *Journal of Power Sources* 427 (2019), pp. 260–270. ISSN: 03787753. DOI: `10.1016/j.jpowsour.2019.04.047`.

[9] X.-G. Yang and C.-Y. Wang. “Understanding the trilemma of fast charging, energy density and cycle life of lithium-ion batteries”. In: *Journal of Power Sources* 402 (2018), pp. 489–498. ISSN: 03787753. DOI: `10.1016/j.jpowsour.2018.09.069`.

[10] J. Wenig, M. Sodenkamp, and T. Staake. “Battery versus infrastructure: Tradeoffs between battery capacity and charging infrastructure for plug-in hybrid electric vehicles”. In: *Applied Energy* 255 (2019), p. 113787. ISSN: 03062619. DOI: `10.1016/j.apenergy.2019.113787`.

[11] Y. Baik, R. Hensley, P. Hertzke, and S. Knupfer. *Making electric vehicles profitable.* 2019 (accessed March 11, 2020). URL: `https://www.mckinsey.com/industries/automotive-and-assembly/our-insights/making-electric-vehicles-profitable`.

[12] B. Nykvist and M. Nilsson. “Rapidly falling costs of battery packs for electric vehicles”. In: *Nature Climate Change* 5.4 (2015), pp. 329–332. ISSN: 1758-678X. DOI: `10.1038/nclimate2564`.

[13] Daniel Kuepper, Kristian Kuhlmann, Sebastian Wolf, Cornelius Pieper, Gang Xu, and and Justin Ahmad. *The Future of Battery Production in Electric Vehicles*. 2018 (accessed March 11, 2020). URL: `https://image-src.bcg.com/Images/BCG-The-Future-of-Battery-Production-for-Electric-Vehicles-Sep-2018%20%281%29_tcm9-202396.pdf`.

[14] E. C. Evarts. “Lithium batteries: To the limits of lithium”. In: *Nature* 526.7575 (2015), S93–5. DOI: `10.1038/526S93a`.

[15] M. Hu, X. Pang, and Z. Zhou. “Recent progress in high-voltage lithium ion batteries”. In: *Journal of Power Sources* 237 (2013), pp. 229–242. ISSN: 03787753. DOI: `10.1016/j.jpowsour.2013.03.024`.

[16] S. Goriparti, E. Miele, F. de Angelis, E. Di Fabrizio, R. Proietti Zaccaria, and C. Capiglia. “Review on recent progress of nanostructured anode materials for Li-ion batteries”. In: *Journal of Power Sources* 257 (2014), pp. 421–443. ISSN: 03787753. DOI: `10.1016/j.jpowsour.2013.11.103`.

[17] T. Vegge, J. M. Garcia-Lastra, and D. J. Siegel. “Lithium–oxygen batteries: At a crossroads?” In: *Current Opinion in Electrochemistry* 6.1 (2017), pp. 100–107. ISSN: 24519103. DOI: `10.1016/j.coelec.2017.10.014`.

[18] J. Liu, Q. Zhang, and Y.-K. Sun. “Recent progress of advanced binders for Li-S batteries”. In: *Journal of Power Sources* 396 (2018), pp. 19–32. ISSN: 03787753. DOI: `10.1016/j.jpowsour.2018.05.096`.

[19] A. Eftekhari and D.-W. Kim. “Sodium-ion batteries: New opportunities beyond energy storage by lithium”. In: *Journal of Power Sources* 395 (2018), pp. 336–348. ISSN: 03787753. DOI: `10.1016/j.jpowsour.2018.05.089`.

[20] J. W. Choi and D. Aurbach. “Promise and reality of post-lithium-ion batteries with high energy densities”. In: *Nature Reviews Materials* 1.4 (2016), p. 359. DOI: `10.1038/natrevmats.2016.13`.

[21] A. Sakti, J. J. Michalek, E. R. Fuchs, and J. F. Whitacre. “A techno-economic analysis and optimization of Li-ion batteries for light-duty passenger vehicle electrification”. In: *Journal of Power Sources* 273 (2015), pp. 966–980. ISSN: 03787753. DOI: `10.1016/j.jpowsour.2014.09.078`.

[22] P. A. Nelson, S. Ahmed, K. G. Gallagher, and D. W. Dees. “Cost savings for manufacturing lithium batteries in a flexible plant”. In: *Journal of Power Sources* 283 (2015), pp. 506–516. ISSN: 03787753. DOI: `10.1016/j.jpowsour.2015.02.142`.

[23] D. L. Wood, J. Li, and C. Daniel. “Prospects for reducing the processing cost of lithium ion batteries”. In: *Journal of Power Sources* 275 (2015), pp. 234–242. ISSN: 03787753. DOI: `10.1016/j.jpowsour.2014.11.019`.

[24] Donald Chung, Emma Elgqvist, and Shriram Santhanagopalan: Clean Energy Manufacturing Analysis Center. “Automotive Lithium-ion Cell Manufacturing: Regional Cost Structures and Supply Chain Considerations”. In: ().

[25] H. Vikström, S. Davidsson, and M. Höök. “Lithium availability and future production outlooks”. In: *Applied Energy* 110 (2013), pp. 252–266. ISSN: 03062619. DOI: `10.1016/j.apenergy.2013.04.005`.

[26] Volker Reber. *Neue Möglichkeiten durch Laden mit 800 Volt.* 2016 (accessed March 15, 2019). URL: `https://www.porscheengineering.com/filestore/download/peg/de/pemagazin-01-2016-artikel-e-power/default/047e5361-3dfb-11e6-8697-0019999cd470/e-power-%E2%80%93-Neue-M%C3%B6glichkeiten-durch-Laden-mit-800-Volt-Porsche-Engineering-Magazin-01-2016.pdf`.

[27] S. M. Rezvanizaniani, Z. Liu, Y. Chen, and J. Lee. "Review and recent advances in battery health monitoring and prognostics technologies for electric vehicle (EV) safety and mobility". In: *Journal of Power Sources* 256 (2014), pp. 110–124. ISSN: 03787753. DOI: `10.1016/j.jpowsour.2014.01.085`.

[28] J. A. G. Rheinfeld. "Performance and Safety of Lithium-Ion Electrodes and Cells: Modeling, Simulation, and Validation at Elevated Temperatures and Currents". Dissertation. München: Technische Universität München, 2019.

[29] C. F. Lopez, J. A. Jeevarajan, and P. P. Mukherjee. "Experimental Analysis of Thermal Runaway and Propagation in Lithium-Ion Battery Modules". In: *Journal of The Electrochemical Society* 162.9 (2015), A1905–A1915. ISSN: 0013-4651. DOI: `10.1149/2.0921509jes`.

[30] D. Ouyang, J. Liu, M. Chen, J. Weng, and J. Wang. "An Experimental Study on the Thermal Failure Propagation in Lithium-Ion Battery Pack". In: *Journal of The Electrochemical Society* 165.10 (2018), A2184–A2193. ISSN: 0013-4651. DOI: `10.1149/2.0721810jes`.

[31] Z. Liao, S. Zhang, K. Li, G. Zhang, and T. G. Habetler. "A survey of methods for monitoring and detecting thermal runaway of lithium-ion batteries". In: *Journal of Power Sources* 436 (2019), p. 226879. ISSN: 03787753. DOI: `10.1016/j.jpowsour.2019.226879`.

[32] L. Jiang, Z. Luo, T. Wu, L. Shao, J. Sun, C. Liu, G. Li, K. Cao, and Q. Wang. "Overcharge Behavior and Early Warning Analysis of LiNi 0.5 Co 0.2 Mn 0.3 O 2 /C Lithium-Ion Battery with High Capacity". In: *Journal of The Electrochemical Society* 166.6 (2019), A1055–A1062. ISSN: 0013-4651. DOI: `10.1149/2.0661906jes`.

[33] A. W. Golubkov, S. Scheikl, R. Planteu, G. Voitic, H. Wiltsche, C. Stangl, G. Fauler, A. Thaler, and V. Hacker. "Thermal runaway of commercial 18650 Li-ion batteries with LFP and NCA cathodes – impact of state of charge and overcharge". In: *RSC Advances* 5.70 (2015), pp. 57171–57186. DOI: `10.1039/C5RA05897J`.

[34] C. Fear, D. Juarez-Robles, J. A. Jeevarajan, and P. P. Mukherjee. "Elucidating Copper Dissolution Phenomenon in Li-Ion Cells under Overdischarge Extremes". In: *Journal of The Electrochemical Society* 165.9 (2018), A1639–A1647. ISSN: 0013-4651. DOI: `10.1149/2.0671809jes`.

[35] M. Ecker, P. Shafiei Sabet, and D. U. Sauer. "Influence of operational condition on lithium plating for commercial lithium-ion batteries – Electrochemical experiments and post-mortem-analysis". In: *Applied Energy* 206 (2017), pp. 934–946. ISSN: 03062619. DOI: `10.1016/j.apenergy.2017.08.034`.

[36] M. Petzl, M. Kasper, and M. A. Danzer. "Lithium plating in a commercial lithium-ion battery – A low-temperature aging study". In: *Journal of Power Sources* 275 (2015), pp. 799–807. ISSN: 03787753. DOI: `10.1016/j.jpowsour.2014.11.065`.

[37] L. Lu, X. Han, J. Li, J. Hua, and M. Ouyang. "A review on the key issues for lithium-ion battery management in electric vehicles". In: *Journal of Power Sources* 226 (2013), pp. 272–288. ISSN: 03787753. DOI: `10.1016/j.jpowsour.2012.10.060`.

[38] W. Waag, S. Käbitz, and D. U. Sauer. “Experimental investigation of the lithium-ion battery impedance characteristic at various conditions and aging states and its influence on the application”. In: *Applied Energy* 102 (2013), pp. 885–897. ISSN: 03062619. DOI: `10.1016/j.apenergy.2012.09.030`.

[39] D. Andrea. *Battery Management Systems for Large Lithium Ion Battery Packs.* EBL-Schweitzer. Artech House, 2010. ISBN: 9781608071050. URL: `https://books.google.de/books?id=o-QpFOROPTcC`.

[40] J. Schnell, C. Nentwich, F. Endres, A. Kollenda, F. Distel, T. Knoche, and G. Reinhart. “Data mining in lithium-ion battery cell production”. In: *Journal of Power Sources* 413 (2019), pp. 360–366. ISSN: 03787753. DOI: `10.1016/j.jpowsour.2018.12.062`.

[41] B. Kenney, K. Darcovich, D. D. MacNeil, and I. J. Davidson. “Modelling the impact of variations in electrode manufacturing on lithium-ion battery modules”. In: *Journal of Power Sources* 213 (2012), pp. 391–401. ISSN: 03787753. DOI: `10.1016/j.jpowsour.2012.03.065`.

[42] T. Baumhöfer, M. Brühl, S. Rothgang, and D. U. Sauer. “Production caused variation in capacity aging trend and correlation to initial cell performance”. In: *Journal of Power Sources* 247 (2014), pp. 332–338. ISSN: 03787753. DOI: `10.1016/j.jpowsour.2013.08.108`.

[43] P. Haussmann and J. Melbert. “Self-Discharge Observation for Onboard Safety Monitoring of Automotive Li-Ion Cells: Accelerated Procedures and Application Concept”. In: *SAE Technical Paper Series.* SAE Technical Paper Series. SAE International400 Commonwealth Drive, Warrendale, PA, United States, 2018. DOI: `10.4271/2018-01-0449`.

[44] K. Rumpf, M. Naumann, and A. Jossen. “Experimental investigation of parametric cell-to-cell variation and correlation based on 1100 commercial lithium-ion cells”. In: *Journal of Energy Storage* 14 (2017), pp. 224–243. ISSN: 2352152X. DOI: `10.1016/j.est.2017.09.010`.

[45] A. Fill, S. Koch, and K. P. Birke. “Analytical model of the current distribution of parallel-connected battery cells and strings”. In: *Journal of Energy Storage* 23 (2019), pp. 37–43. ISSN: 2352152X. DOI: `10.1016/j.est.2019.02.031`.

[46] C. Campestrini, P. Keil, S. F. Schuster, and A. Jossen. “Ageing of lithium-ion battery modules with dissipative balancing compared with single-cell ageing”. In: *Journal of Energy Storage* 6 (2016), pp. 142–152. ISSN: 2352152X. DOI: `10.1016/j.est.2016.03.004`.

[47] C. Pastor-Fernández, T. Bruen, W. D. Widanage, M. A. Gama-Valdez, and J. Marco. “A Study of Cell-to-Cell Interactions and Degradation in Parallel Strings: Implications for the Battery Management System”. In: *Journal of Power Sources* 329 (2016), pp. 574–585. ISSN: 03787753. DOI: `10.1016/j.jpowsour.2016.07.121`.

[48] M. Baumann, L. Wildfeuer, S. Rohr, and M. Lienkamp. “Parameter variations within Li-Ion battery packs – Theoretical investigations and experimental quantification”. In: *Journal of Energy Storage* 18 (2018), pp. 295–307. ISSN: 2352152X. DOI: `10.1016/j.est.2018.04.031`.

[49] S. F. Schuster, M. J. Brand, P. Berg, M. Gleissenberger, and A. Jossen. “Lithium-ion cell-to-cell variation during battery electric vehicle operation”. In: *Journal of Power Sources* 297 (2015), pp. 242–251. ISSN: 03787753. DOI: `10.1016/j.jpowsour.2015.08.001`.

[50] A. Tang, J. Li, L. Lou, C. Shan, and X. Yuan. “Optimization design and numerical study on water cooling structure for power lithium battery pack”. In: *Applied Thermal Engineering* 159 (2019), p. 113760. ISSN: 13594311. DOI: `10.1016/j.applthermaleng.2019.113760`.

[51] C. Zhao, W. Cao, T. Dong, and F. Jiang. "Thermal behavior study of discharging/charging cylindrical lithium-ion battery module cooled by channeled liquid flow". In: *International Journal of Heat and Mass Transfer* 120 (2018), pp. 751–762. ISSN: 00179310. DOI: `10.1016/j.ijheatmasstransfer.2017.12.083`.

[52] B. Wu, V. Yufit, M. Marinescu, G. J. Offer, R. F. Martinez-Botas, and N. P. Brandon. "Coupled thermal–electrochemical modelling of uneven heat generation in lithium-ion battery packs". In: *Journal of Power Sources* 243 (2013), pp. 544–554. ISSN: 03787753. DOI: `10.1016/j.jpowsour.2013.05.164`.

[53] X. M. Xu and R. He. "Research on the heat dissipation performance of battery pack based on forced air cooling". In: *Journal of Power Sources* 240 (2013), pp. 33–41. ISSN: 03787753. DOI: `10.1016/j.jpowsour.2013.03.004`.

[54] M. Ecker, N. Nieto, S. Käbitz, J. Schmalstieg, H. Blanke, A. Warnecke, and D. U. Sauer. "Calendar and cycle life study of Li(NiMnCo)O2-based 18650 lithium-ion batteries". In: *Journal of Power Sources* 248 (2014), pp. 839–851. ISSN: 03787753. DOI: `10.1016/j.jpowsour.2013.09.143`.

[55] M. Naumann, M. Schimpe, P. Keil, H. C. Hesse, and A. Jossen. "Analysis and modeling of calendar aging of a commercial LiFePO4/graphite cell". In: *Journal of Energy Storage* 17 (2018), pp. 153–169. ISSN: 2352152X. DOI: `10.1016/j.est.2018.01.019`.

[56] S. Paul, C. Diegelmann, H. Kabza, and W. Tillmetz. "Analysis of ageing inhomogeneities in lithium-ion battery systems". In: *Journal of Power Sources* 239 (2013), pp. 642–650. ISSN: 03787753. DOI: `10.1016/j.jpowsour.2013.01.068`.

[57] S. Ahmed et al. "Enabling fast charging – A battery technology gap assessment". In: *Journal of Power Sources* 367 (2017), pp. 250–262. ISSN: 03787753. DOI: `10.1016/j.jpowsour.2017.06.055`.

[58] M. Schimpe, M. Naumann, N. Truong, H. C. Hesse, S. Santhanagopalan, A. Saxon, and A. Jossen. "Energy efficiency evaluation of a stationary lithium-ion battery container storage system via electro-thermal modeling and detailed component analysis". In: *Applied Energy* 210 (2018), pp. 211–229. ISSN: 03062619. DOI: `10.1016/j.apenergy.2017.10.129`.

[59] U. Datta, A. Kalam, and J. Shi. "The relevance of large-scale battery energy storage (BES) application in providing primary frequency control with increased wind energy penetration". In: *Journal of Energy Storage* 23 (2019), pp. 9–18. ISSN: 2352152X. DOI: `10.1016/j.est.2019.02.013`.

[60] F. Zhang, X. Hu, R. Langari, and D. Cao. "Energy management strategies of connected HEVs and PHEVs: Recent progress and outlook". In: *Progress in Energy and Combustion Science* 73 (2019), pp. 235–256. ISSN: 03601285. DOI: `10.1016/j.pecs.2019.04.002`.

[61] Y. Huang, H. Wang, A. Khajepour, H. He, and J. Ji. "Model predictive control power management strategies for HEVs: A review". In: *Journal of Power Sources* 341 (2017), pp. 91–106. ISSN: 03787753. DOI: `10.1016/j.jpowsour.2016.11.106`.

[62] Y. Zhou, R. Wen, H. Wang, and H. Cai. "Optimal battery electric vehicles range: A study considering heterogeneous travel patterns, charging behaviors, and access to charging infrastructure". In: *Energy* (2020), p. 116945. ISSN: 03605442. DOI: `10.1016/j.energy.2020.116945`.

[63] C. Hu, B. D. Youn, and J. Chung. “A multiscale framework with extended Kalman filter for lithium-ion battery SOC and capacity estimation”. In: *Applied Energy* 92 (2012), pp. 694–704. ISSN: 03062619. DOI: `10.1016/j.apenergy.2011.08.002`.

[64] H. Dai, X. Wei, Z. Sun, J. Wang, and W. Gu. “Online cell SOC estimation of Li-ion battery packs using a dual time-scale Kalman filtering for EV applications”. In: *Applied Energy* 95 (2012), pp. 227–237. ISSN: 03062619. DOI: `10.1016/j.apenergy.2012.02.044`.

[65] L. Hu, X. Hu, Y. Che, F. Feng, X. Lin, and Z. Zhang. “Reliable state of charge estimation of battery packs using fuzzy adaptive federated filtering”. In: *Applied Energy* 262 (2020), p. 114569. ISSN: 03062619. DOI: `10.1016/j.apenergy.2020.114569`.

[66] X. Tang, Y. Wang, and Z. Chen. “A method for state-of-charge estimation of LiFePO4 batteries based on a dual-circuit state observer”. In: *Journal of Power Sources* 296 (2015), pp. 23–29. ISSN: 03787753. DOI: `10.1016/j.jpowsour.2015.07.028`.

[67] X. Tang, B. Liu, Z. Lv, and F. Gao. “Observer based battery SOC estimation: Using multi-gain-switching approach”. In: *Applied Energy* 204 (2017), pp. 1275–1283. ISSN: 03062619. DOI: `10.1016/j.apenergy.2017.03.079`.

[68] A. Farmann and D. U. Sauer. “A study on the dependency of the open-circuit voltage on temperature and actual aging state of lithium-ion batteries”. In: *Journal of Power Sources* 347 (2017), pp. 1–13. ISSN: 03787753. DOI: `10.1016/j.jpowsour.2017.01.098`.

[69] C. Campestrini, S. Kosch, and A. Jossen. “Influence of change in open circuit voltage on the state of charge estimation with an extended Kalman filter”. In: *Journal of Energy Storage* 12 (2017), pp. 149–156. ISSN: 2352152X. DOI: `10.1016/j.est.2017.04.011`.

[70] W. Waag, C. Fleischer, and D. U. Sauer. “Critical review of the methods for monitoring of lithium-ion batteries in electric and hybrid vehicles”. In: *Journal of Power Sources* 258 (2014), pp. 321–339. ISSN: 03787753. DOI: `10.1016/j.jpowsour.2014.02.064`.

[71] M. M. Hoque, M. A. Hannan, A. Mohamed, and A. Ayob. “Battery charge equalization controller in electric vehicle applications: A review”. In: *Renewable and Sustainable Energy Reviews* 75 (2017), pp. 1363–1385. ISSN: 13640321. DOI: `10.1016/j.rser.2016.11.126`.

[72] J. V. Barreras, C. Pinto, R. de Castro, E. Schaltz, S. J. Andreasen, and R. E. Araujo. “Multi-Objective Control of Balancing Systems for Li-Ion Battery Packs: A Paradigm Shift?” In: *2014 IEEE Vehicle Power and Propulsion Conference (VPPC)*. IEEE, 27.10.2014 - 30.10.2014, pp. 1–7. ISBN: 978-1-4799-6783-4. DOI: `10.1109/VPPC.2014.7007107`.

[73] Y. Zheng, M. Ouyang, L. Lu, J. Li, X. Han, and L. Xu. “On-line equalization for lithium-ion battery packs based on charging cell voltages: Part 1. Equalization based on remaining charging capacity estimation”. In: *Journal of Power Sources* 247 (2014), pp. 676–686. ISSN: 03787753. DOI: `10.1016/j.jpowsour.2013.09.030`.

[74] J. Gallardo-Lozano, E. Romero-Cadaval, M. I. Milanes-Montero, and M. A. Guerrero-Martinez. “Battery equalization active methods”. In: *Journal of Power Sources* 246 (2014), pp. 934–949. ISSN: 03787753. DOI: `10.1016/j.jpowsour.2013.08.026`.

[75] F. Baronti, R. Roncella, and R. Saletti. “Performance comparison of active balancing techniques for lithium-ion batteries”. In: *Journal of Power Sources* 267 (2014), pp. 603–609. ISSN: 03787753. DOI: `10.1016/j.jpowsour.2014.05.007`.

[76] K. Xu. “Nonaqueous liquid electrolytes for lithium-based rechargeable batteries”. In: *Chemical reviews* 104.10 (2004), pp. 4303–4417. ISSN: 0009-2665. DOI: `10.1021/cr030203g`.

[77] D. Aurbach. “Review of selected electrode–solution interactions which determine the performance of Li and Li ion batteries”. In: *Journal of Power Sources* 89.2 (2000), pp. 206–218. ISSN: 03787753. DOI: `10.1016/S0378-7753(00)00431-6`.

[78] M. Armand, F. Endres, D. R. MacFarlane, H. Ohno, and B. Scrosati. “Ionic-liquid materials for the electrochemical challenges of the future”. In: *Nature materials* 8.8 (2009), pp. 621–629. ISSN: 1476-1122. DOI: `10.1038/nmat2448`.

[79] X. Huang. “Separator technologies for lithium-ion batteries”. In: *Journal of Solid State Electrochemistry* 15.4 (2011), pp. 649–662. ISSN: 1432-8488. DOI: `10.1007/s10008-010-1264-9`.

[80] H. Maleki and J. N. Howard. “Effects of overdischarge on performance and thermal stability of a Li-ion cell”. In: *Journal of Power Sources* 160.2 (2006), pp. 1395–1402. ISSN: 03787753. DOI: `10.1016/j.jpowsour.2006.03.043`.

[81] R. Guo, L. Lu, M. Ouyang, and X. Feng. “Mechanism of the entire overdischarge process and overdischarge-induced internal short circuit in lithium-ion batteries”. In: *Scientific reports* 6 (2016), p. 30248. DOI: `10.1038/srep30248`.

[82] J. W. Braithwaite. “Corrosion of Lithium-Ion Battery Current Collectors”. In: *Journal of The Electrochemical Society* 146.2 (1999), p. 448. ISSN: 0013-4651. DOI: `10.1149/1.1391627`.

[83] A. H. Whitehead and M. Schreiber. “Current Collectors for Positive Electrodes of Lithium-Based Batteries”. In: *Journal of Power Sources* 152.11 (2005), A2105. ISSN: 03787753. DOI: `10.1149/1.2039587`.

[84] J. Chen, J. Liu, Y. Qi, T. Sun, and X. Li. “Unveiling the Roles of Binder in the Mechanical Integrity of Electrodes for Lithium-Ion Batteries”. In: *Journal of The Electrochemical Society* 160.9 (2013), A1502–A1509. ISSN: 0013-4651. DOI: `10.1149/2.088309jes`.

[85] S. Mandal, J. M. Amarilla, J. Ibáñez, and J. M. Rojo. “The Role of Carbon Black in LiMn[sub 2]O[sub 4]-Based Composites as Cathodes for Rechargeable Lithium Batteries”. In: *Journal of The Electrochemical Society* 148.1 (2001), A24. ISSN: 0013-4651. DOI: `10.1149/1.1339026`.

[86] Y. Lee, B. Son, J. Choi, J. H. Kim, M.-H. Ryou, and Y. M. Lee. “Effect of back-side-coated electrodes on electrochemical performances of lithium-ion batteries”. In: *Journal of Power Sources* 275 (2015), pp. 712–719. ISSN: 03787753. DOI: `10.1016/j.jpowsour.2014.11.029`.

[87] J. B. Quinn, T. Waldmann, K. Richter, M. Kasper, and M. Wohlfahrt-Mehrens. “Energy Density of Cylindrical Li-Ion Cells: A Comparison of Commercial 18650 to the 21700 Cells”. In: *Journal of The Electrochemical Society* 165.14 (2018), A3284–A3291. ISSN: 0013-4651. DOI: `10.1149/2.0281814jes`.

[88] R. E. Ciez and J. F. Whitacre. “Comparison between cylindrical and prismatic lithium-ion cell costs using a process based cost model”. In: *Journal of Power Sources* 340 (2017), pp. 273–281. ISSN: 03787753. DOI: `10.1016/j.jpowsour.2016.11.054`.

[89] A. Jain et al. “Commentary: The Materials Project: A materials genome approach to accelerating materials innovation”. In: *APL Materials* 1.1 (2013), p. 011002. DOI: `10.1063/1.4812323`.

[90] F. Lin, I. M. Markus, D. Nordlund, T.-C. Weng, M. D. Asta, H. L. Xin, and M. M. Doeff. “Surface reconstruction and chemical evolution of stoichiometric layered cathode materials for lithium-ion batteries”. In: *Nature communications* 5 (2014), p. 3529. DOI: `10.1038/ncomms4529`.

[91] S. K. Martha, O. Haik, E. Zinigrad, I. Exnar, T. Drezen, J. H. Miners, and D. Aurbach. “On the Thermal Stability of Olivine Cathode Materials for Lithium-Ion Batteries”. In: *Journal of The Electrochemical Society* 158.10 (2011), A1115. ISSN: 0013-4651. DOI: `10.1149/1.3622849`.

[92] J. B. Goodenough and Y. Kim. “Challenges for Rechargeable Li Batteries †”. In: *Chemistry of materials : a publication of the American Chemical Society* 22.3 (2010), pp. 587–603. ISSN: 0897-4756. DOI: `10.1021/cm901452z`.

[93] N. Nitta, F. Wu, J. T. Lee, and G. Yushin. “Li-ion battery materials: present and future”. In: *Materials Today* 18.5 (2015), pp. 252–264. ISSN: 13697021. DOI: `10.1016/j.mattod.2014.10.040`.

[94] H. Fujimoto, K. Tokumitsu, A. Mabuchi, N. Chinnasamy, and T. Kasuh. “The anode performance of the hard carbon for the lithium ion battery derived from the oxygen-containing aromatic precursors”. In: *Journal of Power Sources* 195.21 (2010), pp. 7452–7456. ISSN: 03787753. DOI: `10.1016/j.jpowsour.2010.05.041`.

[95] J. R. Szczech and S. Jin. “Nanostructured silicon for high capacity lithium battery anodes”. In: *Energy Environ. Sci.* 4.1 (2011), pp. 56–72. ISSN: 1754-5692. DOI: `10.1039/C0EE00281J`.

[96] C. S. Yoon, M. H. Choi, B.-B. Lim, E.-J. Lee, and Y.-K. Sun. “Review—High-Capacity Li[Ni 1-x Co x/2 Mn x/2]O 2 (x = 0.1, 0.05, 0) Cathodes for Next-Generation Li-Ion Battery”. In: *Journal of The Electrochemical Society* 162.14 (2015), A2483–A2489. ISSN: 0013-4651. DOI: `10.1149/2.0101514jes`.

[97] H.-J. Noh, S. Youn, C. S. Yoon, and Y.-K. Sun. “Comparison of the structural and electrochemical properties of layered Li[NixCoyMnz]O2 (x = 1/3, 0.5, 0.6, 0.7, 0.8 and 0.85) cathode material for lithium-ion batteries”. In: *Journal of Power Sources* 233 (2013), pp. 121–130. ISSN: 0378-7753. DOI: `https://doi.org/10.1016/j.jpowsour.2013.01.063`.

[98] S.-T. Myung, F. Maglia, K.-J. Park, C. S. Yoon, P. Lamp, S.-J. Kim, and Y.-K. Sun. “Nickel-Rich Layered Cathode Materials for Automotive Lithium-Ion Batteries: Achievements and Perspectives”. In: *ACS Energy Letters* 2.1 (2017), pp. 196–223. ISSN: 2380-8195. DOI: `10.1021/acsenergylett.6b00594`.

[99] V. G. Khomenko, V. Z. Barsukov, J. E. Doninger, and I. V. Barsukov. “Lithium-ion batteries based on carbon–silicon–graphite composite anodes”. In: *Journal of Power Sources* 165.2 (2007), pp. 598–608. ISSN: 03787753. DOI: `10.1016/j.jpowsour.2006.10.059`.

[100] B. Fuchsbichler, C. Stangl, H. Kren, F. Uhlig, and S. Koller. “High capacity graphite–silicon composite anode material for lithium-ion batteries”. In: *Journal of Power Sources* 196.5 (2011), pp. 2889–2892. ISSN: 03787753. DOI: `10.1016/j.jpowsour.2010.10.081`.

[101] R. Dash and S. Pannala. “Theoretical Limits of Energy Density in Silicon-Carbon Composite Anode Based Lithium Ion Batteries”. In: *Scientific reports* 6 (2016), p. 27449. DOI: `10.1038/srep27449`.

[102] D. Andre, S.-J. Kim, P. Lamp, S. F. Lux, F. Maglia, O. Paschos, and B. Stiaszny. “Future generations of cathode materials: An automotive industry perspective”. In: *Journal of Materials Chemistry A* 3.13 (2015), pp. 6709–6732. ISSN: 2050-7488. DOI: `10.1039/C5TA00361J`.

[103] National Platform for Electric Mobility. *Roadmap for an Integrated Cell and Battery Production in Germany.* 2016 (accessed February 1, 2019). URL: `http://nationale-plattform-elektromobilitaet.de/fileadmin/user_upload/Redaktion/Publikationen/AG2_Roadmap_Zellfertigung_eng_bf.pdf`.

[104] J. Sturm, A. Rheinfeld, I. Zilberman, F. B. Spingler, S. Kosch, F. Frie, and A. Jossen. “Modeling and simulation of inhomogeneities in a 18650 nickel-rich, silicon-graphite lithium-ion cell during fast charging”. In: *Journal of Power Sources* 412 (2019), pp. 204–223. ISSN: 03787753. DOI: `10.1016/j.jpowsour.2018.11.043`.

[105] M. Park, X. Zhang, M. Chung, G. B. Less, and A. M. Sastry. “A review of conduction phenomena in Li-ion batteries”. In: *Journal of Power Sources* 195.24 (2010), pp. 7904–7929. ISSN: 03787753. DOI: `10.1016/j.jpowsour.2010.06.060`.

[106] C. Wang and J. Hong. “Ionic/Electronic Conducting Characteristics of LiFePO[sub 4] Cathode Materials”. In: *Chemistry of materials : a publication of the American Chemical Society* 10.3 (2007), A65. ISSN: 0897-4756. DOI: `10.1149/1.2409768`.

[107] A. Nyman, T. G. Zavalis, R. Elger, M. Behm, and G. Lindbergh. “Analysis of the Polarization in a Li-Ion Battery Cell by Numerical Simulations”. In: *Journal of The Electrochemical Society* 157.11 (2010), A1236. ISSN: 0013-4651. DOI: `10.1149/1.3486161`.

[108] A. Jossen. “Fundamentals of battery dynamics”. In: *Journal of Power Sources* 154.2 (2006), pp. 530–538. ISSN: 03787753. DOI: `10.1016/j.jpowsour.2005.10.041`.

[109] M. D. Levi and D. Aurbach. “Diffusion Coefficients of Lithium Ions during Intercalation into Graphite Derived from the Simultaneous Measurements and Modeling of Electrochemical Impedance and Potentiostatic Intermittent Titration Characteristics of Thin Graphite Electrodes”. In: *The Journal of Physical Chemistry B* 101.23 (1997), pp. 4641–4647. ISSN: 1520-6106. DOI: `10.1021/jp9701911`.

[110] J. Vetter et al. “Ageing mechanisms in lithium-ion batteries”. In: *Journal of Power Sources* 147.1-2 (2005), pp. 269–281. ISSN: 03787753. DOI: `10.1016/j.jpowsour.2005.01.006`.

[111] S. Gantenbein, M. Weiss, and E. Ivers-Tiffée. “Impedance based time-domain modeling of lithium-ion batteries: Part I”. In: *Journal of Power Sources* 379 (2018), pp. 317–327. ISSN: 03787753. DOI: `10.1016/j.jpowsour.2018.01.043`.

[112] P. Keil and A. Jossen. “Charging protocols for lithium-ion batteries and their impact on cycle life—An experimental study with different 18650 high-power cells”. In: *Journal of Energy Storage* 6 (2016), pp. 125–141. ISSN: 2352152X. DOI: `10.1016/j.est.2016.02.005`.

[113] J. S. Newman and K. E. Thomas-Alyea. *Electrochemical systems*. 3. ed. Electrochemical Society series. Hoboken, N.J.: Wiley, 2004. ISBN: 978-0-471-47756-3.

[114] T. Ohzuku, I. Yasunobi, and S. Keijiro. “Formation of Lithium-Graphite Intercalation Compunds in Nonaqueous Electrolytes and Their Application as a Negative Electrode for a Lithium Ion (Shuttlecock) Cell”. In: *Journal of The Electrochemical Society* 140.9 (1993), pp. 2490–2498. DOI: `10.1149/1.2220849jes`.

[115] M. Dubarry, C. Truchot, and B. Y. Liaw. “Synthesize battery degradation modes via a diagnostic and prognostic model”. In: *Journal of Power Sources* 219 (2012), pp. 204–216. ISSN: 03787753. DOI: `10.1016/j.jpowsour.2012.07.016`.

[116] C. R. Birkl, M. R. Roberts, E. McTurk, P. G. Bruce, and D. A. Howey. “Degradation diagnostics for lithium ion cells”. In: *Journal of Power Sources* 341 (2017), pp. 373–386. ISSN: 03787753. DOI: `10.1016/j.jpowsour.2016.12.011`.

[117] K. Kleiner, P. Jakes, S. Scharner, V. Liebau, and H. Ehrenberg. “Changes of the balancing between anode and cathode due to fatigue in commercial lithium-ion cells”. In: *Journal of Power Sources* 317 (2016), pp. 25–34. ISSN: 03787753. DOI: `10.1016/j.jpowsour.2016.03.049`.

[118] I. Bloom, A. N. Jansen, D. P. Abraham, J. Knuth, S. A. Jones, V. S. Battaglia, and G. L. Henriksen. “Differential voltage analyses of high-power, lithium-ion cells”. In: *Journal of Power Sources* 139.1-2 (2005), pp. 295–303. ISSN: 03787753. DOI: `10.1016/j.jpowsour.2004.07.021`.

[119] P. Keil and A. Jossen. “Calendar Aging of NCA Lithium-Ion Batteries Investigated by Differential Voltage Analysis and Coulomb Tracking”. In: *Journal of The Electrochemical Society* 164.1 (2017), A6066–A6074. ISSN: 0013-4651. DOI: `10.1149/2.0091701jes`.

[120] X. Han, M. Ouyang, L. Lu, J. Li, Y. Zheng, and Z. Li. “A comparative study of commercial lithium ion battery cycle life in electrical vehicle: Aging mechanism identification”. In: *Journal of Power Sources* 251 (2014), pp. 38–54. ISSN: 03787753. DOI: `10.1016/j.jpowsour.2013.11.029`.

[121] M. Wetjen, D. Pritzl, R. Jung, S. Solchenbach, R. Ghadimi, and H. A. Gasteiger. “Differentiating the Degradation Phenomena in Silicon-Graphite Electrodes for Lithium-Ion Batteries”. In: *Journal of The Electrochemical Society* 164.12 (2017), A2840–A2852. ISSN: 0013-4651. DOI: `10.1149/2.1921712jes`.

[122] M. Klett, J. A. Gilbert, S. E. Trask, B. J. Polzin, A. N. Jansen, D. W. Dees, and D. P. Abraham. “Electrode Behavior RE-Visited: Monitoring Potential Windows, Capacity Loss, and Impedance Changes in Li 1.03 (Ni 0.5 Co 0.2 Mn 0.3) 0.97 O 2 /Silicon-Graphite Full Cells”. In: *Journal of The Electrochemical Society* 163.6 (2016), A875–A887. ISSN: 0013-4651. DOI: `10.1149/2.0271606jes`.

[123] M. Wetjen, S. Solchenbach, D. Pritzl, J. Hou, V. Tileli, and H. A. Gasteiger. “Morphological Changes of Silicon Nanoparticles and the Influence of Cutoff Potentials in Silicon-Graphite Electrodes”. In: *Journal of The Electrochemical Society* 165.7 (2018), A1503–A1514. ISSN: 0013-4651. DOI: `10.1149/2.1261807jes`.

[124] S. Müller, P. Pietsch, B.-E. Brandt, P. Baade, V. de Andrade, F. de Carlo, and V. Wood. “Quantification and modeling of mechanical degradation in lithium-ion batteries based on nanoscale imaging”. In: *Nature communications* 9.1 (2018), p. 2340. DOI: `10.1038/s41467-018-04477-1`.

[125] O. Dolotko, A. Senyshyn, M. J. Mühlbauer, K. Nikolowski, F. Scheiba, and H. Ehrenberg. “Fatigue Process in Li-Ion Cells: An In Situ Combined Neutron Diffraction and Electrochemical Study”. In: *Journal of The Electrochemical Society* 159.12 (2012), A2082–A2088. ISSN: 0013-4651. DOI: `10.1149/2.080212jes`.

[126] W. M. Dose, V. A. Maroni, M. J. Piernas-Muñoz, S. E. Trask, I. Bloom, and C. S. Johnson. “Assessment of Li-Inventory in Cycled Si-Graphite Anodes Using LiFePO 4 as a Diagnostic Cathode”. In: *Journal of The Electrochemical Society* 165.10 (2018), A2389–A2396. ISSN: 0013-4651. DOI: `10.1149/2.1271810jes`.

[127] S. Shiotani, T. Naka, M. Morishima, M. Yonemura, T. Kamiyama, Y. Ishikawa, Y. Ukyo, Y. Uchimoto, and Z. Ogumi. “Degradation analysis of 18650-type lithium-ion cells by operando neutron diffraction”. In: *Journal of Power Sources* 325 (2016), pp. 404–409. ISSN: 03787753. DOI: `10.1016/j.jpowsour.2016.06.026`.

[128] N. Paul et al. “Aging in 18650-type Li-ion cells examined with neutron diffraction, electrochemical analysis and physico-chemical modeling”. In: *Journal of Energy Storage* 17 (2018), pp. 383–394. ISSN: 2352152X. DOI: `10.1016/j.est.2018.03.016`.

[129] T. Waldmann, M. Wilka, M. Kasper, M. Fleischhammer, and M. Wohlfahrt-Mehrens. “Temperature dependent ageing mechanisms in Lithium-ion batteries – A Post-Mortem study”. In: *Journal of Power Sources* 262 (2014), pp. 129–135. ISSN: 03787753. DOI: `10.1016/j.jpowsour.2014.03.112`.

[130] T. Waldmann, B.-I. Hogg, and M. Wohlfahrt-Mehrens. “Li plating as unwanted side reaction in commercial Li-ion cells – A review”. In: *Journal of Power Sources* 384 (2018), pp. 107–124. ISSN: 03787753. DOI: `10.1016/j.jpowsour.2018.02.063`.

[131] M. Ouyang, Z. Chu, L. Lu, J. Li, X. Han, X. Feng, and G. Liu. “Low temperature aging mechanism identification and lithium deposition in a large format lithium iron phosphate battery for different charge profiles”. In: *Journal of Power Sources* 286 (2015), pp. 309–320. ISSN: 03787753. DOI: `10.1016/j.jpowsour.2015.03.178`.

[132] C. von Lüders, J. Keil, M. Webersberger, and A. Jossen. “Modeling of lithium plating and lithium stripping in lithium-ion batteries”. In: *Journal of Power Sources* 414 (2019), pp. 41–47. ISSN: 03787753. DOI: `10.1016/j.jpowsour.2018.12.084`.

[133] D. Ren, K. Smith, D. Guo, X. Han, X. Feng, L. Lu, M. Ouyang, and J. Li. “Investigation of Lithium Plating-Stripping Process in Li-Ion Batteries at Low Temperature Using an Electrochemical Model”. In: *Journal of The Electrochemical Society* 165.10 (2018), A2167–A2178. ISSN: 0013-4651. DOI: `10.1149/2.0661810jes`.

[134] C. von Lüders, V. Zinth, S. V. Erhard, P. J. Osswald, M. Hofmann, R. Gilles, and A. Jossen. “Lithium plating in lithium-ion batteries investigated by voltage relaxation and in situ neutron diffraction”. In: *Journal of Power Sources* 342 (2017), pp. 17–23. ISSN: 03787753. DOI: `10.1016/j.jpowsour.2016.12.032`.

[135] C. Uhlmann, J. Illig, M. Ender, R. Schuster, and E. Ivers-Tiffée. “In situ detection of lithium metal plating on graphite in experimental cells”. In: *Journal of Power Sources* 279 (2015), pp. 428–438. ISSN: 03787753. DOI: `10.1016/j.jpowsour.2015.01.046`.

[136] M. J. Brand, M. H. Hofmann, M. Steinhardt, S. F. Schuster, and A. Jossen. “Current distribution within parallel-connected battery cells”. In: *Journal of Power Sources* 334 (2016), pp. 202–212. ISSN: 03787753. DOI: `10.1016/j.jpowsour.2016.10.010`.

[137] M. H. Hofmann, K. Czyrka, M. J. Brand, M. Steinhardt, A. Noel, F. B. Spingler, and A. Jossen. “Dynamics of current distribution within battery cells connected in parallel”. In: *Journal of Energy Storage* 20 (2018), pp. 120–133. ISSN: 2352152X. DOI: `10.1016/j.est.2018.08.013`.

[138] K. Rumpf, A. Rheinfeld, M. Schindler, J. Keil, T. Schua, and A. Jossen. “Influence of Cell-to-Cell Variations on the Inhomogeneity of Lithium-Ion Battery Modules”. In: *Journal of The Electrochemical Society* 165.11 (2018), A2587–A2607. ISSN: 0013-4651. DOI: `10.1149/2.0111811jes`.

[139] Y. Ozawa, R. Yazami, and B. Fultz. “Self-discharge study of LiCoO2 cathode materials”. In: *Journal of Power Sources* 119-121 (2003), pp. 918–923. ISSN: 03787753. DOI: `10.1016/S0378-7753(03)00227-1`.

[140] M. Lewerenz, S. Käbitz, M. Knips, J. Münnix, J. Schmalstieg, A. Warnecke, and D. U. Sauer. “New method evaluating currents keeping the voltage constant for fast and highly resolved measurement of Arrhenius relation and capacity fade”. In: *Journal of Power Sources* 353 (2017), pp. 144–151. ISSN: 03787753. DOI: `10.1016/j.jpowsour.2017.03.136`.

[141] X. Zeng et al. "Kinetic Study of Parasitic Reactions in Lithium-Ion Batteries: A Case Study on LiNi(0.6)Mn(0.2)Co(0.2)O2". In: *ACS applied materials & interfaces* 8.5 (2016), pp. 3446–3451. DOI: `10.1021/acsami.5b11800`.

[142] J. P. Schmidt, A. Weber, and E. Ivers-Tiffée. "A novel and fast method of characterizing the self-discharge behavior of lithium-ion cells using a pulse-measurement technique". In: *Journal of Power Sources* 274 (2015), pp. 1231–1238. ISSN: 03787753. DOI: `10.1016/j.jpowsour.2014.10.163`.

[143] T. Deutschen, S. Gasser, M. Schaller, and J. Siehr. "Modeling the self-discharge by voltage decay of a NMC/graphite lithium-ion cell". In: *Journal of Energy Storage* 19 (2018), pp. 113–119. DOI: `10.1016/j.est.2018.07.003`.

[144] D. Bernardi. "A General Energy Balance for Battery Systems". In: *Journal of The Electrochemical Society* 132.1 (1985), p. 5. ISSN: 00134651. DOI: `10.1149/1.2113792`.

[145] J. P. Schmidt, A. Weber, and E. Ivers-Tiffée. "A novel and precise measuring method for the entropy of lithium-ion cells: Delta S via electrothermal impedance spectroscopy". In: *Electrochimica Acta* 137 (2014), pp. 311–319. ISSN: 00134686. DOI: `10.1016/j.electacta.2014.05.153`.

[146] V. V. Viswanathan, D. Choi, D. Wang, W. Xu, S. Towne, R. E. Williford, J.-G. Zhang, J. Liu, and Z. Yang. "Effect of entropy change of lithium intercalation in cathodes and anodes on Li-ion battery thermal management". In: *Journal of Power Sources* 195.11 (2010), pp. 3720–3729. ISSN: 03787753. DOI: `10.1016/j.jpowsour.2009.11.103`.

[147] N. S. Hudak, L. E. Davis, and G. Nagasubramanian. "Cycling-Induced Changes in the Entropy Profiles of Lithium Cobalt Oxide Electrodes". In: *Journal of the Electrochemical Society* 162.3 (2014), A315–A321. ISSN: 0013-4651. DOI: `10.1149/2.0071503jes`.

[148] P. J. Osswald, M. d. Rosario, J. Garche, A. Jossen, and H. E. Hoster. "Fast and Accurate Measurement of Entropy Profiles of Commercial Lithium-Ion Cells". In: *Electrochimica Acta* 177 (2015), pp. 270–276. ISSN: 00134686. DOI: `10.1016/j.electacta.2015.01.191`.

[149] C. Forgez, D. Vinh Do, G. Friedrich, M. Morcrette, and C. Delacourt. "Thermal modeling of a cylindrical LiFePO4/graphite lithium-ion battery". In: *Journal of Power Sources* 195.9 (2010), pp. 2961–2968. ISSN: 03787753. DOI: `10.1016/j.jpowsour.2009.10.105`.

[150] A. Eddahech, O. Briat, and J.-M. Vinassa. "Thermal characterization of a high-power lithium-ion battery: Potentiometric and calorimetric measurement of entropy changes". In: *Energy* 61 (2013), pp. 432–439. ISSN: 03605442. DOI: `10.1016/j.energy.2013.09.028`.

[151] S. J. Bazinski and X. Wang. "The Influence of Cell Temperature on the Entropic Coefficient of a Lithium Iron Phosphate (LFP) Pouch Cell". In: *Journal of the Electrochemical Society* 161.1 (2013), A168–A175. ISSN: 0013-4651. DOI: `10.1149/2.082401jes`.

[152] K.-C. Chiu, C.-H. Lin, S.-F. Yeh, Y.-H. Lin, C.-S. Huang, and K.-C. Chen. "Cycle life analysis of series connected lithium-ion batteries with temperature difference". In: *Journal of Power Sources* 263 (2014), pp. 75–84. ISSN: 03787753. DOI: `10.1016/j.jpowsour.2014.04.034`.

[153] X. Wang, Z. Wang, L. Wang, Z. Wang, and H. Guo. "Dependency analysis and degradation process-dependent modeling of lithium-ion battery packs". In: *Journal of Power Sources* 414 (2019), pp. 318–326. ISSN: 03787753. DOI: `10.1016/j.jpowsour.2019.01.021`.

[154] S. Santhanagopalan and R. E. White. "Quantifying Cell-to-Cell Variations in Lithium Ion Batteries". In: *International Journal of Electrochemistry* 2012.12 (2012), pp. 1–10. DOI: `10.1155/2012/395838`.

[155] M. P. Klein and J. W. Park. “Current Distribution Measurements in Parallel-Connected Lithium-Ion Cylindrical Cells under Non-Uniform Temperature Conditions”. In: *Journal of The Electrochemical Society* 164.9 (2017), A1893–A1906. ISSN: 0013-4651. DOI: `10.1149/2.0011709jes`.

[156] A. Cordoba-Arenas, S. Onori, and G. Rizzoni. “A control-oriented lithium-ion battery pack model for plug-in hybrid electric vehicle cycle-life studies and system design with consideration of health management”. In: *Journal of Power Sources* 279 (2015), pp. 791–808. ISSN: 03787753. DOI: `10.1016/j.jpowsour.2014.12.048`.

[157] Y. Zheng, M. Ouyang, L. Lu, and J. Li. “Understanding aging mechanisms in lithium-ion battery packs: From cell capacity loss to pack capacity evolution”. In: *Journal of Power Sources* 278 (2015), pp. 287–295. ISSN: 03787753. DOI: `10.1016/j.jpowsour.2014.12.105`.

[158] D. Linden and T. B. Reddy. *Linden’s handbook of batteries.* 3ed ed. New York: McGraw-Hill, 2001. ISBN: 0071359788.

[159] I. Hadjipaschalis, A. Poullikkas, and V. Efthimiou. “Overview of current and future energy storage technologies for electric power applications”. In: *Renewable and Sustainable Energy Reviews* 13.6-7 (2009), pp. 1513–1522. ISSN: 13640321. DOI: `10.1016/j.rser.2008.09.028`.

[160] F. M. Kindermann, A. Noel, S. V. Erhard, and A. Jossen. “Long-term equalization effects in Li-ion batteries due to local state of charge inhomogeneities and their impact on impedance measurements”. In: *Electrochimica Acta* 185 (2015), pp. 107–116. ISSN: 00134686. DOI: `10.1016/j.electacta.2015.10.108`.

[161] C. Weng, J. Sun, and H. Peng. “A unified open-circuit-voltage model of lithium-ion batteries for state-of-charge estimation and state-of-health monitoring”. In: *Journal of Power Sources* 258 (2014), pp. 228–237. ISSN: 03787753. DOI: `10.1016/j.jpowsour.2014.02.026`.

[162] J. P. Schmidt, H. Y. Tran, J. Richter, E. Ivers-Tiffée, and M. Wohlfahrt-Mehrens. “Analysis and prediction of the open circuit potential of lithium-ion cells”. In: *Journal of Power Sources* 239 (2013), pp. 696–704. ISSN: 03787753. DOI: `10.1016/j.jpowsour.2012.11.101`.

[163] C. R. Birkl, E. McTurk, M. R. Roberts, P. G. Bruce, and D. A. Howey. “A Parametric Open Circuit Voltage Model for Lithium Ion Batteries”. In: *Journal of The Electrochemical Society* 162.12 (2015), A2271–A2280. ISSN: 0013-4651. DOI: `10.1149/2.0331512jes`.

[164] F. Zheng, Y. Xing, J. Jiang, B. Sun, J. Kim, and M. Pecht. “Influence of different open circuit voltage tests on state of charge online estimation for lithium-ion batteries”. In: *Applied Energy* 183 (2016), pp. 513–525. ISSN: 03062619. DOI: `10.1016/j.apenergy.2016.09.010`.

[165] C. Lin, Q. Yu, R. Xiong, and Y. Le Wang. “A study on the impact of open circuit voltage tests on state of charge estimation for lithium-ion batteries”. In: *Applied Energy* 205 (2017), pp. 892–902. ISSN: 03062619. DOI: `10.1016/j.apenergy.2017.08.124`.

[166] L. J. Krause, L. D. Jensen, and J. R. Dahn. “Measurement of Parasitic Reactions in Li Ion Cells by Electrochemical Calorimetry”. In: *Journal of The Electrochemical Society* 159.7 (2012), A937–A943. ISSN: 0013-4651. DOI: `10.1149/2.021207jes`.

[167] K. E. Thomas and J. Newman. “Thermal Modeling of Porous Insertion Electrodes”. In: *Electrochimica Acta* 150.2 (2003), A176. ISSN: 00134686. DOI: `10.1149/1.1531194`.

[168] I. Zilberman, A. Rheinfeld, and A. Jossen. “Uncertainties in entropy due to temperature path dependent voltage hysteresis in Li-ion cells”. In: *Journal of Power Sources* 395 (2018), pp. 179–184. ISSN: 03787753. DOI: `10.1016/j.jpowsour.2018.05.052`.

[169] F. Baronti, N. Femia, R. Saletti, C. Visone, and W. Zamboni. “Preisach modelling of lithium-iron-phosphate battery hysteresis”. In: *Journal of Energy Storage* 4 (2015), pp. 51–61. ISSN: 2352152X. DOI: `10.1016/j.est.2015.09.004`.

[170] W. Dreyer, J. Jamnik, C. Guhlke, R. Huth, J. Moskon, and M. Gaberscek. “The thermodynamic origin of hysteresis in insertion batteries”. In: *Nature materials* 9.5 (2010), pp. 448–453. ISSN: 1476-1122. DOI: `10.1038/nmat2730`.

[171] Y. Wu and A. Jossen. “Entropy-induced temperature variation as a new indicator for state of health estimation of lithium-ion cells”. In: *Electrochimica Acta* 276 (2018), pp. 370–376. ISSN: 00134686. DOI: `10.1016/j.electacta.2018.04.203`.